ISSN number 0971 - 9709

The Journal of Indian Geophysical Union

VOLUME 22, ISSUE 5 | SEPTEMBER 2018

AN OPEN ACCESS BIMONTHLY JOURNAL OF IGU

EDITORIAL OFFICE
Indian Geophysical Union, NGRI Campus, Uppal Road, Hyderabad- 500 007
Telephone: +91 -40-27012799; 27012734; Telefax:+91-04-27171564
E. mail: jigu1963@gmail.com, website: www.j-igu.in

The Open Access Journal with six issues in a year publishes articles covering
Solid Earth Geosciences; Marine Geosciences; and Atmospheric, Space and Planetary Sciences.

Annual Subscription

Individual ₹ 1000 per issue and Institutional ₹ 5000 for six issues

Payments should be sent by DD drawn in favour of "The Treasurer, Indian Geophysical Union", payable at Hyderabad, Money Transfer/NEFT/RTGS (Inter-Bank Transfer), Treasurer, Indian Geophysical Union, State Bank of India, Habsiguda Branch, Habsiguda, Uppal Road, Hyderabad- 500 007
A/C: 52191021424, IFSC Code: SBIN0020087, MICR Code: 500002318, SWIFT Code: SBININBBHO9.

For correspondence, please contact, Hon. Secretary, Indian Geophysical Union, NGRI Campus, Uppal Road, Hyderabad - 500 007, India; Email: igu123@gmail.com; Ph: 040 27012799, 272012734

ISSN: 0257-7968 (Clarivate Analytics)
ISSN: 0971-9709 (NISCAIR)
Approved as bimonthly ESCI journal by Clarivate Analytics
Cited in Indian Citation Index (ICI), New Delhi
Evaluated by NISCAIR, New Delhi

CONTENTS

J. Ind. Geophys. Union (September 2018)
v.22, no.5, pp: 459-467

2D Seismic reflection data filtering using Time Slice Singular Spectrum Analysis for noise suppression: A case study from Singareni coalfield, India

R.K. Tiwari, R. Rajesh*, K. Dhanam and T. Seshunarayana
CSIR- National Geophysical Research Institute, Uppal Road, Hyderabad-500007, India.
*Corresponding Author: rekapalli@gmail.com

ABSTRACT
Complex noises that arise due to the nonlinear interaction of unwanted seismic signals (coherent and random noises), alter the primary reflections and create severe problems than the simple random noise in recognizing geological structures from seismic stack sections. We present here Time Slice Singular Spectrum Analysis (TSSSA) for the suppression of such noises from seismic records in time domain. The TSSSA involves organizing the spatial data (corrected for NMO) which corresponds to constant time into trajectory matrix for the reduction of noises that do not show large spatial coherency. The singular value decomposition based rank reduction of the trajectory matrix formulated from constant time slice helps to identify the noise in TSSSA with low Eigen values. We test the method on synthetic data contaminated with complex noises to demonstrate its 'robustness' for the identification of faults and then apply to high-resolution seismic reflection observations from Singareni coalfield, India. We find a good correlation between de-noised and pure synthetic data, which indicates the suppression of complex noise without any loss of seismic features. The application of TSSSA to pre and post stack seismic field data suggests significant improvement in signal to noise ratio. The reflections resembling the coal beds in the pre and post stack TSSSA processed depth sections clearly match with the reflectors in the synthetic trace generated from well log data. Finally, improvement in SNR and clear matching of fault structures and coal beds identified in the TSSSA processed data with regional fault structures and available geological information suggest the TSSSA as a robust method for seismic data conditioning.

Keywords: Complex noise suppression, Rank reduction, Singular Spectrum Analysis (SSA), Seismic reflection data, Singareni coalfield.

INTRODUCTION

High-resolution seismic records are useful for locating the geological structures like faults, folds, caved pillars, mined-out areas, and coal seam etc (Greenhalgh et al., 1986; Tselentis and Paraskevopoulos, 2002). However, seismic reflection data from the coal field suffer from interference of seismic waves that produce composite reflection pattern (Lawrence, 1991, 1992). Regardless of constructive or destructive interference, the primary reflections from the coal bed of interest undergo significant alterations. Consequently, the interference of seismic waves reflected from different coal beds lead to the complex reflection patterns, which deter the identification of individual beds (Lawrence, 1991, 1992). For example, interference of seismic waves with the same phase may produce pseudo high amplitudes in the recorded data. In addition to the complex reflection pattern, diffraction of seismic waves at sharp discontinuities also produces pseudo reflection amplitudes. The presence of such pseudo amplitudes due to the combined effect of aforementioned processes significantly alters the primary reflection amplitudes. Furthermore, there are always certain amounts of other (random and coherent) noises present in the seismic records. Thus, the seismic data obtained from the field represent the amalgamated response of earth's layered structure and complex noise.

The complex noise, for brevity, we refer here as a combination of various noises e.g. random, coherent, and erratic etc., which might have arisen from the human activities, source footprints, structural discontinuities or sharp geological boundaries etc. Unlike the random noise, which produces the "flat spectrum" in frequency domain, it is often difficult to predict complex noise easily due to their deceptive nature. Hence, it is imperative to look for alternate robust schemes to recognize the reflector patterns and discontinuities more precisely in the seismic records. The accurate processing and interpretation of field seismic data require only primary reflections. Researchers have employed several techniques involving the domain conversions to suppress the random and coherent noises and to recover the missing amplitudes from the seismic data acquired at regular and irregular intervals.

Ulrych (1988) and Trickett (2003) have presented Eigen Image processing approaches in time and frequency domains respectively for noises suppression and missing data reconstruction. The singular spectrum of the data helps to identify the noise in Eigen Image processing as the additive noise and data gaps increase the rank of the matrix. De-noised signal reconstruction from Eigen triplets (row and column eigenvectors and Eigen value) with high variance is a kind of rank reduction procedure in the above methods. Another singular spectrum based efficient algorithm, which utilizes the data trajectory matrices for separating signal and noise is the Singular Spectrum Analysis (SSA) (Broomhead and King, 1986a, 1986b; Fraedrich, 1986; Golyandina and Zhigljavsky, 2013; Rekapalli and Tiwari., 2015). The SSA designed for the analysis of non-linear geophysical data, successfully removes the noise along with simultaneous reconstruction of missing or scattered signal amplitudes (Vautard et al., 1992; Ghil et al., 2002). The decomposition of the data using data-adaptive basis functions in SSA helps accurate reconstruction of signal compared to the methods which are using fixed basis functions. Recently, Sacchi (2009) and Oropeza and Sacchi (2011) have developed and employed SSA based FXSSA and Multichannel SSA for simultaneous de-noising and data gap filling of seismic signals in frequency domain. However, these methods have been applied to data in frequency domain. The domain (time domain to frequency domain) conversion of non-stationary seismic data with discontinuities and abrupt changes generates artifacts. The SSA and MSSA of the frequency domain data further enhance the artifacts in the processed output (Rekapalli et al., 2014; Rekapalli and Tiwari, 2016). It is difficult to provide physical interpretation of seismic data assorted with such artifacts, especially for recognizing thin coal beds and their discontinuities. Therefore, we present here Time Slice Singular Spectrum Analysis (TSSSA) in time domain, to suppress the complex noise from seismic reflection data. The signal decomposition and reconstruction in the TSSSA is based on SSA and involves the data adaptive basis functions of the spatial seismic data (i.e., the data of all channels correspond to a fixed time).

We illustrate the methodology of TSSSA for complex noise suppression and also for scattered amplitude reconstruction of seismic reflection data. First we provide testing of the method on synthetic data assorted with complex noise and then its application to pre and post stack seismic datasets from Singareni coalfield, Telangana, India to indentify the fault structures and coal beds. Finally, we verify the validity of identified faults and coal beds using available geology of the study region and well data.

METHODOLOGY

Although there are wide varieties of frequency domain techniques for data de-noising and missing amplitude recovery, the data adaptive decomposition in SSA based time domain techniques are robust for accurate signal recovery. We apply the SSA to spatial series (i.e., data of all channels) corresponding to fixed time. The crustal layers show high lateral quasi-homogeneity on regional scales compared to chaotic variations in depth direction. Since the correlation among the primary amplitudes from a constant time/depth slice is always stronger than the noise correlation, it is possible to extract the correlated lateral signal to distinguish the primary signals from complex noise background. In this way, the analyses of seismic data of all channels at a fixed time as spatial series, allow us to suppress the noise in the TSSSA method. The reconstruction in this method is also a singular or Eigen spectrum based rank reduction (Trickett, 2003; Tiwari and Rajesh, 2014). Hence, we can use the Eigen spectra to identify the signal with significant Eigen values and noise with relatively low Eigen values. Using basic mathematical description of SSA (Golyandina et al., 2013), the TSSSA methodology is explained as follows:

Embedding the trajectory matrix: The TSSSA processing begins with embedding the trajectory matrix from the spatial data series represented by $Y(x) = \{y(x_1), y(x_2) \ldots y(x_N)\}$ using a window length L ($2>L<=N/2$).Here N is number of traces in the data and K ($=N-L+1$) represents the number of lagged vectors of Y(x) that form the trajectory matrix (**T**) of size $L\times K$.

$$\mathbf{T}_{L\times K} = [X_1 : \ldots : X_i : \ldots : X_K] \tag{1}$$

Where X_i represents a vector of length L given by $X_i = \{y(x_i), y(x_{i+1}), \ldots, y(x_{i+L-1})\}$ and x_i (for i=1 to N) represent the spatial position of geophones/ receivers.

Singular Value Decomposition of trajectory matrix: In the second step, the trajectory matrix was decomposed into eigenvector(Left and Right) and a diagonal eigen value matrix using Singular Value Decomposition (SVD).The decomposition of T given by

$$T = \sum_{i=1}^{d} \sqrt{\lambda_i}\, U_i V_i^T \tag{2}$$

Where, λ_i is the i^{th} eigenvalue corresponding to the i^{th} eigenvector $\mathbf{U_i}$ of TT^T and d is the no of nonzero eigenvalues. The triple denoted by ($\sqrt{\lambda_i}$, **Ui**, $\mathbf{V_i}$) is called the i^{th} Eigen triple. As discussed above, the seismic data is a combination of amplitudes from different processes (reflection, interference, diffraction etc.). The SVD allows us to estimate the signal amplitudes of different Eigen processes using respective Eigen value. Thus it is possible to identify the Eigen processes of noise with low eigenvalues and randomly fluctuating eigenvectors.

Eigen triplet grouping and reconstruction of trajectory matrix: In the next step, the Eigen triplets with significant variance and periodicity are grouped to reconstruct the trajectory matrix using the following equation

$$Tr = \sum_{G} \sqrt{\lambda_i}\, U_i V_i^T = \begin{bmatrix} x_{(1,1)} & \cdots & x_{(1,K)} \\ \vdots & \ddots & \vdots \\ x_{(L,1)} & \cdots & x_{(L,K)} \end{bmatrix} \tag{3}$$

Here G represents the group of Eigen triples satisfying the criteria of variance and eigenvector periodicity. The Eigenvector periodicity is useful to eliminate the very low frequency carrier and high frequency noise components.

Diagonal averaging of reconstructed trajectory matrix: Finally, we average the reconstructed trajectory matrix (Tr) along its anti-diagonals to obtain de-noised data series. Let us denote the reconstructed series by $X_{rc}=\{g_1, g_2 \ldots g_k \ldots\ldots g_N\}$. The averaging procedure can be written as follows

$$\mathbf{g_k} = \frac{1}{k}\sum_{m=1}^{k} x_{m,k-m+1} \quad \text{for } 0 < k < L \tag{4a}$$

$$\mathbf{g_k} = \frac{1}{L}\sum_{m=1}^{L} x_{m,k-m+1} \quad \text{for } L-1 < k < K+1 \tag{4b}$$

$$\mathbf{g_k} = \frac{1}{N-k+1}\sum_{m=k-K+1}^{L} x_{m,k-m+1} \quad \text{for } K < k \le N \tag{4c}$$

The TSSSA pseudo code used for the seismic data de-noising is shown below.

```
Pseudo Code
for i=1:Nt   (Nt→Number of sampling times/ time slices)
1) Take the i th  time slice of the data
2) Formulate the trajectory matrix
   Using an optimal window length (L)
3) Decompose the trajectory matrix into Eigentriplets
   i.e., (√λi , Ui , Vi) Eigenvalues and Eigenvectors
4) Group the eigentriplets
   Using Eiegnvector periodicity and Eigenvalue
5) Reconstruct the trajectory matrix (Tr) from selected triplets
6) Diagonally average Tr to obtain denoised data
end
```

Window length and Triplet group selection

The window length selection is crucial in the singular spectrum analysis (Patterson et al, 2011; Hassani et al, 2011). Accordingly, the window length equal to the classical limit N/2 would resolve the principal components completely. But, for large data sets, the decomposition of signal at window length N/2 is computationally expansive and more over the number of signal component present in the data would be much smaller than N/2. In such cases, it is appropriate to choose an optimal window length much smaller than N/2 that serve to resolve the independent signals from different processes. Based on theoretical verification, Hassani et al, (2011) have suggested that median of (1…..N) would be an appropriate choice of L for most of the real world data. However, the selection of appropriate window length should be made on the apriori knowledge of the curvature of the reflectors in the TSSSA, such that the primary reflections must be linear within a window. Hence, one should be careful while dealing the seismic data with curved events/ reflectors, which would require smaller window lengths than usually adopted in other analyses. It would be appropriate to applying the TSSSA method to normal move out (NMO) corrected data to circumvent hyperbolic curvature of the reflections to avoid conflicts arising in the window length selection.

The second important parameter needed to be discussed here is the appropriate selection Eigen triple group for de-noised signal reconstruction. The improper grouping would generate artifacts in the reconstructed data. There are several recent approaches (Hassani et al, 2012) for estimating the separation between individual Eigen components. In general, de-noising scheme adopts the variance/ eigenvalue based grouping (Trickett, 2003; Golyandina et al., 2013; Rekapalli and Tiwari, 2015). The paired Eigen triplets with nearly same Eigen value share the same physical process. Hence in dealing such paired Eigen triplets, either both the triplets are to be considered for reconstruction or both should be dropped to avoid the artifact generation. Following the above procedure, we have grouped the Eigen triples on the basis of variance of eigenvalue and periodicity of the eigenvectors, which is appropriate for the objectives of de-noising and reconstruction.

ANALYSIS AND RESULTS

Testing the TSSSA on synthetic data of fault model with Complex noise

Initially, we test the efficacy of TSSSA on synthetic data. The synthetic reflection data (Figure 1a) of a normal fault model was generated using the finite difference method. The complex noise is generated using the following equation

$$a_{t+1} = \mu . a_t . (1 - a_t) \tag{5}$$

Here μ can take the values between 0 and 4. We have selected μ=3.9 and a_1=0.1 to generate the synthetic noise. Diffracted and scattered energies are assumed to give rise to chaotic/ complex noise in the composite seismic signal. The effect of such complex noise is more severe at far offset. We use mixture of the noise generated using the equation 5 and random noise to contaminate the data.

We applied the TSSSA algorithm at various complex noise levels ranging from 10% to 40%. In each of the cases, 10% random noise was added as the background to simulate more realistic field situation. The noisy synthetic data with 20% noise (10% random +10% complex noise) and its de-noised output reconstructed using TSSSA are respectively shown in Figure 1b and Figure 1c. The results suggest that the signal reconstruction is fairly good and the scattered energy has been recovered in TSSSA output even

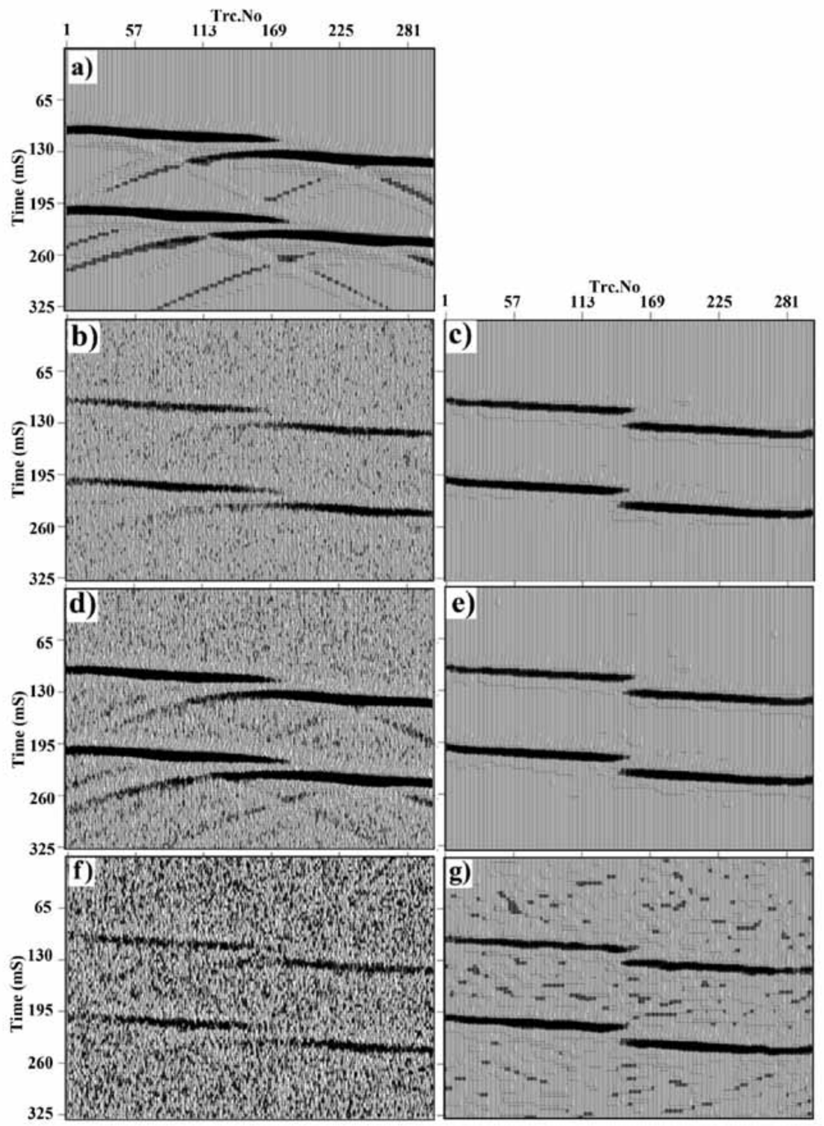

Figure 1. (a) Synthetic data of normal fault model with diffraction energy (b) Synthetic data contaminated with 20% complex noise (10% random +10% chaotic) (c)TSSSA output of Synthetic data shown in Figure 1b (d) Synthetic data contaminated with 30% complex noise (10% random +20% chaotic) (e) TSSSA output of Synthetic data shown in Figure 1d (f) Synthetic data contaminated with 50% complex noise (10% random noise +40% chaotic noise) (g)TSSSA output of Synthetic data shown in Figure 1f.

in the presence of diffraction energy. We have successfully removed the diffraction energy in addition to the added noise from the synthetic data. The synthetic data with 30% noise (10% random +20% complex noise) and 50% noise (10% random + 40% complex noises) and their TSSSA de-noised outputs are shown in Figure 1d to Figure 1g. The synthetic example demonstrates that the TSSSA is efficient up to 30% complex noise level (Figure 1e). Above this threshold, the method fails to suppress the noise. The noise in the TSSSA de-noise output shown in Figure 1g is an example that demonstrated the effect of above stated noise threshold.

Application to the field data

The study area Singareni coalfields (Telangana, India) as shown in Figure 2, is located near Ramagundam, in the Pranhita-Godavari (PG) Gondwana graben that formed in between the boundaries of Bastar and Dharwar cratons (Murthy and Rao, 1994). The Lower Gondwana rock formations in this region are affected by a complex system of faulting, which lead to the general eastern tilting, followed by erosion. The Overall strike is ~ NNW-SSE with ENE and WSW dipping. The NW-SE faults parallel to the PG basin boundary faults and NE-SW oriented faults

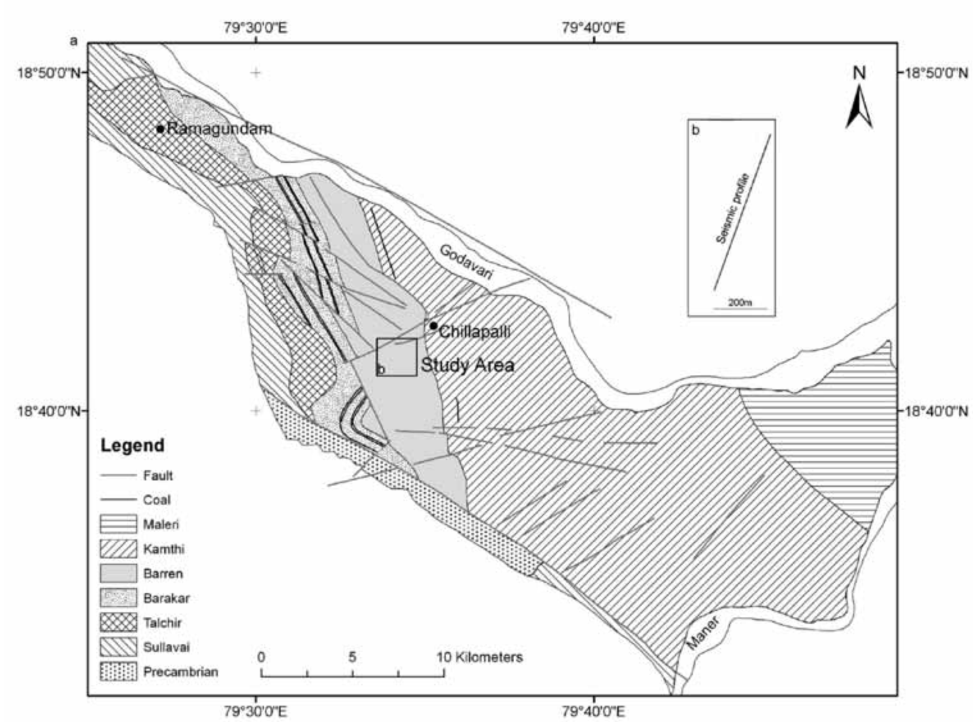

Figure 2. a) Geological map of the study area along with b) Location of the seismic profile.

are the two kinds of geologically probable faults which are could be observed in the study region. These faults are largely dip-slip faults (normal-sense) and appear to cut across all the Lower Gondwana formations, although there is a minor left-lateral strike-slip component (Murthy and Rao, 1994). According to the researchers, the fault systems observed are related to the Permian or Mesozoic fault systems (Biswas, 2003). The borehole litho-logs (<500 m deep) in the study area reveal that the coal seams are found in the lower segments of the boreholes, and are associated with carbonaceous shale, clay and sandstones in the depth range of ~200 to 500m. There are 7 coal seams, of which 4 are prominent with thickness varying in range 1 m to ~ 10 m. The above rock formations have been deformed, giving rise to dipping sedimentary bedding surfaces. The overall strike is ~ NNW-SSE and dips gently towards ENE. The amount of dipping varies from 6^{o} to 9^{o}. Borehole litho-logs also suggest the existence of two sets of wrench NW-SE to NNW-SSE and NNE-SSW oriented faulting in the study area. It appears that the fault interactions lead to the formation of complex graben and/or rifts in the study area. The vertical displacement of the faults in this region is nearly less than or equal to 5m. It is interesting to note that these small faults have kinematics history similar to the large-scale faults of the PG basin.

The high resolution seismic reflection data used in the present study was acquired from the study area shown in Figure 2 using 0.25mS sampling interval along the profile shown in Figure 2b. The 60 channels Geode system manufactured by geometrics was used in the data acquisition. Emulsion based explosive was used to generate high frequency energy to incorporate high resolution data. The common midpoint technique with end on shooting geometry, was used for data acquisition with 15m average shot depth and 5m geophone interval. The near and far offsets are chosen as 120 m and 415 m respectively and the recoding geometry ensures a nominal CMP fold of 15. After preliminary processing (e.g. reversal correction, muting, surgical mute etc.), the data was converted into CMP gather and velocity analysis was performed for NMO correction. The NMO corrected CMP gathers converted to shot gathers. We have applied the TSSSA to the NMO corrected field data for suppression of complex noise and scattered amplitude recovery.

Figure 3 depict the shot gathers before (top panel) and after (bottom panel) the application of TSSSA. Here, spatial data series corresponds to 60 channels in each shot gather which was processed using TSSSA with window length 21. The data of total 100 shots was processed. The reflection amplitudes in the raw data as shown in the top panel of Figure 3 are scattered due to the presence of complex noise. Thus it looks somewhat fuzzy to identify the primary reflections and their continuity from raw data. The TSSSA output reconstructed from the first 10 Eigen triplets is shown in the bottom panel of Figure 3. It can be

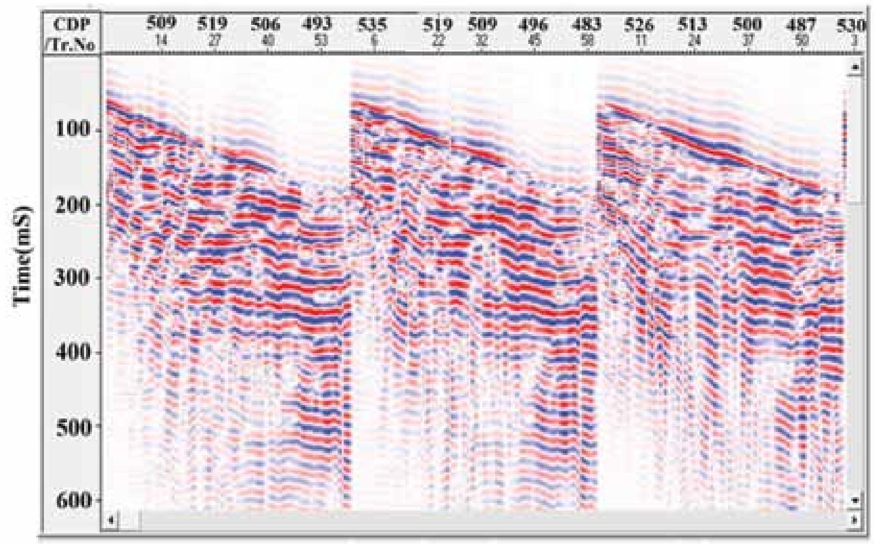

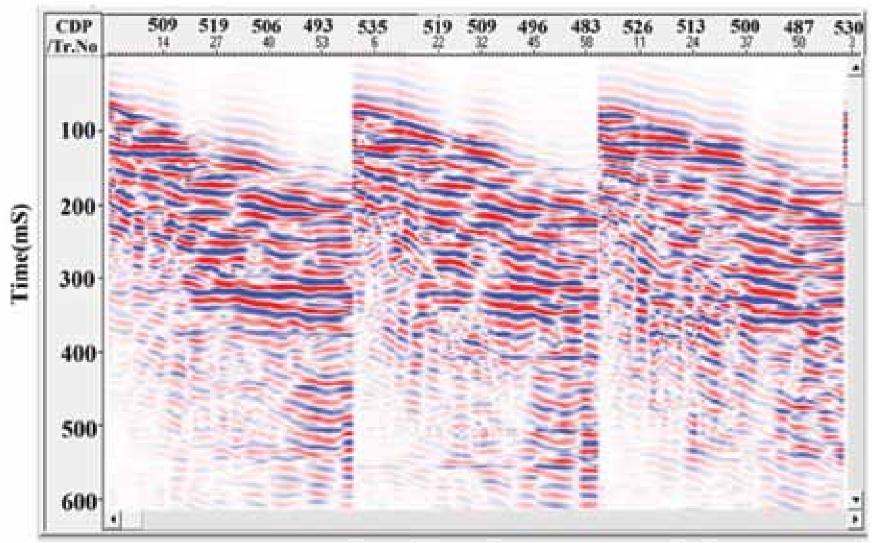

Figure 3. NMO corrected shot gather data before (top panel) and after (bottom panel) the application of TSSSA.

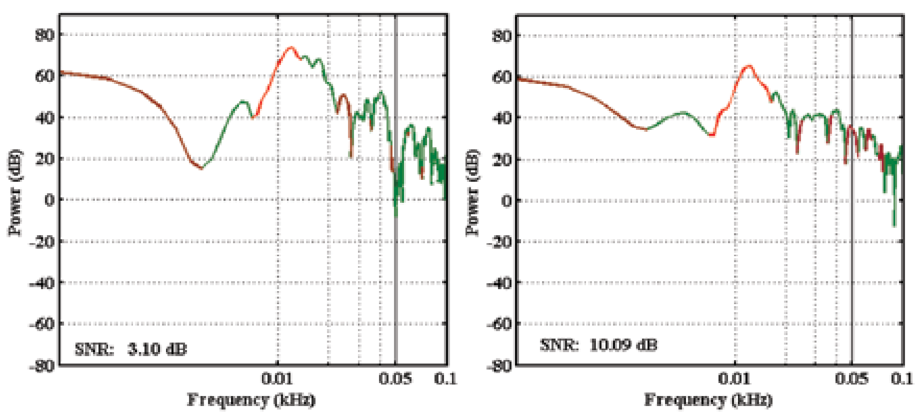

Figure 4. Spectral content of signal and noise portions compted for NMO correlcted gathers before (Left panel) and after (Right panel) the application TSSSA. Red color line indicate the component of fundamental mode, green color is the Noise and brown denotes the signal portion excluding DC and harmonic component.

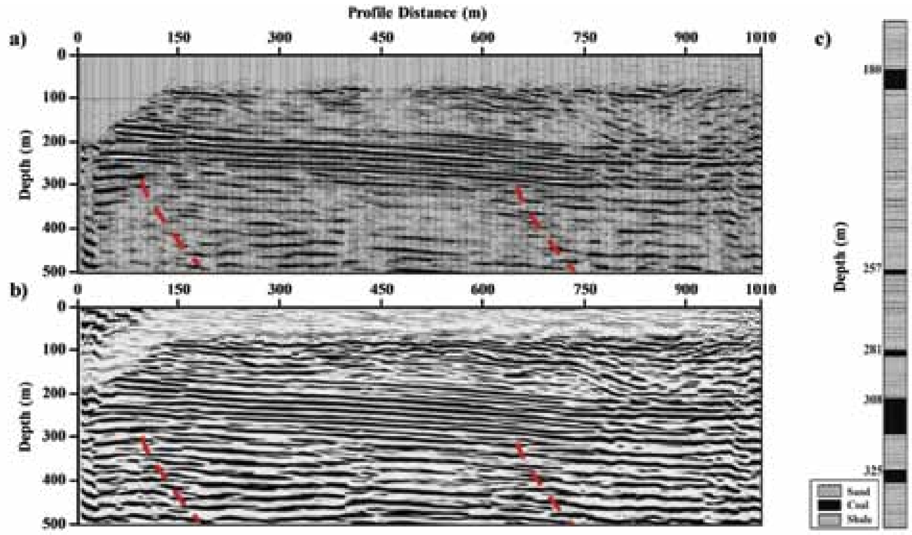

Figure 5. a) Stack section without TSSSA application (using convetional processing). (b) Stack section obtained from TSSSA processed shot gather data from singareni coal basin. (c) Bore hole litholog from the study region.

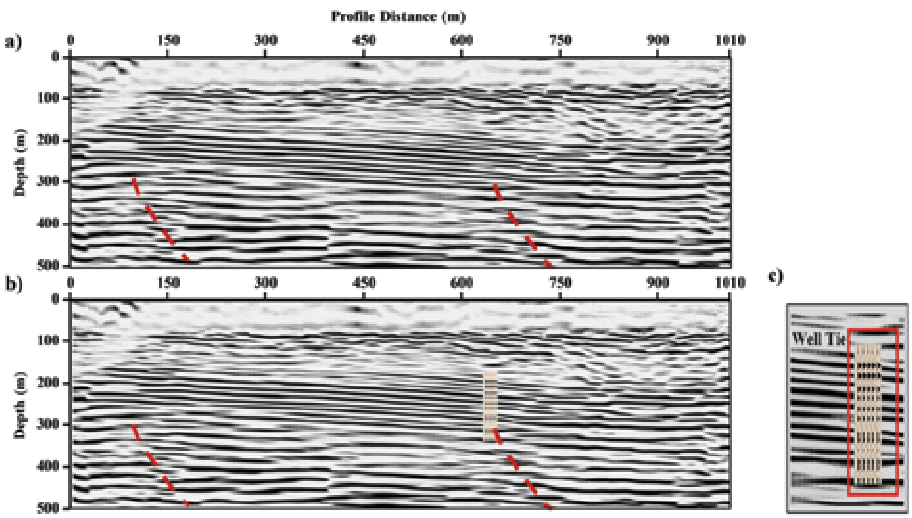

Figure 6. TSSSA output of stacked data shown in Figure 5b. (a) Reconstructed using window length 230. (b) Reconstructed using window length 30 along with Well tie (in rectangular box). (c) Zomed display of well tie.

observed that there is significant improvement in signal to noise ratio of the data after the TSSSA processing. Figure 4 shows the signal and noise spectral content present in the original NMO corrected data and its TSSSA processed output. One can notice that the SNR has increased from 3.10dB to 10.09dB in the TSSSA processing. The underlying method also facilitated the recovery of scattered reflection amplitudes for the clear identification of primary reflector patterns. Comparison of shot gathers before and after the TSSSA processing and respective signal to noise ratio demonstrate the robustness of the proposed method for noise suppression and signal reconstruction. We applied the deconvolution on TSSSA filtered data to sharpen the wavelet then band pass filtering to limit the frequency content of the data between 30 to 140 Hz. The shot gather data was converted into CMP gathers. Then preformed second pass velocity analysis on NMO removed CMP gathers to get best stacking velocity. The data was stacked to produce final stack section using best aligned NMO corrected CMP gathers.

Figure 5a and 5b respectively show the depth converted stack section of length 1010 m obtained from original (without TSSSA processing) and TSSSA processed shot gathers as explained above. The noise was significantly suppressed in the TSSSA processed data (Figure 5b) and the pseudo amplitudes in the stack section of original data

(Figure 5a) are also appropriately corrected in the TSSSA processed stack section (Figure 5b). The reflections below the depth 300m were smeared due to the non-linear interaction of scattered and diffracted signals from faults in the original stack data shown in Figure 5a. Whereas, such reflections are recovered for clear visualization in the TSSSA processing, as can be seen in Figure 5b. Although it is well known that the stacking procedure removes the effect of random noise, there are still certain amounts of deceptive complex colored noises in the data, possibly arising due to the various other sources as discussed earlier. Hence, we applied the TSSSA de-noising on post stack data shown in Figure 5b to alleviate the complex colored noises. The TSSSA output of the stack section data (Figure 5b) corresponding to the window lengths 230 and 30 are respectively shown in Figures 6a and Figure 6b. The TSSSA suppressed the low frequency (complex and colored) noise in the output at window length 30 (Figure 6b) comparative to the output at window length 230. There are strong reflections between the depth range of 200 m to 450 m in the TSSSA processed stack section corresponding to coal beds (Figure 6b), which agrees well with the available geological data in the study area (Murthy and Rao, 1994; Biswas, 2003).

To validate the field data, we use synthetic seismic traces generated from the borehole information within the study region that lies approximately around 200m distance perpendicular to the seismic line. The observed reflections from the stack section substantiated well with the synthetic data shown in Figure 6c. The geological information (Murthy and Rao, 1994; Biswas, 2003) of the study region also corroborate well with the minor as well as major faults as mapped on the post stack TSSSA processed section. Also the reflections observed in the stack section match well with the geologically inferred coal seam in the study area. A disturbance in the amplitude and continuity of seismic reflectors (inferences for faulting) is also observed at two places in the stack section. These disturbances are noticed as the signatures of a normal faulting detected at a distance of ~150 m from the WSW end and another fault at a distance of ~720 m from WSW direction. These faults locations are with geologically known faults. Our results show the presence of near normal faults with low vertical displacement in the stack section. In addition, few minor normal and near vertical faults present in the stack section are intrinsic to coal basin. The faults in the seismic sections show NE-SW direction across the half PG graben structure in the study area.

CONCLUSION

We have developed a robust Eigen analysis based Time Slice Singular Spectrum Analysis for time domain seismic reflection data de-noising. The method was tested on noisy synthetic seismic reflection data for its efficacy and then applied to the field data for complex noise suppression. Experiments on noisy synthetic data generated over the normal fault model with diffraction energy suggest that the underlying method is robust to suppress complex noise up to 30%. The application of the method to high resolution seismic reflection shot gather data from Singareni coal fields reveals that the method has significantly improved the signal to noise ratio paving the way to recognize geological structures more accurately. Finally, the applicability of the method for coherent noise suppression is demonstrated on post stack data. The results from post stack TSSSA application suggest that the underlying algorithm successfully suppressed the complex colored noise. The fault structures and coal beds mapped on the de-noised stack section correlated well with the geological information. High correlation (>75%) between the synthetic trace computed from the log data and the TSSSA processed stack section suggests the robustness of the method. Hence, we conclude that the TSSSA method is robust for complex noise suppression from seismic reflection data for the identification of geological structures.

ACKNOWLEDGEMENTS

We thank Director CSIR-NGRI for his permission to publish this paper. We are also grateful to DAE and CSIR for funding first and second author respectively. We thank team members of Engineering Geophysics Division for their support in the field data acquisition and Singareni Collieries Company limited for funding the project.

We also thank Editor for his encouragement and constructive suggestion.

Compliance with Ethical Standards

The authors declare that they have no conflict of interest and adhere to copyright norms.

REFERENCES

Biswas, S.K., 2003. Regional tectonic framework of the Pranahita–Godavari basin, India. J Asian Earth Sci., 21, 543-551.

Broomhead, D.S. and King, G.P., 1986a. Extracting qualitative dynamics from experimental data. Physica D, 20, 217–236.

Broomhead, D.S. and King, G.P., 1986b. On the qualitative analysis of experimental dynamical systems. Nonlinear phenomena and chaos, Sarkar S (Ed.), Adam Hilger, Bristol, 113-144.

Fraedrich, K., 1986. Estimating dimensions of weather and climate attractors. J. Atmos. Sci., 43, 419–432.

Ghil, M., Allen, M.R., Dettinger, M.D., Ide, K., Kondrashov, D., Mann, M.E., Robertson, A.W., Saunders, A., Tian, Y., Varadi, F. and Yiou, P., 2002. Advanced spectral methods for climatic time series. Rev. Geophys., 40, 1- 41.

Golyandina, N. and Zhigljavsky, A., 2013. Singular spectrum analysis for time series. Springer briefs in Statistics, ISBN: 978-3-642-34912-6 (Print) 978-3-642-34913-3.

Greenhalgh, S.A., Suprajitno, M. and King, D.W., 1986. Shallow seismic reflection investigations of coal in the Sydney basin. Geophysics, 51(7), 1426-1437.

Hassani, H., Mahmoudvand, R. and Zokaei, M., 2011. Separability and window length in singular spectrum analysis. Comptes rendus mathematique, 349, 987-990

Hassani, H., Mahmoudvand, R., Zokaei, M. and Ghodsi, M., 2012. On the separability between signal and noise in singular spectrum analysis. Fluctuation and noise letters, 11(2), doi: 10.1142/S0219477512500149.

Lawrence, M.G., 1992. Modeling studies of interference reflections in thin layered media bounded by coal seams. Geophysics, 57(9), 209-1216.

Lawrence, M.G., 1991. Tuning effect and interference reflections from thin beds and coalseams. Geophysics, 56 (8), 1288-1295.

Murthy, B.V.R. and Rao, C.M., 1994. A new Lithostratigraphic classification of Permian (Lr. Gondwana) succession of PG Basin with special reference to Ramagundam coal belt, A.P. India, In Gondwana Nine, Oxford and IBH publishing, p.67.

Oropeza, V. and Sacchi, M., 2011. Simultaneous seismic data de-noising and reconstruction via multichannel Singular Spectrum Analysis. Geophysics, 76(3), V25-V32.

Patterson, K., Hassani, H., Heravi, S. and Zhigljavsky, A., 2011. Multivariate singular spectrum analysis for forecasting revisions to real-time data. J. Appl. Statistics, 38, 2183-2211.

Rekapalli, R., Tiwari, R.K. and Seshunarayana, T., 2012. De-noising and clean reconstruction of seismic signals using space lagged Singular Spectrum Analysis. AGU Fall Meeting, San Francisco, USA, 3-7 December 2012.

Rekapalli, R., Tiwari, R.K., Dhanam, K. and Seshunarayana, T., 2014. T-x frequency filtering of high resolution seismic reflection data using singular spectral analysis. J. Appl. Geophys., 105, 180-184.

Rekapalli, R. and Tiwari, R.K., 2015. A short note on the application of singular spectrum analysis for geophysical data processing. J. Ind. Geophys. Union, 19(1), 77-85.

Rekapalli, R. and Tiwari, R.K., 2016. Frequency filtering using Singular Spectrum Analysis involving Eigen weighted spectrogram. J. Appl. Geophys., 132, 33-37.

Sacchi, M.D., 2009. FX Singular spectrum analysis. CSPG CSEG CWLS Convention, Abstracts, 392-395.

Tiwari, R.K. and Rajesh, R., 2014. Factorized Hankel optimal singular spectral approach for erratic and noisy seismic signal denoising. J. Appl. Geophys., 111, 95-101.

Trickett, S.R., 2003. F-xy Eigen image noise suppression. Geophysics, 68, 751-759.

Tselentis, G.A. and Paraskevopoulos, P., 2002. Application of a high-resolution seismic investigation in a Greek coalmine. Geophysics, 67(1), 50-59.

Ulrych, T.J., Freire, S. and Siston, P., 1988. Eigen image processing of seismic sections. 58th Annual Internat. Mtg., Soc. Expl. Geophys., Expanded Abstracts.

Vautard, R., Yiou, P. and Ghil, M., 1992. Singular-spectrum analysis: A toolkit for short, noisy, chaotic signals. Physica D, 58, 95-126.

Received on: 9.5.18; Revised on: 6.7.18; Accepted on: 16.7.18

J. Ind. Geophys. Union (September 2018)
v.22, no.5, pp: 468-477

Potential of shale gas in Cambay basin, Gujarat, India

Anurodh Mohan Dayal
Former Emeritus Scientist, CSIR-National Geophysical Research Institute, Uppal Road, Hyderabad 500007 (India)
Email: anurodhisotope@gmail.com

ABSTRACT

Carbonaceous shale is an organic rich sedimentary rock that forms the main source for all conventional and nonconventional hydrocarbons. Though, formation of oil and gas takes place in shale but due to very low porosity, it cannot be reservoir rock for hydrocarbons in case of conventional hydrocarbons. Shale is an excellent source rock for nonconventional natural gas and in the last one and half decade, the development of hydrofracturing and horizontal drilling has made it possible to exploit the carbonaceous shale as nonconventional gas source. The exploration and exploitation of shale gas changed the global economics of hydrocarbons and the oil prices came down from 110$ per barrel to 30$ per barrel. With the exploitation of shale gas, USA stopped importing oil and gas. It has now more than 2 million barrel of shale oil as surplus and thus exports it to various countries, including India.

In India, the Cambay basin, which is a oil producing basin, contains thick deposits of carbonaceous shale. These Tertiary shales are fine grained and organic-rich and thus considered a good source for shale gas. For shale gas exploration, the thickness of shale in subsurface and the type of organic matter it contains, are important parameters for the generation of nonconventional shale gas. Rock Eval pyrolysis of the shale, is one of the most important basic organic geochemistry to understand such parameters. As an initial study, interbedded shale samples from Middle Eocene lignite sequence of Cambay formation (Nagori et al., 2013) of Tadkeshwar in Surat and Rajpardi in Bharuch, were sampled and analysed using Rock Eval Pyrolysis system. Total organic carbon in these shales varies from 0.2% to 47%, which are indicative of good source of shale gas deposits. The T_{max} varies between 342°C to 450°C, and the hydrogen index (HI) ranges between 32 to 754 mg HC/ g TOC. The variation of HI vs. T_{max} suggests an immature to mature stage for the hydrocarbons. The organic matter in shales suggest Type II or Type III kerogen, which are responsible for the generation of these hydrocarbons.

Key Words: Shale, Shale gas, Total Organic Carbon, Rock-Eval pyrolysis, Cambay Basin

INTRODUCTION

Since the last one and half decades, the exploitation of shale gas has become very promising as unconventional source of energy. Carbonaceous shale is very fine grained sedimentary rock and has good potential for nonconventional source of energy. Being more environment friendly, it is considered one of the alternative source of energy for the future. With fast development in USA, shale gas is being further explored at many other places also, like Arizona (USA), China, UK, Australia etc. Carbonaceous shale, which is a fine grained clastic sedimentary rock, has good potential as source-cum-reservoir rock for natural gas, depending on richness and thermal maturity of organic matter (Curtis, 2002; Boyer et al., 2006; Horsfield and Schulz, 2012). The light hydrocarbon gases generated in the organic rich shales, remain trapped in the micro-pores and micro-fractures or in the thin layers of these rocks (Ross and Bustin, 2008; Milliken et al., 2013). With geological time and under pressure and temperature, the organic matter is converted into kerogen to produce hydrocarbons. Further, in marine conditions, biological activities produce large quantity of organic matter. In general, for any shale-gas system, the marine conditions support biologic activities, and thus produce large quantities of organic matter. The depositional conditions concentrate the organic matter, while post-depositional conditions allows their preservation and maturation to gaseous hydrocarbon (McCarthy et al., 2011). The storage conditions are governed by the micropores/ micro-fractures and the sorption surfaces of kerogen and clay minerals of the shales (Curtis, 2002; Ross and Bustin, 2008). Low permeable shales require extensive fractures to produce commercial quantities of gas. With advancement in techniques, such as hydro-fracturing, in conjunction with horizontal drilling, massive production of shale gas is being carried out in the United States since past decade (EIA, 2013, USGS, 2012). In comparision, the Shale gas exploration in India is at an early stage. Major oil company has identified the potential basins and plan to explored these basins with available data, as well as new data using geochemical, geological and petrophysics studies, which will allow them to initialize the exploration program in most promising zones to find the sweet spots, where it would be most beneficial to drill. Cambay basin is one such basin in their priority list, which is already a producing basin for conventional hydrocarbons. The Cambay Shale is the main source rock sequence in the basin, with contribution of oil from Kalol and Tarapur Formations and their

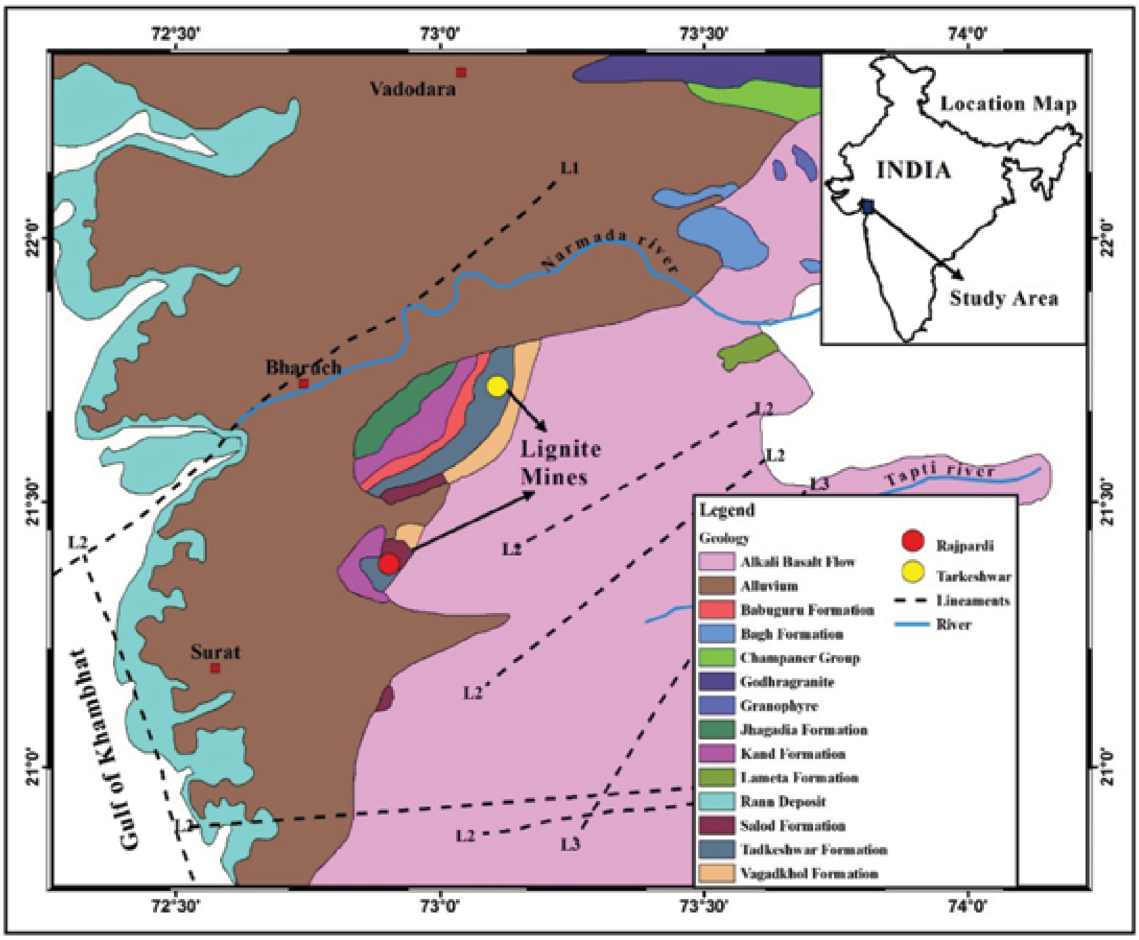

Figure 1. Geological map of South Cambay basin, showing the locations of sampled lignite mines (after Singh et al., 2012a).

equivalents in the Broach-Jambusar block (Chowdhary, 2004). Earlier, this basin has been explored extensively for conventional hydrocarbons. The available explored data suggests that about 20 trillion cubic feet (tcf) of shale gas can be produced from this basin (DGH, 2012; USGS, 2012). These estimates are based on already available exploration data but for shale gas exploration, there are certain other characteristics which are necessary for the exploitation. Like geochemical, petrophysical, petrological and mineralogy studies on these shales. Geochemistry of these shales for their organic richness, kerogen types and thermal maturity are basic requirement for shale gas exploration as these parameters control the gas generation in shales (Jarvie et al., 2007). Rock Eval Pyrolysis is one of the most important and basic technique to evaluate the hydrocarbon generating capacity of the source rocks.

In the present study, preliminary investigation on the geochemical properties of organic matter of the shales from the Cambay basin has been carried out using the above technique. The shale samples were collected from the open cast mines, namely Tadkeshwar and Rajpardi in Surat, Bharuch districts, respectively (Figure 1). The fossil data recovered from the sedimentary sequences in these mines suggest an analogy of Cambay shales for these shale horizons (Singh et al., 2012a, 2012b; Sahni et al., 2006; Nagori et al., 2013). As mentioned earlier, Cambay shales are well established hydrocarbon source rock in the basin. In the preset work, the shales associated with lignite mines, have been characterized for the organic matter present in the shales in terms of its TOC content, thermal maturity and kerogen type using Rock-Eval pyrolysis. The geochemical parameters studied here, provide basic information on the qualitative and quantitative aspects of the organic matter in shales, which are interpreted in the light of basin geology to assess the gas generation potential of these shales.

GEOLOGIC SETTING AND STRATIGRAPHY

The Cambay basin is a narrow elongated (NNW-SSE) intracratonic rift basin situated in the northern part of western India. It extends northward from the Gulf of Cambay in the south Gujarat to Jaisalmer-Mari ridge in the central Rajasthan (Kundu et al., 1997; Mathur et al.,

Table 1. Stratigraphic succession of the Cambay basin (after Agarwal, 1986)

Age		Formation and Thickness	Lithology
Quaternary	Holeocene	*Narmada Fm.*	Sandstone, silt,clay and gravels
……………	……………………	..Unconformity…...	…………………………………
	Lower Pliocene	*Jhagadia Fm.(200m)*	Sandstone, gritstone, conglomerate, breccia, clay, silt
	……………………	…Unconformity….	………………………………..
	Miocene	*Kand Fm. (200-400m)*	Conglomerate, fossil,limestone,calcareous sandstone and gravelly clay
Tertiary		……………………	……Unconformity……….……
		Babaguru Fm. (200-300m)	Conglomerate, sandstone,clays cherry red and highly ferruginous
	…………………..	…Unconformity...	…………………………………
	Oligocene	*Tadkeshwar Fm. (125 -346m)*	
	…………………..	..Unconformity….	…………………………………
	Eocene	*Ankleshwar Fm. (603m)*	
		………………… *Cambay shale (+1500m)*	…Unconformity……………….. Grey to dark grey thinly bedded shales.
	…………………..	..Unconformity…	…………………………………
	Paleocene	*Vagadkhol Fm (+50m)*	Conglomerate, grit, sandstone, variegated clays and siltstone
	……………………	..Unconformity…….	…………………………………
	Cretaceous	*Deccan Trap*	Basalt, trachyte etc.

1968; Biswas, 1982). The Saurashtra craton lies to its West, Aravalli to the north east and Deccan Traps to the south east. Cenozoic sediment outcrops are rare and occur only on the fringes of the basin. The basin is covered by Gujarat alluvium in the south and sands of Rajasthan desert in the north. The Narmada and Barmer depression are, respectively, the southern and northernmost part of the basin (Kundu et al., 1997; Mathur et al., 1968).

This basin evolved during Late Mesozoic era with the development of major tensional faults, following widespread extrusion of Deccan Trap basalts (Biswas, 1982, 1987), which form the basement for the Tertiary and Quaternary sediments in the Cambay basin. The sediments have a thickness of over 5,000 m in the deepest part (Jambusar-Broach area) of this basin. The sequence comprises greywackes, dark grey to black grey shales, coal seams, silts, fine to medium grained sands and grey reddish-brown clays (Biswas, 1987). The whole basin can be dissected into five major tectonic blocks demarcated by transverse basement faults within the traps, which continue to some extent into the overlying sediments also. These blocks are Sanchor-Patan, Mehsana-Ahmedabad, Tarapur-Cambay, Broach-Jambusar and Narmada-Tapti from north to south (Biswas, 1982, 1987). They are characterized by different types of folds, faults and basement depths. The manifestations of the major tectonic trends is evident from their parallelism to the Satpura trend between the Narmada and Tapti rivers and to the Dharwar trends in the northern and central part of the basin (Raju et al., 1971). The Cambay basin shows two major tectonic lineaments, NNW-SSE, probably related to the Dharwar orogenic belt and ENE-WSW, probably related to the Satpura orogenic belt, which are evident and extend into the Cambay basin. These two major trends are manifested both on the surface and in the subsurface as well (Raju et al., 1971).

Stratigraphically, the basin can be divided into eleven Formations with Deccan Trap as the basement (Table 1). The depositional floor is characterized by narrow linear horst and graben (Bhandari and Chowdhary, 1975). The older Olpad Formation overlies the Deccan Trap with an erosional unconformity. The sedimentation in these areas took place in fluviatile to shallow water environment under oxidizing conditions (Chandra and Chowdhary, 1969). The Olpad Formation is overlain unconformably by Cambay Shale Formation, which was deposited under deep marine and highly reducing condition. The Kadi Formation, which is present only in Ahmedabad-Mehsana Block, is an intervening non-marine clastic wedge, with a thickness of almost 300 m within the Cambay shale (Bhandari and Chowdhary, 1975). The sedimentation in the region took place in a deltaic environment. The Cambay Shale is conformably overlain by Kalol Formation of Middle Eocene age, which got deposited in alternating regressive and transgressive marine settings. The marine Tarapur Shale Formation conformably overlies the Kalol Formation. The former is unconformably overlain by Babaguru Formation of Upper Miocene age, which is further overlain by Kand Formation (Middle Miocene) and Broach Formation (Pliocene age), deposited under shallow marine oxidizing environment. The Jambusar Formation conformably overlies the Jhagadia Formation (Bhandari and Chowdhary, 1975).

In addition, Cambay basin contains four sedimentary source rocks. These are the Tarapur Shale and its coeval units of upper Eocene-Oligocene; Kalol Formation and its coeval units of middle Eocene; Cambay Shale of lower Eocene; and Olpad Formation of volcanic conglomerate, shale and claystone of Paleocene (Yalcin et al., 1987; Chowdhary, 2004). Some localized sandstone reservoirs (Unawa, Linch, Mandhali, Mehsana, Sobhasan fields), are also present within the Cambay Shale of this region. The lithological heterogeneity and associated unconformity in Olpad Formation, appear to have helped in the entrapment of such hydrocarbons. Besides, transgressive shales within deltaic sequences provided a good cap rock. The peak of oil generation and migration is understood to have taken place during Early to Middle Miocene (DGH, 2012).

The studied region of Tadkeshwar lignite mine in Surat and Rajpardi lignite mines at Bharuch districts, are situated in the southern part of the Cambay basin. Subsurface lignite bearing sequences are exposed in these open cast mines. The Rajpardi lignite deposits are associated with two major litho units: Babaguru Formation which is underlain by Tadkeshwar Formation, followed by Nummulitic Formation. The Tadkeshwar Formation begins with grey clay-bed which is overlain by the carbonaceous clay-bed, which in turn, is conformably overlain by a five-meter-thick lignite seam which is a marker bed (Singh, 2012). Based on relative stratigraphic position, depositional environment and occurrence of paleo-fauna of the lignite sequences, it has been considered analogous to the Cambay Formation (Singh et al., 2012a; 2012 b; Sahni et al., 2006; Nagori et al., 2013; Rust et al., 2010). The predominance of mud rich sediments, together with lignites and siderites in the Tadkeshwar and Rajpardi mines, suggest deposition in shallow marine condition (Rust et al., 2010). Well preserved, consolidated shales samples were collected after removing the weathered part in the exposed horizons.

METHODOLOGY

Rock Eval pyrolysis was carried out on shale rock samples collected from open cast lignite mines of Tadkeshwar in Surat district and Rajpardi in Bharuch district. The instrument was calibrated in standard mode using the French Institute of Petroleum standard, (IFP 160000), (T_{max} = 416°C; S2= 12.43). The shale samples were powdered homogenously (<63μ) and weighed in pre-oxidized crucibles depending upon the organic matter content (~50-70 mg of the shale; and 8-15 mg of coaly shale).

Rock Eval pyrolysis is used to estimate the petroleum potential of rock samples by cracking of organic matter according to a programmed temperature pattern in the Rock Eval pyrolyzer. Released hydrocarbons are monitored by a Flame Ionization Detector (FID), forming the peaks S1, the thermo-vaporized free hydrocarbons and peak S2, the hydrocarbons from cracking of organic matter. The CO and CO_2 released during pyrolysis have been monitored by an infrared cell. This data allows the determination of total organic carbon and mineral carbon content of the samples.

The basic cycle of Rock Eval analysis consists of two steps. Firstly, the pyrolysis is carried in pyrolysis oven, with an initial temperature of 300°C, which increases to 650°C at the rate of 25°C per minute. The samples are pyrolysed in an inert atmosphere of nitrogen. The free hydrocarbons evolved at lower temperature of 300°C, are detected by the FID, resulting in formation of S1 peak. This is followed by the hydrocarbon evolution through cracking of kerogen, which results in S2 peak. Thus, S1 and S2 represent milligrams of free and kerogen cracked hydrocarbons in one gram of rock sample (mgHC/gRock). The S3 peak corresponds to CO_2 formed from thermal cracking of kerogen during pyrolysis and is expressed in milligrams per gram of rock.

Following pyrolysis, residual organic carbon is oxidized in an oxidation oven. The oxidation oven is programmed with an initial temperature of 300°C, which increases to 850°C at the rate of 20°C per minute. The resulting S4 peak comprises of carbon dioxide and carbon monoxide components defined by $S4CO_2$ and S4CO peaks during

Table 2. Rock Eval pyrolysis data of shales from the Cambay basin.

Sample	S1	S2	Tmax	S3	TOC	HI	OI	MINC
	(mgHC/gRock)		°C	mgCO2/gRock	(%)	mgHC/gTOC	mgCO2/gTOC	(%)
Tadkeshwar								
TG-01	3.58	58.42	420	8	24.27	241	33	0.7
TG-02	0.12	1.75	434	2.04	3.19	55	64	0.41
TG-03	0.13	1.2	428	1.5	2.34	51	64	0.23
TG-04	0.09	1.57	425	2.43	4.69	33	52	0.22
TG-05	0.05	0.08	394	0.55	0.18	44	306	0.46
TG-06	0.18	4.35	432	3.07	7.21	60	43	0.3
TG-07	0.07	0.14	378	0.57	0.32	44	178	0.08
TG-08	0.04	0.17	342	0.83	0.19	89	437	0.93
TG-09	0.06	1.28	431	0.35	0.59	217	59	0.07
TG-10	0.07	0.18	450	1.62	0.21	86	771	0.79
TG-11	3.12	78.84	414	16.03	47.39	166	34	1.22
TG-12	2.82	68.42	415	14.34	42.28	162	34	1.13
Rajpardi								
RJ-01	7.12	190.11	435	3.69	25.21	754	15	0.35
RJ-02	6.62	184.6	429	3.79	26.03	709	15	0.36
RJ-03	3.29	60.6	432	1.51	9.35	648	16	0.19
RJ-04	4.04	102.61	432	2.08	14.42	712	14	0.25
RJ-05	4.94	106.76	430	2.15	14.73	725	15	0.26

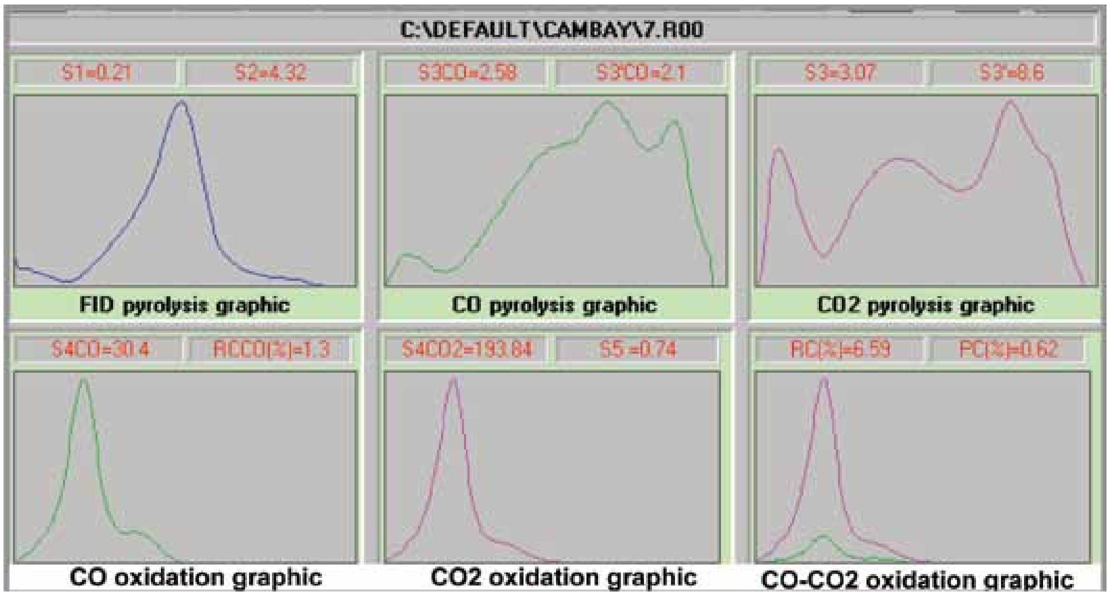

Figure 2. RE pyrolysis and oxidation curves for the shale sample (TG-07) from the Tadkeshwar lignite mines, Cambay basin.

oxidation. A separate CO_2 peak designated as S5 reflects decomposed carbon dioxide from carbonate minerals in the sample. T_{max}, which is the thermal maturity indicator, corresponds to the highest yield of S2 hydrocarbons, is recorded during the pyrolysis. Total Organic Carbon (TOC) is calculated by Rock Eval through the addition of the obtained values of pyrolised carbon and residual carbon. The relationship between these components forms the basis for various indices used for interpretation of rock characteristics. The hydrogen index, (HI) is defined here by 100 × S2/TOC, while the oxygen index, (OI) is defined as 100 × S3/TOC. These indices help in tracking kerogen types and maturation (User's guide, Rock Eval 6; McCarthy et al., 2011).

RESULTS

The important parameters obtained by the pyrolysis of shales from Cambay basin using Rock Eval, are given in Table 2 and representative pyrolysis and oxidation curves for the samples, are shown in Figure 2. In general, the shales from Rajpardi area show a high TOC content along

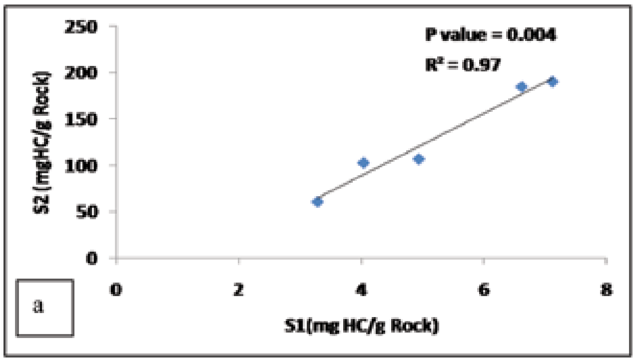

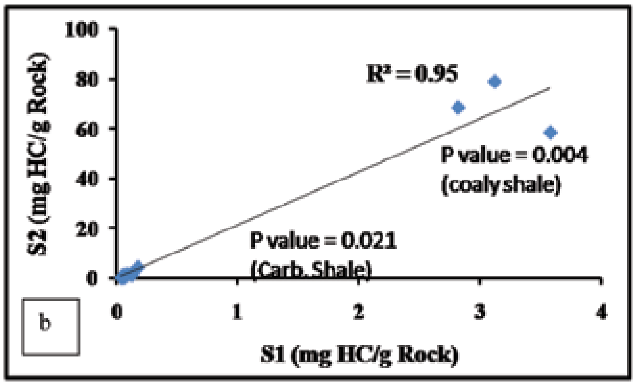

Figure 3. Correlation of S1 and S2 hydrocarbons released from the pyrolysis of shales from the (a) Tadkeshwar lignite mine, Surat, and (b) Rajpardi lignite mine, Bharuch, respectively, Cambay basin.

with other Rock Eval parameters, compared to that of Tadkeshwar (Table 2). The TOC content from Rajapardi shales ranges between 9.35 and 26.03%. The S1values range between 3.29 and 7.12 mgHC/gRock and are characteristic of the entire sample (Table 2). The S2 values show an elevated range from 60.6 - 190.11 mgHC/gRock. The T_{max} ranges from 429-435°C. The HI is high between 648 and 754 mgHC/gTOC, whereas OI for all the samples is near 15. The mineral carbon content is <0.5 %. For the Tadkeshwar shales, the TOC varies from 0.19 to 47.39 %. The S1 values are between 0.05 and 3.58 mgHC/gRock and the S2 values range from 0.14 to 78.84 mgHC/gRock. Similarly, the T_{max} varies from 342 to 450°C, whereas the HI values vary from 33 to 241 mgHC/gTOC.

DISCUSSIONS

In a shale gas play, high gas content is controlled by the amount and maturity of the organic matter. The total organic carbon content and pyrolysis parameters help in the evaluation of the sedimentary organic matter. A TOC content in wt % of sample < 0.50 is considered poor; 0.50 - 1.0 as fair; 1.0 - 2.0 as good and that > 2.0 as excellent for the source rocks (Hunt, 1996). The shales from Rajpardi show a TOC >9 %, whereas those from Tadkeshwar vary widely (Table 2). Three shale samples from Tadkeshewar area have very high TOC content (>58%). These shales are coaly in texture and can possibly have the contribution from adjacent lignite sequences. Rest of the shales from the area have relatively lower TOC (0.18 - 3.19%). The correlation analysis in coaly shales is constrained by less number of observations (n=3). Similarly, P-test and correlation analysis performed on S1 and S2 values of Rajpardi shales indicate similar source for the generation of the hydrocarbons (Figure 3). These values also vary linearly with the TOC content of the organic matter (Figure 4). With an increase of organic matter, the produced hydrocarbons are also increasing. These characteristics are observed in the organic matter derived from good/ potential source rocks. These observations also indicate that there is minimal surficial contamination of the organic matter in shales, which if happened, would have resulted in scattered and poorly correlated hydrocarbon variables and TOC contents. The quality and maturation state of kerogen is based on the hydrogen and oxygen indices (HI/ OI values) generated by the RE pyrolysis. HI is a measure of the hydrogen richness of the source rock, and is used to estimate the thermal maturity and petroleum generative potential of the rock (Tissot and Welte, 1978). OI measures the oxygen richness of a source rock and can be used in conjunction with the hydrogen index to estimate the quality and thermal maturity of source rocks. Organic rich shales deposited in reducing anoxic marine environments have high HI and quite low OI values (Tissot and Welte, 1978).

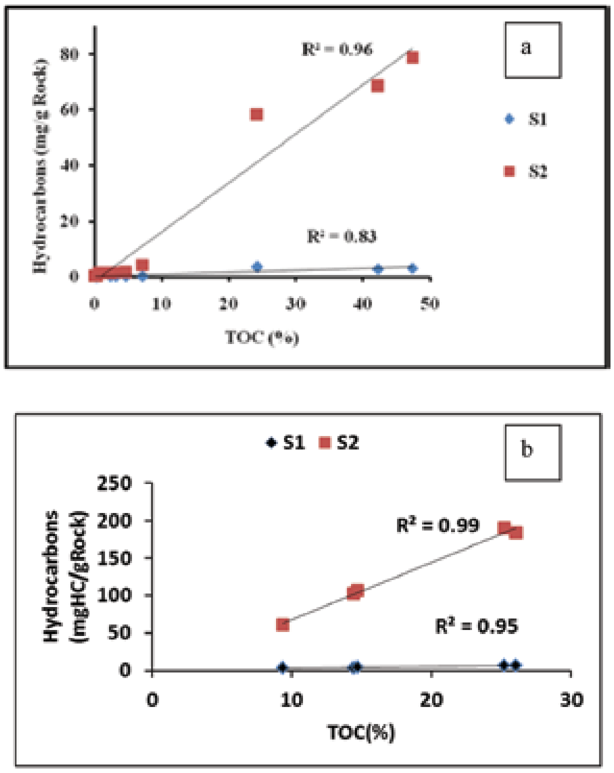

Figure 4. Correlation of S1 and S2 hydrocarbons with the TOC (%) of the shales from (a) Tadkeshwar lignite mine, Surat, and (b) Rajpardi lignite Mine, Bharuch, respectively, Cambay basin.

The shales from Rajpardi area show high HI values and low OI values, where as those from Tadkeshwar show moderate HI and a low OI values. An inverse correlation is observed between the hydrogen and oxygen indices with each other and that with the TOC content (Figure 5). The hydrogen and oxygen indices are characteristics type of kerogen and generally bear inverse correlation with each other. The HI value < 50 mg HC/ g TOC, suggests no oil and gas generation from the kerogen, whereas HI >600 mg HC/ g TOC suggests oil prone kerogen (Peters and Cassa, 1994). These indices indicate the source organic input and the environment of deposition, which is essentially reducing, characterized by low oxygenation conditions resulting in preservation of organic matter in shales. The high HI and low OI values represent a favourable depositional condition of Cambay shales in a reducing, hydrogen rich and low oxygenation environment.

Based on Carbon (C), hydrogen (H) and oxygen (O) contents, kerogens have been divided as Type I, II, III, and IV (Van Krevelen, 1961; Hunt, 1996; Tissot and Welte, 1978). Type I and II generate oil. Type I is generated in marine environments and is derived from algal lipids that are enriched in lipids by microbial activity. It contains several aliphatic chains and the H/C ratio is originally high (H/C >1.5) (Tissot and Welte, 1978; Peters et al., 2005). Type-II kerogen also contains aliphatic chains, but have more aromatic and naphthenic rings. The oil and gas potential in Type-II kerogen are lower (H/C= 1.2 to 1.5) than observed for type-I kerogen. Type-III kerogen with low H/C range (H/C= 0.7 to 1.0) generates primarily gas, condensates and some waxes. The organic matter is mostly derived from terrestrial higher plants. Type-IV kerogen generates only small amount of methane and CO_2.

The HI value < 50 mg HC/ g TOC suggests Type-IV kerogen (No oil and gas), those ranging between 50-200 mg HC/ g TOC suggests Type-III kerogen (Gas), 200-300 mg HC/ g TOC suggests Type- II/III kerogen (Mixed oil and gas), 300-600 mg HC/ g TOC suggests Type- II kerogen (Oil) and >600 mg HC/ g TOC suggests Type-I kerogen (Oil) (Peters and Cassa, 1994). The HI vs OI plot of the shales associated with the lignite mines from Tadkeshwar shows that the organic matter is characterized by Type III kerogen (Figure 6). The HI vs T_{max} values also indicate the presence of Type III kerogen, (Figure 7). These shales show an immature phase for the generation of hydrocarbons. With a high TOC characterized by Type III kerogen, these shales can be a potential source for the generation of gas at greater depths and burial. Couple of shales from Tadkeshwar, (TG-05, 07, 08, 09, 10) show high oxygen index (>100 mgHC/gTOC). These samples are also characterized by low TOC values and are possibly contaminated by weathering and oxidation. The shale from the Rajpardi area show very high HI values (>600 mg HC/ gTOC). The HI vs. T_{max} suggests that the organic matter is

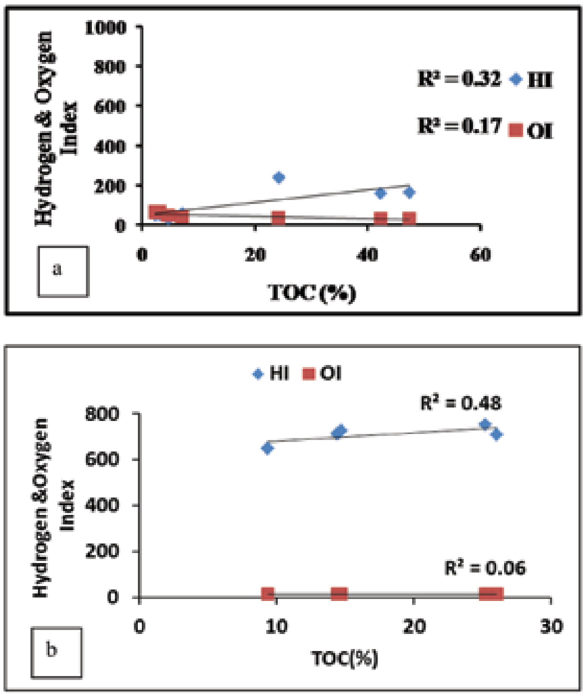

Figure 5. Correlation of HI and OI with the TOC (%) of the shales from the (a)Tadkeshwar lignite mine,Surat, and (b) Rajpardi lignite mine, Bharuch, respectively, Cambay basin.

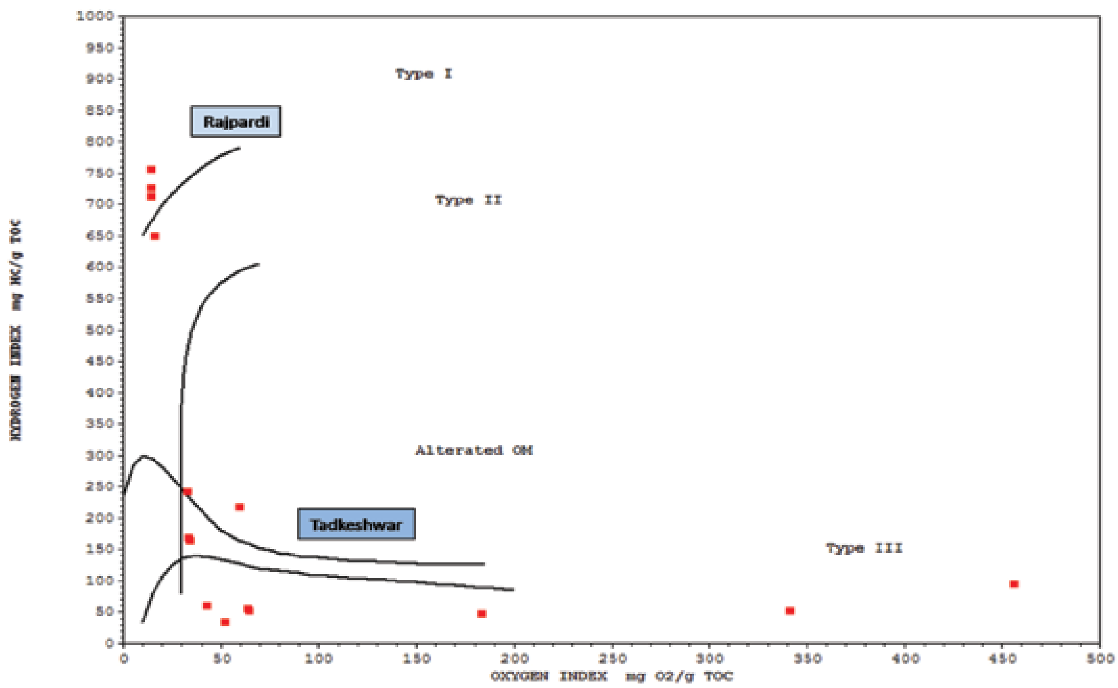

Figure 6. The HI vs OI plot for the shales from the Tadkeshwar and Rajpardi lignite mines, Cambay basin.

characterized by Type II kerogen, which has the potentially of oil and gas. The samples show an immature to mature stage for the hydrocarbon generation.

The Tadkeshwar lignites of Cambay basin belong to Early Eocene age. The data generated on nature, composition, origin, maturation and mineral matter contents of the organic deposits, through petrological investigations, show that these lignites are rich in huminite macerals, followed by liptinite and inertinite with moderate to high proportions of associated mineral matter (Singh

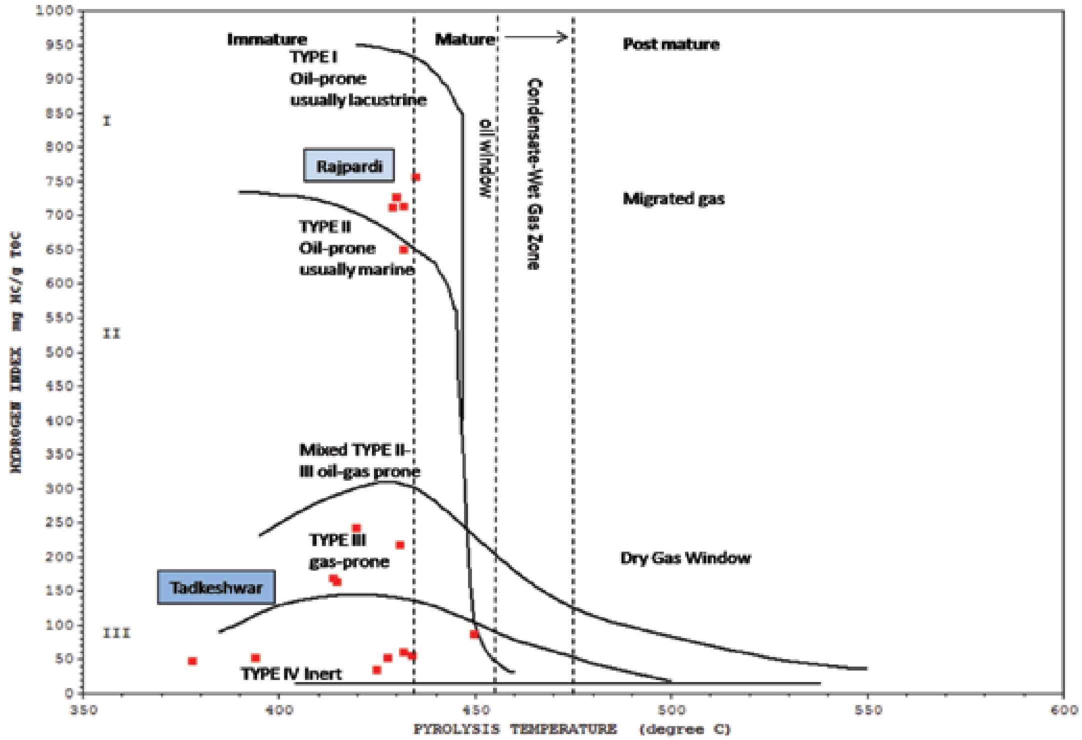

Figure 7. HI versus T_{max} Fig plot for the shales from Tadkeshwar lignite mine, Surat, and Rajpardi lignite mine, Bharuch, Cambay basin**.**

et al., 2012a; 2012b). Petrographical studies on Rajpardi lignites suggest that these are enriched in huminite and are low in liptinite and inertinite (Singh, 2012). Their elevated hydrogen content, in relation to carbon, has probably made them per-hydrous in nature and oil prone (Singh, 2012). This is also corroborated by the Rock Eval pyrolysis of the interbedded shale horizons, where the organic matter is characterized by the presence of type II/III kerogen, suggesting the oil/gas prone nature of these shales.

In the Cambay basin, each of the five blocks has multiple source rocks of different lithologic compositions at various maturity levels (Chowdhary, 2004). A direct correlation has been observed between the organic matter richness, its quality and the thickness of the source sequences. Central and axial parts of the depositional centers have best quality and greatest quantity of source rock (Yalcin et al., 1987, Chowdhary, 2004) The Cambay shale and its stratigraphic equivalents are the predominant source rock for the entire Cambay basin.

CONCLUSION

The pyrolysis results of the interbedded shales from Tadkeshwar Formation, exposed in the open cast mines of Rajpardi and Tadkeshwar in Surat and Bharuch districts of Gujarat, are encouraging. The TOC content is quite high and an immature to mature stage is inferred from the HI vs T_{max} data of the shales. The organic matter is characterized by Type II and III kerogen, which is suitable for the generation of gas. The lateral and vertical extents of these shale horizons and the petrological and petrophysical details in integration with the organic geochemical attributes of the shales on subsurface core samples, shall help further in precise delineation of horizons for the shale gas plays.

ACKNOWLEDGEMENT

The authors acknowledge Oil Industry Development Board, New Delhi for providing financial aid in setting up of the laboratory. Gujarat Mineral Development Corporation is acknowledged for allowing the field visits to the lignite mines. The Director, NGRI is acknowledged for permitting the publication of this work.

Compliance with Ethical Standards

The author declares that he has no conflict of interest and adheres to copyright norms.

REFERENCES

Agarwal, C.G., 1986. Structure and tectonics of exposed rocks between Narmada and Kim rivers in South Gujarat. J. Geol. Soc. India, 27, 531-542.

Bhandari, L.L. and Choudhary, L.R., 1975. Stratigraphic analysis of Kadi and Kalol formations, Cambay basin, India. Am. Assn. Petrol. Geologist Bull., 59, 856-871.

Biswas, S.K., 1982. Rift basins in western margin of India and their hydrocarbon prospects with special reference to Kutch basin. Am. Assn. Petrol. Geologist Bull., 66, 1497-1513.

Biswas, S.K., 1987. Regional tectonic framework, structure, and evolution of the western margin basins of India. Tectonophysics, 137, 307-327.

Boyer, C., Keischnick, J. and Lewis, R.E., 2006. Producing gas form its source. Oil field Rev., 36, 49pp.

Chandra, P.K. and Chowdhary, L.R., 1969. Stratigraphy of Cambay basin, Bull. Oil Nat. Gas Comm. 6(2), 37-50.

Chowdhary, L.R., 1975. Reversal of basement-block motions in Cambay basin, India, and its importance in petroleum exploration: Am. Assn. Petrol. Geologist Bull., 59(1), 85-96.

Chowdhary, L.R., 2004. Petroleum geology of the Cambay basin, Gujarat India. Indian Petroleum Publisher, Dehradun, 74-111.

Curtis, J.B., 2002. Fractured shale-gas systems. Am. Assn. Petrol. Geologist Bull., 86, 1921-1938.

DGH, 2012. Directorate General of Hydrocarbons, India. Retrieved from www.dghindia.org

EIA, 2013. United States Energy Information Administartion, Retreived form http://www.eia.gov/energy_in_brief/article/about_shale_gas.cfm.

Hunt, J.M., 1996. Petroleum geology and geochemistry, W.H., Freeman and company, San Francisco, 617pp

Horsfield, B. and Schulz, H.M., 2012. Marine and Petroleum Geology, 31(1), 1-136.

Jarvie, D.M., Hill, D.J., Ruble, T.E. and Pollastro, R.M., 2007. Unconventional shale-gas systems: The Mississippian barnett shale of north-central Texas as one model for thermogenic shale-gas assessment, Am. Assn. Petrol. Geologist Bull., 91(4), 475–499.

Kundu, J., Prasad, B. and Prakash, A., 1997. Structural framework and distribution of synrift depocentres in Cambay rift basin, Western India, Am. Assn. Petrol. Geologist Bull., 81(1), 1392-1393.

Mathur, L.P., Rao, K.L.N. and Chaube, A.N., 1968. Tectonic framework of Cambay basin, India. Oil and Natural Gas Corporation Bull., 5, 7-28.

Milliken, K.L., Rudnicki, M., Awwiller, D.N. and Zhang, T., 2013. Organic matter–hosted pore system, marcellus formation (Devonian), Pennsylvania. Am. Assn. Petrol. Geologist Bull., 97(2), 177–200.

McCarthy, K., Niemann, M., Palmowski, D., Peters, K. and Stankiewicz, A., 2011. Basic Petroleum Geochemistry for Source Rock Evaluation. In: Oilfield rev., 23(2), 32-43.

Nagori, M.L., Khosla, S.C. and Jakhar, S.R., 2013. Middle eocene ostracoda from the Tadkeshwar Lignite Mine, Cambay Basin, Gujarat. J. Geol. Soc. India, 81, 514-520.

Peters, K.E., Walters, C.C. and Moldowan, J.M., 2005. The Biomarker guide. Biomarkers and isotopes in the environment and human history, 1, pp 1155, Cambridge press, .

Peters, K.E. and Cassa, M.R., 1994. Applied source rock geochemistry. In: Magoon, L.B, and W.G. Dow, (Eds.), The petroleum system from source to trap AAPG Memoirs 60, 93-120.

Raju, A.T.R., Chaube, A.N. and Choudhary, L.R., 1971. Deccan trap and geological framework of Cambay basin. Bull. Volcanologique, 35(3), 521-538.

Ross, D.J.K. and Bustin, R.M., 2008. Characterizing the shale gas resource potential of Devonian–Mississippian strata in the Western Canada sedimentary basin: Application of an integrated formation evaluation Am. Assn. Petrol. Geologist Bull., 92, 187-125.

Rust, J.E.S., Singh, H., Rana, R.S., McCann, T., Singh, L., Anderson, K., Sarkar, N., Nascimbene, P.C., Stebner, F., Thomas, J.C., Kraemer, M.S., Williams, C.J., Engel, M.S., Sahni, A. and Grimaldi, D., 2010. Biogeographic and evolutionary implications of a diverse paleobiota in amber from the early Eocene of India. Proceedings of the National Academy of Sci. United States of Am., 107(43), 18360-18365.

Sahni, A., Saraswati, P.K., Rana, R.S., Kumar, K., Singh, H., Alimohammadian, H., Sahni, N., Rose, K.D., Singh, L. and Smith, T., 2006. Temporal constraints and depositional palaeoenvironments of the Vastan lignite sequence, Gujarat: Analogy for the Cambay shale hydrocarbon source rock. Indian J. Petrol. Geol., 15(1), 1-20.

Singh, P.K., 2012. Petrological and geochemical considerations to predict oil potential of Rajpardi and Vastan lignite deposits of Gujarat, Western India. J. Geol. Soc. India, 80, 759-770.

Singh, A., Thakur, O.P. and Singh, B.D., 2012a. Petrographic and depositional characteristics of Tadkeshwar lignite deposits (Cambay basin), Gujarat. J. Geol. Soc. India, 80, 329-340.

Singh P.K., Singh, M.P., Singh, A.K., Naik A.S., Singh, V.K., Singh V.K. and Rajak, P.K., 2012b. Petrological and geochemical investigations of Rajpardi lignite deposit, Gujarat, India. Energy exploration and exploitation, 30(1), 131–152.

Tissot, B.P. and Welte D.H., 1978. Petroleum formation and occurance. A new approach for oil and gas exploration Springer Verlag, 529 pp.

USGS, 2012. United States Geological Survey. Retrieved from http://pubs.usgs.gov/fs/2011/3131/pdf/fs2011-3131.pdf

Van Krevelin, D.W., 1961. Coal: Typology-chemistry-physics-constitution. Amsterdam: Elsevier Sci., 514 pp.

Yalcin, M.N., Welte D.H., Misra K.N., Mandal S.K., Balan K.C., Mehrotra K.L., Lohar B.L., Kumar S.P. and Misra H.S., 1987. 3-D computer aided basin modelling of Cambay basin, India- a case history of hydrocarbon generation: In Petroleum geochemistry and exploration in the Afro-Asian region (Kumar, R.K. et al. (Eds) (Balkema, Rotterdam), 417–450.

Received on: 24.4.18; Revised on: 4.6.18; Accepted on: 24.6.18

J. Ind. Geophys. Union (September 2018)
v.22, no.5, pp: 478-484

Significance of regional gravity survey in parts of Sidhi and Shahdol districts, M.P.

R. Kumar* and D.V. Punekar

Geophysics Division, Geological Survey of India, Central Region, Nagpur, India
*Corresponding Author: rajan.08.ism@gmail.com

ABSTRACT

This article highlights the significance of regional gravity survey in parts of Sidhi and Shahdol districts of Madhya Pradesh. Gravity values vary from a minimum of -84mGal to maximum of -16mGal, with an overall variation of 68mGal. The general trend of Bouguer gravity anomaly contour pattern is E-W and NE-SW direction. The high gravity along with swelling and pinching is recorded near Chauphal, Nibuha, Harbaro, and Dol over Mahakoshal Group. The inferred structural features (Inferred fault/ Lineament/ Contact) are reflected in Bouguer gravity anomaly map, which is corroborated with geological map of the study area. The prominent shallow nature anomalies, recorded in the vertical derivative and residual gravity maps, correlate with the Bouguer gravity anomaly map. The Euler depth solutions provided depths less than 0.5km, 0.5 to 1.5km, 1.5 to 2.5km and beyond 2.5km. The majority of solutions are falling at the contact between two litho-units faults/ contacts, with varying depths from 0.5 to 2.5km. All these depth solutions nearly corroborate with the inferred structural features.

Keywords: Regional gravity studies, Mahakoshal Group, Chotanagapur, Sidhi, Shahdol,

INTRODUCTION

Regional gravity field can be employed effectively to delineate the subsurface structural features, such as faults/ fractures/ shear zones/ altered zones, which are significant loci for the occurrences of mineral resources and emplacement of intrusivesuite of rocks (Dahanayake and Subasinghe 1988; Gorle et al. 2016; Subasinghe 1998). Gravity and Differential Global Positioning System (DGPS) data are collected by employing the Autograv gravimeter CG-5 and DGPS 1200 over the area covered by Latitude 24º 00′00′′ N to 24º 30′ 00′′ N and Longitude 81º 45′ 00′′ E to 82º 45′ 00′′ E, which falls in the Survey of India Toposheet Nos. 63H/15, 16 and 63L/04, 08, 12, corresponding parts of Sidhi and Shahdol districts, M.P. (Figure 1). The area exhibits the mixed topography of both plains and rugged hills. The rugged topography consists of a series of roughly parallel to sub-parallel, ENE-WSW trending ridges and intervening narrow valleys. Structure and lithology mainly control the drainage pattern, which varies from sub-dendritic to dendritic and sub-parallel. The study area is mainly drained by Son river and its tributaries Gopad river, Ghiganal Nala and Deonar Nadi, Sehra Nadi, Barchar Nala, Mohan Nadi, Kansad Nadi, Karaundia Nala and Dhunnai Nala (Jha et al., 1980; Jha and Devarajan 2002a; Subramanvam et al., 1972, 1975).

GEOLOGY

Geologically, the area is represented by Vindhyan Supergroup, Sidhi gneisses, Chotanagapur gneissic complex, Mahakoshal Group, Gondwana Supergroup and Deccan Traps. The Vindhyan Supergroup is represented by Semri and Kaimur group of rocks. The Semri Group lies unconformably over the older granite gneiss and Mahakoshal Group of rocks. The Mahakoshal Group of rocks is affected by tectonic disturbances forming the weaker planes, which area later occupied by quartz veins. The granite belonging to Barambaba granite formation of Palaeoproterozoic age, occurs as isolated outcrops. The Chhotanagpur gneissic complex group is represented by quartzite, biotite schist, and granite gneiss. Similarly, the Gondwana Supergroup includes the Talchir, Barakar, Barren Measure and Pali Frmations of Lower Gondwana group and mainly consists of ferruginous sandstone and sandstone. The rocks of Chhotanagpur gneissic complex group and Lower Gondwana group have been further intruded by basic and ultra-basic intrusives, syenite, quartz veins and pegmatites (Jha et al., 1980; Jha and Devarajan, 2002b; Majumdar, 1980; Pandhare, 1972; Subramanvam et al., 1972, 1975).

GRAVITY INVESTIGATION

Regional gravity survey is carried out with a station density of 1 GM station per 2.5Sq Km along the available roads, forest tracks, cart tracks and foot tracks and covered 3500Sq Km. Elevations of each gravity stations were connected to the available bench mark and triangulation point by DGPS. The gravity observations are taken with reference to gravity bases established. Gravity data is corrected for instrument drift, and entire data were subjected to free air and Bouguer slab corrections. The gravity data have been reduced to mean sea level (MSL)

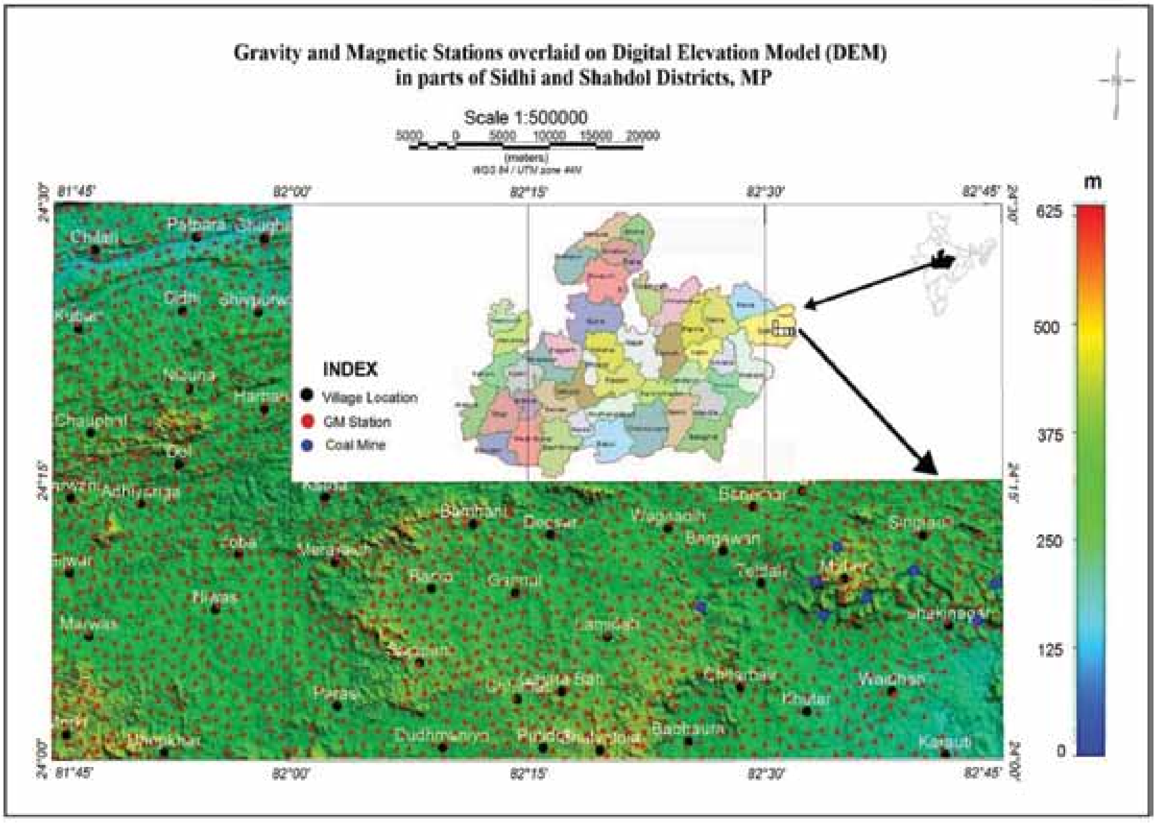

Figure 1. Gravity stations overlaid on Digital Elevation Model of the study area.

after applying elevation correction. Bouguer gravity anomaly over the study area was computed forcrustal density of 2.67 g/cm3. For latitude correction, international gravity formula 1980 was used (Bharati et al., 2016; Gorle et al., 2016).

RESULTS AND DISCUSSION

Bouguer gravity anomaly map

Bouguer gravity anomaly map has been prepared with a contour interval of 1 mGal as shown in Figure 2. The general trend of Bouguer gravity anomaly is E-W and NE-SW directions in southern and northwestern part of the area, respectively. Gravity values vary from -84 mGal to -16 mGal, with an overall variation of 68 mGal. Bouguer gravity anomaly is characterized by broad gravity 'low' in northwestern of Merki, around Parsi, Lmidah and northeastern of Shaktinagar villages and the gravity anomaly 'high' near Chaupal, Nibuha and Karda, south of Larvani and Southwestern of Adhiyariga villages.

The first major gravity gradient (F1-F1′) aligned in NW-SE direction, is observed from Pali to Singrauli in the northeastern part, which is inferred fault in boundary/ tectonic contact between Mahakoshal Group and Lower Gondwana group. The second major gravity gradient (F3-F3′) trend in SW-NE direction is recorded from Marwas to Joba villages and its continued up to Bargawan in approximate E-W direction, which is a inferred fault in boundary tectonic contact between the Chhotanagpur gneissic complex group (Granite gneiss) and Lower Gondwana group. The gravity 'high' (H1)with moderate gradient is recorded near Karda which is basically reflected the contact between the Mahakoshal group (Phyllite) and Chhotanagpur gneissic complex group (Granite gneiss) (F4-F4′). The high gravity (H2) along with negative contour pattern is observed swelling and pinching around Chauphal, Nibuha, Harbaro and Dol over Mahakoshal group which is due to the grading in metamorphism of Mahakoshal Group Formation. Due to the grading of metamorphism, the density variation frequently occurs in Mahakoshal Formation. The first moderate gravity gradient (F2-F2′) aligning approximate NW-SE direction, is observed from Waghadih to Khutar, which may be inferred fault/ contact in between two low gravity anomaly zones (L1 and L2) over coal mines area. The high gravity anomaly is recorded in between these two low gravity anomaly zones (L1 and L2) which may be due to the upliftment of basement. The second moderate gradient (F5-F5′) is observed in NE-SW direction from Chauphal to Shivpurwa, which is inferred fault as the boundary between Sidhi gneiss group (Granite Gneiss) and Mahakoshal group. This fault is also discovered earlier and called Amsi-Jiawan fault. The third

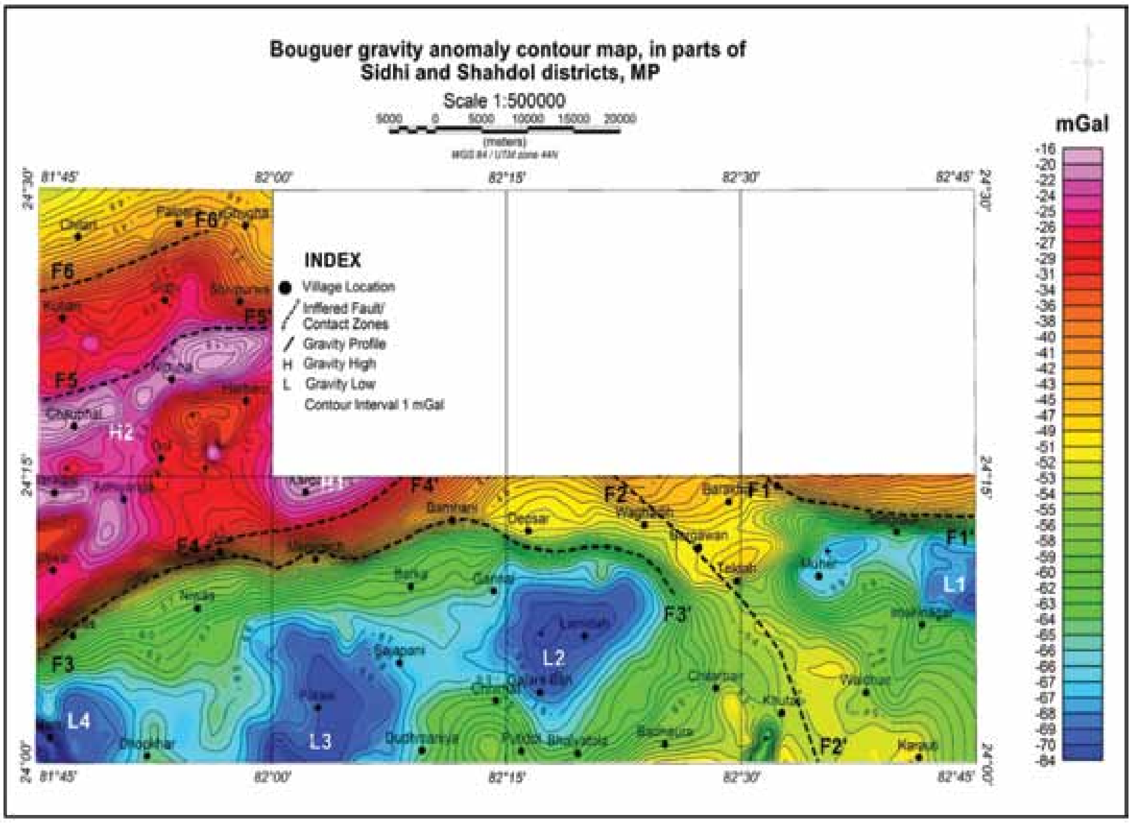

Figure 2. Bouguer gravity anomaly contour map.

major gravity gradient (F6-F6′) aligning in NE-SW direction, is recorded in northwestern part from Kubari to Ghugha, which may be inferred as a fault in the boundary between Semri Group (Sandstone), Vindhyan formation and Sidhi gneiss group (Granite gneiss). This fault is also discovered earlier and called Jamui-Markundi fault.

Regional gravity and residual gravity anomaly map

Regional and residual separations were carried out for better understanding of the sub-surface responses from deeper and shallower causative sources. Various techniques are available to carry out regional-residual separation viz. visual analysis, trend analysis, upward continuation and wave number analysis (Lowrie, 2007; Mallick et al., 2012; Telford et al., 1976, 1988, 1990). Regional gravity anomaly map is prepared by low pass filter using a cutoff wavelength of 12 km and presented in Figure 3. Gravity high, in the northwestern part of the area still exists in the regional map, indicating that causative sources of these anomalies are from a deeper level. The regional gravity map demarcated boundary of Chhotanagapur gneissic complex group (Granite gneiss) and Lower Gondwana group by high gradients.

Residual gravity anomaly map is prepared by regional-residual separation technique, which recorded various residual gravity 'high' (RH) and 'low' (RL) anomaly zones (Figure 4). The residual gravity high near Chauphal to Nibuha (RH-8), in the northwestern part, is due to the presence of meta-basalt which may be reflected from shallow depth. Residual gravity high near Gijwar (RH-9), Joba (RH-6) and Deosar (RH-5) over Granite gneiss is sharpened and clearly demarcated. The residual gravity high (RH-1) is also recorded in northeastern part, near Singrauli over Biotite schist. The residual gravity low near Singrauli (RL-1), in the eastern part is recorded over sandstone, which may be reflected from shallow depth. Residual gravity low near Khutar (RL-2) and Barka (RL-3) may be due to altered sandstone/ low dense material.

Vertical derivative of Bouguer gravity anomaly map

The Derivative maps have been used for many years to delineate edges in gravity and magnetic field data (Evjen, 1936; Hood and Teskey, 1989; Thurston and Smit, 1997). The vertical derivative technique is one of several methods of removing the regional trend. Some gravity anomalies may be distinct on examination of the Bouguer map, while other weak anomalies arising from sources that are shallow and limited in depth and lateral extent, may be obscured by the presence of stronger gravity effects associated with deeper features of larger dimensions. The primary function of the vertical derivative map is to accentuate shallow

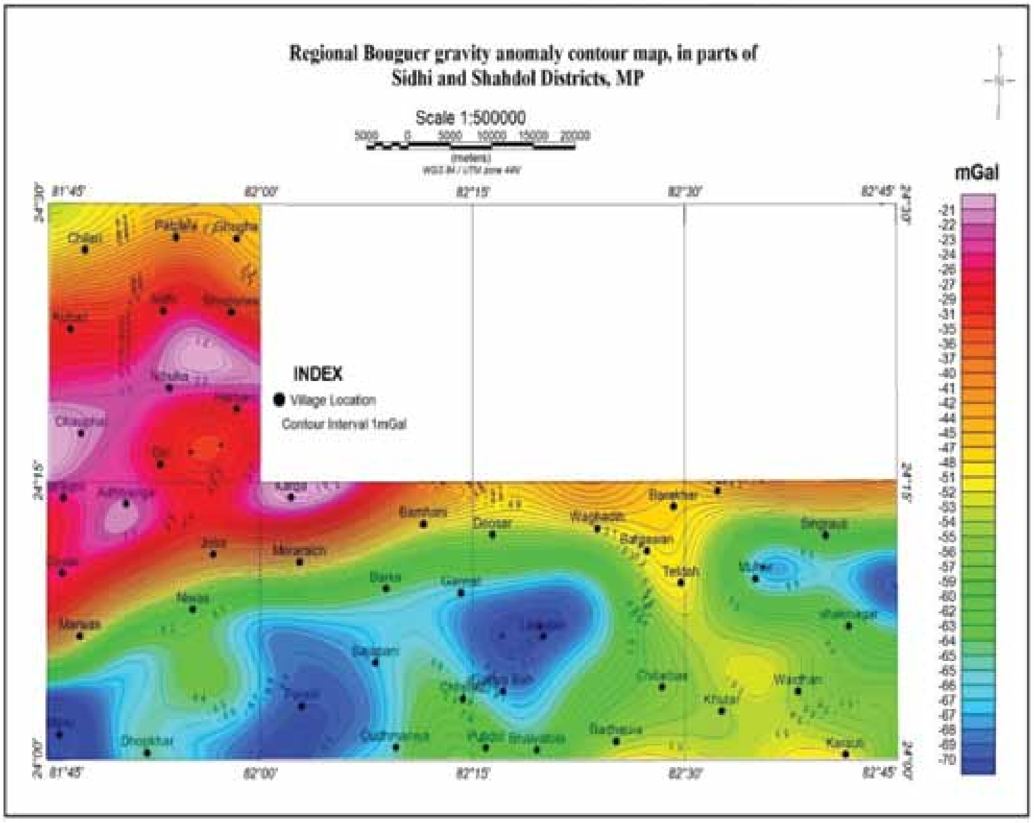

Figure 3. Regional Bouguer gravity anomaly contour map.

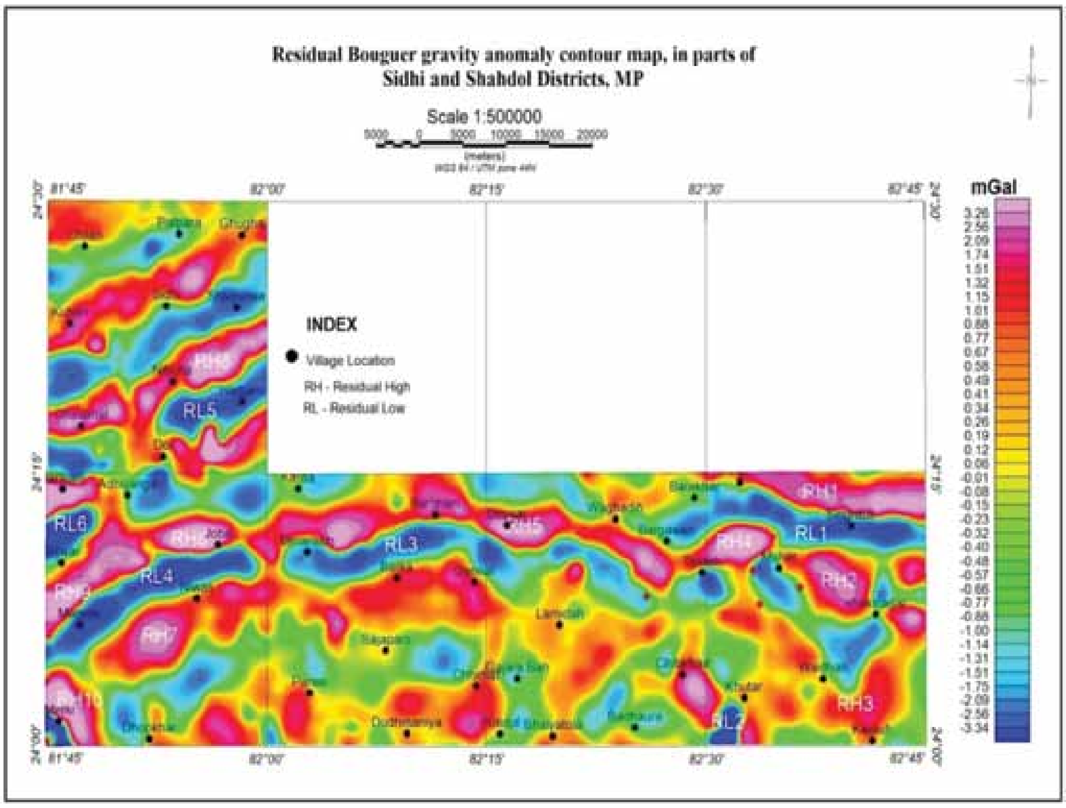

Figure 4. Residual Bouguer gravity anomaly contour map.

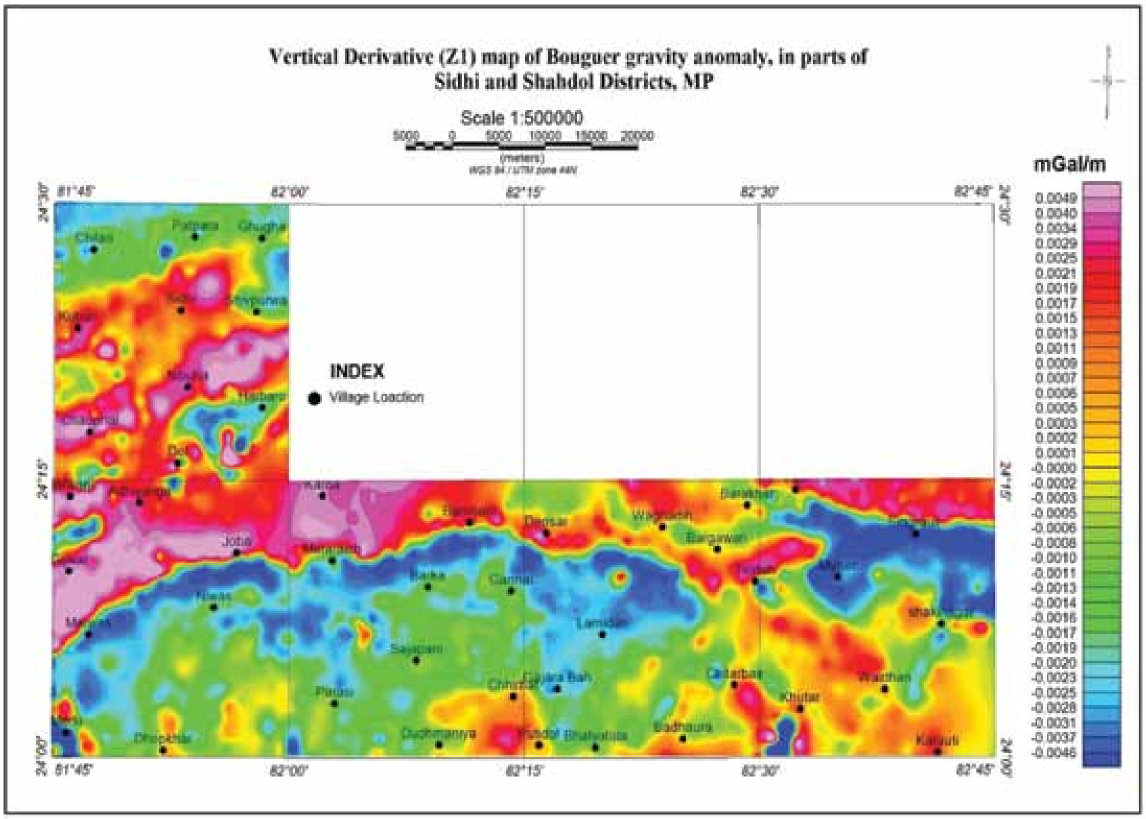

Figure 5. Vertical derivative (Z1) map of Bouguer gravity anomaly.

features at the expense of buried features. The application of the vertical derivative in gravity interpretation to enhance localized small and weak near-surface features (i.e., improving the resolving power of the gravity map) has long been established (Baranov, 1975; Gupta and Ramani, 1982). The prominent shallow nature anomalies, aligned approximately NE-SW direction (Figure 5), are observed near Singrauli, Teldah, Chitarbair, Waghadih, Deosar, Bamhani, Putidol, Karda, Gijwar, Kubari, and Nibuha.

Analytical signal map of Bouguer gravity anomaly

The analytical signal map is shown in Figure 6 which has sharpened the boundaries of the geological features more clearly in northeastern, southwestern, northwestern and central parts of the survey area. Hence, the analytical signal map was utilized in delineating sources and with high intensity gravity gradients observed in the western part near Marwas-Meraraich-Deosar trending in SW-NE and approximate E-W direction, respectively, that has been inferred as a fault in boundary tectonic contact zone between the Chhotanagpur gneissic complex group (Granite gneiss) and Lower Gondwana group which is also corroborated with Bouguer gravity anomaly map. Linear bodies in analytic signal map are recorded over north of Singrauli, north of Waghadih and Bargawan, south of Khutar, south of Merki, east of Chauphal, North-east of Nibuha, east of Dol, north of Chilari, Patpara and Ghugha and also north of Kubari, Sidhi and Shivpurwa.

Euler 3D depth solutions of gravity anomaly

The standard Euler 3D deconvolution method is based on Euler's homogeneity equation that relates to estimate the depth of causative sources obtained from Bouguer gravity anomaly and its first order gradient components in three directions to the location of the sources of the data and gridded data with the degree of homogeneity, which may be interpreted as a structural index (SI). The structural index (SI) is based on the geometry of the gravity anomaly and is a measure of the rate of change of the anomaly with distance from the source (Thompson, 1982).

The Euler 3D depth solutions are obtained by using the Euler 3D module of Geosoft software version 9.1 shown in Figure 7. The window length of 5km and Structural Index = 0, were used to estimate depths of various sub-surface structures. The Euler depth solutions provided depths less than 0.5 km, 0.5 to 1.5 km, 1.5 to 2.5 km and beyond 2.5 km. The majority of solutions are falling at the contact between two litho-units faults/ contacts, with varying depth from 0.5 to 2.5km. All these depth solutions nearly corroborate with the inferred structural features.

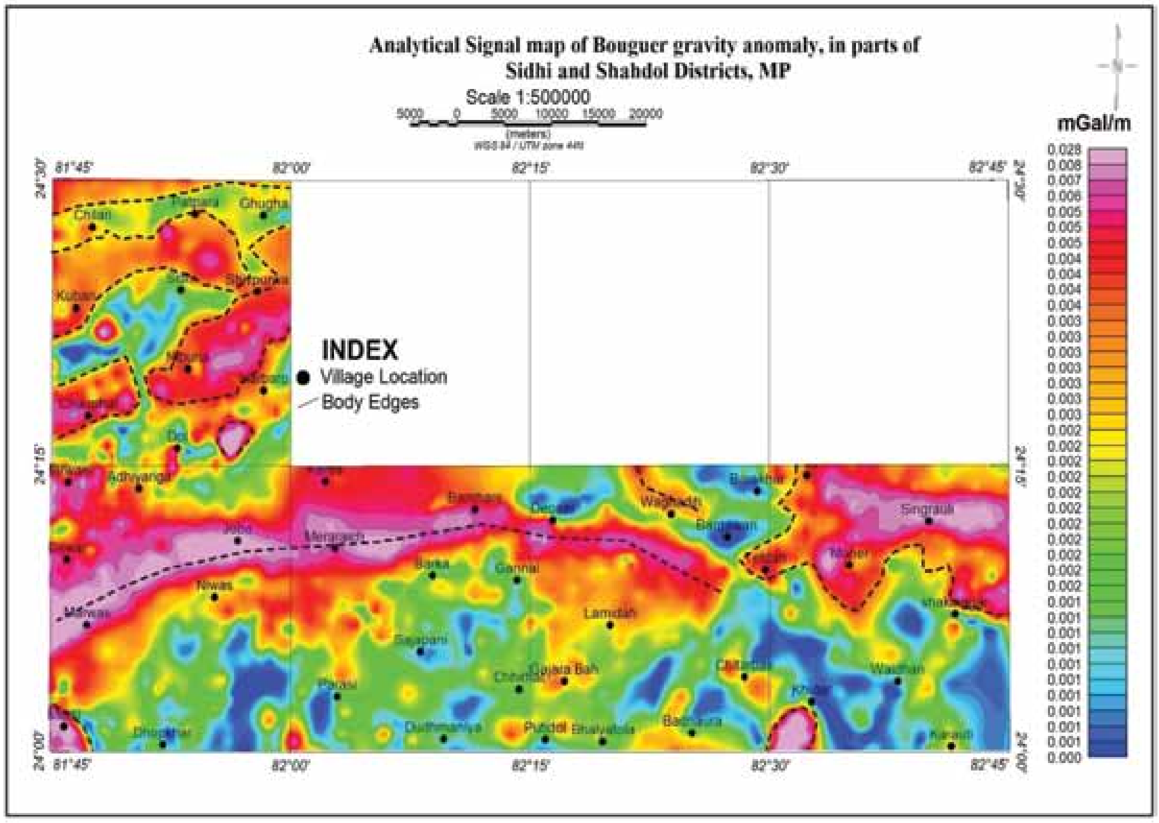

Figure 6. Analytical signal map of Bouguer gravity anomaly.

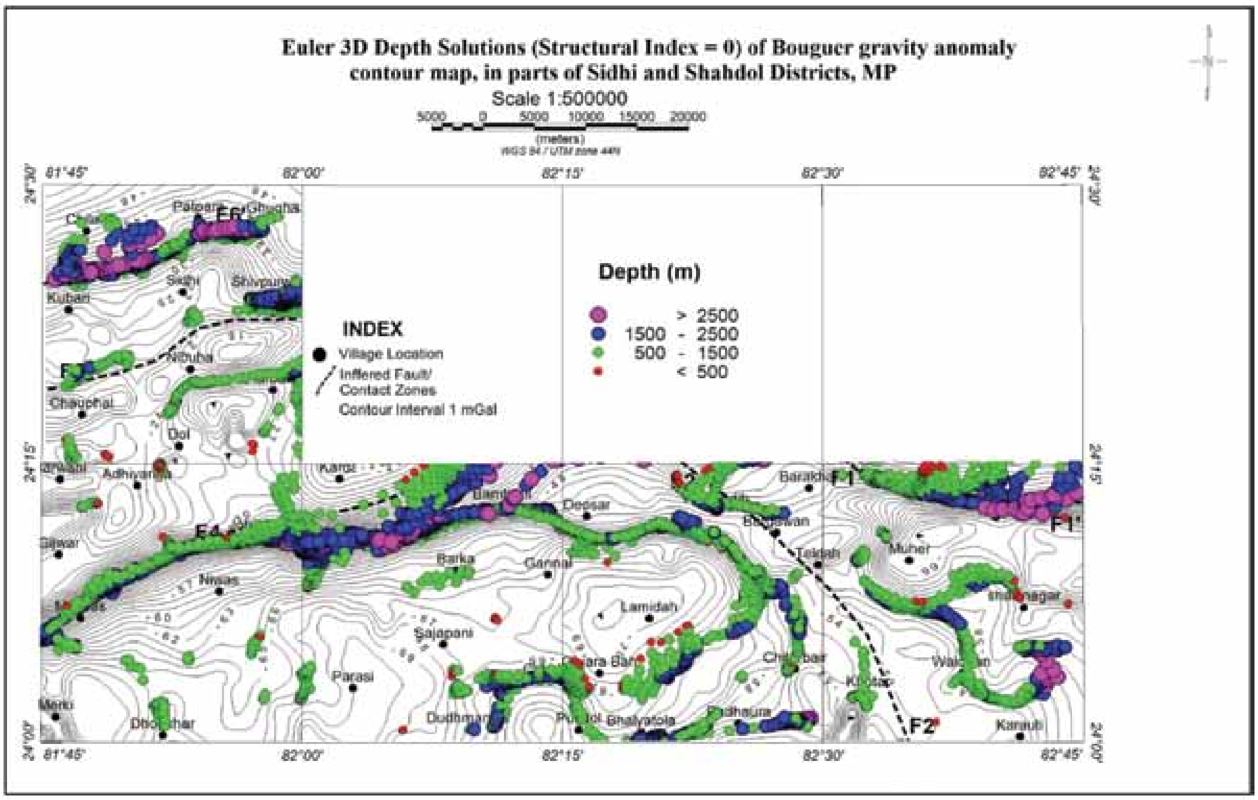

Figure 7. Euler 3D depth solutions (Structural Index = 0).

CONCLUSIONS

The significant gravity gradient (F2-F2′), aligning approximately NW-SE direction and observed from Waghadih to Khutar, may be inferred as fault/ contact, which lies in between two low gravity anomaly zones (L1 and L2) over coal mines area. The high gravity (H2) along with swelling and pinching is recorded near Chauphal, Nibuha, Harbaro, and Dol that lie over Mahakoshal formation. The swelling and pinching of Bouguer gravity anomaly can be considered as characteristic of Mahakoshal group, due to the density contrast caused by metamorphism. The gravity gradient (F5-F5′) is observed in the NE-SW direction from Chauphal to Shivpurwa, which is again inferred as fault/ contact between Sidhi gneiss group (Granite gneiss) and Mahakoshal Group. This fault is called Amsi-Jiawan fault. Another prominent gravity gradient (F6-F6′) is recorded in northwestern part that aligns in NE-SW direction from Kubari to Ghugha, which can be inferred as fault between Semri group (Sandstone), Vindhyan formation and Sidhi gneiss group (Granite gneiss). This fault is known as Jamui-Markundi fault. The majority of Euler solutions are falling at the contact between two litho-units faults/ contacts with varying depth from 0.5 to 2.5km. All these depth solutions are nearly corroborating with the inferred structural features.

ACKNOWLEDGEMENT

The authors express their sincere gratitude to Shri N. Kutumba Rao, Additional Director General and HOD, Geological Survey of India, Central Region, Nagpur for providing all logistics in carrying out the work. We are a great depth of gratitude to D. Hanmanthu for his kind assistance during the geophysical data collection. We are thankful to the reviewers, Publication Division of GSI, CR, and Nagpur who have given critical and thoughtful suggestions.

Compliance with Ethical Standards

The authors declare that they have no conflict of interest and adhere to copyright norms.

REFERENCES

Baranov, V., 1975. Potential fields and their transformations in applied geophysics. Expl. Monograph Series, no.65.

Bharati, S.K., Ramachandrappa and Hanmanthu, D., 2016. A Report on geophysical mapping in toposheet nos. 64L/1, 2, 3, 4, and 64H/15, parts of Raipur, Dhamtari Districts, Chhattisgarh, Unpublished NGPM, Report, Geol. Surv. India, Central Region, Nagpur, India.

Dahanayake, K. and Subasinghe, S.M.N.D., 1988. Development of recent stromatolitic structures and phosphatic enrichment in precambrian marble of Sri Lanka, Economic Geol., 83, 1468-1474.

Evjen, H.M., 1936. The place of the vertical gradient in gravitational interpretations, Geophysics, 1, 127-136.

Gorle, R., Anusha, Y. and Hanmanthu, D., 2016. A Report on geophysical mapping in toposheet nos. 64H/6, 9, 10, 13, and 14, parts of Raipur, Districts, Chhattisgarh, Unpublished NGPM, Report, Geol. Surv. India, Central Region, Nagpur, India.

Gupta, V.K. and Ramani, N., 1982. Optimum second vertical derivatives in geologic mapping and mineral exploration. Geophysics, 42, 1706 –1715.

Hood, P.J. and Teskey, D.J., 1989. Airborne gradiometer program of the Geological Survey of Canada, Geophysics, 54, 1012-1022.

Jha, D.K., Banerjee S.K. and Narain, A., 1980. Systematic geological mapping of the area around Dudhamaniya, Singrauli Tehsil, Sidhi district, M.P, Unpublished, Report, Geol. Surv. India., India.

Jha, D.K. and Devarajan, M.K., 2002a. The large scale mapping and regional geochemical sampling of the area around Chanariya gold prospect, Sidhi district, M.P., Unpublished, Report, Geol. Surv. India., India.

Jha, D.K. and Devarajan, M.K., 2002b. Preliminary exploration for gold in Chakariya block, Sidhi district, M.P., Unpublished, Report, Geol. Surv. India., India.

Lowrie, W., 2007. Fundamentals of geophysics, 2ed., Cambridge University Press, New York, 84-87.

Majumdar, M., 1980. Geology of Sarai-Bharsera area, north western part of Singrauli coalfield, Sidhi district, Madhya Pradesh, Unpublished, Report, Geol. Surv. India.

Mallick, K., Vasanthi, A. and Sharma, K.K., 2012. Bouguer gravity regional and residual separation: Application to Geology and Environment, Springer.

Pandhare, S.A., 1972. The systematic geological mapping in parts of Gopad-Banas Tahsil, Sidhi district, M.P., Unpublished, Report, Geol. Surv. India.

Subramanvam, B., Sankaram, S.P. and Ghatak, S.K., 1972. Geophysical investigations for Sulphide ores in Guriara area, Sidhi district, M.P., Unpublished, Report, Geol. Surv India.

Subrahmanyam, B.,Sankaram, S.P.,Ghatak, S.K. and Khotpal, A.S., 1975. Geophysical investigations for sulphide ores in Byria-Bahertola area Sidhi district, M.P., Unpublished, Report, Geol. Surv. India., India.

Subasinghe, N.D., 1998. Formation of a phosphate deposit through weathering and diagenesis—An Example from Sri Lanka. PhD Thesis (Unpubl.), University of Reading.

Telford, W.M., Geldart, L.P., Sheriff, R.E. and Keys, D.A., 1976. Applied Geophysics, Cambridge University., Press, 860.

Telford, W.M., Geldart, L.P., Sheriff, R.E. and Keys, D.A., 1988. Applied geophysics,2ed., Cambridge University Press.

Telford, W.M., Geldart, L.P. and Sheriff, R.E., 1990. Applied geophysics, 2nded., Cambridge, New York.

Thompson, D.T., 1982. EULDPH: A new technique for making computer assisted depth estimates from Magnetic data, Geophysics, 47, 31-37.

Thurston, J.B. and Smit, R.S., 1997. Automatic conversion of magnetic data to depth, dip, and susceptibility contrast using the SPITM method, Geophysics, 62, 807-813.

Received on: 13.6.18; Revised on: 2.8.18; Accepted on: 4.8.18

J. Ind. Geophys. Union (September 2018)
v.22, no.5, pp: 485-506

Possible seismic hazards in Chandigarh city of North-western India due to its proximity to Himalayan frontal thrust

Nitish Puri[1]* and Ashwani Jain[1]

[1]Department of Civil Engineering, NIT Kurukshetra, Kurukshetra, Haryana – 136119, India

*Corresponding author: nitishpuri.ce.89@gmail.com

ABSTRACT

Chandigarh, the first ever planned city in India, currently having an urban agglomeration of 1.2 million, is situated in the proximity of the Himalayan Frontal Thrust (HFT) zone. It falls under the seismic zone IV as per IS 1893 Part-1 (2016). It is ranked as second most seismically vulnerable city in India, based on expected peak ground acceleration (PGA) as per National Disaster Management Authority (NDMA). In the present study, the results of seismic hazard analysis for Chandigarh city, carried out adopting probabilistic approach are reported. The PGA values are estimated for rock sites, and a seismic hazard map for the city is prepared. Based on the observed PGA values, one-dimensional nonlinear wave amplification analysis and liquefaction potential assessment are also made. For this purpose, geotechnical data are collected for 41 boreholes from various government and private organizations, to have an assessment of soil properties and ground water conditions. For the sites under consideration, it is observed that ground motions get amplified at 5 sites due to local site effects and 18 sites in the city are prone to liquefaction. Therefore, a site-specific design approach should be adopted in the city for the design of important structures at vulnerable sites.

Keywords: Probabilistic seismic hazard, wave amplification, liquefaction potential, Himalayan thrust system.

INTRODUCTION

Earthquake is an event which can inflict severe damage to the infrastructure of a city and take it back to a few decades. The recent example is the Canterbury earthquakes of 2010 and 2011 that caused heavy damages in the Christchurch city of New Zealand. The estimated cost to rebuild is around 20% of total GDP of New Zealand, i.e. about NZ$40 billion approximately (Potter et al., 2015). Similarly, in 2001 Bhuj earthquake, total property damage was estimated at about $7.5 billion. The multi-storey structures in Ahmedabad city, being located on younger alluvial deposits, experienced heavy damage, inspite of greater distance of the city (more than 300 km) from the earthquake epicenter (Ranjan, 2005). Hence, it is necessary for areas located in the vicinity of tectonically active sources to be ready with proper mitigation measures and rescue arrangements, for example cities close to Himalayan range, which were formed due to the collision between Indian plate and Asian plate that are still converging at a rate of 55 mm/year (Peltzer and Saucier, 1996). The earthquakes occurring in this region are due to the formation and uplift of the mountains.

The Himalayan thrust system, consisting (from north to south) the Main Central Thrust (MCT), the Main Boundary Thrust (MBT) and the Himalayan Frontal Thrust (HFT), are considered one of the most seismically active tectonic zones in the world (Malik et al., 2010). This has been demonstrated by the occurrence of several large magnitude earthquakes in the area (Table 1). It is believed that since the 1897 Shillong earthquake of M_w 8.0, the Himalayan region seems to have ruptured ranging from 15 to 20% to as much as 45%, and the risk of an imminent great earthquake is thus high (e.g. Molnar and Pandey, 1989). Moreover, the central Himalaya, which is considered as a prominent 'seismic gap' (Khattri et al., 1984), is believed to be the most vulnerable segment and is due for a great plate boundary earthquake of greater than M_w 8.0 (Rajendran and Rajendran, 2005). A large area adjacent to the Himalayan thrust system may be subjected to severe damage during an earthquake.

The geographical location of the Chandigarh city, which is located in the Himalayan foothills to the south of HFT, makes it susceptible to huge damage due to earthquakes in the Himalayan thrust system (MCT, MBT and HFT). Moreover, the alluvial land cover also makes it prone to hazards due to wave amplification and soil liquefaction. The gradual increase in population density has also increased vulnerability of the city. This calls for an immediate site-specific seismic hazard analysis (SHA) and estimation of other earthquake induced hazards. Besides, the damage inflicted by the large earthquakes in this region which occurred earlier (Table 1), also calls for taking appropriate mitigation measures.

In the present study, possible seismic hazards in the city of Chandigarh have been evaluated. It includes estimation of seismic hazard by probabilistic seismic hazard analysis, wave amplification analysis and determination of liquefaction potential. Results have been formulated in terms of seismic hazard maps for various return periods, response spectra, peak ground acceleration amplification factors and a liquefaction hazard map.

Table 1. Major earthquake events in the Himalayan thrust system (source: en.wikipedia.org).

Earthquake	Date	Magnitude	Damage report
1905 Kangra earthquake	4 April 1905	7.8 M_s	Death toll: 20,000
			Massive destruction of structures
1934 Bihar–Nepal earthquake	15 January 1934	8.0 M_w	Death toll: 12,000
			Massive damage to structures, roads and telephone lines
1950 Assam earthquake	15 August 1950	8.6 M_w	Death toll: 4,800
			Massive landslides,70 villages destroyed
2005 Kashmir earthquake	8 October 2005	7.6 M_w	Death toll: 87,000
			Massive damage to structures, 75,000 injured and 2.8 million displaced
2015 Gorkha earthquake	25 April 2015	7.8 M_w	Death toll: 9,000
			Massive damage to structures, 24,000 injured and 3.5 million homeless

REVIEW OF LITERATURE

Seismic hazard analysis is the first step towards mitigation of earthquake hazards. It is carried out for quantitative evaluation of expected earthquake hazard at a site. Two approaches, probabilistic (PSHA) and deterministic (DSHA), are commonly adopted for seismic hazard assessment. In DSHA, a particular earthquake scenario is assumed, based on past data and tectonic set up of the study area, and hazard is estimated based on attenuation characteristics of the region. The DSHA provides the worst-case scenario earthquake that can occur in the region and the strong-motion parameters are estimated for the maximum credible earthquake assumed to occur at the closest possible distance from the site of interest. This is done without considering the likelihood of its occurrence for a specified exposure period during the design life of the structure. It is used widely for nuclear power plants, large dams, large bridges, hazardous waste containment facilities and as a 'cap' for PSHA (e.g. Puri and Jain, 2016). Several studies have been carried out in India based on this approach; for example, Chennai city (Boominathan et al., 2008), Gujrat region (Chopra et al., 2012), Kolkata city (Shiuly and Narayan, 2012), India (Kolathayar et al., 2012a), major cities of Gujrat (Shukla and Choudhury, 2012), Andaman and Nicobar Islands (Kataria et al., 2013), Goa (Naik and Choudhury, 2015) and Haryana (Puri and Jain, 2016).

On the contrary, PSHA rectifies several problems inherent in its deterministic analysis, viz. lack of quantification of uncertainties in size, location of an earthquake and probability of its occurrence. It quantitatively represents the relationship between potential seismic sources, associated ground motion parameters and respective probabilities of occurrence. It also computes the probability of exceeding of specified level of ground motion at a particular site, which is represented as function of return period and fault displacement. Due to its capability to accommodate uncertainties, more and more seismic hazard analyses are being carried out using probabilistic approach (e.g. for Delhi by Sharma et al., 2003; Tripura and Mizoram states by Sitharam and Sil, 2014; Surat city by Thaker et al., 2012; Patna by Anbazhagan et al., 2015a). However, the present DSHA and PSHA methodologies account for the earthquake hazard for rock sites only and the effect of wave amplification is rarely considered in ground motion models. Therefore, identification of soil layers susceptible to ground motion amplification is an important task for accurate assessment of seismic hazard in earthquake prone areas. The development of site specific ground motions involves the study of both seismic hazard and wave amplification.

It is known that the wave amplification, soil liquefaction, landslides and tsunami are the most devastating after-effects of an earthquake. However, landslides and tsunami can only be observed in hilly and coastal areas respectively, thereby making the first two, i.e. seismic wave amplification and soil liquefaction as the crucial parameters observed in plain areas, where the earthquake manifests itself as shaking of ground and sometimes its displacement. Earthquake engineers are primarily interested in the strong ground motions which are sufficiently strong to be felt during an earthquake.

Table 2. Magnitude conversion equations.

Source	Conversion Equations
Scordilis (2006)	$M_w = 0.67\ M_s + 2.07$, for $(3.0 \le M_S \le 6.1)$ $M_w = 0.99\ M_s + 0.08$, for $(6.2 \le M_S \le 8.2)$
Scordilis (2006)	$M_w = 0.85\ m_b + 1.03$, for $(3.5 \le m_b \le 6.2)$
Kolathayar, Sitharam and Vipin (2012b)	$M_w = 0.815\ M_L + 0.767$, for $(3.3 \le M_L \le 7.0)$
Yenier, Erdoğan and Akkar (2008)	$M_w = 0.764\ M_d + 1.379$, for $(3.7 \le M_d \le 6.0)$

M_s-surface wave magnitude, m_b-body wave magnitude, M_L-local magnitude, M_d-duration magnitude

Characteristics of seismic waves get modified as they travel through different soil conditions. This phenomenon is referred to as 'local site effects'. Local site conditions have profound influence on all the important seismic characteristics, i.e. amplitude, frequency content and duration of strong ground motions. The extent of influence depends upon thickness and properties of the soil cover, site topography, and on the characteristics of the input motion itself. The phenomenon of wave amplification due to local site effects has been well demonstrated, in case of many earthquakes , like 1985 Michoacán, Mexico earthquake M_w 8.0, the 1989 Loma Prieta, San Francisco earthquake M_w 6.9, the 2000 Totoriken-seibu, Japan earthquake M_w 6.7 (Kramer, 2013), the 1999 Chamoli earthquake M_w 6.8 (Nath et al., 2002) and the 2001 Bhuj earthquake M_w 7.6 (Ranjan, 2005).

Similarly, the phenomenon of loss of strength of loose saturated cohesionless soils subjected to dynamic loading due to increase in pore water pressure is termed as soil liquefaction. It is manifested in the form of sand boils and mud spouts at the ground surface formed by seepage of water, or in some cases by the development of quick sand condition. In such cases, buildings may sink substantially into the ground or tilt excessively; lightweight structures and foundations may get displaced laterally causing structural failures. Such phenomenon was well demonstrated for several earthquakes around the world, for example, the 1934 Bihar-Nepal earthquake M_w 8.2, the 1964 Niigata, Japan earthquake M_w 7.6, the 2001 Bhuj, western India earthquake M_w 7.6 and the 2011 Christchurch, New Zealand earthquake M_w 6.3. Hence, it is important to assess liquefaction potential of the susceptible soils that plays a major role for seismic hazards. An initial screening of whether the site would undergo liquefaction can be done on the basis of various factors such as geology of the area, depth of ground water table, grain size distribution etc. (Puri and Jain, 2014). For example, loose, fine, saturated and poorly graded sands are more susceptible to liquefaction in comparison to dense and well-graded soils. However, a detailed assessment of liquefaction susceptibility requires analysis of stresses induced by the earthquake and resistance offered by the soil deposit. Various semi-empirical methods have been reported based on SPT N-value, shear wave velocity (V_s), cone penetration resistance etc. (e.g. Tokimatsu and Uchida, 1990; Youd et al., 2001; Cetin et al., 2004; Idriss and Boulanger, 2006).

SEISMOTECTONICS OF THE STUDY AREA

Chandigarh city is located at the foothills of Himalayas, occupying an area of 120 km^2. It is a Union Territory and common capital of the states of Haryana and Punjab. The city falls under Seismic Zone IV as per IS 1893 Part-1 (2016). It is located along Himalayan Thrust System and is considered to be highly prone to earthquakes. Paleo-seismic investigations across the Chandigarh fault in the frontal Himalayan region reveal that two major earthquakes occurred during the 15th - 16th century (Malik et al., 2008).

Development of earthquake catalogue and tectonic map

An area covering 300 km around Chandigarh (30.73° N, 76.77° E) has been considered as the study area. A comprehensive earthquake catalogue for a period from January 1291 to September 2016 (~725years) has been compiled, using data collected from various national and international seismological agencies, like National Disaster Management Authority (NDMA), India Meteorological Department (IMD), International Seismological Center (ISC-UK) and United States Geological Survey (USGS). The catalogue comprises of 2160 earthquake events of magnitude $M_w \ge 4$ in the region (Lat 28°-33°.5 N and Long 73°.5-80° E). The catalogue has been carefully homogenized to a common scale of moment magnitude (M_w) and de-clustered to remove dependent events like foreshocks and aftershocks. Homogenization has been carried out using equations as reported in Table 2.

Declustering is carried out considering space and time windows proposed by Gardner and Knopoff (1974) which are: Distance=$e^{-1.024+0.804M}$ and Time=$e^{-2.87+1.235M}$. Some 142 dependent events are removed and an epicenter map for the study area is prepared (Figure 1).

The catalogue is examined for completeness. For this purpose, catalogue is divided into several magnitude classes, and completeness periods are calculated using Cumulative Visual Inspection (CUVI) method of Tinti and Mulargia (1985), and Stepp (1972) method as shown in Figure 2 and

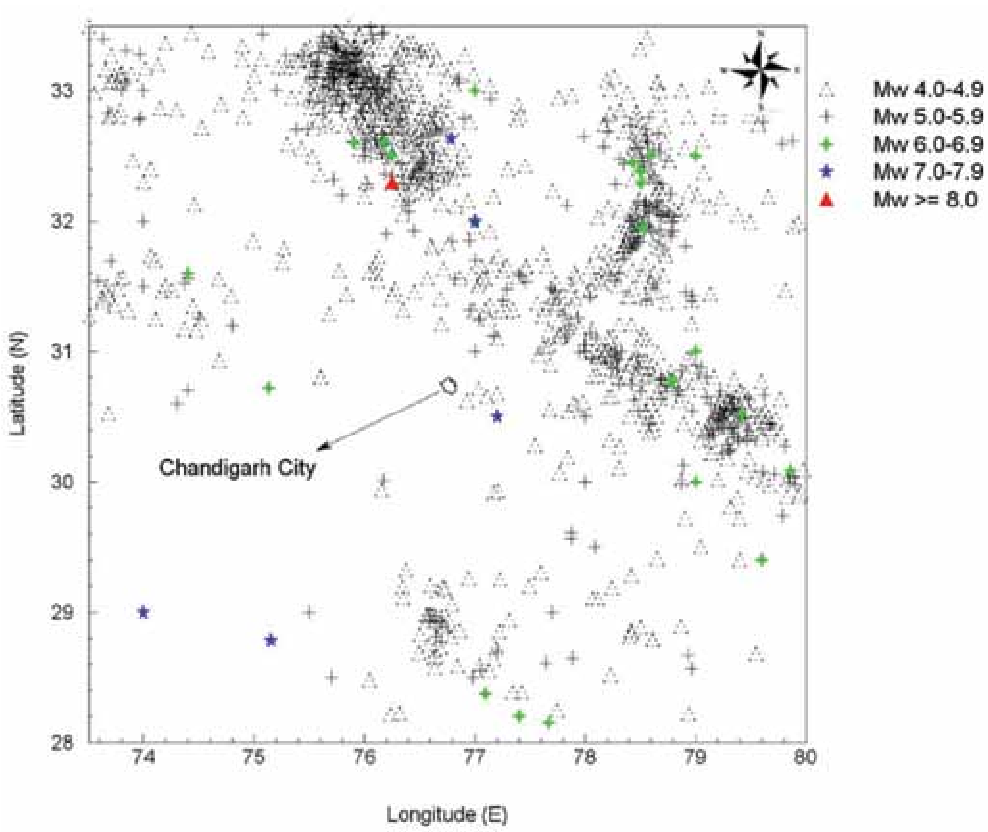

Figure 1. Epicenter map of the studied region situated around Chandigarh city.

Table 3. Completeness analysis of catalogue.

Magnitude Class (M_w)	CUVI method		Stepp method	
	Period	Interval (Years)	Period	Interval (Years)
4.0-4.9	1962-2015	53	1963-2015	52
5.0-5.9	1926-2015	89	1925-2015	90
6.0-6.9	1901-1975	74	1900-1970	70
7.0-7.9	1905-1999	94	1904-1999	95

3 respectively. The completeness periods as obtained by both the methods are quite comparable (Table 3). The catalogue is found to be complete for a sufficient period of time.

A tectonic map of the study area is prepared using Seismotectonic Atlas of India and its Environs (SEISAT) (Dasgupta et al., 2000) (Figure 4). SEISAT lists all the linear tectonic features which may or may not be active. Twenty tectonic features are identified which are likely to produce substantial ground motions. This has been done by overlaying epicenters of recorded events on the tectonic map.

Gutenberg-Richter seismicity parameters (a and b)

The seismicity parameters 'a' and 'b' are the key input parameters for PSHA. For simplicity, the study region has been divided into three sub-regions considering each sub-region as an area source of earthquakes. Considering the complete part of the catalogue for all the magnitude ranges, the seismicity parameters have been calculated for each area source through linear least squares regression method following an exponential distribution of magnitude as shown in Figures 5 to 7. The exponential distribution is given in equation (1) below:

$$\lambda_m = 10^{a-bM_w} = \exp(\alpha - \beta M_w) \quad (1)$$

where λ_m = mean annual rate of exceedance, a = coefficient such that ath power of 10 gives the mean yearly number of earthquakes of magnitude greater than or equal to zero, α = 2.303a, b = coefficient which describes the relative likelihood of large and small earthquakes and β = 2.303b. The reciprocal of the annual rate of exceedance (λ_m) for a particular magnitude is commonly referred to as the return period (T_R) of an earthquake exceeding that magnitude and is very important for earthquake resistant design. The

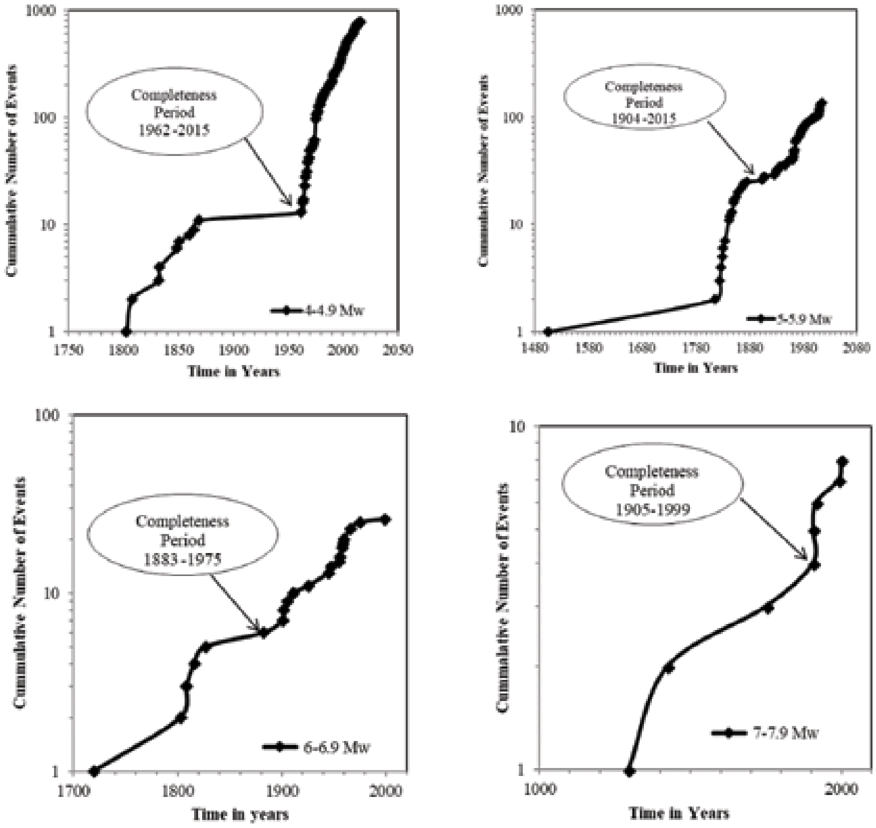

Figure 2. Completeness analysis using CUVI method.

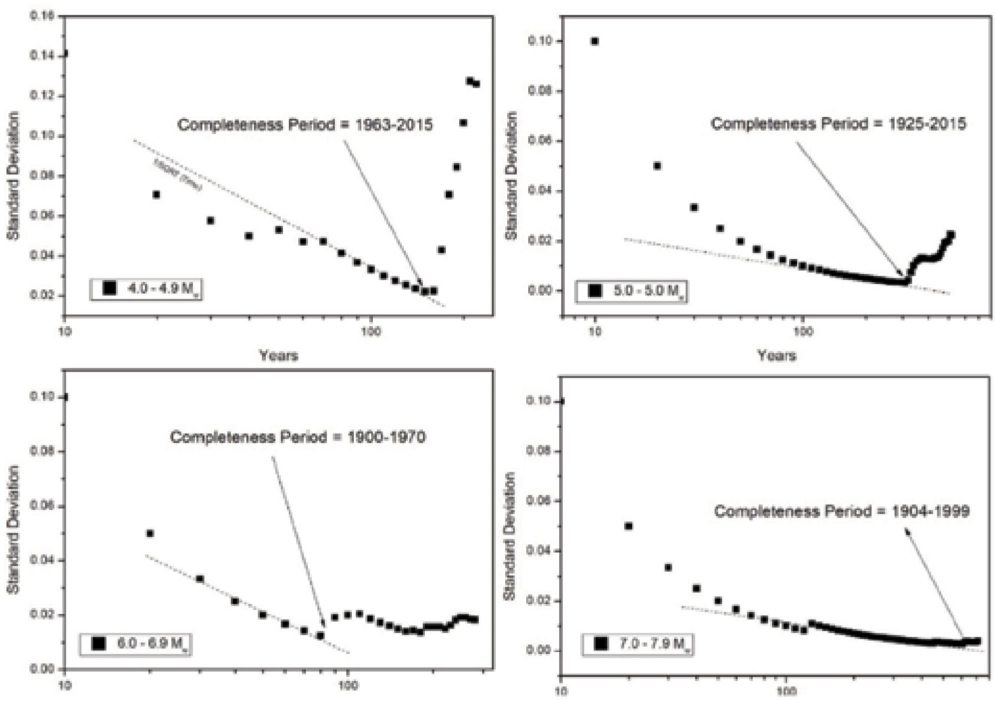

Figure 3. Completeness analysis using Stepp (1972) method.

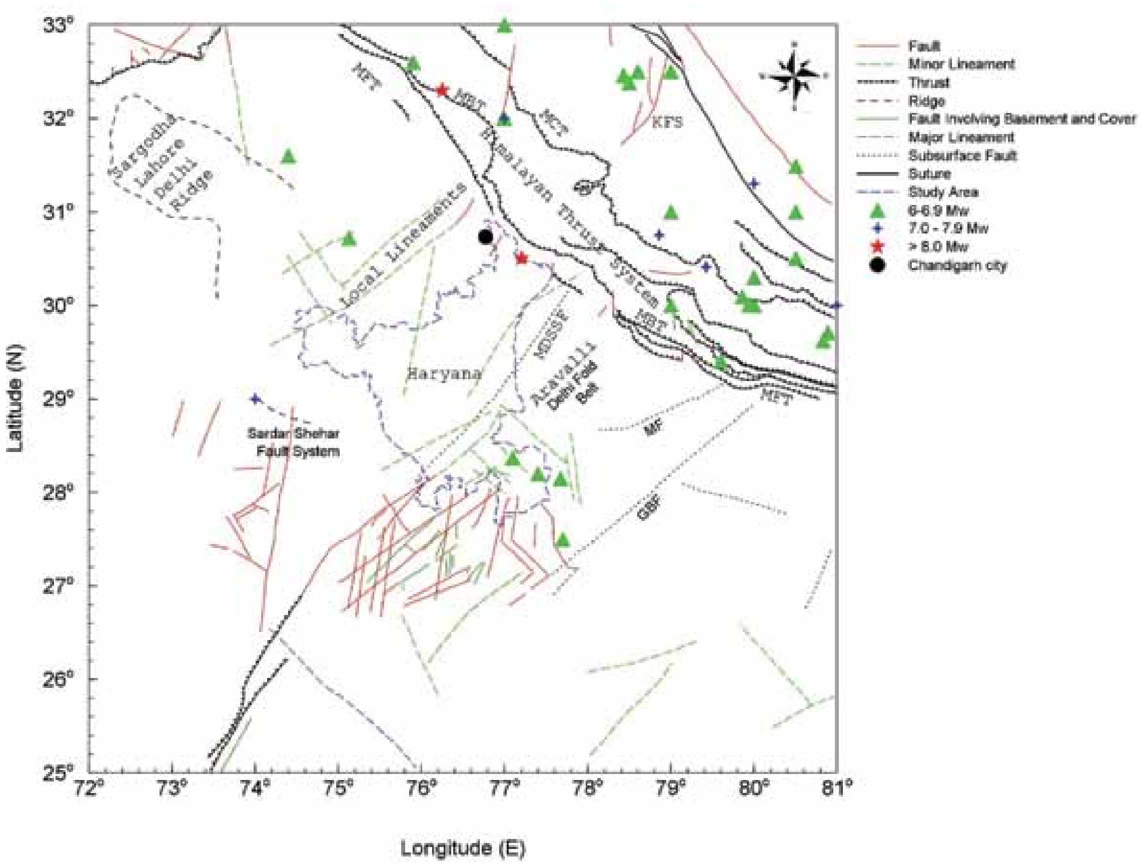

Figure 4. Tectonic map showing detailed tectonic features alongwith epicenter of significant earthquakes in the study region (after Dasgupta et al., 2000).

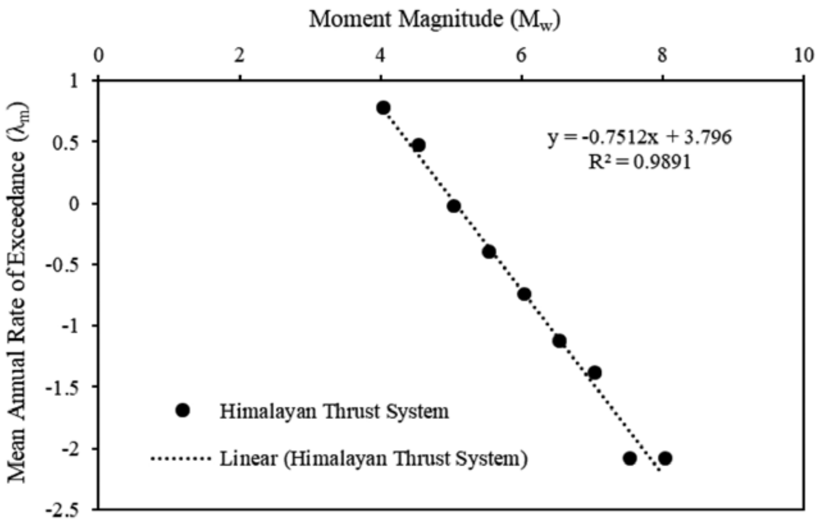

Figure 5. Seismicity parameters for Himalayan Thrust System.

seismicity parameters estimated along with the typical return periods for M_{obs} for all the area sources have been reported in Table 4. The value of return period calculated for different area sources demonstrates the capability of tectonic sources in Himalayan Thrust System to generate frequent large earthquakes.

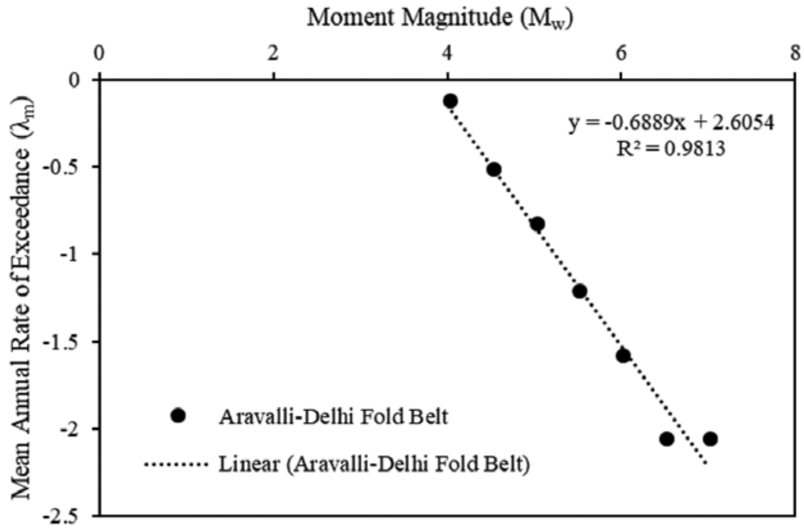

Figure 6. Seismicity parameters for Aravalli-Delhi Fold Belt.

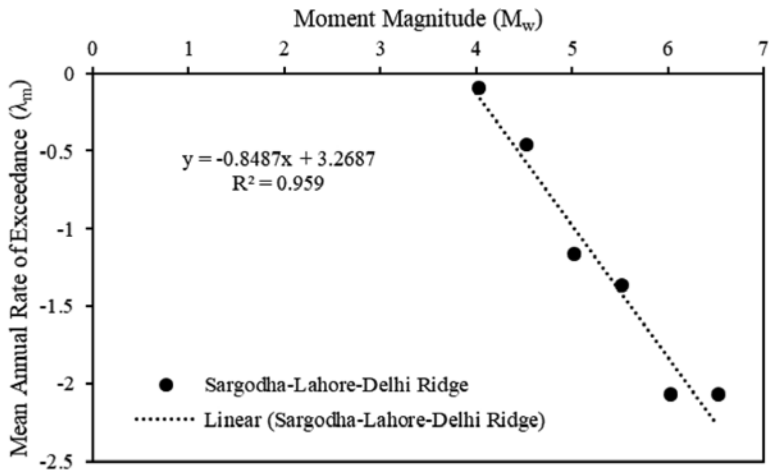

Figure 7. Seismicity parameters for Sargodha-Lahore-Delhi Ridge.

Table 4. Seismicity parameters for different area sources.

Area source	b	a	Range of magnitude (M_w) class	R^2	M_{obs}	Return Period (T_R) for M_{obs} (in years)
Himalayan Thrust System	0.75	3.8	4.0-8.0	0.989	8.0	159
Aravalli-Delhi Fold Belt	0.69	2.61	4.0-7.0	0.981	7.1	195
Sargodha-Lahore-Delhi Ridge	0.85	3.27	4.0-6.5	0.959	6.5	180

Estimation of maximum credible earthquake magnitude (M_{max})

Maximum credible earthquake magnitude (M_{max}) earthquakes for different seismogenic sources are estimated using appropriate empirical relations (Table 5). Total fault length (TFL) for various seismogenic sources are estimated. The sub-surface rupture length (RL) is considered as 1/3 of the TFL (Mark, 1977).

To estimate maximum credible earthquake magnitude (M_{max}), an increment of 0.5 is added to the maximum observed magnitude, wherever the available methods are not applicable (Gupta, 2002). Maximum observed magnitudes (M_{obs}) for various seismogenic sources are shown in Table 6. The maximum credible earthquake magnitudes (M_{max}) estimated for various seismogenic sources in the seismic study area are found to range from 5.1 to 8.5 (Table 7).

Table 5. Methods for estimating $M_{max.}$

Source	Empirical Relation	Magnitude Range	Total Fault Length (km)
Wells and Coppersmith (1994)	Mw=4.38+1.49 log(RL)	M_w 4.8 to 8.1	0 - 350
Bonilla et al., (1984)	Ms=6.04+0.708 log(RL)	$M_s > 6.0$	0 - 444
Vakov (1996)	Ms=4.422+1.448 log(RL)	M_w 4.5 to 8.5	0 - 470

Table 6. Earthquakes with maximum observed magnitude (M_{obs}) at the active seismogenic sources.

S.No.	Seismogenic Source	M_{obs}
1.	Main Boundary Thrust (MBT)	8.0
2.	Lineament System of Delhi Sargodha Ridge (LSDSR)	6.1
3.	Ropar Fault (RF)	5.0
4.	Fault Near Chandigarh (FNC)	4.6
5.	Jwala Mukhi Thrust (JMT)	5.5
6.	Main Frontal Thrust (MFT)	5.5
7.	Mahendragarh Dehradun Sub Surface Fault (MDSSF)	5.4
8.	Rohtak Dehradun Lineament (RDL)	5.0
9.	Main Central Thrust (MCT)	7.9
10.	Sardar Shahar Fault (SSF)	7.1
11.	Kaurik Fault (KF)	6.9
12.	Ramgarh Thrust (RT)	6.0
13.	Moradabad Fault (MF)	5.8
14.	Great Boundary Fault (GBF)	4.9
15.	North Almora Thrust (NAT)	5.7
16.	South Almora Thrust (SAT)	4.4
17.	Delhi Fold Belt (DFB)	6.7
18.	Aravalli Delhi Fold Belt (ADFB)	4.5
19.	Sundar Nagar Fault (SNF)	7.0
20.	Sargoda Lahore Delhi Ridge (SLDR)	6.5

Table 7. M_{max} for potential seismogenic sources.

Seismogenic Source	TFL (km)	RL (km)	**Bonilla et al. (1984)**	**Wells and Coppersmith (1994)**	**Vakov (1996)**	**Gupta (2002)**	M_{max}
MBT	825	275	-	-	-	8.5	8.5
LSDSR	97	32.33	-	-	-	6.6	6.6
RF	38	12.66	6.9	6.1	6.1	5.5	6.9
FNC	36	12	-	-	-	5.1	5.1
JMT	387	129	7.6	-	7.5	6.0	7.6
MFT	46	15.33	6.9	6.2	6.2	6.0	6.9
MDSSF	297	99	7.5	7.4	7.4	5.9	7.5
RDL	202	67.33	-	-	-	5.5	5.5
MCT	769	256.33	-	-	-	8.4	8.4
SSF	271	90.33	7.5	7.3	7.3	7.6	7.6
KF	120	40	7.2	6.8	6.8	7.4	7.4
RT	37	12.33	6.9	6.1	6.1	6.5	6.9
MF	162	54	7.3	7	7	6.3	7.3
GBF	316	105.33	7.5	7.4	7.4	5.4	7.4
NAT	280	93.33	7.5	7.4	7.3	6.2	7.5
SAT	130	43.33	7.3	-	6.9	4.9	7.3
ADFB	Area Source	-	-	-	-	7.2	7.2
SNF	101	33.67	7.2	6.7	6.7	7.5	7.5
SLDR	Area Source	-	-	-	-	7.0	7.0

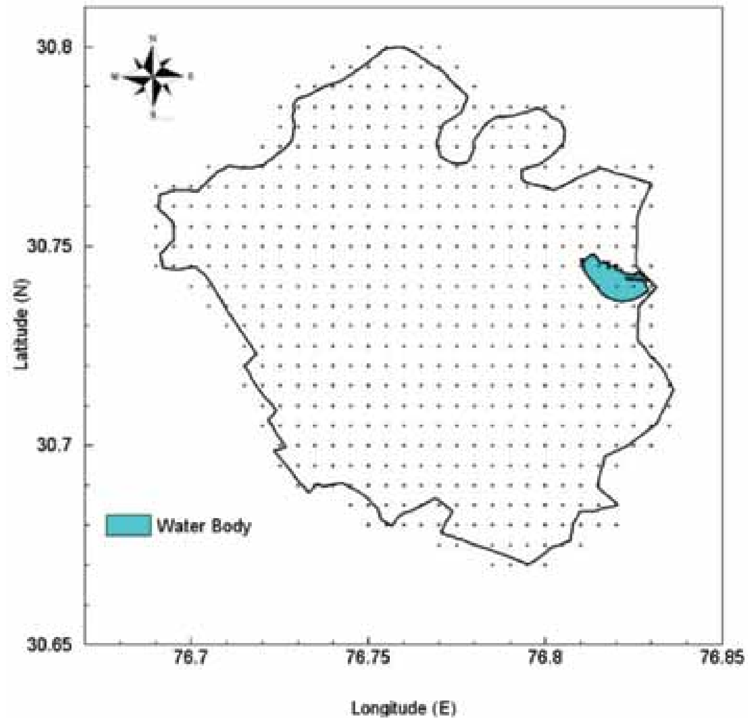

Figure 8. The map shows 549 grid points covering the entire area of Chandigarh city.

SEISMIC HAZARD ANALYSIS

A complete seismic hazard analysis involves various steps including preparation of comprehensive earthquake catalogue, identification of potential seismogenic sources, calculation of seismicity parameters a and b, estimation of M_{max} of the tectonic features, selection of suitable Ground Motion Prediction Equation (GMPE) and development of hazard map. Seismic hazard is estimated using probabilistic approach. The PSHA is considered to be more reliable as it provides a framework to accommodate uncertainties in size, location and rate of occurrence of earthquakes using total probability theorem. The detailed procedure for PSHA was first given by Cornell (1968) and explained in detail recently by Baker (2008).

The ground motion model is generally developed on the basis of strong motion characteristics of the region (plate boundary, subduction and intraplate) and accelerogram records at different epicentral distances for different magnitude of earthquakes. A regression analysis is then carried out based on different PGA values considering the distances and magnitudes to get the mean value of acceleration with minimum variance and subsequently, site coefficients are calculated for different periods. Due to scarcity of strong motion data, only a few region-specific attenuation relations are developed. Globally available GMPEs (Douglas, 2014) are reviewed to select equations suitable for the study region.

The following GMPE developed by Abrahamson and Silva (1997) for regions prone to shallow crustal earthquakes is adopted for the study area.

$$\ln Sa(g) = f_1(M, r_{rup}) + Ff_3(M) + HWf_4(M, r_{rup}) + Sf_5(\widehat{PGA_{rock}}) \quad (2)$$

where Sa(g) is spectral acceleration in g, M is moment magnitude, r_{rup} is closest distance to rupture plane in km, F is fault type (1 for reverse, 0.5 for reverse/oblique and 0 otherwise), HW is dummy variable for hanging wall sites (1 for sites over the hanging wall, 0 otherwise), and S is dummy variable for site class (0 for rock or shallow soil, 1 for deep soil).

for $M \leq c_1$

$$f_1(M, r_{rup}) = a_1 + a_2(M - c_1) + a_{12}(8.5 - M)^n + [a_3 + a_{13}(M - c_1)] \ln R$$

for $M > c_1$ (3)

$$f_1(M, r_{rup}) = a_1 + a_4(M - c_1) + a_{12}(8.5 - M)^n + [a_3 + a_{13}(M - c_1)] \ln R$$

where $\sqrt{r_{rup}^2 + c_4^2}$, a_1-a_{13}, c_1, c_4, c_5, a_1-a_{13}, c_1, c_4, c_5 and n are site coefficients.

A grid of 0.005° × 0.005° (0.555 km × 0.555 km) is used for the entire area of the Chandigarh city (Figure 8). The PSHA is carried out considering three sub-regions, viz. Himalayan Thrust System, Sargodha-Lahore-Delhi Ridge and Aravalli-Delhi Fold Belt as area sources of earthquakes and based on the developed catalogue, average focal depths are taken as 15 km, 17 km and 10 km for the selected three sub-regions, respectively.

The hazard has been calculated for 1%, 2% and 10% probability of exceedance in a time frame of 50 years as per the recommendations of Eurocode 8 (2005). For ordinary

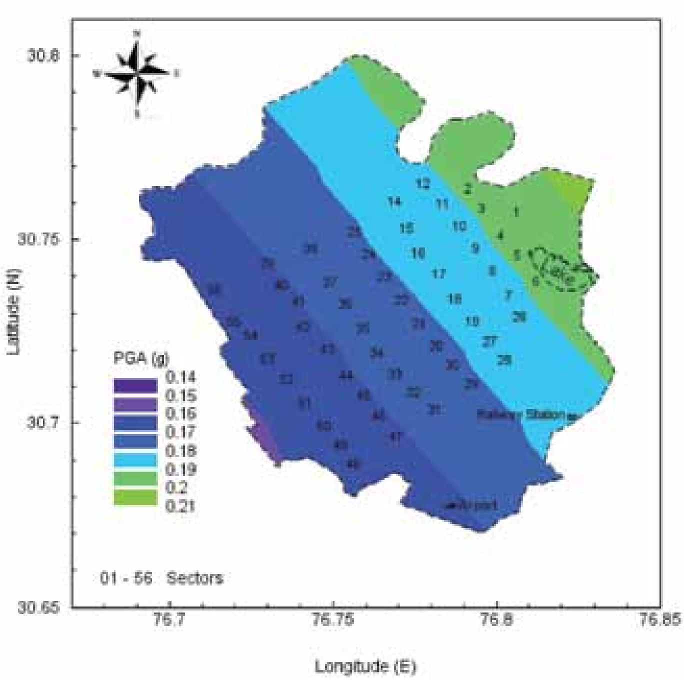

Figure 9. Seismic hazard map of Chandigarh city for 10% probability of exceedance in 50 years (return period of 475 years).

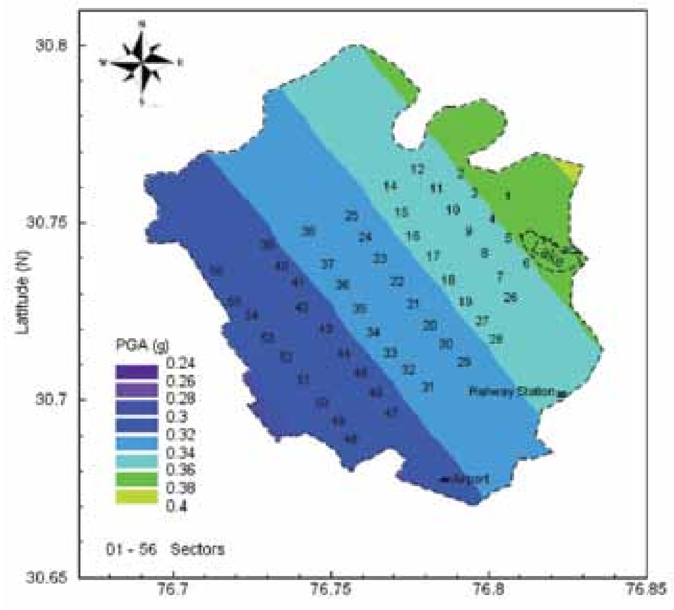

Figure 10. Seismic hazard map of Chandigarh city for 2% probability of exceedance in 50 years (return period of 2475 years).

structures, the seismic hazard map corresponding to 10% probability of exceedance in 50 years is recommended. However, for important structures like Nuclear Power Plants and other megastructures, the seismic hazard maps corresponding to 2% and 1% probability of exceedance in 50 years are recommended. The PSHA software R-CRISIS v. 18.2 (Ordaz and Salgado-Gálvez, 2017) is used for the purpose. R-CRISIS is a Windows based software with the capability of performing probabilistic seismic hazard analysis (PSHA), using a fully probabilistic approach allowing the calculation of results in terms of outputs with different characteristics (i.e., exceedance probability plots, set of stochastic events). In the computational scheme of the program, parameters such as a, b, M_{min}, M_{max}, λ_m and attenuation models are the input parameters, and PGA and PSA are the outputs.

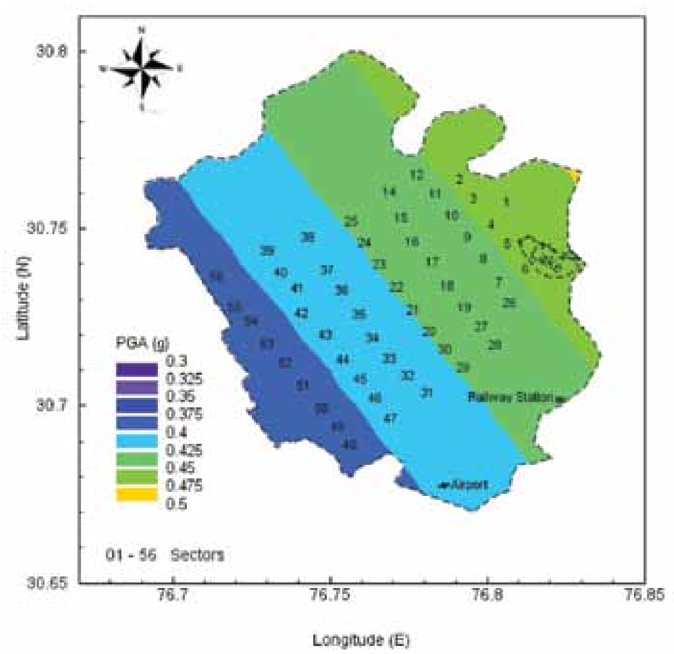

Figure 11. Seismic hazard map of Chandigarh city for 1% probability of exceedance in 50 years (return period of 4975 years).

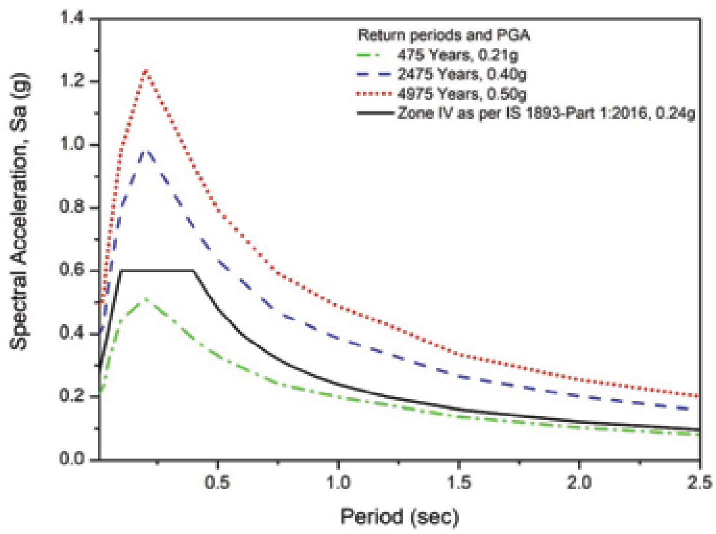

Figure 12. Response spectra for different return periods on rock outcrop corresponding to maximum PGA observed for Chandigarh.

The estimated PGA values range from 0.14g to 0.21g, 0.24g to 0.40g and 0.3g to 0.5g at 10%, 2% and 1% probability of exceedance respectively in 50 years. The hazard maps are prepared for 10%, 2% and 1% probability of exceedance at return periods of 475 years, 2475 years and 4975 years, respectively, in a time frame of 50 years (Figures 9 to 11). Response spectra is evaluated for various return periods corresponding to maximum observed PGA (Figure 12). It is observed that for a return period of 475 years, PSHA based hazard parameters are quite comparable with IS 1893 Part-1 (2016). For return periods of 2475 and 4975 years, PSHA based hazard parameters are much higher than the parameters specified in IS 1893 Part-1 (2016). For important structures, a site-specific approach is recommended due to possibility of amplification of ground motions for soil sites.

ONE-DIMENSIONAL NONLINEAR WAVE AMPLIFICATION

There are a number of analyses available to estimate the degree of wave amplification, e.g. linear, equivalent linear and non-linear analysis offering varying dimensionality (1-D, 2-D and 3-D) based on the problem. Over the years, nonlinear method is evolved to give a precise characterization of the nonlinear behaviour of soil (Stewart and Kwok, 2008). Generally, amplification of seismic waves is evaluated using one-dimensional model, which assumes that horizontal shear waves originating from the bedrock propagate in vertical direction through several layers of the soil profile. In line with various wave amplification studies carried out in India (e.g. Desai and Choudhury, 2015; Dammala et al., 2017), one dimensional nonlinear model is adopted to estimate wave amplification at soil sites of Chandigarh city using DEEPSOIL software (Hashash et al., 2016). This software is a one-dimensional site response analysis program that can perform: (a) 1-D nonlinear time domain analyses with and without pore water pressure generation, and (b) 1-D equivalent linear frequency domain analyses including convolution and deconvolution. The calculation of response is described below.

The nonlinear analysis of the wave propagation equation in soils allows the soil properties to change with the time with variation in strain. All the sites are assumed to have horizontal layers which extend infinitely. The soil profiles have been modelled as a series of lumped masses connected by springs and dashpots making a multiple degree freedom system. The nonlinear dynamic analysis of the soil column is performed by solving the incremental dynamic equation of motion as follows:

$$M\Delta\ddot{u} + C\Delta\dot{u} + K\Delta u = -M\Delta\ddot{u}_g \tag{4}$$

where the coefficients M, C and K represent mass, viscous damping and stiffness respectively and $\ddot{u}$, u, $\dot{u}$, $\ddot{u}_g$ represent acceleration, velocity, displacement and exciting acceleration at the base respectively.

The soil response is obtained from a constitutive model that describes the cyclic behaviour of soil. The most widely used softwares use variation of hyperbolic model to represent the backbone curve of the soil with the extended unload-reload Masing rules (Masing, 1926) to model hysteretic behaviour. The loading and unloading equations of modified Konder-Zelasko (MKZ) model (Matasovic, 1993), further modified by Hashash and Park (2001) used in DEEPSOIL software are as follows:

$$\tau = \frac{\gamma G_{max}}{1 + \beta\left(\frac{\gamma}{\gamma_r}\right)^S} \tag{5}$$

$$\tau = \frac{2G_{max}\left(\frac{\gamma - \gamma_{rev}}{2}\right)}{1 + \beta\left(\frac{\gamma - \gamma_{rev}}{2\gamma_r}\right)^S} + \tau_{rev} \tag{6}$$

where τ = shear strength, G_{max} = low strain shear modulus, γ = shear strain, reference shear strain, τ_{rev} = shear stress at reversal, γ_{rev} = shear strain at reversal, β, S = model fitting parameters.

The modification in MKZ model allows the effect of confining pressure on secant shear modulus of soil. In addition, there is no coupling between the confining pressure and shear stress. Coupling is introduced by making reference shear strain (γ_r) effective stress dependent using the following equation:

$$\gamma_r = a\left(\frac{\sigma'_v}{\sigma_{ref}}\right)^b \tag{7}$$

where a and b are curve fitting parameters, τ'_v = vertical effective stress, τ_{ref} = reference shear stress of 0.18 MPa.

However, the modified model is almost linear at low strains and hence provides zero hysteretic damping at lower strains. Low strain damping (ξ) is added separately to simulate actual soil behavior which exhibits damping even at very small strains and is defined as

$$\xi = \frac{c}{(\sigma'_v)^d} \tag{8}$$

where c and d are curve fitting parameters. The parameter 'd' can be set to zero in case a pressure independent small strain damping is desired.

It is observed that overestimation of damping at large strain can result when the hysteretic damping is calculated using unload-reload cycles as per Masing rules based on the modulus reduction curves. This overestimation can be avoided by multiplying ξ_{Masing} with a damping reduction factor $F(\gamma_m)$ as follows:

$$F(\gamma_m) = p_1 - p_2\left(1 - \frac{G_{\gamma_m}}{G_{max}}\right)^{p_3} \tag{9}$$

where $G\gamma_m$ = shear modulus at maximum strain and p_1, p_2, p_3 are fitting parameters. This factor provides the best fit for both modulus reduction and damping ratio curves.

The reduction factor modifies the reloading cycle and the expression is as follows:

$$\tau = F(\gamma_m)\left[\frac{2G_{max}\left(\frac{\gamma - \gamma_{rev}}{2}\right)}{1 + \beta\left(\frac{\gamma - \gamma_{rev}}{2\gamma_r}\right)^S} - \frac{G_{max}\,(\gamma - \gamma_{rev})}{1 + \beta\left(\frac{\gamma_m}{\gamma_r}\right)^S}\right] + \frac{G_{max}\,(\gamma - \gamma_{rev})}{1 + \beta\left(\frac{\gamma_m}{\gamma_r}\right)^S} + \tau_{rev} \tag{10}$$

where γ_m = maximum shear strain. The Newmark β method is then used to solve the system of equations and to obtain response of the soil column.

Such analysis has been carried out for 8 sites in Chandigarh, which includes 4 sites with boreholes drilled up to refusal and others drilled down to depth of 20 m or greater (Figure 13).

Based on geotechnical data collected, sites are classified as class D sites by calculating average SPT N-value of the profile as per the recommendations of NEHRP (FEMA 368, 2000). The stiffness and damping of soil layer play fundamental role in estimating wave amplification parameters in seismic microzonation studies. The analysis requires characterization of the stiffness of an element of soil considering low strain shear modulus (G_{max}), variation of modulus ratio (G/G_{max}) with cyclic strain amplitude (γ) and other parameters. For this, several correlations between shear modulus (G) and SPT N-value for different soil types are considered. In the present study, the following equations developed by Ohba and Toriumi (1970) and Ohsaki and Iwasaki (1973) are used for clays and sands respectively, as per recommendations of Anbazhagan et al., (2012, 2015b, 2016):

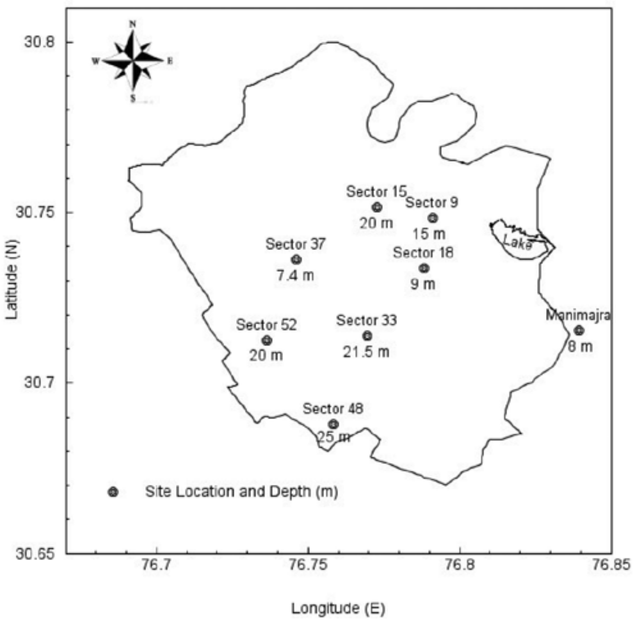

Figure 12. Response spectra for different return periods on rock outcrop corresponding to maximum PGA observed for Chandigarh.

Table 8. Input parameters for soil column at Sector 33.

Depth	IS Symbol	Plasticity Index	Bulk Density	SPT N Value	Angle of internal friction (φ)	Coefficient of earth pressure at rest (K_o)	G_{max} (MPa)
2.5	ML	2	15.47	8	28.63	0.52	43.43
3.5	ML-CL	7	17.43	7	28.31	0.53	39.98
5	ML	2	17.58	9	28.94	0.52	46.72
7	ML-CL	7	18.05	15	30.81	0.49	64.13
8	CL	9	18.68	23	33.31	0.45	83.59
9	CL	9	18.21	17	31.44	0.48	69.30
10	SM	NP	17.54	30	35.50	0.42	155.93
12.5	SM	NP	16.03	14	30.50	0.49	76.17
14	SM	NP	16.41	18	31.75	0.47	96.47
15	CL	9	18.99	27	34.56	0.43	92.33
15.8	CL	9	20.25	43	39.56	0.36	123.21
17	SM	NP	20.11	48	41.13	0.34	242.55
19	SM	NP	17.54	30	35.50	0.42	155.93
21.5	SM	NP	20.38	50	41.75	0.33	252.04

$$G_{max}=1220N^{0.62} \quad (11)$$

$$G_{max}=650N^{0.94} \quad (12)$$

where G_{max} = low strain shear modulus in t/m^2 and N = SPT-N value.

In the absence of site specific modulus reduction and damping ratio curves, standard curves proposed by Darendeli (2001) are used for sands, and curves proposed by Vucetic and Dobry (1991) are used for clays. Typical input parameters for the site in Sector 33 are given in Table 8.

The thickness of the layers is so adjusted that the maximum frequency that a layer can propagate is always above 25 Hz. Bedrock has been assumed at refusal, i.e. for N>50 for 15 cm penetration and N>100 for 30 cm penetration of SPT split-spoon sampler. Conventionally, the engineering bedrock is assumed to be the uppermost layer of the soil column having a shear wave velocity (V_s) ≥ 760 m/s in accordance with NEHRP provisions (Nath and Thingbaijam, 2011). In general, the shear wave velocity

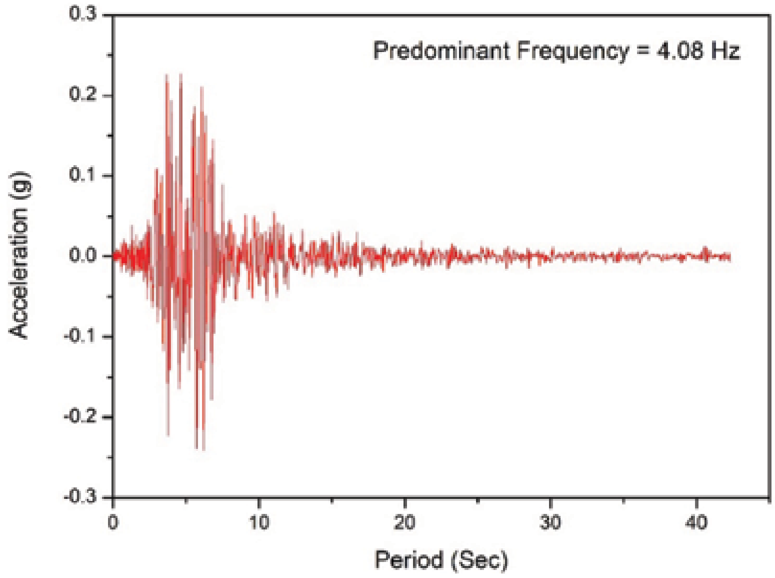

Figure 14. Input acceleration time history of the 1991 Uttarkashi earthquake 6.8 M_w (source: http://www.strongmotioncenter.org).

Table 9. Results of nonlinear wave amplification analysis.

Sites	PGA Rock (g)	Depth (m)	Site Class	Natural Frequency of Site (Hz)	Amplification Factor	PGA Soil (g)	Ground Displacement (m)	Maximum Strain	
								Value (%)	Depth (m)
Manimajra	0.191	9	D	7.04	1.583	0.302	0.010	0.46	5.5
Sector 09	0.188	15	D	3.42	1.186	0.223	0.020	1.12	5.5
Sector 15	0.183	20	D	2.16	1.165	0.213	0.030	1.75	16.5
Sector 18	0.183	9	D	5.82	1.736	0.318	0.011	0.35	4.5
Sector 33	0.173	21.5	D	2.49	0.963	0.167	0.025	0.54	11.5
Sector 37	0.172	7.4	D	6.81	1.963	0.338	0.012	0.64	2.5
Sector 48	0.164	25	D	2.06	0.748	0.123	0.036	1.52	19.5
Sector 52	0.165	20	D	2.54	0.777	0.128	0.031	0.63	13.5

of the bedrock is greater than that of the overlying soil profile. It should be noted that regardless of the value specified, the bedrock damping ratio has no effect in time domain analyses and only a negligible effect in frequency domain analyses (Hashash et al., 2016). For the present study, bedrock is modelled as an elastic half space with 2% damping, 2.5 gm/cm^3 density and 760 m/s shear wave velocity (V_s).

The final step in wave amplification analysis involves generating or getting an acceleration time history, which is compatible with the maximum dynamic loading expected at the site of interest. Suitable acceleration time histories can be selected based on PGA value, magnitude of controlling earthquake, source to site distance and site class. PGA values for rock sites obtained from PSHA are used for the selection of input motions at each site. Acceleration time history of the 1991 Uttarkashi earthquake M_w 6.8 (focal depth = 10 km) recorded at the Uttarkashi station with PGA = 0.242g is used for the analysis (Figure 14).

The results of the wave amplification analysis have been reported in Table 9. Due to limited borehole data (eight boreholes), interpretation cannot be made for the amplification trend across the city. However, on the basis of significant amplification observed at five sites, it can be concluded that the city may experience high ground accelerations. Moreover, high strains are observed for all the eight sites and there is a possibility of substantial settlements during an earthquake.

The amplification factors for the analysed sites range from 0.748 to 1.963 with an average value of 1.3. The maximum PGA of 0.338g and minimum PGA of 0.123g are observed for Sector 37 and Sector 48 sites, respectively. The seismic hazard map at return period of 475 years is updated using average observed amplification factor for PGA (Figure 15). The response spectrum corresponding to a return period of 475 year is modified using average observed amplification factors for Sa (Figure 16). It is observed that the response spectrum developed for soil sites

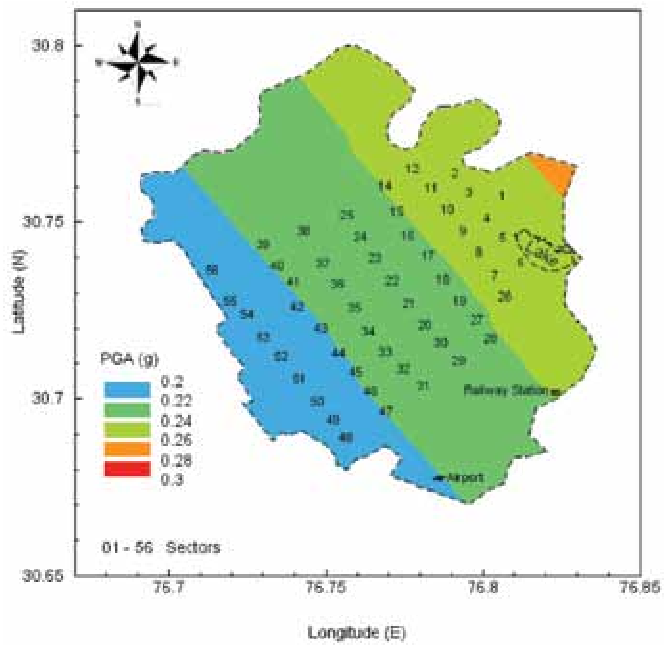

Figure 15. Seismic hazard map of Chandigarh city for 10% probability of exceedance in 50 years (return period of 475 years).

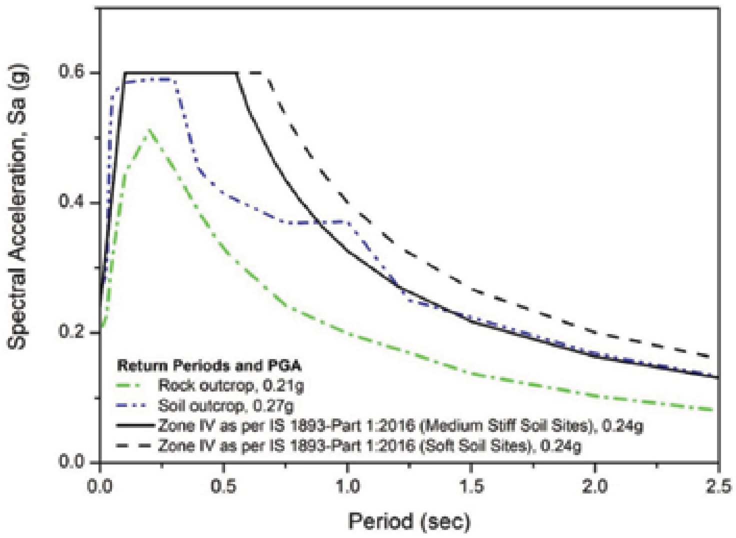

Figure 16. Comparison of response spectrum for rock and soil outcrop with soil response spectra specified in IS 1893 Part-1 (2016).

of Chandigarh is comparable with the spectrum specified in IS 1893 Part-1 (2016) for medium stiff soil sites. It is observed that the estimated seismic scenario for the Chandigarh city is worse than that proposed by the Indian Seismic Code (IS 1893 Part-1, 2016).

LIQUEFACTION HAZARD MAPPING

Liquefaction hazard assessment for Chandigarh city is carried out using semi-empirical procedure developed by Idriss and Boulanger (2006). The location of 41 boreholes are shown in Figure 17 and the profiles in Appendix A. For all the sites, water table has been assumed to be present at ground surface (NDMA, 2011; Vipin et al., 2013) and PGA and magnitude of earthquake (M_w) are taken as 0.28g and 8.228 respectively as per PSHA. Assessment of liquefaction susceptibility of soils requires calculation of cyclic stress ratio (CSR) which is the cyclic stress induced by an earthquake, and cyclic resistance ratio (CRR) which is the resistance offered by the soil against liquefaction.

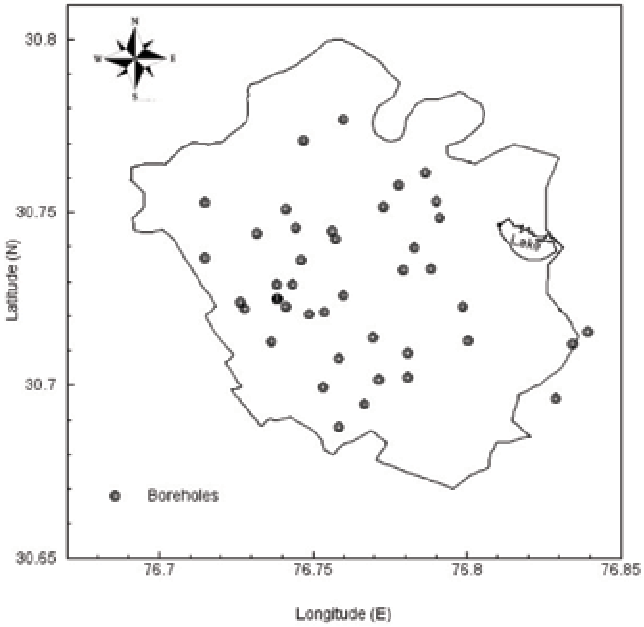

Figure 17. Map showing location of 41 boreholes.

Cyclic stress ratio (CSR)

It can be given by following equation:

$$(CSR)_{M=7.5,\sigma=1} = 0.65\left(\frac{\sigma_{vo}}{\sigma'_{vo}}\right)(a_{max})(r_d)\left(\frac{1}{MSF}\right)\left(\frac{1}{K_\sigma}\right) \quad (13)$$

where $(CSR)_{M=7.5,\ \sigma=1}$ is the adjusted value of CSR for equivalent uniform shear stress induced by earthquake ground motions having moment magnitude of 7.5 and equivalent overburden pressure of 1 atmosphere, σ_{vo}, = total overburden stress, σ'_{vo} = effective overburden stress, a_{max} = peak ground acceleration, r_d = stress reduction coefficient, MSF = magnitude scaling factor, K_σ = overburden correction factor, a_{max} = PGA corresponding to 475-year return period.

Stress reduction coefficient (r_d) accounts for the flexibility and dynamic response of the soil and represents the variation of shear stress amplitude with depth which can be given as:

$$r_d = \exp(\alpha + \beta M) \quad (14)$$

where,

$$\alpha = -1.012 - 1.126\sin\left(\frac{z}{11.73} + 5.133\right) \quad (15)$$

$$\beta = 0.106 + 0.118\sin\left(\frac{z}{11.28} + 5.142\right) \quad (16)$$

and z is depth and M is moment magnitude.
These equations are applicable for $z \leq 34$m.
For $z > 34$m, the following expression is used:

$$r_d = 0.12\ \exp(0.22M) \quad (17)$$

Magnitude scaling factor (MSF) is used to adjust the CSR induced by an earthquake magnitude (M) to account for the duration effect of seismic ground motions, which is not reflected in PGA. The MSF is limited to a maximum value of 1.8 for small magnitude earthquakes of $M_w \leq 5.4$ and is expressed as:

$$MSF = 6.9\exp\left(\frac{-M}{4}\right) - 0.058 \leq 1.8 \quad (18)$$

Overburden correction factor is used to adjust CSR values to an equivalent overburden pressure of 1 atmosphere. Overburden correction factor (K_σ) is evaluated by the following expression:

$$K_\sigma = 1 - C_\sigma \ln(\sigma'_{vo}/P_a) \leq 1.0 \quad (19)$$

$$C_\sigma = \frac{1}{18.9 - 2.55\sqrt{(N_1)_{60}}} \quad (20)$$

where P_a is the reference pressure.

Cyclic resistance ratio (CRR)

CRR can be represented by the following equation:

$$CRR = \left(CRR_{\sigma=1,\alpha=0}\right)K_\sigma K_\alpha \quad (21)$$

where K_σ = overburden correction factor and K_α = static shear stress correction factor.

The SPT N-values need to be normalized to an equivalent effective vertical overburden pressure σ'_{vo} of about 101 kPa to obtain blow count values that are more uniquely dependent on relative density (D_R), rather than on the overburden pressure coming from the above soil layers. The corrected blow count can be expressed as:

$$(N_1)_{60} = C_N(N)_{60} \quad (22)$$

$$C_N = \left(\frac{P_a}{\sigma'_{vo}}\right)^\alpha \leq 1.7 \quad (23)$$

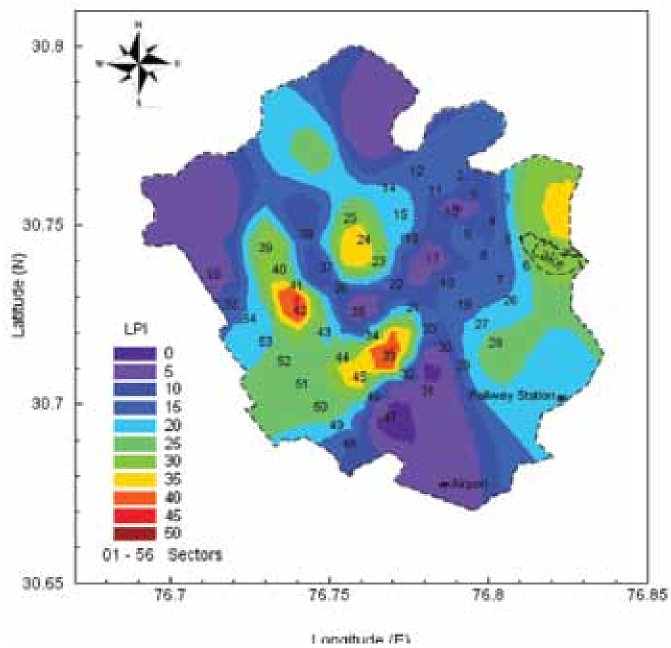

Figure 18. Liquefaction hazard map of Chandigarh city.

$$\alpha = 0.784 - 0.0768\sqrt{(N_1)_{60}} \quad (24)$$

Where $N_1 = C_N(N_m)$, N_m is the SPT value at field, C_N = overburden correction factor to normalize SPT value, N_{60} = SPT value after correction to an equivalent 60% hammer efficiency. The value of $(N_1)_{60}$ is limited to 46. The calculation of C_N is iterative as both C_N and $(N_1)_{60}$ depend on each other. The expression for N_{60} is as follows:

$$N_{60} = N_m C_R C_S C_B E_m / 0.60 \quad (25)$$

Where C_R = rod length correction, C_S = sampling method correction, C_B = borehole diameter correction and E_m = hammer efficiency. The value of correction factors for N_{60} is adopted from Youd et al., (2001).

Presence of fine content (FC) in the soil plays a role in liquefaction; higher the FC percentage in the sediment more resistive it would be towards liquefaction. Therefore, FC correction has to be applied to $(N_1)_{60}$ if FC > 5% to convert it into equivalent clean sand value. The description of correction factor is as follows:

$$(N_1)_{60CS} = (N_1)_{60} + \Delta(N_1)_{60} \quad (26)$$

where

$$\Delta(N_1)_{60} = \exp\left\{1.63 + \frac{9.7}{FC + 0.1} - \left(\frac{15.7}{FC + 0.1}\right)^2\right\} \quad (27)$$

for FC ≤ 35. These $(N_1)_{60cs}$ values are further used to compute CRR by using the following formulation:

$$CRR_{\sigma=1,\alpha=0} = \exp\left\{\frac{(N1)60cs}{14.1} + \left(\frac{(N1)60cs}{126}\right)^2 - \left(\frac{(N1)60cs}{23.6}\right)^3 + \left(\frac{(N1)60cs}{25.4}\right)^4 - 2.8\right\} \quad (28)$$

However, the layers with FC > 35% are considered non-liquefiable.

Factor of Safety and Liquefaction Potential Index (LPI)

The factor of safety (FOS) against liquefaction is determined as follows:

$$FOS = \frac{CRR}{CSR} \quad (29)$$

The FOS shows the potential of a given layer of soil against liquefaction. Generally, if the FOS value is less than 1, the site is considered to be liquefiable and if it is greater than 1, the site is considered to be non-liquefiable. However, soil that has a FOS slightly greater than 1.0 may still liquefy during an earthquake. For example, if a lower layer liquefies, then the upward flow of water could induce liquefaction of the layer that has a factor of safety slightly greater than 1.0.

On the other hand, liquefaction potential index (LPI) quantifies the severity of liquefaction at a given location for down to a depth of 20m (Iwasaki et al., 1978; Luna and Frost, 1998). It is computed by taking integration of one minus the factors of safety (FOS) against liquefaction for liquefiable layers along the entire depth of soil column below the ground surface at a specific location. The LPI value is considered zero for a layer with FOS ≥1. A weighting function has also been added to give more weight to the layers closer to the ground surface. The LPI is calculated using the following expression:

$$LPI = \sum_{i=1}^{n} w_i F_i H_i \quad (30)$$

Table 10. Liquefaction severity.

LPI	Severity of Liquefaction
LPI = 0	Little to None
0 < LPI < 5	Minor
5 < LPI < 15	Moderate
LPI > 15	Major

Table 11. Liquefaction potential index (LPI) for various sites in Chandigarh city.

Sites	Borehole Depth (m)	PGA Soil (g)	LPI	Severity
Village Sarangpur	9	0.242	5.00	Moderate
Village Mauli Jagram	6	0.241	20.16	Major
Village Manimajra	9	0.248	25.48	Major
Village Maloya	10	0.218	5.58	Moderate
Village Kaimbwala	9	0.235	35.45	Major
Sector 9	15	0.244	20.61	Major
Sector 10	12	0.246	0	None
Sector 11	9	0.247	18.78	Major
Sector 15	20	0.238	22.52	Major
Sector 17	12	0.238	4.52	Minor
Sector18	9	0.238	17.19	Major
Sector 24	9	0.230	39.94	Major
Sector 28	9	0.237	26.09	Major
Sector 31	15	0.225	6.26	Moderate
Sector 32	9	0.228	2.78	Minor
Sector 33	21.5	0.225	46.83	Major
Sector 35	13	0.225	5.33	Moderate
Sector 37	7.4	0.224	9.2	Moderate
Sector 38	16	0.226	10.5	Moderate
Sector 39	9	0.221	34.17	Major
Sector 42D	9	0.221	47.26	Major
Sector 43	9	0.222	23.64	Major
Sector 45	9	0.220	38.25	Major
Sector 46	9	0.222	4.02	Minor
Sector 47	9	0.218	3.92	Minor
Sector 48	25	0.213	14.45	Moderate
Sector 50B	9	0.216	27.15	Major
Sector 52	20	0.215	27.21	Major
Sector 54A	9	0.215	20.28	Major
Sector 56	13.4	0.215	7.7	Moderate
Village Dhanas	15	0.235	27.17	Major

and

$$F_i = 1 - FOS \tag{31}$$

where H_i is thickness of the discretized soil layer, n is number of layers; F_i is liquefaction severity for i^{th} layer; FOS_i is the factor of safety for i^{th} layer; w_i is the weighting factor = 10 - 0.5z_i and z_i is the depth of i^{th} layer (m). The level of liquefaction severity with respect to LPI (Luna and Frost, 1998) is given in Table 10.

The LPI values calculated for various boreholes across the city are shown in Table 11. Based on the results, a liquefaction hazard map is prepared for the city (Figure 18). The liquefaction hazard map shows that the villages Mauli Jagram, Manimajra, Kaimbwala, Dhanas, Sectors 9, 11, 15, 18, 24, 28, 33, 39, 42, 43, 45, 50B, 52 and 54A are highly prone to liquefaction during earthquakes if water table is assumed to be present at ground level. The village Sarangpur, Maloya, Sectors 31, 35, 37, 38, 48 and 56 have moderate susceptibility towards liquefaction. However, areas like Sector 10, 17, 32, 46 and 47 have none to low susceptibility towards liquefaction.

CONCLUSION

Chandigarh is one of the important cities in India and is famous for its infrastructure, industries and tourism. The city is always under the threat from earthquakes due to its proximity to Himalayan frontal fault. Possible seismic hazards in the city is evaluated by probabilistic seismic hazard analysis (PSHA), wave amplification analysis and liquefaction potential assessment. The results are presented in terms of seismic hazard maps for various return periods, response spectra, peak ground acceleration, amplification factors and liquefaction hazards. The results show that the city can experience strong ground motions due to earthquakes in Himalayan thrust system. The expected PGA with 10% probability of exceedance is 0.28g. The average wave amplification factor for the analysed sites has been observed as 1.3. It has been observed that many areas in the city are prone to earthquake induced liquefaction. The results of the study can be useful for upcoming design and construction works in the city.

ACKNOWLEDGEMENT

Authors would like to acknowledge DST, India for providing financial assistance to carry out the study under INSPIRE Fellowship Scheme (Candidate Code IF130892). Authors would also acknowledge the help provided by UT Secretariat Chandigarh and Geotech Engineering Services (Mohali) by sharing geotechnical data for the study. Authors thank the anonymous reviewers for their valuable comments towards improving the quality of the manuscript.

Compliance with Ethical Standards

The authors declare that they have no conflict of interest and adhere to copyright norms.

REFERENCES

Abrahamson, N.A. and Silva, W.J., 1997. Empirical response spectral attenuation relations for shallow crustal earthquakes. Seism. Res. Lett., 68(1), 94-127.

Anbazhagan, P., Aditya, P. and Rashmi, H.N., 2012. Review of correlations between SPT N and shear modulus: a new correlation applicable to any region. Soil Dyn. Earthq. Eng., 36, 52-69.

Anbazhagan, P., Bajaj, K. and Patel, S., 2015a. Seismic hazard maps and spectrum for Patna considering region-specific seismotectonic parameters. Natural Hazards, 78, 1163-1195.

Anbazhagan, P., Manohar, D.R., Moustafa, S.S.R. and Nassir, S.A., 2015b. Effect of shear modulus correlation on site response study. Disaster Adv., 8(2), 16-30.

Anbazhagan, P., Manohar, D.R., Moustafa, S.S.R. and Nassir, S.A., 2016. Selection of shear modulus correlation for SPT N values based on site response analysis. J. Eng Res., 4(3), 18-42.

Baker, J.W., 2008. An Introduction to Probabilistic Seismic Hazard Analysis (PSHA), White Paper, Version 1.3, Stanford University, California.
https://scits.stanford.edu/sites/default/files/baker_2013_intro_psha_v2.pdf

Bonilla, M.G., Mark, R.K. and Lienkaemper, J.J., 1984. Statistical relations among earthquake magnitude, surface rupture length, and surface fault displacement. Bull. Seism. Soc. Am., 74(6), 2379-2411.

Boominathan, A., Dodagoudar, G.R., Suganthi, A. and Maheswari, U.R., 2008. Seismic hazard assessment of Chennai city considering local site effects. J. Earth System Sci., 117(2), 853-863.

Cetin, K.O., Seed, R.B., Kiureghian, A.D., Tokimatsu, K., Harder Jr., L.F., Kayen, R.E. and Moss, R.E.S., 2004. Standard penetration test-based probabilistic and deterministic assessment of seismic soil liquefaction potential. J. Geotech. Geoenviron. Eng., 130(12), 1314-1340.

Chopra, S., Kumar, D., Rastogi, B.K., Choudhury, P. and Yadav R.B.S., 2012. Deterministic seismic scenario for Gujrat region, India. Natural Hazards, 60, 517-540.

Cornell, C.A., 1968. Engineering seismic risk analysis. Bull. Seism. Soc. Am., 58, 1583-1606.

Dammala, P.K., Krishna, A.M., Bhattacharya, S., Nikitas, G. and Rouholamin, M., 2017. Dynamic soil properties for seismic ground response studies in Northeastern India. Soil Dyn. Earthq. Eng. 100, 357-370.

Darendeli, M.B., 2001. Development of a new family of normalized modulus reduction and material damping curves. Ph.D diss., University of Texas.

Dasgupta, S., Pande, P., Ganguly, D., Iqbal, Z., Sanyal, K., Venkatraman, N.V., Dasgupta, S., Sural, B., Harendranath, L., Mazumdar, K., Sanyal, S., Roy, A., Das, L.K., Misra, P.S. and Gupta, H., 2000. Seismotectonic atlas of India and its environment. Geol. Surv. India, Calcutta.

Desai, S.S. and Choudhury, D., 2015. Non-linear site-specific seismic ground response analysis for port sites in Mumbai, India. Japanese Geotech. Soc. Spl. Publ., 2(19), 733-736.

Douglas, J., 2014. Ground motion prediction equations 1964-2014. White paper, University of Strathclyde, Glasgow, United Kingdom. http://www.gmpe.org.uk/gmpereport2014.pdf

Eurocode 8: BS-EN 1998-1, 2005. Design of structures for earthquake resistance – part 1: General rules, seismic actions and rules for buildings. European committee for standardization, Brussels.

FEMA 368, 2000. National earthquake hazard reduction program (NEHRP) recommended provisions for seismic regulations for new buildings and other structures, part 1: Provisions. USA: Building Seismic Safety Council (BSSC).

Gardner, J.K. and Knopoff L., 1974. Is the sequence of earthquakes in Southern California with aftershocks removed, poissonian?. Bull. Seism. Soc. Am., 64(5), 1363–1367.

Gupta, I.D., 2002. The state of the art in seismic hazard analysis, ISET J. Earthq. Techn., 39(4), 311–346.

Hashash, Y.M.A. and Park, D., 2001. Non-linear one-dimensional seismic ground motion propagation in the Mississippi embayment. Eng. Geol., 62(1-3), 185-206.

Hashash, Y.M.A., Park, D., Tsai, C.C., Philips, C. and Groholski, D.R., 2016. DEEPSOIL - 1-D Wave Propagation Analysis Program, Version 6.1, Tutorial and User Manual. University of Illinois at Urbana-Campaign.

Idriss, I.M. and Boulanger, R.W., 2006. Semi-empirical Procedures for Evaluating Liquefaction Potential during Earthquakes. Soil Dyn. Earthq. Eng., 26, 115- 130.

Iwasaki, T., Tatsuoka, F., Tokida, K. and Yasuda, S., 1978. A practical method for assessing soil liquefaction potential based on case studies at various site in Japan. 5th Japan Earthquake Engineering Symposium, 2, 641-648.

IS 1893. Part-1, 2016. Criteria for Earthquake Resistant Design of Structures. Bureau of Indian Standard (BIS), New Delhi, India.

Kataria, N.P., Shrikhande, M. and Das, J.D., 2013. Deterministic seismic hazard analysis of Andaman and Nicobar Islands. J. Earthq. Tsunami., 7(4), 1-19.

Khattri K.N., Rogers A.M., Perkins D.M. and Algermissen S.T., 1984. A seismic hazard map of India and adjacent areas. Tectonophysics, 108, 93–134.

Kolathayar, S., Sitharam, T.G. and Vipin, K.S., 2012a. Deterministic seismic hazard macrozonation of India. J. Earth System Sci., 121(5), 1351-1364.

Kolathayar, S., Sitharam, T.G. and Vipin, K.S., 2012b. Spatial variation of seismicity parameters across India and adjoining areas. Natural Hazards, 60, 1365-1379.

Kramer, S.L., 2013. Geotechnical Earthquake Engineering. Pearson Publications.

Luna, R. and Frost, J.D., 1998. Spatial liquefaction analysis system J. Comput. Civil Eng., 12(1), 48-56.

Mark, R.K., 1977. Application of linear statistical model of earthquake magnitude versus fault length in estimating maximum expectable earthquake. Geology, 5, 464-466.

Malik, J.N., Nakata, T., Philip, G., Suresh, N. and Virdi, N.S., 2008. Active fault and paleoseismic investigation: evidence of a historic earthquake along Chandigarh Fault in the Frontal Himalayan zone, NW India. Himalayan Geology, 29(2), 109-117.

Malik, J.N., Shah, A.A., Sahoo, A.K., Puhan, Banerjee. C., Shinde D.P., Juyal N., Singhvi A.K. and Rath S.K., 2010. Active fault, fault growth and segment linkage along the Janauri anticline (frontal foreland fold), NW Himalaya, India. Tectonophysics, 483, 327–343.

Masing, G., 1926. Eigenspannungeu und verfertigung beim Messing. Proceedings of the 2nd Int. Cong. on Appl. Mech., Zurich, 332-335. (in German)

Matasovic, N., 1993. Seismic response of composite horizontally-layered soil deposits, Ph.D diss., University of California.

Molnar, P. and Pandey, M.R., 1989. Rupture zones of great earthquakes in the Himalayan region. Proc. Indian Acad. Sci. – Earth Planet. Sci., 98(1), 61-70.

Naik, N. and Choudhury, D., 2015. Deterministic seismic hazard analysis considering different seismicity levels for the state of Goa, India. Natural Hazards, 75, 557-580.

Nath, S.K. and Thingbaijam, K.K.S., 2011. Assessment of seismic site conditions: a case study from Guwahati city, northeast India. Pure Appl Geophys., 168, 1645-1668.

Nath S.K., Sengupta, P. and Kayal, J.R., 2002. Determination of S-Wave Site Response in the Garhwal Himalaya from the Aftershock Sequence of the 1999 Chamoli Earthquake. Bull. Seism. Soc. Am., 92(3), 1072-1081.

National Disaster Management Authority (NDMA), 2011. Geotechnical/geophysical investigations for seismic microzonation studies of urban centres in India. Technical report. Government of India.

Ohba, S. and Toriumi, I., 1970. Research on vibration characteristics of soil deposits in Osaka, Part 2, On velocities of wave propagation and predominant periods of soil deposits. Abstract, Technical meeting of Architectural Institute of Japan.

Ohsaki, Y. and Iwasaki, R., 1973. Dynamic shear moduli and Poisson's ratio of soil deposits. Soils and Foundations, 13(4), 61-73.

Ordaz M. and Salgado-Gálvez, M.A., 2017. R-CRISIS Validation and Verification Document. Technical Report, Mexico city, Mexico.

Peltzer, G. and Saucier, F., 1996. Present day kinematics of Asia derived from geological fault rates. J. Geophys. Res., 101, 27943 - 27956.

Puri, N. and Jain, A., 2014. Preliminary investigation for screening of liquefiable areas in the state of Haryana, India, ISET J. Earthq. Tech., 51(1-4), 19-34.

Potter, S.H., Becker, J.S., Johnston, D.M. and Rossiter, K.P., 2015. An overview of the impacts of the 2010-2011 Canterbury earthquakes, Int. J. Disaster Risk Reduction, 14, 6-14.

Puri, N. and Jain, A., 2016. Deterministic Seismic Hazard Analysis for the State of Haryana, India. Indian Geotech. J., 46(2), 164-174.

Rajendran, C.P. and Rajendran, K., 2005. The status of central seismic gap: a perspective based on the spatial and temporal aspects of the large Himalayan earthquakes. Tectonophysics, 395(1-2), 19-39.

Ranjan, R., 2005. Seismic Response Analysis of Dehradun city, India. MS Thesis, International Institute for Geo-information Science and Earth Observation, Netherlands.

Scordilis, E.M., 2006. Empirical global relations converting Ms and mb to moment magnitude, J. Seismology, 10, 225-236.

Sharma, M.L., Wason, H.R., and Dimri, R., 2003. Seismic zonation of Delhi region for bedrock ground motion. Pure. Appl. Geophys., 160, 2381-2398.

Shiuly, A., and Narayan, J.P., 2012. Deterministic seismic microzonation of Kolkata city, Natural Hazards, 60, 223-240.

Shukla, J. and Choudhury, D., 2012. Estimation of seismic ground motions using deterministic approach for major cities of Gujarat, Natural Hazards. Earth System Sci., 12, 2019-2037.

Sitharam, T.G. and Sil, A., 2014. Comprehensive seismic hazard assessment of Tripura and Mizoram states. J. Earth System Sci., 123(4), 837-857.

Stewart, J.P. and Kwok, A.O.L., 2008. Nonlinear seismic ground response analysis: code usage protocols and verification against vertical array data, Proceedings of Geotechnical Earthquake Engineering and Soil Dynamics IV Congress, Sacramento, California.

Stepp, J.C., 1972. Analysis of the completeness of the earthquake sample in the Puget Sound area and its effects on statistical estimates of earthquakes hazard, Proc. Int. Conf. on Microzonation for Safer Construction Research and Application, Seattle, Washington.

Thaker, T.P., Rathod, G.W., Rao, K.S. and Gupta, K.K., 2012. Use of seismotectonic information for the seismic hazard analysis for Surat city, Gujrat, India: Deterministic and probabilistic approach. Pure. Appl. Geophys., 169, 37-54.

Tinti, S. and Mulargia, F., 1985. Completeness analysis of a seismic catalog. Annales Geophysicae, 3(3), 407-414.

Tokimatsu, K., and Uchida, A., 1990. Correlation between liquefaction resistance and shear wave velocity, Soils and Foundations, 30(2), 33-42.

Vakov, A.V., 1996. Relationships between earthquake magnitude, source geometry and slip mechanism. Tectonophysics, 261(1), 97-113.

Vipin, K.S., Sitharam, T.G. and Kolathayar, S., 2013. Assessment of seismic hazard and liquefaction potential of Gujarat based on probabilistic approaches, Natural Hazards 65, 1179–1195.

Vucetic, M. and Dobry, R., 1991. Effect of Soil Plasticity on Cyclic Response, J. Geotech. Eng. Div., 111(1), 89-107.

Wells, D.L. and Coppersmith, K.J., 1994. New empirical relationships among magnitude, rupture length, rupture area, and surface displacement, Bull. Seism. Soc. Am., 84(4), 974-1002.

Yenier, E., Erdoğan, Ö. and Akkar, S., 2008. Empirical relationships for magnitude and source-to-site distance conversions using recently compiled Turkish strong-ground motion database, Proceedings of 14th World Conf. on Earthquake Engineering, Beijing, China.

Youd, T.L., Idriss, I.M., Andrus, R.D., Arango, I., Castro, G., Christian, J.T. and Dobry, R. et al., 2001. Liquefaction resistance of soils: summary report from the 1996 NCEER and 1998 NCEER/NSF workshops on evaluation of liquefaction resistance of soils, J. Geotech. Geoenviron. Eng., 127(10), 817–33.

Received on: 17.4.18; Revised on: 19.6.18; Accepted on: 15.7.18

Appendix-A: Borehole logs showing depth (m) and IS Classification of soil at various locations in Chandigarh city

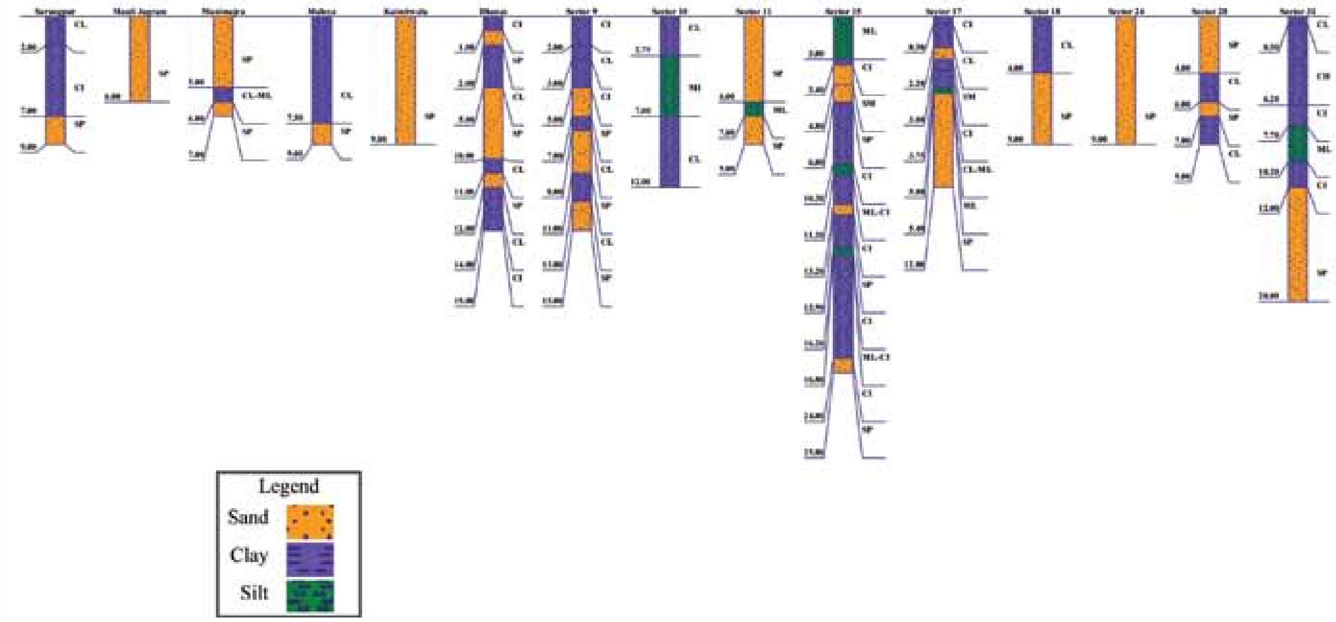

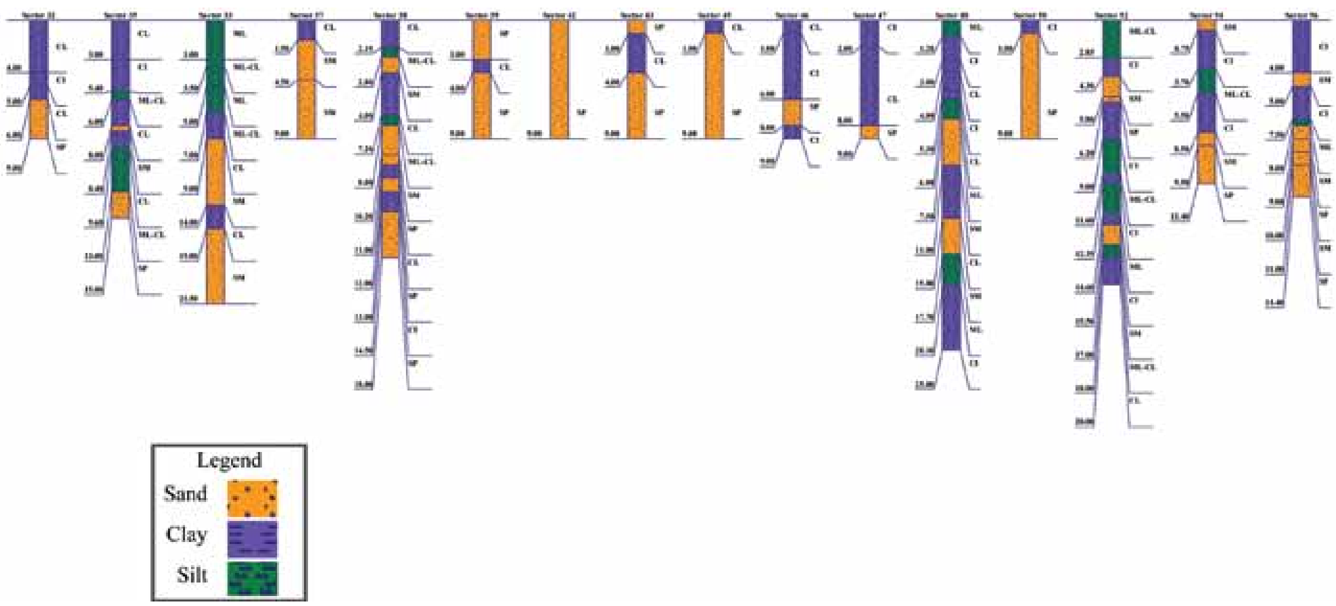

J. Ind. Geophys. Union (September 2018)
v.22, no.5, pp: 507-517

Quartz syenites from the Prakasam alkaline province, Southern India; A comparative study with special emphasis on their rare earth element contents

N. Sridhar[1], R. Mallikarjuna Reddy[*1], and G. Nagendrababu [2]

[1]Department of Geology, Kakatiya University, Warangal-506009.
[2] Former Scientific officer, Atomic Mineral Directorate for Exploration and Research, Begumpet, Hyderabad.
*Corresponding Author: mallikragi@gmail.com

ABSTRACT

This paper elucidates the petrographic, geochemical and petrogenetic aspects of the quartz syenites from the Purimetla and other quartz syenite bearing plutons of the Prakasam Alkaline Province (PAP), which are towards the east of the Cuddapah basin within the Cuddapah Intrusive Province (CIP), Southern India. A comparative study of the REE contents of these quartz syenite bodies is presented with emphasis on their LREE abundance. Petrographically these quartz syenites are composed of K-feldspar perthite, quartz and plagioclase, while hornblende and biotite are the mafic minerals. These metaluminous rocks are enriched in total alkalies especially K_2O, moderate in FeO^t and impoverished in MnO, MgO, and CaO. The normative hypersthene indicates that these rocks can be designated under sub alkaline category. The chondrite normalized REE patterns indicate the LREE enrichment over HREE with a significant negative Eu anomaly. Allanite, apatite, zircon and monazite are the accessory phases that host significant LREE in these syenites. Based on the geological settings of the syenite plutons, which has quartz syenites as an integral part and considering their proximity to gabbros has led to a new petrogenetic model. The thermal trigger caused by the induction of gabbroic magma into the continental crust initiated the partial melting of LREE enriched amphibolite crust, yielding a melt with the composition corresponding to melasyenite. This melasyenite upon fractional crystallization produced the quartz syenites within the various syenite plutons emplaced into the PAP.

Key words: Cuddapah intrusive province, Quartz syenites, LREE enrichment, negative Eu anomaly.

INTRODUCTION

Alkaline igneous rocks however are sparse in volumetric abundance in geological record. Significant syenitic magmatism corresponding to the Proterozoic eon has been found in various continental platforms around the world. This Proterozoic eon is characterized by an unusual abundance of ferroan feldspathic rocks that range in composition from granite to quartz syenites to feldspathoid-bearing syenites (Frost and Frost, 2013). Parental magmas for the Alkaline rocks are generally thought to be derived from the partial melting of metasomatised (LILE, LREE enriched lithospheric mantle) source (Fitton and Upton 1987), or asthenosphere mantle (Menzies, 1987) or mixed of these two. Some others opined that the alkaline rich syenitic magmas could generate by partial melting of lower crust with variable upper crustal contamination (Smithies and Champion 1999). Several syenite plutons – for reference, Superior Province (Sutcliffe et al., 1990), Yilgarn Craton (Smithies and Champion 1999) and Karelia (Mikkola et al., 2011, Heilimo et al., 2016) – known to contain alkali-rich quartz syenites, syenites and less abundant quartz monzonite.

Mesoproterozoic rifting between 1.35 and 1.5 Ga, resulted in the emplacement of alkaline complexes within the Great Proterozoic Fold Belt (GIPFB) of India (Vijaya Kumar et al., 2011). The emplacement of syenites in the Prakasam Alkaline Province (PAP) and Eastern Ghat Granulite Belt (EGGB) along with the granitic rocks in Nellore-Khammam schist belt (NKSB) between 1.3 to 1.5 Ga indicates rift related magmatism in East Gondwana (Babu, 2008; Sesha Sai, 2013). Alkaline (feldspathoidal and non feldspathoidal) and subalkaline rocks with varied mineralogical and geochemical characteristics are found in spatial and temporal association with each other and confined to the east of the cuddapah basin within rift and subduction settings respectively (Upadhyay et al., 2006; Upadhyay, 2008; Vijaya Kumar et al., 2015; Subramanyam et al., 2016).

In the PAP the association of undersaturated, saturated and oversaturated rocks in major alkaline plutons i.e. Elchuru (Leelanandam, 1980, 1981, 1989; Madhavan and Leelanandam, 1988; Nag et al., 1984; Czygan and Goldenberg, 1989; Upadhyay et al., 2006); Purimetla (Leelanandam and Ratnakar,1983; Ratnakar and Leelanandam, 1986; Subramanyam et al., 2016); Uppalapadu (Leelanandam, 1981; Krishna Reddy et al., 1998; Vijaya Kumar et al., 2007) offer interesting association to understand their interrelation. Such an association is witnessed in the above stated plutons confined to the rift zones in the eastern part of the cuddapah basin. This association along with gabbros and granitoids constitute the cuddapah intrusive province (CIP) (Madhavan et al., 1995a, 1999; Madhavan, 2002). The petrology, geochemistry, geochronology and genesis of diverse alkaline and subalkaline rock types in this province have been subjected to investigations during the last few decades (Leelanandam et al., 1989, Leelanandan, 1989; Madhavan et al., 1995a). Quartz syenite together with other syenite variants (saturated and undersaturated) constitutes either large plutons or minor intrusives in the PAP, which have spatial and temporal association with gabbros and granitoids.

The present study is aimed to decipher the geological, mineralogical and geochemical characteristics along with the REE concentrations of quartz syenites from Purimetla and to compare with those from other quartz syenites of the PAP (figure 1A) i.e. Vikurthi (Srinivas, 1992, Madhavan, et al., 1995b), Kotappakonda (Madhavan, et al., 1995b), Elchuru (Ratnakar and Vijaya Kumar, 1995), Settupalle (Srinivasan, 1981, Leelanandam et al.,1989), Purimetla (Ratnakar and Leelanandam, 1986) and Uppalapadu (Krishna Reddy et al.,1998; Czygan and Goldenberg, 1989), intrusive quartz syenites of the Proterozoic Podili granite towards the east of Cuddapah basin (Prasada Rao and Ahluwalia, 1974; Madhavan and Sugrive Reddy, 1990; Sesha Sai, 2013) and Chanduluru (Sharma and Ratnakar, 2000). Minor quartz syenite occurrences are also found at Mundlamuru of Pasupugallu gabbro pluton (Jyothender Reddy, 1989) and Vemanabanda, which are not covered in the present study. All the syenites are emplaced within the suture/rift zone confined to the east of the cuddapah basin and exactly in between the Dharwar craton and the Eastern Ghat Mobile Belt (EGMB) (Leelanandam, 1981, 1989, Leelanandam et al., 1989; Sharma and Ratnakar, 1994; Subba Rao, 1994; Madhavan, et al., 1999; Upadhyay et al., 2006). The above mentioned syenite bodies are constituted by undersaturated saturated and few oversaturated components. All these alkaline and subalkaline intrusives form a part of the recently recognized deformed alkaline rocks and carbonatites (DARC) (Leelanandam et al., 2006). Elchuru, Purimetla and Uppalapadu syenite complexes are predominantly composed of feldspathoidal rocks, which dominate the non feldspathoidal counterparts. Whereas the Vikurthi, Settupalle, Chanduluru syenite plutons are mainly constituted by non feldspathoidal syenites.

GEOLOGICAL SETTING

The discrete syenite complexes associated with quartz syenites show variation in their geology and areal extensions as they are emplaced within suture/rift zone/subduction zones close to eastern margin of the cuddapah basin. All the syenite complexes trend in a row parallel to NE-SW direction. The distorted spindle shaped Purimetla alkaline pluton (Figure 1B) (Prasada Rao et al., 1988; Ratnakar et al., 1980) has an aerial extension of 7 sq km and is located midway between the Elchuru and Uppalapadu alkaline complexes. The Rb-Sr isochron and U-Pb of zircon dating ages indicate that the Purimetla alkaline complex was emplaced during 1369±33 Ma (Sarkar et al., 1994) and 1334±15 Ma (Subramanyam et al., 2016) respectively with an initial Sr_i ratio of 0.70409.

Subsolvus and hypersolvus nepheline syenite is the predominant constituent of the pluton followed by subordinate hornblende syenite and less abundant quartz syenite. The mafic rocks are mainly represented by gabbros, malignite and later formed ocellar lamprophyres. The alkaline lamprophyres (Comptonite) show an intrusive relationship. The details of the quartz syenite representing other syenite plutons are listed in (Table 1).

PETROGRAPHY

The nepheline syenite which is the major rock type of the pluton is found as minor outcrops as it is mostly concealed under the soil. A minor quartz syenite exposure is found at the junction of amphibolites and hornblende syenite towards the NE part of the Purimetla pluton (Figure 1B). The quartz syenite of Purimetla which is grey in colour and medium to coarse grained exhibits hypidiomorphic texture. Subhedral to euhedral amphibole shows moderate pleochroism in shades of dark green to brownish green. Subhedral orthoclase frequently exhibits perthitic and myrmekitic textures. The discrete plagioclase conspicuously shows lamellar twinning. Granular quartz is mainly found interstitial between the feldspar grain boundaries. Amphibole and biotite are occasionally seen as clusters along with feldspar and quartz. Opaque phases are represented by magnetite with hematite lamina. Allanite, zircon, diamond shaped sphene, garnet along with prominent apatite and calcite are the accessory phases (Table 2). Zircon occurs as inclusions within K-feldspar perthite and mafic clusters.

All the quartz syenites of the PAP are leucocratic to mesocratic, coarse to medium grained and hypidiomorphic textured (seldom porphyroclastic). Principally, they are constituted by microcline or orthoclase perthitic feldspar (vein or braided, ≥ 60), amphibole (dark green to brownish green, 15-20%, with very few less than15%) as the major components along with granular quartz (5-12%), discrete plagioclase (3-5%) and biotite (brownish yellow to reddish brown) as the minor components. Calcite, sphene, garnet, zircon, allanite and apatite are found in trace amounts. However, allanite, euhedral zircon, elongated apatite and monazite are more abundant in Purimetla quartz syenites (Figure 2). Myrmekitic intergrowths are found often in most of the quartz syenites of the PAP. Invariable presence

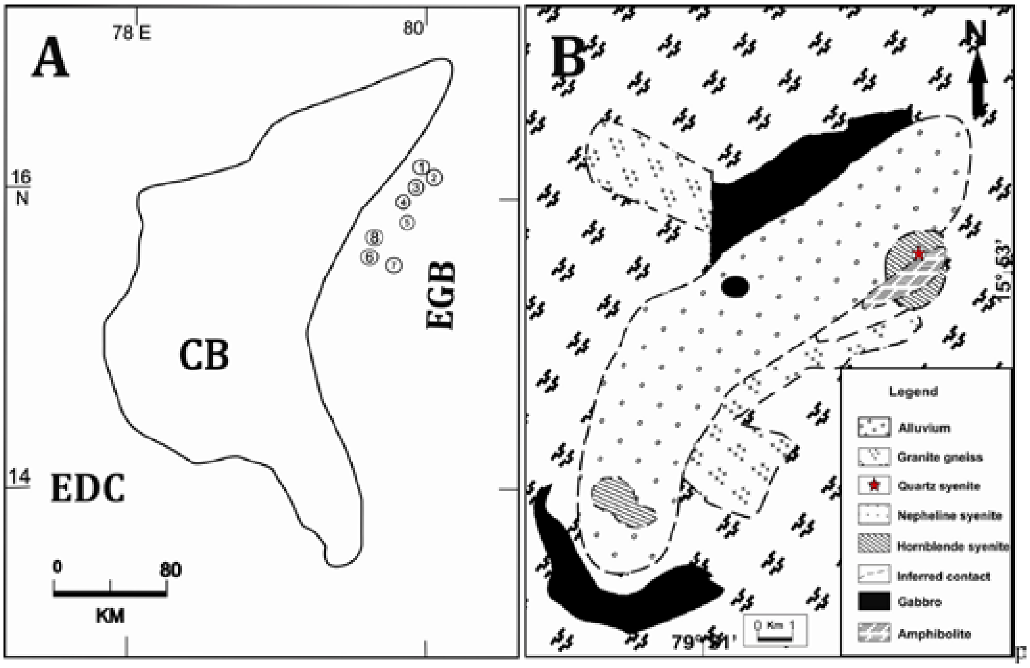

Figure 1. A. Map showing the generalized outline of the Cuddapah basin and its contiguous EDC (Eastern Dharwar Craton) and EGB (Eastern Ghats Belt) with the quartz syenite locations on the eastern margin. 1.Vikurthi; 2.Kotappakonda; 3.Elchuru; 4.Settupalle; 5.Purimetla; 6.Podili; 7. Uppalapadu; 8. Chanduluru. B. Geological map of Purimetla alkaline pluton (after Leelanandam and Ratnakar, 1983) showing the quartz syenite location (indicated as star).

Table 1. Major Quartz syenite occurrences in the Prakasam Alkaline Province (PAP).

S. No	Location	Age	Areal extension	Major rock types	Country rock	Category
1	Vikurthi	Mesoproterozoic	4 Km^2	Quartz syenite, fine grained quartz syenite, mafic xenolith enclave, pegmatite, quartz reef	Archean Granite	SOS
2	Kotappakonda	NA	NA	nepheline syenite and quartz syenite	Archean Granite and Eastern Ghat charnokites	SUS, SOS
3	Elchuru	Mesoproterozoic	16 Km^2	Shonkinite, malignite, nepheline syenite, mica lamprophyre, quartz syenite	Charnokite, Khondalite, gabbros, quartzo feldspathic schists, Archean gneiss	SUS, SOS
4	Settupalle	Mesoproterozoic	40 Km^2	Quartz syenite, hornblende syenite, ferrosyenite and minor nepheline syenite	Archean granite gneiss, gabbro, amphibolite	SUS, SS,SOS
5	Purimetla	Mesoproterozoic	7 Km^2	Shonkinite, malignite, nepheline syenite, hornblende syenite, quartz syenite	Archean gneiss, gabbro, amphibolite	SUS,SS,SOS
6	Chanduluru	NA	NA	Melasyenite, hornblende-quartz syenite, biotite-quartz syenite, syenite	Granite, gabbro, quartzite, biotite schist/ phyllite	SS,SOS
7	Uppalapadu	Mesoproterozoic	30 Km^2	Nepheline syenite, hornblende syenite, Quartz syenite, ferrosyenite	Granite gneiss, gabbros, amphibolite, biotite schist	SUS,SS,SOS
8	Podili	NA	12Km^2	Quartz syenite, nepheline normative micro syenite, alkali ferrosyenite	Granite, gabbro	SS,SOS

SUS: Silica undersaturated; SS: Silica saturated; SOS: Silica oversaturated. NA-Not available of discrete plagioclase denotes that these rocks must have crystallized under subsolvus conditions (Madhavan, et al., 1995b). Among all the quartz syenites of the PAP, those from Vikurthi and Kotappakonda consist of modal pyroxenes (Table 3). The petrographic characters of the PAP quartz syenites are listed in Table 2.

GEOCHEMISTRY

Analytical Methods

The major oxide analysis of quartz syenites of both the Purimetla and Settupalle are carried out in NGRI, Hyderabad. A Philips MagiX PRO, Model PW 2440, wavelength dispersive X-ray fluorescence spectrometer, coupled with an automatic sample changer PW 2540 and provided with suitable software SUPER Q 3.0, was used for this study (Philips, Eindhoven, Netherlands). SY-2 is the standard used for the correlation. The REE data is obtained from the AMD laboratories, Hyderabad. REE concentrations are determined by ICPAES (Inductively coupled plasma atomic emission spectrometer) ULTIMA-2, JOBINYVON, France made instrument. ICPAES is calibrated using mixed standard solution. The solution samples are introduced into plasma for measuring the emission intensities. Unknown concentrations are calculated from the calibration curves.

RESULTS AND DISCUSSIONS

Major oxides

For this comparative study, the geochemical data of quartz syenites of PAP, published by different authors is used. The Purimetla quartz syenites have higher amounts of SiO_2, total alkalies chiefly K_2O over Na_2O and are of metaluminous nature. On the other hand, these are low in FeO_t, MnO, MgO, CaO, TiO_2 and P_2O_5. Among all the quartz syenites of the PAP, the Vikurthi and Kotappakonda quartz syenites are peculiar in their geochemical characteristics as they are enriched in alkalies, FeOt, MgO, CaO, TiO_2, and P_2O_5, moderate in Al_2O_3 and relatively low in silica. All the remaining quartz syenites from the PAP show enrichment in total alkalies, with the K_2O over Na_2O denoting a high K_2O/Na_2O ratios (generally >1.5), along with variable Al_2O_3 (Table 4). Higher K_2O content is however noted to be a general feature in all other alkaline plutons of PAP (Krishna Reddy et al., 1998; Madhavan et al., 1999). Except the Vikurthi and Kotappakonda quartz syenites all the others are impoverished in MnO, MgO, CaO, TiO_2, P_2O_5 and enriched in SiO_2 contents. When the quartz syenites of PAP are plotted in the DI (Differentiation index (normative Q+or+ab+ne+lc, Thornton and Tuttle 1960) vs major oxide diagram they form a perfect fractionated trend from the melasyenite (inferred here as the parentage for the quartz syenites of the PAP) (Figure 3).

All the quartz syenites are hypersthene normative (Table 4), although some samples do not contain normative hypersthene, may be because of their alkaline affinity. The present study (Purimetla and Settupalle) samples show very low to moderate hypersthene abundance in their norm this could be due to their alkaline affinity. Thus, normative hypersthene imparts the subalkaline character to these quartz syenites. The high differentiation index (DI) (Table 4) of all the quartz syenites of the PAP reflects their most evolved compositions.

REE concentrations

The chondrite normalized REE patterns (Figure 4) of Purimetla quartz syenite depict a characteristic anomalous LREE enrichment over HREE with a steep inclination towards the HREE from LREE along with a significant strong negative Eu anomaly. Among all the studied quartz syenites of the PAP, the Purimetla and Chanduluru quartz syenites show enrichment in total REE concentration with special reference to LREE 1484-1826 ppm and 1116-1147 ppm respectively. The total REE concentrations (Table 5) of the quartz syenites from different suits of the PAP show a wide range. The PAP quartz syenites depict enrichment in LREE and depletion in HREE, with a pronounced negative Eu anomaly. The LREE/HREE ratios of these rocks are high in Purimetla, Vikurthi and moderate in Chanduluru and low in Elchuru and Settupalle. A pronounced negative Eu anomaly is probably produced by the progressive fractionation of plagioclase from the residual melts. Absence of considerable negative Eu anomaly in the melasyenite and presence of it in the quartz syenites imply that the quartz syenites are evolved from the melasyenite. Besides the above the Vikurthi and Uppalapadu quartz syenites also have considerable LREE enrichment. The remaining suits contain an extremely low to moderate concentrations of REE especially LREE. The LREE budget of these quartz syenites is thought to be controlled by the presence of allanite, apatite, zircon and monazite. The variability in the HREE patterns of the present study could have been controlled by garnet, sphene, which were probably retained with the residuum (Sharma and Ratnakar, 2000).

A similarity is seen in the major oxide and high LREE concentrations with negative Eu anomaly in quartz syenites of Purimetla, Chanduluru (Table 4 and 5) and Barrel Spring pluton, southeastern California, USA (Gleason et al., 1994). The quartz syenite of Barrel Spring pluton shows La (488 ppm), Ce (846 ppm) and Nd (292 ppm). Both in Barrel spring pluton and Purimetla, Chanduluru plutons the LRRE enrichment is connected to the presence of allanite, apatite, zircon and monazite.

Table 2. Details of the petrographic characteristics and mineral assemblages of quartz syenites of PAP, Vikurthi & Kotappakonda (Madhavan, et al., 1995b); Elchuru (Ratnakar and Vijaya Kumar, 1995); Settupalle (Leelanandam et al.,1989); Purimetla (Ratnakar and Leelanandam 1986 & Present authors) ; Uppalapadu (Krishna Reddy et al.,1998); Podili (Madhavan and Sugrive Reddy, 1990); Chanduluru (Sharma and Ratnakar, 2000)

S. No	Location		Crystallinity	Texture	Petrography	
					Essential minerals	**Accessory minerals**
1	Vikurthi		Coarse to medium grained	Equigranular hypidiomorphic	Perthitic microcline, pyroxene, hornblende, biotite, quartz, plagioclase	Sphene, ilmenite, magnetite, Apatite, calcite
2	Kotappakonda		Coarse to medium grained	Equigranular hypidiomorphic	Perthitic microcline, pyroxene, hornblende, biotite, , plagioclase, quartz,	Sphene, ilmenite, magnetite, Apatite, calcite
3	Elchuru		Medium grained	hypidiomorphic	Perthitic microcline, albite, amphibole (ferrohastingsite), biotite, quartz	Apatite
4	Settupalle		Medium to coarse	Equigranular hypidiomorphic	Microcline perthite, microcline, plagioclase, quartz, amphibole, biotite	Calcite, zircon, opaques
5	Purimetla		Coarse grained	Hypidiomorphic and seldom Porphyroclastic	Orthoclase perthite, amphibole, quartz, plagioclase, biotite	Magnetite, ilmenite, garnet, monazite, zircon, allanite, sphene, apatite
6	Chanduluru	HQS	Medium to coarse	hypidiomorphic	Perthitic orthoclase, amphibole, quartz, plagioclase	Zircon, sphene, garnet, apatite and fluorite
		BQS	Coarse grained	hypidiomorphic	Orthoclase perthite, quartz, biotite, amphibole	apatite, sphene, zircon, garnet, fluorite, magnetite
		M.Sye	Fine to medium	hypidiomorphic	Plagioclase, hornblende, K-feldspar perthite, quartz	apatite, sphene, zircon, garnet
7	Uppalapadu		Medium to Coarse grained	hypidiomorphic	K-feldspar perthite, quartz, amphibole, biotite, plagioclase	Calcite, zircon, magnetite, apatite
8	Podili		Medium to coarse	Equigranular hypidiomorphic	Microcline meso perthite, quartz, plagioclase, amphibole, biotite.	Magnetite, ilmenite, apatite

HQS: Hornblende quartz syenite; BQS: Biotite quartz syenite; M.Sye- Mela syenite.

Table 3. Average modal compositions of (Vol %) of quartz syenites of PAP (References are mentioned at table 4)

S.No	**1**	**2**	**3**	**4**	**5**	**6**	**7**	**8**	**9**	**10**	**11**	**12**	**13**	**14**	**15**	**16**	**17**	**18**	**19**
	IS42	**IS11**	**QSK11**	**QSK10**	**J15/93b**	**S1**	**S20**	**Stp**	**P7**	**P11**	**PT81**	**PT52**	**U18**	**U66**	**U11**	**D26**	**D49**	**D30**	**PO**
K-Fl	53.8	57.4	47	56.4	93	51	53.8	53.6	52.4	51.9	39.8	58.4	61	72	64.9	44.8	50	62.9	57.27
Qtz	11.3	10.9	4.3	12.3	2	10.9	11.2	11.5	9.8	10	6.8	10	9	11	17.7	10.2	12.6	22.7	15.85
Plag	0.4	1.4	----	0.4	3	18	20.9	25	18.9	19.8	28.3	14.3	5	4	12.2	8.7	7.9	3.1	3.92
Pyr	3.6	5.2	7.5	0.9	----	----	----	----	----	----	----	----	----	----	----	----	----	----	0.8
Amp	10.7	13.8	22.5	6.9	2	7.6	8.2	8.2	19.2	18.7	22.5	10.7	16	8	3.3	25.7	18.9	0.5	15.97
Bio	18.2	9.6	11.2	20	Tr	2.8	3.2	3.52	1.2	1	Tr	1.8	3	2	0.4	8.2	6.8	7.3	3.95
Sph	0.9	0.5	6.2	2.5	----	0.5	0.5	0.7	0.5	0.4	0.4	0.5	----	----	0.4	Tr	0.4	0.6	1.2
Mag	1.2	0.4	0.6	1.1	----	0.8	0.7	0.9	0.7	0.9	0.8	1		----	0.7	0.2	0.3	----	2.63
Cal	----	0.4	0.4	----	----	0.4	0.3	0.4	0.3	0.2	0.4	0.4	----	----	----	----	----	----	----
Apa	----	0.4	0.3	----	----	0.3	0.6	0.8	1.5	1.6	1.6	1.5	3	2	1	0.8	0.9	0.9	0.7
Alla	----	----	----	----	----	0.4	0.3	----	2.3	2	1.2	1.4	----	----	----	----	----	----	----
Zir	----	----	----	----	----	0.6	0.9	0.9	1.3	1.7	1.3	1	Tr	1	0.8	1.5	2.5	0.8	0.6
Mon	----	----	----	----	----	0.2	0.4	----	0.3	0.6	0.4	0.3	----	----	----	----	----	----	----
Gar	----	----	----	----	----	----	----	----	0.3	0.2	0.2	0.2	----	----	----	----	0.2	0.9	----

Tr: Trace, K-Fl: K Feldspar; Qtz: Quartz; Plag: Plagioclase; Pyr: Pyroxene; Amp: Amphibole; Bio: Biotite; Sph: Sphene; Mag: Magnetite; Cal: Calcite; Apa: Apatite; Alla; Allanite; Zir; Zircon; Mon: Monazite; Gar; Garnet. Abbreviations: IS- Vikurthi; QSK- Kotappakonda; J15/93b-Elchuru; S-Settupalle (Present study); Stp- Settupalle; P-Purimetla (Present study); PT-Purimetla; U-Uppalapadu; D-Chanduluru; Po-Podili.

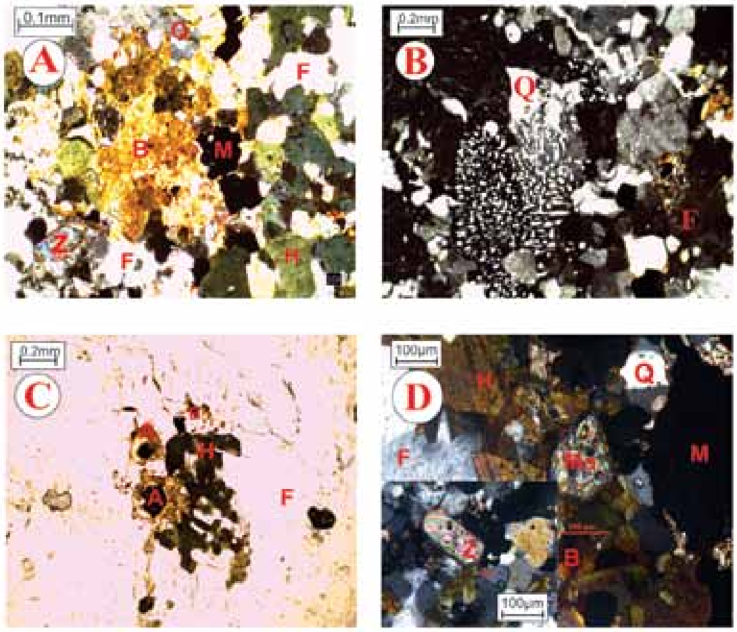

Figure 2. Photomicrographs of Purimetla quartz syenite. A. shows the hypidiomorphic texture. B. Myrmekitic texture. C. association of allanite with hornblende embedded in feldspathic ground mass. D. shows the monazite at its center along with the mafic and felsics. Inset microphotograph in D showing the euhedral zircon. All photomicrographs are taken under crossed nicols except C (Under polarized light). Q: Quartz; F: Feldspar; H: Hornblende; B: Biotite; M: Magnetite; Mo: Monazite; Z: Zircon; A: Allanite.

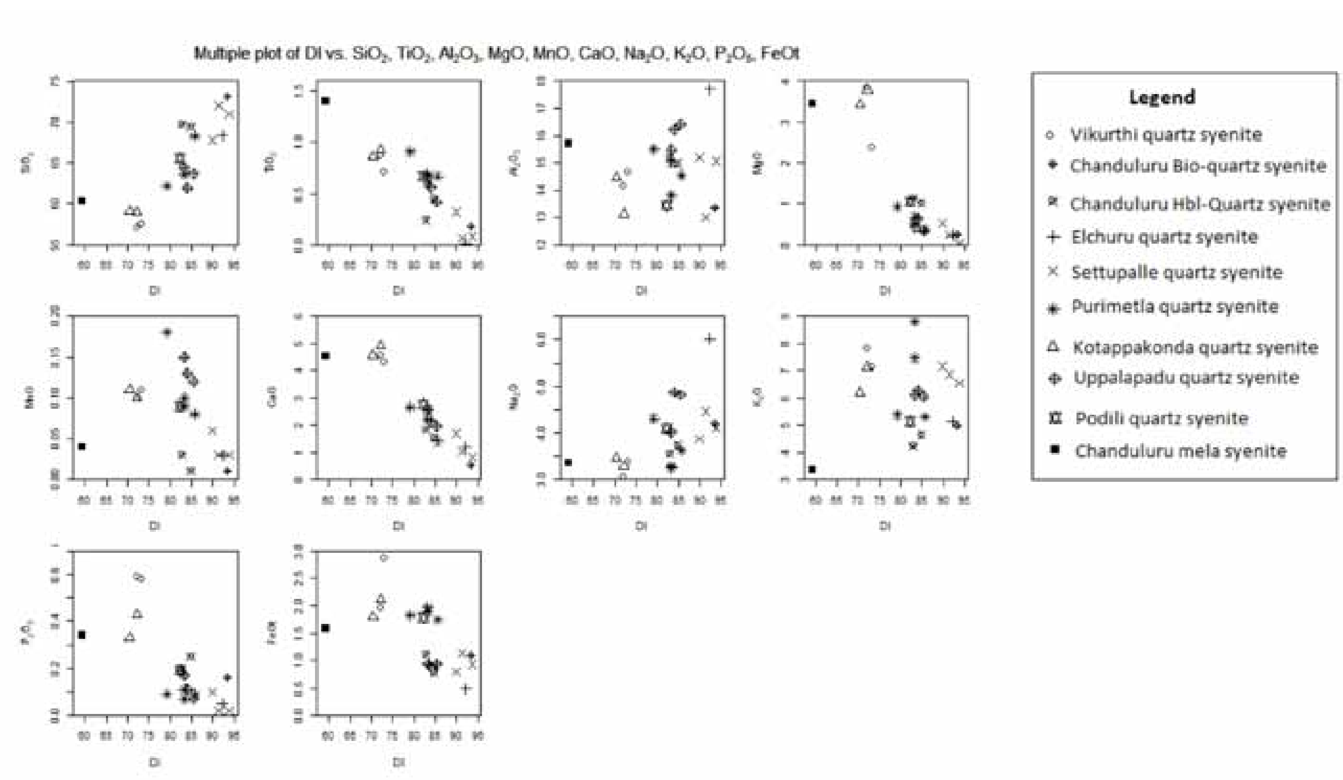

Figure 3. Differentiation index vs major oxides of PAP quartz syenites, exhibits the fractionation trends (Thornton and Tuttle1960).

Table 4. Major elemental concentrations of CIP quartz syenites. M.Sye - Mela syenite; Q.Sye - Quartz syenite; Q.Sye.G- Quartz syenite gneiss.

S.No	1	2	3	4	5	6	7	8	9	10	11	12	13	14	15	16	17	18	19	20
Sp.No	D125I	IS42	IS11	QSK12	QSK10	J15/93b	S1	S20	Stp	P7	P11	PT81	PT52	U18	U66	U11	D26	D49	D30	PO
Rock	M.Sye	Q.Sye	Q.Sye	Q.Sye	Q.Sye	Q.Sye	Q.Sye	Q.Sye	Q.Sye	Q.Sye	Q.Sye	Q.Sye	Q.Sye	Q.Sye	Q.Sye	Q.Sye.G	H.Qsy	H.Qsy	B.Qsy	Qsye
Pluton	Cha	Vik	Vik	Ktp	Ktp	El	Stp	Stp	Stp	Pu	Pu	Pu	Pu	Up	Up	Up	Cha	Cha	Cha	Po
SiO2	60.33	57.56	57.13	59.06	58.92	68.35	70.96	72.03	67.78	63.59	63.62	62.18	68.28	64.44	61.95	63.7	69.72	69.41	73.04	65.6
TiO2	1.4	0.71	0.87	0.86	0.93	0.01	0.08	0.06	0.32	0.6	0.69	0.91	0.67	0.66	0.56	0.42	0.24	0.45	0.18	0.67
Al2O3	15.7	14.66	14.14	14.45	13.13	17.72	15.07	12.99	15.19	15.03	13.81	15.5	14.55	15.49	16.22	16.41	15.23	14.98	13.34	13.44
Fe2O3	1.76	3.2	2.17	1.99	2.35	0.54	1.03	1.25	0.88	2.1	2.19	2.03	1.94	1.03	0.99	1.03	1.23	0.85	1.2	1.99
FeO	5.4	5.28	4.4	4	4.28	0.2	0.21	0.2	1.97	2.46	2.87	5.5	2.6	4.93	4.6	3.83	2.12	2.84	1.24	3.55
MnO	0.04	0.11	0.1	0.11	0.1	0.03	0.03	0.03	0.06	0.1	0.09	0.18	0.08	0.15	0.13	0.12	0.03	0.01	0.01	0.09
MgO	3.45	2.36	3.83	3.43	3.78	0.22	0.05	0.24	0.52	0.68	0.53	0.93	0.37	0.44	0.64	0.34	1.12	1.02	0.25	1.05
CaO	4.52	4.32	4.56	4.56	4.92	1.19	0.81	1.03	1.69	2.55	2.23	2.66	1.4	2.58	2.12	1.96	1.85	1.56	0.54	2.77
Na2O	3.36	3.37	3.05	3.47	3.29	6.02	4.11	4.46	3.87	3.27	3.25	4.31	3.63	4.02	4.87	4.82	3.55	3.74	4.19	4.1
K2O	3.36	7.12	7.84	6.19	7.13	5.12	6.53	6.86	7.16	7.46	8.8	5.38	5.31	6.11	6.27	6.05	4.23	4.65	4.99	5.14
P2O5	0.34	0.58	0.59	0.33	0.43	0.05	0.02	0.02	0.1	0.11	0.07	0.09	0.09	0.17	0.11	0.07	0.2	0.25	0.16	0.19
PI	0.89	0.91	0.96	0.86	1.00	0.87	0.92	1.14	0.93	0.90	1.08	0.83	0.81	0.85	0.91	0.88	0.68	0.75	0.92	0.92
Norm																				
Quartz	14.56	2.55	0	2.41	0.12	11	20.42	22.06	13.66	10.6	7.45	7.58	22.54	9.79	2.56	6.26	26.66	23.98	28.03	15.36
Plagioclase	48.23	32.36	25.61	34.93	27.84	56.52	38.16	28.62	35.68	31.97	22.04	43.53	37.07	40.19	45.09	46.06	37.91	37.75	37.09	37.78
Orthoclase	19.85	42.08	46.33	36.58	42.14	30.26	38.59	40.54	42.31	44.09	52	31.79	31.38	36.11	37.05	35.75	25	27.48	29.49	30.38
Diopside	0	11.43	13.81	12.08	17.47	0	0.27	1.9	4.06	6.35	9.09	4.76	0	4.82	5.12	3.49	0	0	0	7.9
Hypersthene	8.54	5.45	0	7.17	5.53	0.55	0	0	1.71	0.51	0.53	7.12	3.14	5.97	5.89	4.74	5.33	6.33	1.63	2.58
Ilmenite	0.08	1.35	1.65	1.63	1.77	0.02	0.15	0.11	0.61	1.14	1.31	1.73	1.27	1.25	1.06	0.8	0.46	0.85	0.34	1.27
Magnetite	0	4.64	3.15	2.89	3.41	0.71	0.54	0	1.28	3.04	0.76	2.94	2.81	1.49	1.44	1.49	1.78	1.23	1.74	2.89
Hematite	1.7	0	0	0	0	0.05	0.66	0	0	0	0	0	0	0	0	0	0	0	0	0
Apatite	0.8	1.34	1.37	0.76	1	0.12	0.05	0.05	0.23	0.25	0.16	0.21	0.21	0.39	0.25	0.16	0.46	0.58	0.37	0.44
DI	59.27	73.15	72.14	70.40	72.18	92.21	93.79	91.38	89.86	83.26	83.26	79.16	85.65	83.29	83.99	85.41	82.86	84.84	93.44	82.22

Source: S.No- 2-5 (Madhavan et al., 1995b); 6- (Ratnakar and Vijaya Kumar, 1995); 7&8 (present study); 9- (Leelanandam et al., 1989); 10&11 (Present study); 12&13-(Ratnakar and Leelanandam, 1986); 14&15- (Krishna Reddy et al., 1998); 16- (Czygan and Goldenberg, 1989); 1,17,19- (Sharma and Ratnakar, 2000); 20- (Madhavan and Sugrive Reddy, 1990).

Petrogenesis

The quartz syenites of the PAP show spatial and temporal relationship with the associated alkaline (feldspathoidal or non feldspathoidal) and subalkaline plutons with varying degree of silica saturation. Various models were formulated to explain the genesis of over saturated components of the PAP, based on the geochemistry of the syenite plutons intruded at the junction of EDC and EGMB (Ratnakar and Leelanandam 1986; Krishna Reddy, et al., 1998; Madhavan and Sugrive Reddy, 1990; Srinivasan, 1982, Leelanandam, et al., 1989; Madhavan, et al., 1995a,b, 1999; Ratnakar and Vijaya Kumar, 1995; Sharma and Ratnakar, 2000). The subalkaline rocks also constitute a closely interrelated genetic group with a distinct lineage as seen in alkaline rocks (Madhavan, et al., 1995b).

In the PAP, the mantle derived shoshonitic magma is inferred as parent for both the feldspathoidal and non-feldspathoidal alkali syenites, whereas the subalkaline syenites are formed from the gabbroic magma, which upon differentiation produce the trachybasaltic liquid followed by the trachytic fraction (Madhavan et al., 1995b). In PAP the melasyenite, which has compositional similarity with the trachy basalt in various syenite plutons is considered as the primary source for quartz syenites as it has higher modal abundance of mafic minerals and higher MgO, FeOt, CaO along with low REE, especially LREE concentrations (Madhavan et al., 1995b; Sharma and Ratnakar, 2000).
The melasyenite which is presumed as the source for the quartz syenites is produced by an anhydrous partial melting of LREE enriched amphibolite crust. The partial melting is attributed mainly due to the underplating of the gabbroic

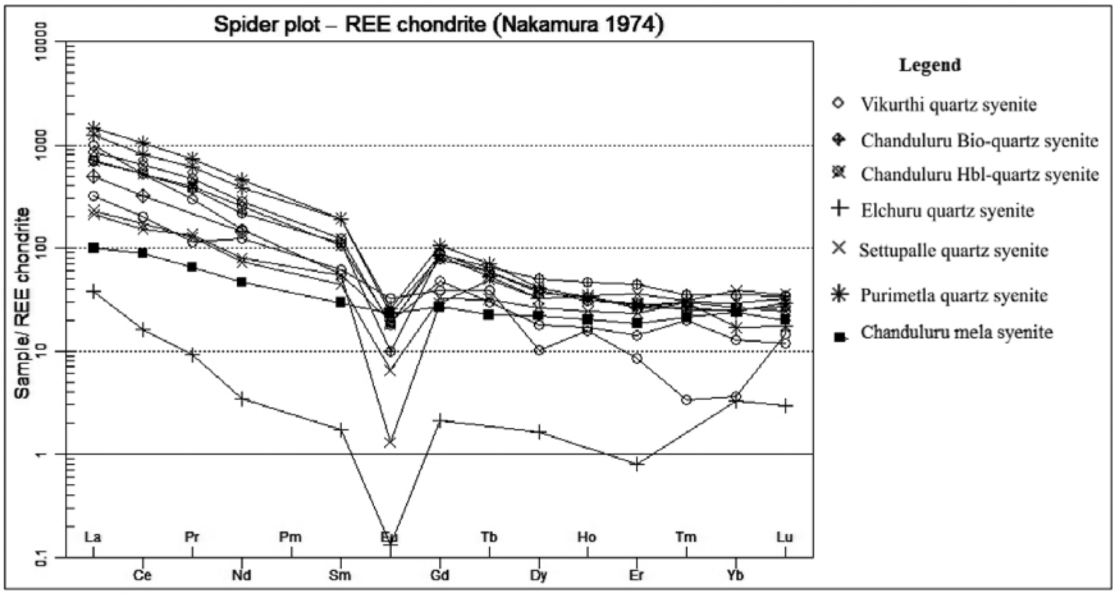

Figure 4. Chondrite normalised REE patterns of PAP Quartz syenites.

Table 5. REE concentrations in ppm of quartz syenites of PAP. S.No, 2,3: Vikurthi; 4: Elchuru; 5,6: Settupalle (authors unpublished data); 7,8:Purimetla (Present study); 9: Uppalapadu; 1,10,11,12: Chanduluru. The references are given at the Table no.4.

S. No	1	2	3	4	5	6	7	8	9	10	11	12
Sp.No	D125I	IS42	IS11	J15/93b	S1	S20	P7	P11	U11	D26	D49	D30
Pluton	Cha	Vik	Vik	El	Stp	Stp	Pu	Pu	Up	Cha	Cha	Cha
Rock	M.Sy	Q.Sye	Q.Sye	Q.Sye	Q.Sye	Q.Sye	Q.Sye	Q.Sye	Q.Sye.G	H.Qsy	H.Qsy	B.Qsy
La	32.87	104.7	328.2	12.42	76	70	482	417	165	228.44	284.17	232.5
Ce	76.19	172.6	455.7	13.86	148	132	904	692	275	450.13	549.83	450.42
Pr	7.28	12.9	33.5	1.03	14	15	82	69	NA	43.99	53	42.07
Nd	29.15	77.9	94.6	2.18	46	50	288	243	91	158.16	178.27	137.21
Sm	6	12.6	11.4	0.35	9	11	39	39	NA	21.43	24.86	22.74
Eu	1.8	2.5	1.5	0.01	0.5	0.1	2	1.8	NA	1.47	1.38	0.76
Gd	7.39	10.8	13.1	0.58	9	8	29	23	NA	21.5	24.6	23.83
Tb	1.05	1.8	1.4		1.5	2.3	3.3	2.5	NA	2.78	2.73	3.06
Dy	7.52	3.5	6.2	0.56	9	11	14	11	NA	13.17	12.7	17.31
Ho	1.41	1.1	1.2		1.7	2.4	2.3	2.4	NA	2.17	2.32	3.25
Er	4.18	1.9	3.2	0.18	5.2	8	5.9	6	NA	6.6	6.27	9.99
Tm	0.64	0.1	0.6		0.9	0.92	0.8	0.89	NA	0.76	0.89	1.06
Yb	5.24	0.8	2.8	0.72	6.5	8.5	5.4	3.7	NA	5.54	5.75	7.64
Lu	0.68	0.5	0.4	0.1	1.1	1.2	1	0.6	NA	0.92	0.83	1.15
Total	181.4	403.7	953.8	31.99	328.4	320.42	1858.7	1511.89	531	957.06	1147.6	952.99
LREE	151.49	394	938	30.43	302.5	286.1	1826	1484.8	531	925.12	1116.11	909.53
HREE	29.91	9.7	15.8	1.56	25.9	34.32	32.7	27.09	NA	31.94	31.49	43.46
LREE/HREE	5.0649	40.62	59.37	19.506	11.68	8.3362	55.841	54.8099	NA	28.964	35.4433	20.928

Note: abbreviations are same as mentioned in table 3, NA- Not available.

magma that produced melasyenite, which upon fractional crystallization has given rise to the quartz syenites in the PAP (Figure 3). A cause and consequence modal (originally envisaged by (Huppert and Sparks, 1988) was adopted for Chanduluru complex to explain the genesis of the sequence which consists of gabbro-diorite-syenite-granite (Sharma and Ratnakar, 2000). In this present study the similar model is considered as the driving mechanism for the formation of quartz syenites in various syenite plutons of the PAP including Purimetla.

Tectonic setting

The emplacement tectonics of various igneous suits are demonstrated by different bivariant and triangular diagrams with the help of major oxides and trace elements (eg. Floyd and Winchester, 1975; Pearce and Cann 1973; Pearce et al., 1977, 1984; Pearce, 2008; Wood et al., 1979). In the global context the syenitic magmatism corresponding to Archean age is quite rare compared to Proterozoic whereas the later is commonly associated with the continental rift/ extensional tectonic settings (eg. Gardar Province, (Upton et al., 2003); Klokken intrusion, (Parsons, 1979, 1981); Ntem Complex, (Tchameni et al., 2001). In PAP the tectonic setting for the Proterozoic magmatism corresponding to alkaline syenitic composition is often found in rift/ extensional settings (e.g. Upadhyay et al., 2006; Upadhyay, 2008; Chalapathi Rao et al., 2012; Hari et al., 2014; Vijaya Kumar et al., 2015). Whereas the tholeitic magmatism is mainly confined to the subduction settings (e.g. Vijaya Kumar et al., 2015; Subramanyam et al., 2016). This Proterozoic bimodal magmatic association confined to PAP tholeitic (IAB type) and alkaline (OIB type) show difference in their geochemical signatures, which imply that they were derived from divergent magmatic sources that contributed to the growth of Eastern Ghats continental crust. The emplacement of quartz syenites along with the other syenites within the various syenite plutons of the PAP are mainly confined to the within plate or extensional rift settings (e.g. see Sharma and Ratnakar, 2000).

CONCLUSION

The suture between the EDC and EGB paved way to the emplacement of several alkaline and subalkaline complexes, which have the quartz syenite as an integral part. Geochemical signatures of the present study indicate their evolved compositions. Presence of normative quartz and hypersthene in the quartz syenites indicates their sub alkaline nature, however few quartz syenites show alkaline affinity. Among the quartz syenites taken up for this study Purimetla and Chanduluru are high in their LREE contents, whereas Uppalapadu and Vikurthi are moderate and Settupalle and Elchuru are low. The high LREE contents are mainly attributed to the presence of zircon, apatite, allanite and monazite. Significant negative Eu anomalies in the quartz syenites portray the removal of plagioclase by the fractional crystalisation from the melasyenite, which is devoid of negative Eu anomaly. Quartz syenites of the PAP are evolved from a melasyenite, which is formed by the partial melting of LREE enriched amphibole crust, triggered by the heat generated during the induction of the gabbroic magma in to the continental crust.

ACKNOWLEDGEMENTS

Authors are thankful to the DAE-BRNS for sanctioning the project on PAP. We are highly indebted to Prof. V. Madhavan for his constant guidance in carrying out this project and help rendered by him during the manuscript preparation. Thanks are also due to the department of geology, Kakatiya University, Warangal, for extending the necessary facilities. Immense thanks are due to the anonymous reviewers for their valuable comments, suggestions in shaping this manuscript. We express our sincere thanks to the editor of this journal for accepting this manuscript.

Compliance with Ethical Standards

The authors declare that they have no conflict of interest and adhere to copyright norms.

REFERENCES

Babu, V.R.R.M., 2008. Nellore-Khammam schist belt- a plate tectonic model. National Symposium on Geodynamics and evolution of Indian Shield-through time and space. Golden Jubilee Geol. Soc. Ind, Proceedings of the national symposium Centre for Earth Science Studies, Trivandrum, No.8. Geol. Soc. India, Memoir, 74.

Chalapathi Rao, N.V., Fu-yuan W.U. and Srinivas, M., 2012. Mesoproterozoic emplacement and enriched mantle derivation of the Racherla alkali syenite, Palaeo-Mesoproterozoic Cuddapah Basin, southern India: insights from in situ Sr–Nd isotopic analysis on apatite. Geol. Soc. London, Spl. Publ., 365, 185–195.

Czygan, W. and Goldenberg, G., 1989. Petrography and geochemistry of the alkaline complexes of Sivamalai, Elchuru and Uppalapadu, India. Geol. Soc. India Memoir, 15, 225-240.

Fitton, J.G. and Upton, B.G.J., 1987. Introduction. In: Fitton, J.G. and Upton, B.G.J. (eds) Alkaline Igneous Rocks. Geol. Soc. London, Spl. Publ., 30, ix– xiv.

Floyd, I.A. and Winchester. A., 1975. Magma type and tectonic setting discrimination using immobile elements. Earth Planet. Sci. Lett, 27, 211-218.

Frost. C.D. and Frost, B.R., 2013. Proterozoic ferroan feldspathic magmatism. Precamb. Res., 228, 151– 163.

Gleason, J.D., Miller, C.F., Wooden, J.L. and Bennett, V.C., 1994. Petrogenesis of the highly potassic 1.42 Ga Barrel Spring pluton, southeastern California, with implications for mid-Proterozoic magma genesis in the southwestern USA. Contrib Mineral Petrol, 118, 182-197.

Hari, K.R., Chalapathi Rao. N.V., Swarnkar, V. and Hou, G., 2014. Alkali feldspar syenites with shoshonitic affinities from Chhotaudepur area: Implication for mantle metasomatism in the Deccan large igneous province. Geoscience Frontiers, 5, 261-276.

Heilimo, E.S.A., Mikkola, P., Huhma, H. and Halla, J., 2016. Alkaline-rich quartz syenite intrusions of the Western Karelia subprovince. Geol. Soc. London, Spl. Publ., 449.

Huppert, E. and Sparks, R.S.J., 1988.The generation of granitic magmas by intrusion of basalt into continental crust. Jour. Petrol, 29, 599-624.

Jyothender Reddy, Y., 1989. Petrological and geochemical studies of the Pasupugallu gabbro- anorthosite pluton, Prakasam district, Andhra Pradesh, Unpub. Ph.D. Thesis Osmania University, Hyderabad.

Krishna Reddy, K., Ratnakar, J. and Leelanandam, C., 1998. A petrochemical study of the Proterozoic alkaline complex of Uppalapadu, Prakasam alkaline province, Andhra Pradesh. J. Geol. Soc. India, 53, 41- 52.

Leelanandam, C., 1980. An alkaline province in Andhra Pradesh. Curr. Sci, 49, 550–551.

Leelanandam, C., 1981. Some observations on the alkaline province in Andhra Pradesh, Curr. Sci, 50, 799-802.

Leelanandam, C. and Ratnakar, J., 1983. The Purimetla alkaline pluton, Prakasam district, Andhra Pradesh, India. Quart. J. Geol. Min. Met. Soc. India, 55, 14-30.

Leelanandam, C. 1989. The Prakasam alkaline province in Andhra Pradesh. J. Geol. Soc. India, 53, 41-52.

Leelanandam, C., Srinivasan, T.P. and Ratnakar. J., 1989. The sub alkaline and alkaline rocks of Settupalle complex, Prakasam district, Andhra Pradesh, India. Memories Geol. Soc. India, 15, 241-263.

Leelanandam, C., Burke, K., Ashwal, L.D. and Webb, S.J., 2006. Proterozoic mountain building in Peninsular India: an analysis based primarily on alkaline rock distribution. Geol. Mag, 143, 195-212.

Madhavan, V. and Leelanandam, C., 1988. Petrology of the Elchuru Alkaline Pluton, Prakasam District, Andhra Pradesh, India. J. Geol. Soc. India, 31, 515–537.

Madhavan, V. and Sugrive Reddy, A., 1990. The Podili syenites – a suite of alkaline and sub alkaline rocks from Andhra Pradesh. J. Geol. Soc. India, 35, 341 -356.

Madhavan, V. Mallikarjuna Rao, J., Chalapathi Rao., N.V. and Srinivas, M., 1995a. The multifaceted manifestations of an intrusive province around the intra cratonic Cuddapah basin, India. In: Magmatism in relation to Diverse Tectonic Settings (Eds; Srivastava, R.K. and Chandra, R) A.A. Balkem, Rotterdam, 93-105.

Madhavan, V., Srinivas, M., Mallikarjuna Rao, J. and Chalapathi Rao. N.V., 1995b. Mineral chemistry and geochemistry of the mesocratic quartz syenite intrusion from Vikurthi and Kotappakonda, Guntur District, Andhra Pradesh. J. Geol. Soc. India, 45, 519–529.

Madhavan, V., Mallikarjuna Rao, J. and Srinivas, M., 1999. Mid Proterozoic Intraplate Alkaline Magmatism in the Eastern Dharwar Craton of India: the Cuddapah Province. J. Geol. Soc. India, 53, 143–162.

Madhavan, V., 2002. The alkaline province of India: An agenda for future investigations. J. Geophysics, XXIII(2), 60-87.

Menzies, M., 1987. Alkaline rocks and their inclusions: a window on the Earth's interior. In: Fitton, J.G. and Upton, B.G.J. (eds) Alkaline Igneous Rocks. Geol. Soc., London, Spl. Publ., 30, 15–27.

Mikkola, P., Salminen, P., Torppa, A. and Huhma, H., 2011. The 2.74 Ga Likama¨nnikko¨ complex in Suomussalmi, East Finland: lost between sanukitoids and truly alkaline rocks? Lithos, 125, 726–728.

Nag, S., Chakravorthy, P.S., Smith, T.E. and Huang, C.H., 1984. The petrology and geochemistry of intrusive alkaline rocks of Elchuru, Prakasam District, Andhra Pradesh, India. Geological J., 19, 57-76.

Parsons, I., 1979. The Klokken gabbro-syenite complex, South Greenland: cryptic variation and origin of inversely graded layering. J. Petrol., 20, 653–694.

Parsons, I., 1981. The Klokken gabbro-syenite complex, South Greenland: quantitative interpretation of mineral chemistry. J. Petrol., 22, 233–260.

Pearce, J.A. and Cann, J.R., 1973. Tectonic setting of basic volcanic rocks determined using trace element analysis. Earth Planet. Sci. Lett, 19, 290-300.

Pearce, T.H., Gormabn, E. and Birkett, T.C., 1977. The relationships between major element chemistry and tectonic environment of basic and intermediate volcanic rocks. Earth Planet. Sci. Lett, 36(12), 121-132.

Pearce, J.A., Harris, N.B.W. and Tindle, A.G., 1984. Trace Element Discrimination diagrams for the Tectonic Interpretation of Granitic Rocks. J. Petrol, 25(4), 956-998.

Pearce, J.A., 2008. Geochemical fingerprinting of oceanic basalts with applications to ophiolite classification and the search for Archean oceanic crust Lithos, 100(1-4), 14–48.

Prasada Rao, A.D. and Ahluwalia, A.D., 1974. Geology of parts of Podili and Darsi taluks, Prakasam district, Andhra Pradesh. Geol. Surv. Ind. Prog. Rep. 1973-74 (Unpublished).

Prasada Rao, A.D., Rao, K.N. and Murthy, Y.G.K., 1988. Gabbro – Anorthosite –Pyroxenite complexes and alkaline rocks of Chimakurthy – Elchuru area, Prakasam District, A.P. Records. Geol. Surv. India, 116, 1-20.

Ratnakar, J., Madhavan, V., Srinivasan, T.P. and Narasimha Reddy, M., 1980. Some preliminary observations on the Purimetla alkaline pluton, Prakasam district, Andhra Pradesh. Geoviews, 8, 93-98.

Ratnakar, J. and Leelanandam, C., 1986. A petrochemical study of the Purimetla alkaline pluton, Prakasam District, Andhra Pradesh, India. Neues. Jb. Mineral. Abh, 156, 99-119.

Ratnakar, J. and Vijaya Kumar, K., 1995. Petrogenesis of quartz-bearing syenite occurring within nepheline syenite of the Elchuru alkaline complex, Prakasam province, Andhra Pradesh, India. J. Geol. Soc. India, 46, 611-618.

Sarkar, A., Rao, K.N., Ghosh, S., Bisui, P.K. and Gupta, S.N., 1994. Rb-Sr geochronology of the Kotappakonda charnokites and the Purimetla alkaline complex, Andhra Pradesh sector, Eastern Ghats Belt (Abst.). Workshop on Eastern Ghats Mobile belt, Visakhapatnam, India, 69-70.

Sesha Sai, V.V., 2013. Proterozoic Granite Magmatism along the Terrane Boundary Tectonic Zone to the East of Cuddapah Basin, Andhra Pradesh – Petrotectonic Implications for Precambrian Crustal Growth in Nellore Schist Belt of Eastern Dharwar Craton. J. Geol. Soc. India, 81, 167-182.

Sharma, V.N. and Ratnakar, J., 1994. Some preliminary observations on the Chanduluru (Darsi) complex, Prakasam Province, Andhra Pradesh, India. J. Indian Acad. Geosci, 37, 13-17.

Sharma,V.N. and Ratnakar, J., 2000. Petrology of the gabbro-diorite-syenite-granite complex of Chanduluru, Prakasam alkaline province, Andhra Pradesh, India J. Geol. Soc. India, 55(5), 553-572.

Smithies, R.H. and Champion, D.C. 1999. Late Archaean felsic alkaline igneous rocks in the Eastern Goldfields,Yilgarn Craton, Western Australia: a result of lower crustal delaminating? J. Geol. Soc., London, 156, 561–576.

Srinivasan, T.P., 1981. The Settupalle alkaline pluton, Prakasam District, Andhra Pradesh. Geoviews, IX(VIII), 379-386.

Srinivasan. T.P. and Ratnakar, J., 1982 Occurrence of nepheline syenite within quartz syenite of

Settupalle Prakasam District, Andhra Pradesh. Curr. Sci, 51, 313-316.

Srinivas, M., 1992. Comprehensive petrological and geochemical studies of the subalkaline and alkaline intrusives of Guntur and Prakasam Districts of Andhra Pradesh, India. Unpub. Ph.D thesis, Osmania University, Hyderabad, 216.

Subba Rao, D.V., 1994. Crustal structure beneath Eastern Ghats based on gravity data. Workshop on Eastern Ghats Mobile Belt, Visakhapatnam, India, 24 (abs).

Subramanyam, K.S.V., Santosh, M., Qiong-Yan Yang., Ze – ming Zhang., Balaram, V. and Reddy. U.V.B., 2016. Mesoproterozoic island arc magmatism along the south-eastern margin of the Indian Plate: Evidence from geochemistry and zircon U-Pb ages of mafic plutonic complexes, J. Asian Earth Sci, 130, 116-138.

Sutcliffe, R.H., Smith, A.R., Doherty, W. and Barnett, R.L., 1990. Mantle derivation of Archaean amphibole- bearing granitoid and associated mafic rocks: evidence from the southern Superior Province, Canada. Contrib. Mineral. Petrol, 105, 255–274.

Tchameni, R., Mezger, K., Nsifa, N.E. and Pouclet, A, 2001. Crustal origin of Early Proterozoic syenites in the Congo Craton (Ntem Complex), South Cameroon. Lithos, 57, 23-42.

Thornton, C.P. and Tuttle, O.F., 1960. Chemistry of Igneous rocks. I. Differentiation index – Amer. J. Sci, 258, 664-684.

Upadhyay, D., Raith, M.M., Mezger, K. and Hammer Schmidt, K., 2006. Meso proterozoic rift-related alkaline magmatism at Elchuru, Prakasam alkaline province, SE India. Lithos, 86, 447-477.

Upadhyay, D., 2008. Alkaline magmatism along the southeastern margin of the Indian shield: Implications for regional geodynamics and constraints on craton–Eastern Ghats belt suturing. Precambrian Res, 162, 59-69.

Upton, B.G.J., Emeleus, C.H., Heaman, L.M., Goodenough K.M. and Finch A.A., 2003. Magmatism of the mid-Proterozoic Gardar Province, South Greenland: chronology, petrogenesis and geological setting. Lithos, 68, 43-65.

Vijaya Kumar, K., Ernst, W.G., Leelanandam, C., Wooden, J.L. and Grove, M.J., 2011. Origin of ~2.5 Ga potassic granite from the Nellore schist belt, SE India: textural, cathodoluminescence, and SHRIMP U-Pb data. Contrib. Mineral. Petrol, 162, 867-888.

Vijaya Kumar, K., Frost, C.D., Frost, R.B. and Chamberlin, R., 2007. The Chimakurthi, Errakonda and Uppalapadu plutons, Eastern Ghats belt, India: an unusual association of tholeiitic and alkaline magmatism. Lithos, 97, 30-57.

Vijaya Kumar, K., Rathna, K. and Leelanandam, C., 2015. Proterozoic subduction-related and continental rift-zone mafic magmas from the Eastern Ghats Belt, SE India: geochemical characteristics and mantle sources. Curr. Sci, 108(2), 184-197.

Wood, D.A., Jordon, J.L. and Treuil, M., 1979. A reappraisal of the use of trace elements to classify anddiscriminate between magma series erupted in different tectonic settings. Earth Planet. Sci. Lett, 45, 326-336.

Received on: 24.3.18; Revised on: 2.6.18; Accepted on: 6.7.18

J. Ind. Geophys. Union (September 2018)
v.22, no.5, pp: 518-523

Eigen Double Derivative Technique to further improve the seismic image generated by conventional data processing

R. Thandan Babu Naik[1]*, Uma Vadapalli[1], Kalachand Sain[1] and K. Satya Prasad[2]

[1]CSIR – National Geophysical Research Institute, Uppal Road, Hyderabad 500 007, India
[2]Department of ECE, Jawaharlal Technological University, Kakinada – 533001,India
*Corresponding Author: thandan@ngri.res.in

ABSTRACT

In conventionally processed seismic image, there is always a possibility of the presence of noise and scope for further improvement. Dealing and suppressing the residual noise, after application of several kinds of filters in conventional data processing, is challenging. Improving seismic image by reducing such noise, strengthens further analysis and interpretations. The Eigen Double Derivative Technique (EDDT) enhances the image by restoring the seismic amplitudes of conventionally processed seismic section, with average of neighbourhood data amplitudes in the low contrast direction. The low contrast orientation is indicated by Eigenvectors of double derivative image. Estimation of derivative images intoduces checkeredboard artefact, which is avoided by up-sampling of seismic amplitudes. In the present study, the efficiency of EDDT for improving seismic image is evaluated, by measuring contrast to noise ratio (CNR). Application of EDDT on seismic section of 3D seismic data from Balol oil field, Cambay basin, India has resulted into improvement of its CNR by 16%. Thus, the EDDT can be used to further improve the conventionally generated seismic image, by reducing inherent residual noise and improving contrast.

Keywords: Seismic image enhancement, Eigen values and vectors, Double derivative image, Up-sampling, Contrast to noise ratio.

INTRODUCTION

An image consists of numerous features. The visualisation of such features, plays an important role in their analysis and interpretation. In that sense, the seismic image can be considered a record of seismic waves, reflected from subsurface geological interfaces underneath. An energy source (dynamite or vibrator) generates a seismic wave, which travel through the subsurface and returns to the receivers on the surface. The receiver converts the variations in the earth's motion to an electrical signal, which is digitally recorded. The recorded seismic waves are then assigned source and receiver coordinates to form a seismic record (Zhou, 2014), which becomes an integral part of various geophysical studies. The recorded seismic data contains several types of noise due to anthropogenic activity at acquisition site, experimental errors (Bahavar et al. 2002) and complex subsurface geological conditions. Several efficient processing techniques (Yilmaz, 2001) exist to improve the signal to noise ratio. The conventional processing attenuates several types of noise, viz. ground roll, airwaves, multiples etc., mostly by using frequency domain filters. Frequency domain filters introduces artefacts, if their parameters are not set properly. A frequently used median filter improves the image quality, however contributes to blurring, thereby limiting interpretation capabilities (Guo et al. 2010). The histogram equalisation to improve the image converts image histogram into a uniform distribution by manipulating seismic amplitudes. It does improve the contrast, however few details invariably disappears (Liu et al. 2010). Similarly, conventional processing improves the signal to noise ratio (SNR) of the traces, but there is always a possibility of residual noise presence and scope to improve it. Any level of seismic image improvement adds strength in successive analysis and interpretation. Such noise suppression in an image results in improved contrast to noise ratio (CNR) and represents the image in a more visibly palatable way by bringing out more visual content which is otherwise not visible for perception and interpretation (Kumar et al. 2009). In medical science, the computed tomography (CT) scan images are improved using double derivative techniques to efficiently monitor dental implants in human (Mendrik et al. 2009). Derivatives do optimise the quality of CT images (Karla et al. 2004) by decreasing noise while maintaining the image contrast.

Present Eigenimage double derivative technique (EDDT), suppresses the noise in low contrast direction by manipulating the seismic amplitudes to improve image visibility. The Eigenvectors computed on double derivative image is used to identify the low contrast direction. In this study, EDDT has been applied on conventionally processed and post-stack migrated seismic section along an inline of seismic data from Balol oil field, Cambay basin, India.

METHODOLOGY

Eigen double derivative technique (EDDT) involves computations of Eigen-values and Eigen-vectors of double

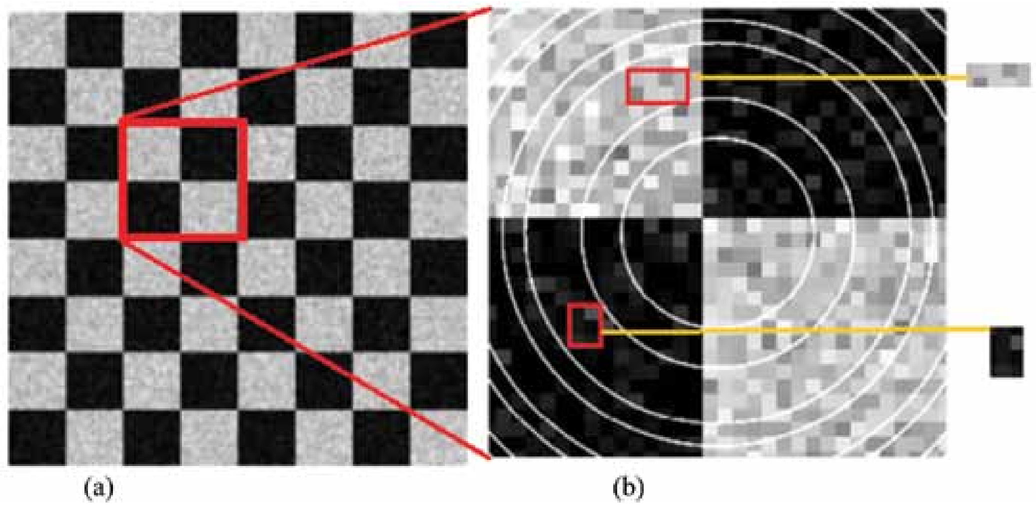

Figure 1. Noisy chess board enhancement through derivatives with resulted checkerboard artefact.

derivative image, to identify data amplitudes corresponding to lower contrast. The data amplitudes corresponding to low contrast in the conventionally processed input image are replaced by average of neighbouring amplitudes. The derivative of an image is computed both in horizontal (X-direction) and vertical (Y-direction) using data amplitudes. The derivative in the x-direction at data point P1 is estimated by computing the difference between Po and P2, which are the data values to the left and right of P1 and similar procedure is adopted in vertical direction also. The image, thus formed, is called first-order derivative image. Repetition of same computational process on the first order derivative image, produces a double derivative image. Image noise results in data amplitudes that look very different from their neighbours. The larger the noise, the more difference among neighbour data amplitudes. Computation of image derivative is nothing but application of difference filters, which smoothens the image and suppresses the noise.

In EDDT, input image is convolved with Gaussian function $G(x,y) = \frac{1}{2\pi\sigma^2} e^{\frac{-(x^2+y^2)}{2\sigma^2}}$, where x, y represents the position of seismic data points. This procedure acts as low pass Gaussian filtering. The width of Gaussian filter is adjusted with variance parameter. Increased variance parameter involves more data amplitudes in the computations and more effectively suppresses the noise. The Gaussian function is nonzero everywhere, but approaches to zero at about three standard deviations from the mean. Thus, the width of Gaussian filter is optimized to 3σ, accounting to about 99.7% of Gaussian curve. Derivative based noise removal techniques, always contribute to checkerboard artefact, which deteriorates image quality at the micro visual level. The standard procedure to avoid checkerboard artefact is up-sampling data amplitudes before the computation of image derivatives. The derivative scheme applied on noisy chess board image, without up-sampling, has resulted in checkerboard artefact as illustrated in Figure 1 (Shapiro and Stockman, 2000).

Checkerboard artefact is a break in picture elements leading to poor visible quality, especially in frequent zooming applications, such as seismic images. Up-sampling is done before calculating derivative images to avoid checker board artefact. In EDDT, the seismic data amplitudes are up-sampled at a rate of ↑10 and ↑4, i.e., after every ten data amplitudes, average of preceding ten seismic data amplitudes is inserted and after every four seismic data amplitudes, average of preceding four data values is inserted in Xand Y-direction respectively. It is a trial and error procedure, however the rate of up-sampling is decided based on computational overload and required visible quality.

DERIVATIVE SCHEME FOR SEISMIC IMAGE IMPROVEMENT

The EDDT is applied on digital seismic section from Balol oil field, Cambay basin, India and reproduced in Figure 2. The double derivative image uniformly distributes seismic amplitudes concentration as a function of virtual time (τ). The successive smoothing of the seismic image at different virtual times is calculated by using following mathematical expressions.

$$\frac{\partial I}{\partial \tau} = \nabla.(D.\nabla I) \quad \text{-- (1)}$$

Where I- represent seismic amplitude, Divergence Operator ∇I – seismic image gradient, D – square matrix known as diffusion tensor, and $\frac{\partial I}{\partial \tau}$ - is rate of change in seismic amplitude with virtual time (τ).

The diffusion matrix, which gives local orientation of data values is computed using structure tensor *J*:

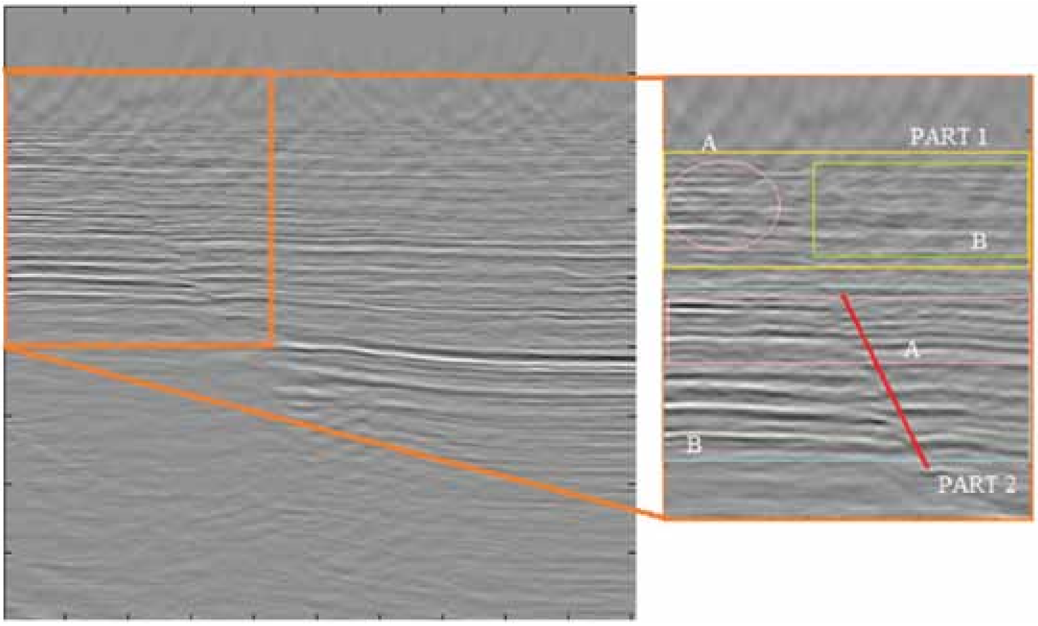

Figure 2. Conventionally processed seismic section along an inline of 3D seismic data from Balol oil field, Cambay basin, India (Data Source: ONGC India).

$$J(\nabla I) = \nabla I . \nabla I^T = \begin{bmatrix} I_x^2 & I_x I_y \\ I_x I_y & I_y^2 \end{bmatrix} \quad \text{- - (2)}$$

Where $I_x = \frac{\partial I}{\partial x}$, $I_y = \frac{\partial I}{\partial y}$ – first order derivative images in x and y directions respectively

$I_x^2 = \frac{\partial^2 I}{\partial x^2}$, $I_y^2 = \frac{\partial^2 I}{\partial y^2}$ – second order derivative images in x and y direction respectively

$I_{xy} = \frac{\partial^2 I}{\partial x \partial y}$ – Second order derivative image in xy direction

The diffusion matrix is redefined in terms of Eigen-values and Eigen-vectors of double derivative image as

$$J(\nabla I) = [V_1 V_2] . \begin{bmatrix} \mu_1 & 0 \\ 0 & \mu_2 \end{bmatrix} . [V_1 V_2]^T \quad \text{- - (3)}$$

Where, V_1, V_2 – Orthogonal Eigenvectors corresponding to Eigen values - μ_1, μ_2.

Eigen-values indicate average contrast and corresponding Eigen-vector points towards low contrast.

The EDDT comprises following computational steps,

I. The input seismic image is convolved with Gaussian function for minimal noise removal.
II. The seismic data amplitudes are up-sampled.
III. The first order derivative image is calculated using central difference at each input image data points and similarly using first derivative double derivative image is calculated.
IV. Eigenvalues and orthogonal Eigenvectors are estimated on each data matrix of sizes 5x5, 7×7 and 9×9. The data matrix is shifted towards low contrast as indicated by Eigen-vectors.
V. In low contrast direction,the data amplitudes of input seismic image are replaced with average of neighbourhood data matrices. This procedure is repeated on entireinput image.
VI. Compute Contrast to Noise Ratio (CNR) of the seismic image generated by EDDT.
VII. Stop the computational process, if estimated CNR of the output seismic image is less than 0.05% of previous two successive estimations,without distorting the visible quality.
VIII. If the condition in step IV is not satisfied repeat the steps IV to VII with set increased data matrix sizes.

The flow chart for application of EDDT is illustrated in Figure 3.

IMAGE ENHANCEMENT METRICS

The qualitative and quantitative assessment is performed to check improvement in the output seismic image. Qualitative evaluation is looking for visual quality improvement of the seismic image generated by EDDT, against the seismic image generated by conventional data processing. Quantitative evaluation is carried out by estimation of performance metrics, CNR (Bechar et al., 2012). The mathematical formulations for estimation of CNR are as follows

$$CNR = \frac{\mu_I - \mu_E}{\sigma_E} \quad \text{- - (4)}$$

Where

$$\mu_I = \frac{1}{MN} \sum_{i=1}^{M} \sum_{j=1}^{N} I(i,j) \quad \text{- - (5)}$$

$$\mu_E = \frac{1}{MN} \sum_{i=1}^{M} \sum_{j=1}^{N} n(i,j) \quad \text{- - (6)}$$

$$n(i,j) = I(i,j) - E(i,j) \quad \text{- - (7)}$$

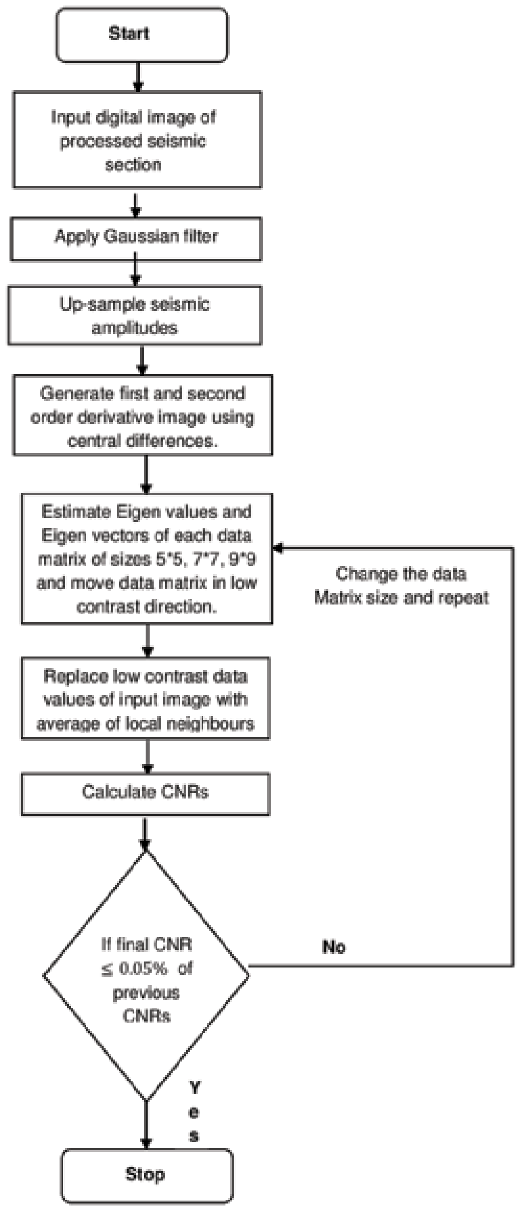

Figure 3. Flowchart of Eigen double derivative Technique.

$$\sigma_E = \sqrt{\frac{1}{MN-1}\sum_{i=1}^{M}\sum_{J=1}^{N}(n(i,j) - \mu_E)^2} \quad \text{-- (8)}$$

$I(i,j)$ - seismic image generated by conventional data processing, $E(i,j)$ - seismic image generated by Eigen double derivative technique and $n(i,j)$ – residual of seismic image is estimated by calculating difference image between images by conventional processing and Eigen double derivative technique.

RESULTS AND DISCUSSIONS

The seismic image enhanced by the application of EDDT is shown in Figure 4, whereas Figure 2 is the input seismic image generated by conventional data processing. On both the Figures, some portions of the seismic image are highlighted by rectangle and circles, to illustrate the efficiency of EDDT for image improvement. The CNR of conventionally processed seismic image and the seismic image enhanced by EDDT is tabulated in Table 1. The CNR of conventionally processed seismic image is 70.235, where as the CNR of output seismic image enhanced by EDDT is 81.335. An increase in CNR by 16% indicates that the image noise has been significantly reduced. Increase in contrast in terms of visual inspection is indicated by enhanced layer and reflector edges/boundaries, as well as smoothing of the layer and fault transition as illustrated in Figure 4.

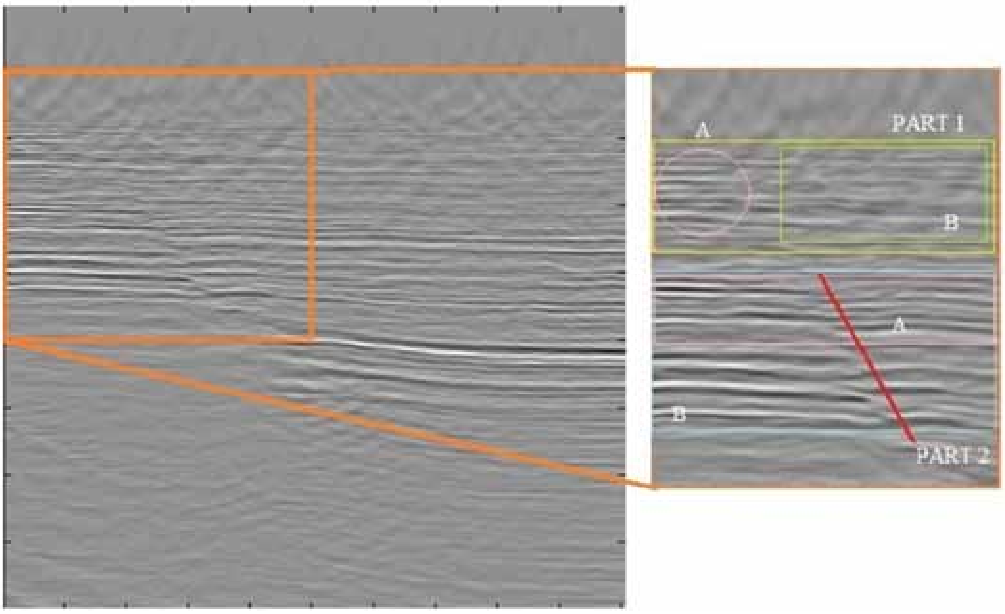

Figure 4. The seismic image enhanced by application of EDDT.

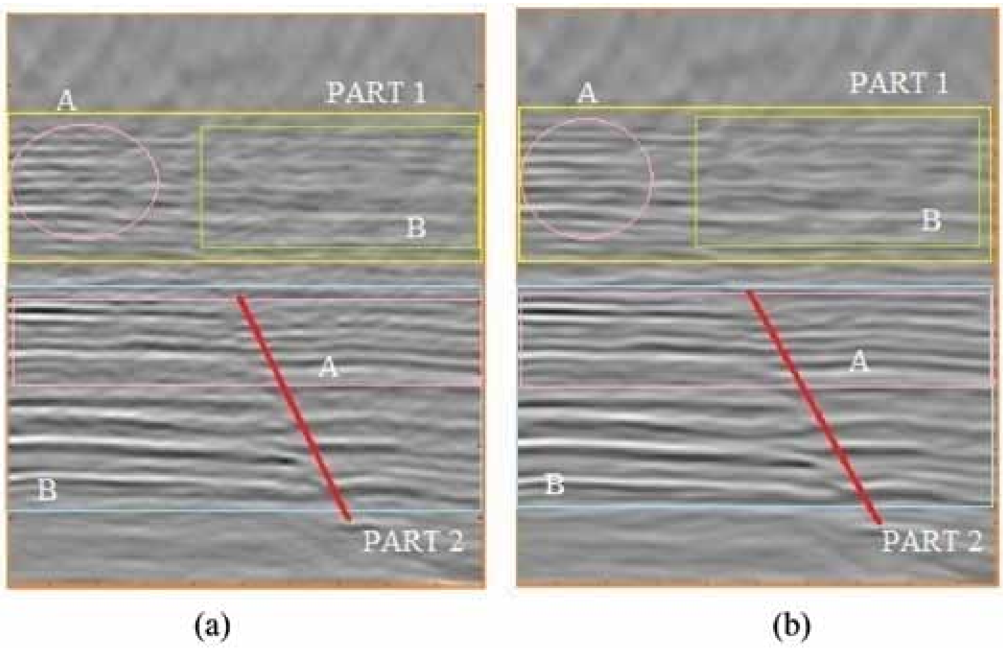

Figure 5. The zoomed version of rectangles highlighted in Figure 2 and Figure 4, (a) Balol seismic image, generated by conventional data processing and (b) The seismic image enhanced by EDDT.

Table 1. Estimated Performance metrics, contrast to noise ratio.

S.No	Description	CNR
1	Seismic Image generated by conventional data processing (Input)	70.235
2	Seismic image enhanced by Eigen double derivative technique (output)	81.335

Seismic images, as shown in Figure 5, are divided into part 1 and part 2. In part 1, both A and B of Figure 5(b) shows enhanced reflector boundaries/edges and smoothened layers. Similarly, in part 2, both A and B of Figure 5(b) shows strong reflector edges, smoothed reflectors and enhanced fault transition (redline). By very close visual inspection of subsections, the enhancement of the output seismic image (Figure 5b) is perceived due to the 16% improvement of CNR over the conventionally well processed seismic image (Figure 5a). This improvement in CNR strengthens the analysis and interpretation. The EDDT generates improved seismic image as a trade-off between CNR and observable visual quality. It appears in Figure 5(b) that fault edges are slightly disturbed, which indicates onset of marginal edge distortion, where tradeoff was made between CNR and visual quality. Even though edges appear to be disturbed, the difference in data concentration around the fault in the residual seismic image is 0.15% which is reasonable for further processing and interpretation of the seismic image. The residual image is generated by calculating the difference between the conventional input image and image produced by EDDT. However, the technique manipulates the seismic amplitudes; thus, the seismic images enhanced by EDDT may limit the application of seismic amplitude analysis techniques.

CONCLUSIONS

The analysis and application Eigen double derivative technique (EDDT) further improves the image quality by reducing the noise of the seismic image, generated by conventional seismic data processing. The use of EDDT has improved the Contrast to Noise Ratio (CNR) to ~81 from ~70, which is approximately ~ 16% image quality improvement. The technique significantly improves contrast of conventionally processed seismic image and thus has the potential to push further interpretation, as the horizons of interest will appear more prominent.

ACKNOWLEDGEMENTS

Authors are thankful to Dr. V.M. Tiwari, Director, CSIR – National Geophysical Research Institute, Hyderabad for according permission to publish this work. We thank all the members of shallow seismic Group of CSIR – NGRI, Hyderabad and ONGC-India for sharing data. Thanks are due to anonymous reviewers for improving manuscript with their comments and suggestions. Special thanks to Chief Editor for apt editing and improving readability.

Compliance with Ethical Standards

The authors declare that they have no conflict of interest and adhere to copyright norms.

REFERENCES

Bahavar, M. and North, R., 2002. Estimation of background noise for international monitoring system seismic stations. In Monitoring the Comprehensive Nuclear-Test-Ban Treaty: Data Processing and Infrasound, Birkhäuser, Basel, 911-944.

Bechar, B.C., McMahan, A., Moore, W.S., Noujeim, M., Geha, H. and F.B. Teixeira, F.B., 2012. Contrast-to-noise ratio difference in the small field of view cone beam computed tomography machines. J. Oral Sci., 54, 227– 232.

Guo, D.F., Zhu, W.H., Gao, Z.M. and Zhang, J.Q., 2000. A study of wavelet thresholding denoising. Signal Processing Proceedings WCCC-ICSP 21-25 Aug 2000, IEEE 5th International Conference, Beijing, China, 1, 329-332.

Kalra, M.K., Maher, M.M., Toth, T.L., Hamberg, L.M., Blake, M.A., Shepard, J.A. and Saini, S., 2004. Strategies for CT radiation dose optimization. Radiology, 230(3), 619-628.

Kumar, M. and Dass, S., 2009. A total variation based algorithm for pixel-level image fusion. IEEE Trans. Image Process. 18(9), 2137– 2143.

Liu, S. and Wu, G., 2010. A novel method for image enhancement based on generalized histogram. Electronics Optics and Control, 17(3), 12-4

Mendrik, A.M., Vonken, E.J., Rutten, A., Viergever, M.A. and Van Ginneken, B., 2009. Noise reduction in computed tomography scans using 3-D anisotropic hybrid diffusion with continuous switch. IEEE transactions on medical imaging, 28(10), 1585-1594.

Perona, P. and Malik, J., 1990. Scale-space and edge detection using anisotropic diffusion. IEEE Transactions on pattern analysis and machine intelligence, 12(7), 629-639.

Shapiro, L.G., and Stockman, G.C., 2000. Chapter 5, filtering and enhancing images, a textbook on computer vision. Prentice Hall, pp.1-608.

Yilmaz, Ö, 2001. Text book on Seismic data analysis: Processing, inversion, and interpretation of seismic data. Society of exploration geophysicists, Tulsa, Oklahoma (USA), doi.org/10.1190/1.9781560801580.

Zhou, H.W., 2014, Excerpt from text book on introduction to seismic data and processing, Practical seismic data analysis, Cambridge University Press, DOI 978- 0-521-19910-0.

Received on: 9.5.18; Revised on: 20.7.18; Accepted on: 26.7.18

J. Ind. Geophys. Union (September 2018)
v.22, no.5, pp: 524-533

Spatial and temporal variability of atmospheric surface albedo over the central north region of India for the period of 2004-2016

Adarsh Kumar[1], N. Jeni Victor[2], T. Dharmaraj[2*], G.R. Chinthalu[2] and Devendraa Siingh[2]

[1]Department of Physics, Amity Institute of Applied Sciences, Amity University, Noida, India
[*2]Indian Institute of Tropical Meteorology, Pune, India
*Corresponding Author: dharam@tropmet.res.in

ABSTRACT

Thirteen years (2004-2016) of solar radiation data of the surface albedo over eight stations in the central north region of India was estimated and annual, seasonal, and geographical variations were also investigated. The selected sites of the central north region of India encounter a wide range of atmospheric conditions. The average annual surface albedo varies from ~ 0.144 to 0.34, and show high synoptic variability between different places and even at individual sites. The differences between the maximum and minimum surface albedo range from 0.02 to 0.44. The lowest mean was occurred in Nainital (~0.152) whereas, highest was recorded in Jaipur (~0.236). In examining the variations of the estimated albedo values with the altitude, sites were divided into three groups: low (<500 m), middle (500-1000 m), and high altitude (mountain sites) (> 1000 m); the mean albedo values for each category are ~ 0.198, ~ 0.167, and ~ 0.177 respectively. In studying the effects of latitude on albedo values, the sites were also further divided into three groups: low (<25 degree), middle (25-30 degree), and high latitudes (>30 degree), for which the mean monthly albedo values are 0.168, 0.222, and 0.183, respectively.

Key words: Surface and solar albedo, aerosol, solar radiation, solar energy, vegetation.

INTRODUCTION

The radiant solar energy of the sun initiates the various processes and mechanisms of the Earth's system (Siingh et al., 2011; Ban-Weiss et al., 2015; Kumar et al., 2018). The solar radiation data has achieved great importance in the recent past years (Hocaoglu et al., 2017; He et al., 2018). In the last decade, the demand of power in India has increased manifold due to large industrial growth (Hoeve et al., 2012). Hence, it becomes significantly important to know the ground reality of large-scale solar energy based resources (Jaidevi et al., 2011). Many researchers have done extensive research on solar radiation relevant to their country in diversified areas such as computing the coefficients of the correlation connecting global solar radiation to sunshine duration, neural network approach for modeling global solar radiation, techniques for the precise estimation of hourly values of global, diffuse and direct solar radiation etc. (Kumar, 2011; Bakirici, 2017). Although a number of global and regional broadband surface albedo products have been generated from satellite observations, most of them contain albedo over land-surfaces only (Lee and Penner, 2011; Sergio et al., 2016). Scientific investigations through satellite remote sensing data provide an effective means to understand and characterize the effect of atmospheric aerosols on solar radiation temporally and globally (Pandithurai et al., 2008; Kumar, 2013; Qin, 2015). It is to be noted that satellite sensors view the entire Earth and produce global images, thus resolving the spatial patterns resulting from the spatial inhomogeneities (Pant et al., 2008). In the present paper, we have attempted to provide some useful solar radiation information to the agricultural scientists and to the designers of solar energy utilization systems, under the climatic conditions of Central North (CN) region of India, which may also serve as a useful reference for system designers and users in other regions, with similar climatic conditions. An extensive analysis were conducted previously in regard to atmospheric radiative properties through the interaction of atmospheric aerosol particles with solar radiation data, which further affects the Earth's energy balance budget (Siingh et al., 2012).

In the present work, a thorough investigations of solar radiation data on the long term (2004-2016) basis has been attempted over the eight selected most populated places of Central North region of India. The present work was focused on to study the monthly, seasonal, and annual variations of surface albedo, over various major cities in Central North India on a long-term basis of thirteen years (2004-2016). Further, the study on solar radiation was made by dividing the long term into the three different groups of four years. Latitudinal and altitude effects have also been considered on the collected solar radiation data over the eight selected sites of Central North region of India.

As far as we understand, no systematic study of surface albedo has been carried in India till now on a long term basis, specially over the central north region of India. The present work is likely to be helpful to the solar power developers in achieving their target for further growth of solar power utilization, apart from its intrinsic benefits to the agriculture sector.

Table 1. Monthly mean atmospheric surface albedo values of all the stations.

Station	Lat, °N	Long, °E	Alt, m	Jan	Feb	Mar	April	May	June	July	Aug	Sep	Oct	Nov	Dec
Delhi	28.56	77.01	233	0.197	0.193	0.185	0.189	0.194	0.2	0.194	0.187	0.188	0.19	0.192	0.2
Shimla	31.01	77.16	2202	0.24	0.265	0.234	0.204	0.188	0.191	0.189	0.187	0.185	0.181	0.186	0.2
Raipur	21.25	81.68	298	0.17	0.167	0.165	0.163	0.17	0.172	0.17	0.164	0.17	0.173	0.172	0.171
Bhopal	23.28	77.35	523	0.182	0.18	0.174	0.164	0.158	0.162	0.161	0.16	0.161	0.16	0.16	0.168
Chandigarh	30.75	76.88	347	0.192	0.188	0.173	0.174	0.163	0.174	0.184	0.189	0.193	0.188	0.186	0.196
Jaipur	26.81	75.8	390	0.243	0.243	0.242	0.242	0.243	0.241	0.227	0.216	0.216	0.223	0.235	0.24
Kanpur	26.4	80.4	127	0.208	0.203	0.194	0.208	0.22	0.223	0.212	0.198	0.195	0.198	0.203	0.211
Nainital	29.25	79.26	2084	0.153	0.15	0.147	0.148	0.149	0.153	0.155	0.156	0.155	0.148	0.148	0.152

Table 2. Annual Maximum, Minimum and Mean surface albedo values of all the stations.

Station	Maximum	Minimum	Mean	Range
Delhi	0.204	0.181	0.192	0.023
Shimla	0.341	0.178	0.201	0.163
Raipur	0.176	0.161	0.169	0.015
Bhopal	0.187	0.15	0.167	0.037
Chandigarh	0.2	0.165	0.187	0.035
Jaipur	0.247	0.211	0.236	0.036
Kanpur	0.218	0.193	0.208	0.025
Nainital	0.155	0.144	0.152	0.011

METHODOLOGY AND DATA ANALYSIS

The selected sites of central north region of India, are located between latitudes (20°-30° N, 74°-84° E) and elevation ranging between 100 - 2500 m above sea level. Albedometer is an instrument that measures global and reflected solar radiation and the solar albedo (Bakirici, 2017). The albedometer is composed of two pyranometers, the up facing one, measuring the global solar radiation, while the down facing measuring the reflected solar radiation (Pant et al., 2008). The irradiance in W/m^2 in each direction is calculated by dividing the pyranometer output, a small voltage, by the sensitivity (Jaidevi et al., 2011). The albedo is calculated by dividing the reflected short wave radiation by the global short wave radiation (Rathore et al., 2017).

The data utilized in the present study was taken from the standard atlas of solar radiation measurements data reported by the India Meteorological Department (IMD), New Delhi which is the principal government agency of India in matters relating to meteorology. Over forty five ground stations are currently being maintained by IMD in its solar radiation network (Kumar, 2013). Climatically, central north region of India lies mainly in the north temperate zone of the Earth (Qu et al., 2016). In the winter season, the lowest temperature on the plains dips to below ~3 °C, whereas during the summer, the temperature often rises as high as ~52°C in the Thar deserts of Rajasthan (Vincendon et al., 2015). The data collected for the present work include mean monthly values of global solar radiation on the horizontal surface in different seasons for the past thirteen years period of 2004 - 2016. Further, an attempt has also been made to study the impact of a location's altitude and latitude on the estimated albedo values over the central north region of India.

RESULTS AND DISCUSSION

The monthly mean clear-sky surface albedo values for the eight different stations of India, calculated using the method was described in Table 1, whereas the annual maximum, minimum, and mean along with their range values of the surface albedo are presented in Table 2.

Annual variations of surface albedo

The annual mean values were obtained by averaging the monthly values of each station. The lowest mean was occurred in Nainital (~ 0.152), while the highest was recorded in Jaipur (~0.236). Although Jaipur and Nainital

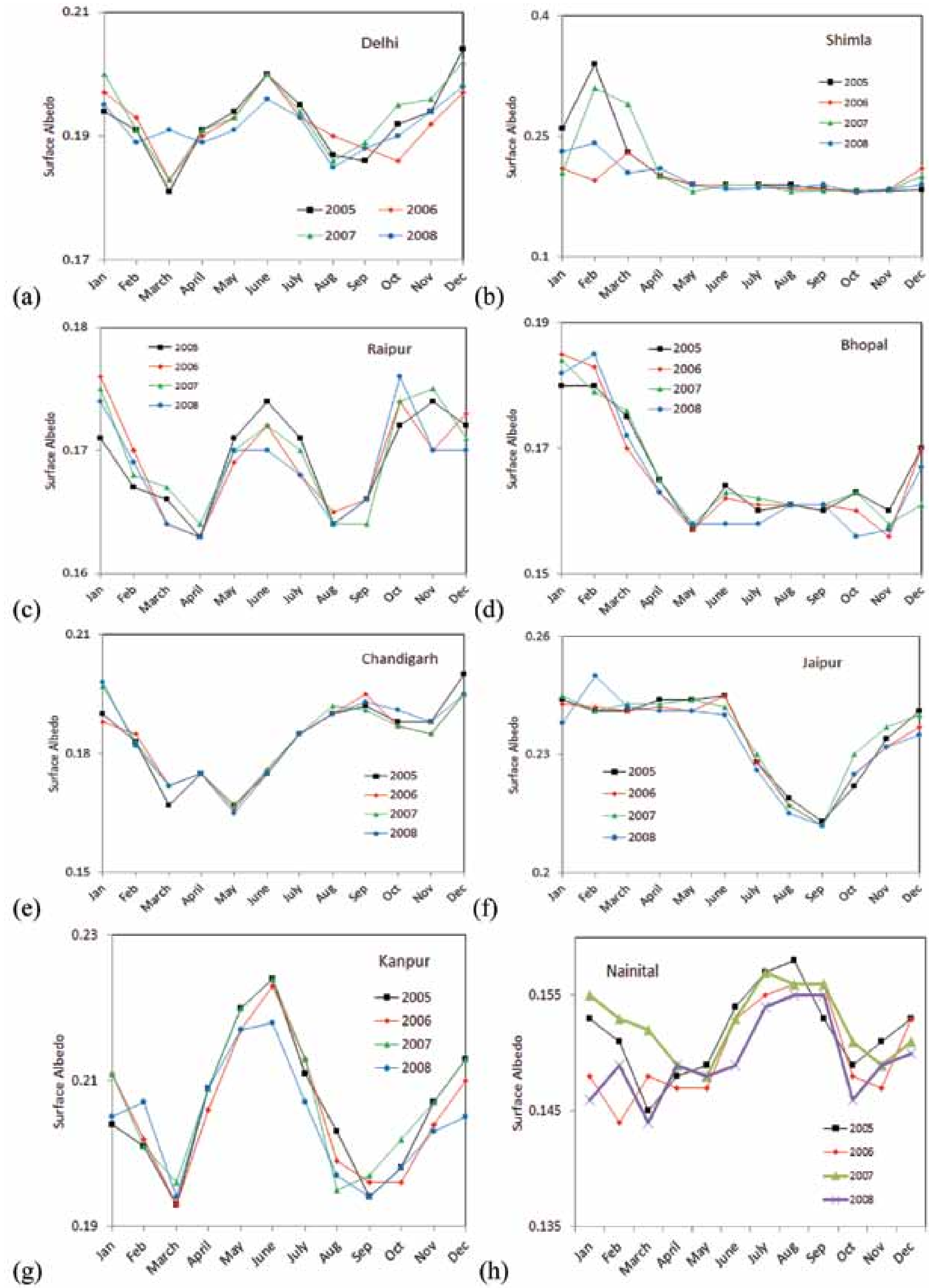

Figure 1(a-h). Monthly mean variation of atmospheric surface albedo over eight selected places of the central north region of India for the four year period of 2005-2008.

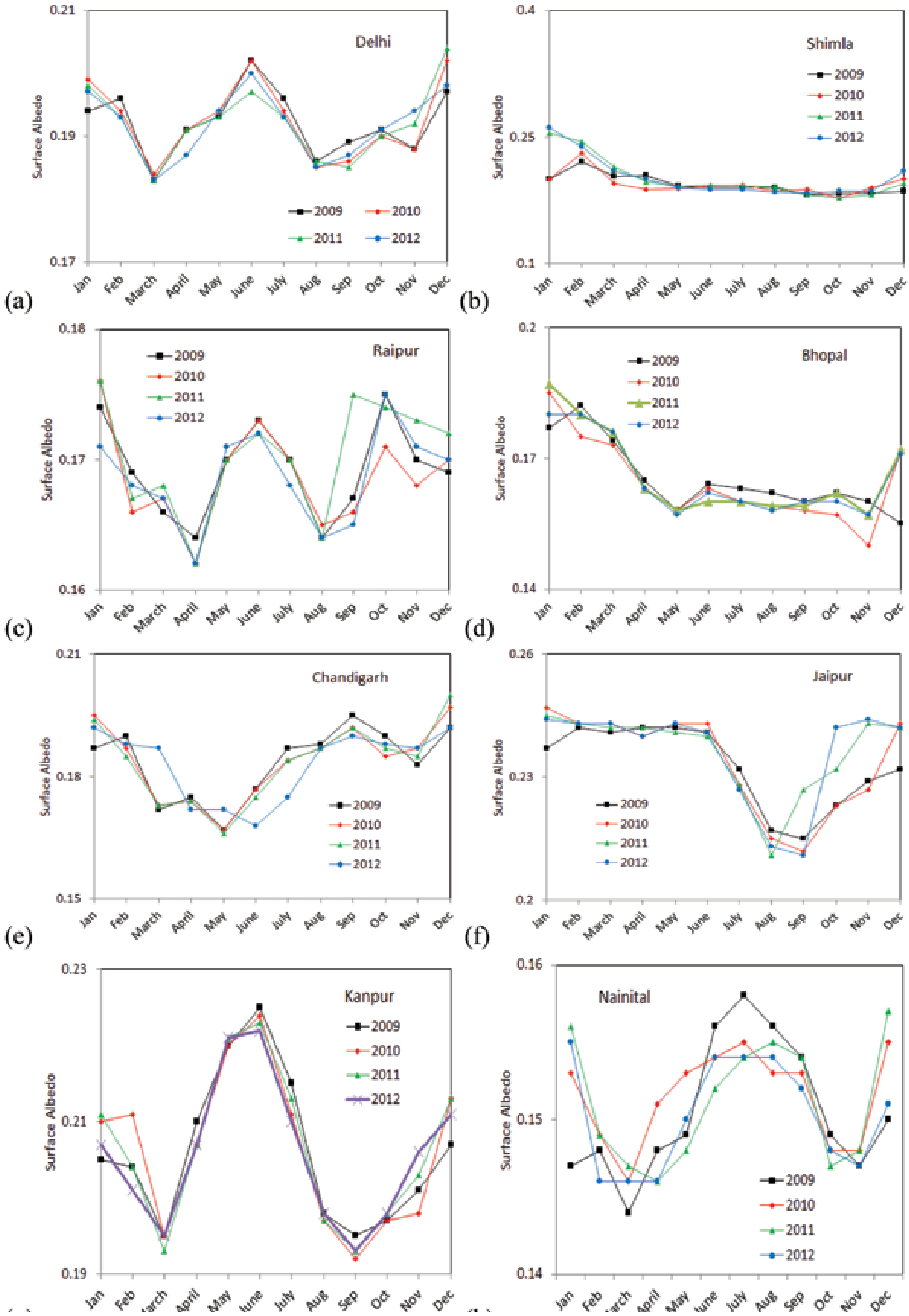

Figure 2(a-h). Monthly mean variation of atmospheric surface albedo over eight selected places of the central north region of India for the four year period of 2009-12.

are not far from the capital Delhi, yet their average albedo values differ from Delhi region by ~0.040 and ~0.042, respectively. These differences may be due to the effects of vegetation in Nainital and low altitude of Jaipur. The mean surface albedo of eight stations of central north region of India falls within the range of ~ 0.011-0.037, while three stations (Kanpur, Jaipur and Shimla) show values ~ 0.201-0.236, and the five stations (Delhi, Raipur, Bhopal, Chandigarh and Nainital) have values ranging from ~0.152 to 0.192. The overall averaged surface albedo (mean average for all stations) in central north regions of India was found to be ~0.152-0.236, which is comparable to the international albedo data values used in energy budget calculations (Bakirici, 2017).

The maximum values range from ~ 0.155 at Nainital to ~ 0.341 at Shimla, while the minimum values also range between Nainital (~ 0.144) and Jaipur (~ 0.211). However, the differences between maximum and minimum albedo values at individual sites were also found to be noteworthy. The lowest difference was 0.011 at the Nainital site, while the highest difference of 0.163 was recorded at Shimla. The average difference between the maximum and the minimum albedo values is ~0.285 for the rest of the stations. The existence of such differences between the highest and lowest albedo values at individual stations may be due to extreme changes in the weather conditions from one season to another. This includes behavior of climate change due to temperature variations and aerosol concentrations in the air (Siingh et al., 2013; Sun et al., 2015; Jahani et al., 2017). However, such broad ranges of values were also reported over Southern Great Plains previously (Yin et al., 2015). Figure (1-3) compares the annual results of different sites of central north region of India by taking years in three groups namely 2005-2008, 2009-2012, and 2013-2016. In the 2005-2008, the maximum and minimum albedo value was found over Shimla (~ 0.34) and Nainital (~ 0.144). These were attributed due to less vegetation effects over these two mountainous locations. The same trend was also found over Shimla (~0.261) and Nainital (~0.144) in 2009-12 and 2013-16 (Figures 4-6).

Seasonal variations of surface albedo

The mean monthly surface albedo values of all the central north stations in India were shown in Figure 4, whereas Figure 5 demonstrates the characteristic seasonal variations of albedo data values, with high values in winter DJF (December, January and February) and low data values in the monsoon months of JJAS (June, July, August and September). The surface albedo values decrease during March and reaches a minimum in July. In August, the albedo starts to increase again, until it reaches its highest value in February. Such a pattern was earlier investigated in the neighboring places of India (Srivastava et al., 2011; Souhail et al., 2015). However, a degree of deviation from this trend is evident at some stations (see Table 1). It was found that some stations show higher albedo values in the month of July than in May. In response to this observed trend, we divided the surface albedo data values into four seasonal groups: DJF (December, January, and February) winter, MAM (March, April, and May) summer, JJAS (June, July, August and September) Monsoon, ON (October and November) Post Monsoon. The average surface albedo values for winter, summer, monsoon and post monsoon were found to be ~ 0.30, 0.25, 0.31, and 0.36, respectively. These values are consistent with the findings of seasonal variations in albedo values in Saudi Arabia (Maghrabi and Al-Mostafa, 2009) as well as global averages (He et al., 2014). An increase of 0.11 in the albedo from summer to winter is noteworthy.

Altitude and latitudinal geographical variations

We, further investigated the impact of a location's altitude and latitude on the estimated albedo values over the central north region of India. For altitude, the surface albedo data values were divided into the following three groups: low altitude, 0–500 m; middle altitude, 500–1000 m; and upper mountain sites at altitudes greater than 1000 m. The mean monthly surface albedo values for these three groups are 0.198, 0.167, and 0.177 respectively. It shows that surface albedo increases as altitude decreases (Siingh et al., 2012). It is to be mentioned here that altitude of Bhopal is 523 m, which is very close low altitude whereas Shimla and Nainital are low pollution sites as compared to sites of altitude less than 500 m, which are more polluted (Singh et al., 2010; Sinnett and Feddersen, 2016). It is to be mentioned here that out of the five sites (Delhi, Raipur, Bhopal, Chandigarh and Nainital) with altitude < 500 m, Delhi is highly polluted. Interestingly, this is opposite to the study by Lee et al., (2011) carried out on three German sites having different altitudes.

However, this trend is not uniform for all of the sites in India (Pant et al., 2008; Pandithurai et al., 2008). The latitudinal variations of surface albedo in central region of India were studied by dividing the sites into three groups: low latitudes (LL), <25° N; middle latitudes (ML), 25–30° N; and high latitudes (HL), greater than 30° N. The average monthly albedo values for these three groups were 0.168, 0.222, and 0.183, respectively. In regard to latitude, the trend is not completely uniform, as some high latitude stations show lower values of albedo than do those at lower latitudes (e.g. Nainital with albedo ~ 0.152). One may note from Figures (3-5) a low surface albedo at Chandigarh during the months of March to June, which may be due to increasing high aerosol concentrations and changing climate pattern at location like Chandigarh which is highly polluted due to industrial growth and increasing vehicular

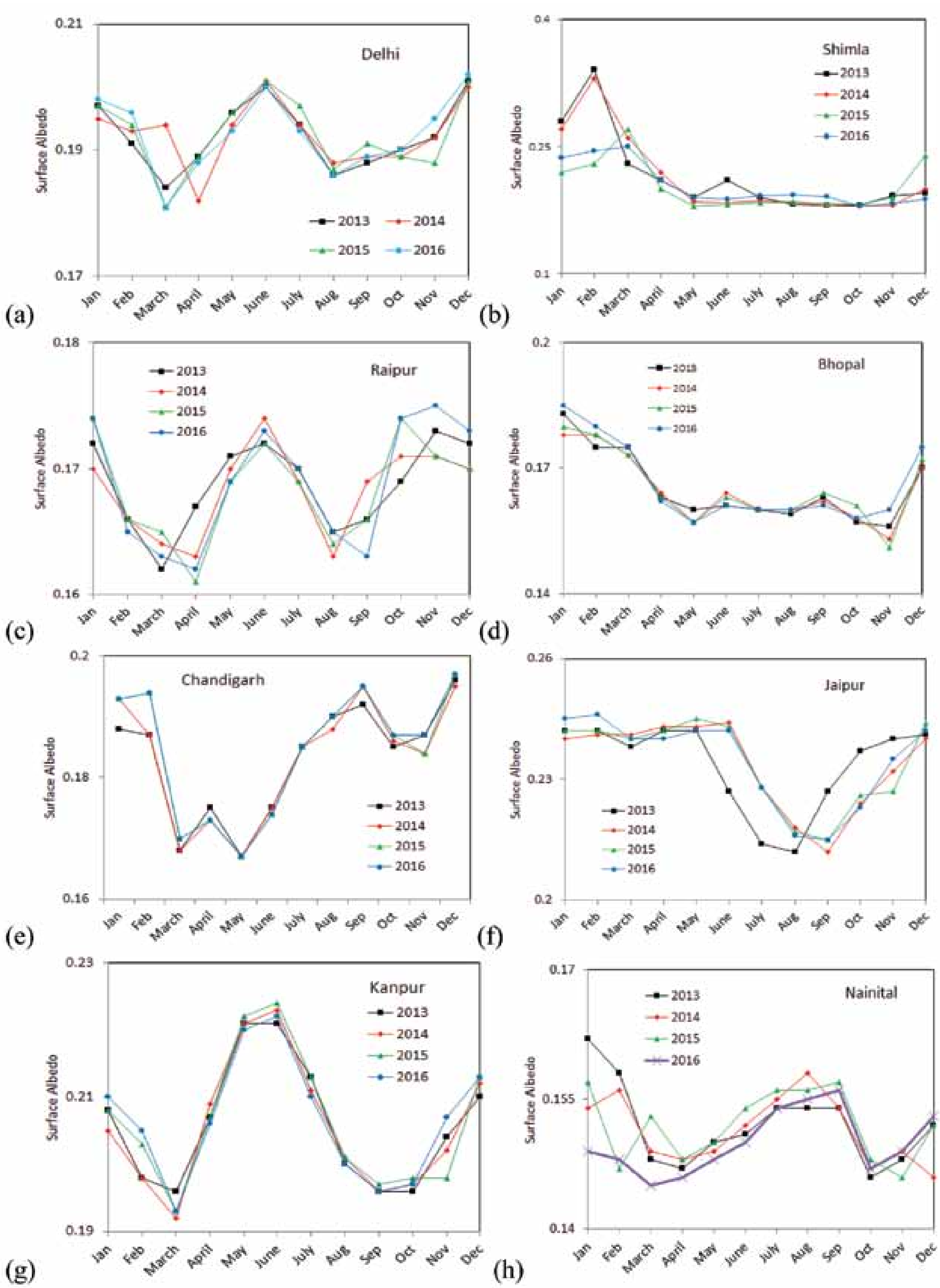

Figure 3(a-h). Monthly mean variation of atmospheric surface albedo over eight selected places of the central north region of India for the four year period 2013-16.

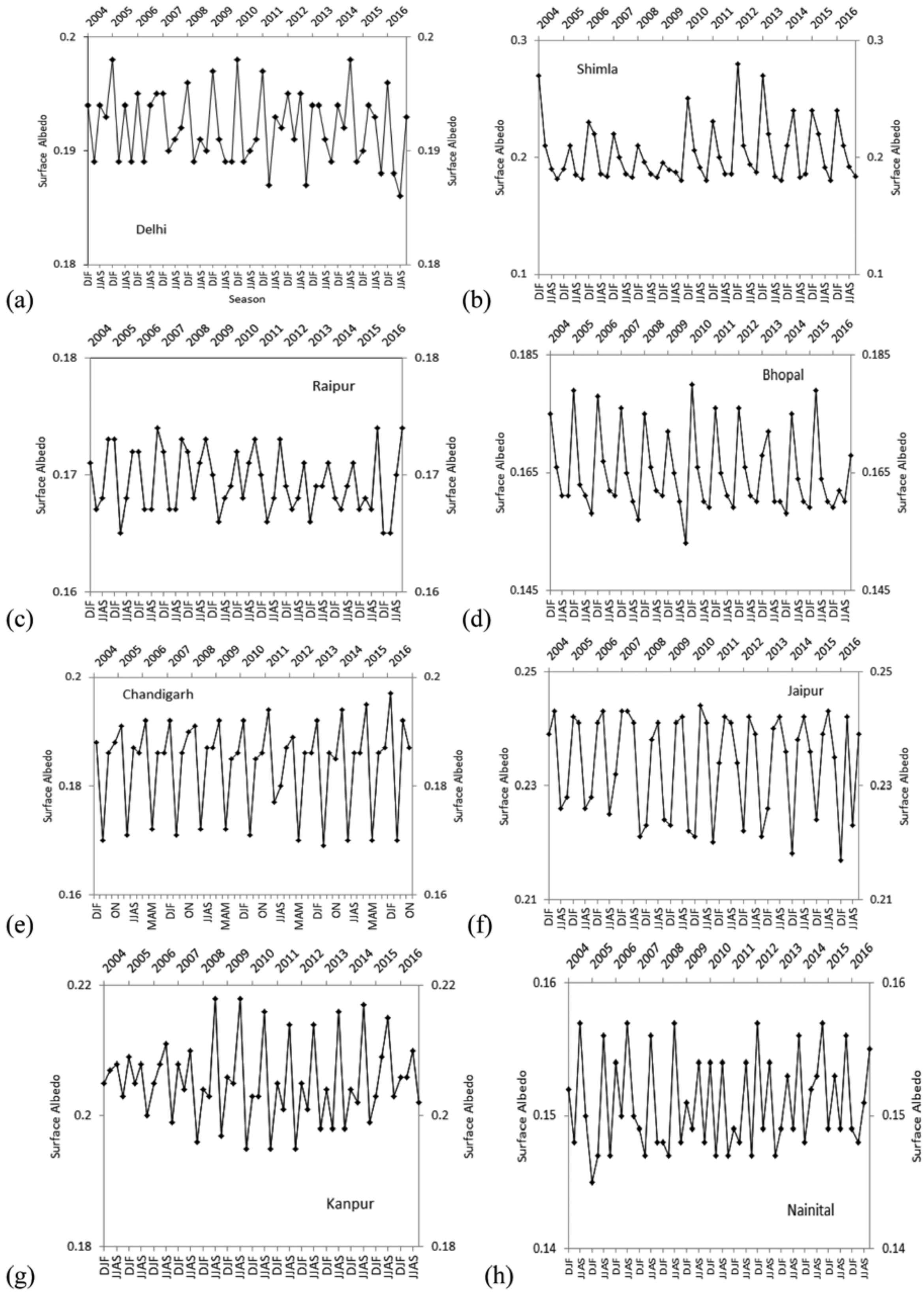

Figure 4(a-h). Seasonal and inter annual mean variation of atmospheric surface albedo over eight selected places of the central north region of India for the period 2004-2016.

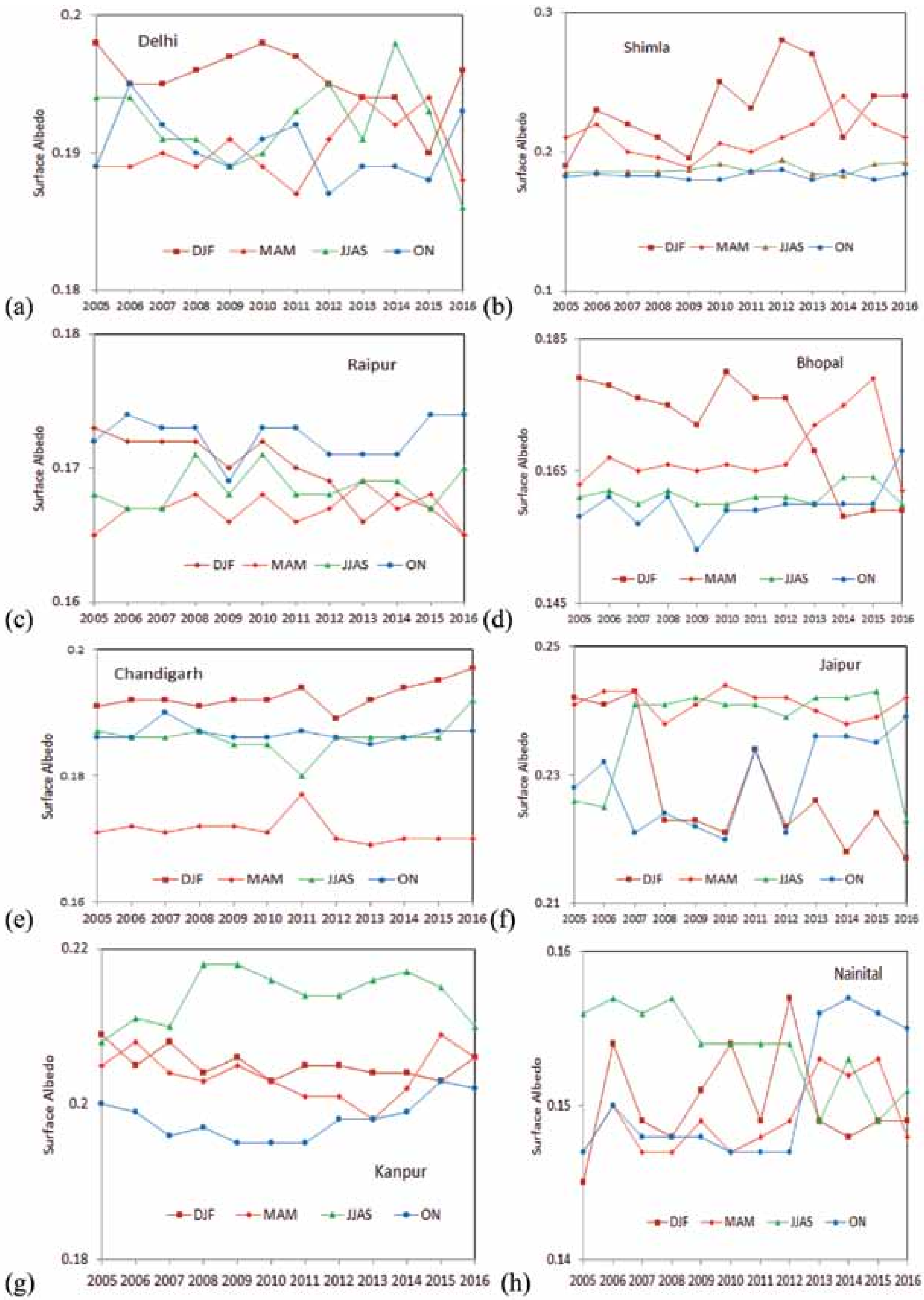

Figure 5(a-h). Mean annual variation of atmospheric surface albedo over eight selected places of the central north region of India for the period 2004-2016.

Table 3. Annual Maximum, Minimum and Mean surface albedo values of all the stations.

Station	2005-08			2009-12			2013-16		
	Maximum	Minimum	Mean	Maximum	Minimum	Mean	Maximum	Minimum	Mean
Delhi	0.204	0.181	0.192	0.204	0.183	0.193	0.201	0.181	0.193
Shimla	0.34	0.18	0.197	0.261	0.178	0.195	0.34	0.18	0.261
Raipur	0.174	0.163	0.169	0.176	0.162	0.169	0.175	0.161	0.169
Bhopal	0.185	0.156	0.167	0.187	0.15	0.164	0.178	0.151	0.166
Chandigarh	0.2	0.165	0.184	0.197	0.166	0.184	0.197	0.167	0.185
Jaipur	0.25	0.212	0.234	0.247	0.211	0.236	0.246	0.212	0.234
Kanpur	0.224	0.193	0.206	0.225	0.192	0.207	0.224	0.192	0.207
Nainital	0.158	0.144	0.15	0.158	0.144	0.15	0.162	0.145	0.152

traffic (Rathore et al., 2017), whereas at Jaipur, the surface albedo value was not found to be too low during these months, but it was comparable with other places (Tables 1-3). Since increased pollution leads to increasing particulate concentrations that clouds may contain with increasing pollution and more drops per unit volume, hence it becomes optically thicker and more reflecting (Hoeve at al., 2012).

Furthermore, some stations located at the nearly same latitude (e.g. Kanpur and Jaipur) show different albedo values. This variation in surface albedo is probably due to the differences in ground cover and altitude because Kanpur has an altitude of ~ 127m, whereas Jaipur has an altitude of ~ 390m. Further, it is to be noted that when two locations of central north regions of India have different average solar altitudes, their surface albedo values were also found to differ. Additionally, the surface albedos of two locations that have the same latitude but different sunshine conditions may likewise differ (Joerg et al., 2015).

CONCLUSIONS

Utilizing solar radiation data, the clear-sky surface albedo values at eight sites in central north region of India, were calculated and their synoptic variations investigated over a long duration of thirteen years. The major findings of the present study are given here.

The mean annual surface albedo values were found to be in the range of 0.144 to 0.34.

The surface albedo values showed high variability between different sites and even at individual sites.

Mean surface albedo over the central north region of India was found to be ~0.196 for the thirteen years period of 2004-2016.

The lowest albedo values occurred in the March month of the summer (~0.147) at Nainital, and the highest value in the February month of the winter (~ 0.265) at Shimla. Further, the surface albedo values tend to increase at higher latitudes, and decrease at higher altitudes. Such findings would be of highly advantageous to future energy balance studies and solar energy based applications.

ACKNOWLEDGEMENTS

The surface albedo data used in the present work were acquired from the India Meteorological Department, New Delhi. Adarsh kumar like to thank the IMD data distribution centers for their valuable support. Further, He would also like to thank Prof. A.L. Verma, Advisor (Science & Technology), Amity Institute of Applied Sciences (AIAS) and Amity University, Noida, Uttar Pradesh for providing necessary motivation to complete this research work. We also thank Chief Editor of JIGU for useful suggestions and appropriate editing.

Compliance with Ethical Standards

The authors declare that they have no conflict of interest and adhere to copyright norms.

REFERENCES

Bakirici, K., 2017. Prediction of global solar radiation and comparison with satellite data. J. Atmos. Solar Terr. Phys., 152–153, 41-49.

Ban-Weiss, G.A., Woods, J. and Levinson, R., 2015. Using remote sensing to quantify albedo of roofs in seven California cities, Part 1: Methods. Solar Energy. 115, 777-790.

He, T., Liang, S. and Song, D.X., 2014. Analysis of global land surface albedo climatology and spatial – temporal variation during 1981-2010 from multiple Satellite products. J. Geophys. Res., 119, 10281-10298, doi: 10.1002/2014JD021667.

He, T., Wang, D. and Qu, Y., 2018. Land Surface Albedo. Reference module in earth systems and environmental sciences. Comprehensive Remote Sensing., 5, 140-162, doi: 10.1016/B978-0-12-409548-9.10370-7.

Hocaoglu, F.O. and Fatih, S., 2017. A novel hybrid (Mycielski-Markov) model for hourly solar radiation forecasting. Renewable Energy, 108, 635-643.

Hoeve, J.E.T., Jacobson, M.Z. and Remer, L.A., 2012. Comparing results from a physical model with satellite and in situ observations to determine whether biomass burning aerosols over the Amazon brighten or burn off clouds. J. Geophys. Res., 117, D08203, 19.

Jahani, B., Dinpashoh, Y. and Nafchi, A.R., 2017. Evaluation and development of empirical models forestimating daily solar radiation, Ren. Sustain. Energy Rev., 73, 878-891.

Jaidevi, J., Tripathi, S.N., Gupta, T., Singh, B.N., Gopalakrishnan, V. and Dey, S., 2011. Observation-based 3-D view of aerosol radiative properties over Indian Continental Tropical Convergence Zone: implications to regional climate. Tellus B., 63, 971-989.

Joerg, C., Philip, Weyermann, J., Morsdorf, F., Zemp, M. and Schaepman, M., 2015. Computation of a distributed glacier surface albedo proxy using airborne laser scanning intensity data and in-situ spectro-radiometric measurements. Remote Sen. Envir., 160, 31-42.

Kumar, A., 2011. Measurement of atmospheric aerosols during monsoon period at Roorkee. Atmos. Sci. Lett., 12, 345-350.

Kumar, A., 2013. Variability of aerosol optical depth and cloud parameters over North Eastern regions of India retrieved from MODIS satellite data. J. Atmos. Solar Terr. Phys., 100-101, 34-49.

Kumar, S., Siingh, D., Singh, R.P., Singh, A.K. and Kamra, A.K., 2018. Lightning discharges, cosmic rays and climate. Sur. Geophys., https://doi.org/10.1007/s10712-018-9469-z.

Lee, S.S. and Penner, J.E., 2011. Dependence of aerosol-cloud interactions in stratocumulus clouds on liquid-water path. Atmos. Environ., 45(35), 6337-6346.

Maghrabi, A.H. and Al-Mostafa, Z.A., 2009. Estimating surface albedo over Saudi Arabia, Renewable Energy., 34, 1607-1610.

Pandithurai, G., Dipu, S., Dani, K.K., Tiwari, S., Bisht, D.S., Devara, P.C.S. and Pinker, R.T., 2008. Aerosol radiative forcing during dust events over New Delhi. J. Geophys. Res., 113: D13209.

Pant, P., Hegde, P., Dumka, U.C., Sagar R., Satheesh, S.K., Moorthy, K.K., Saha, A. and Srivastava, M.K., 2008. Aerosol characteristics at a high altitude location in central Himalayas: optical properties and radiative forcing. J. Geophys. Res., 111: D17206.

Qin, Y., 2015. Urban canyon albedo and its implication on the use of reflective cool pavements. Energy and Buildings., 96, 86-94.

Qu, Y., Liang, S., Liu, Q., Li, X., Feng, Y. and Liu, S., 2016. Estimating Arctic sea-ice shortwave albedo from MODIS data. Remote Sensing Environ., 186, 32-46.

Rathore, P.K.S., Rathore, S., Singh, R.P. and Agnihotri, S., 2017. Solar power utility sector in india: Challenges and opportunities, Ren. Sustainable Energy Rev., 81, 2703-2713.

Sergio, G., Gil, A., Guiomar, N., Costa, M.J. and Neves, N., 2016. Assessing the role of Mediterranean evergreen oaks canopy cover in land surface albedo and temperature using a remote sensing-based approach. Appl. Geography., 74, 84-94.

Siingh, D., Singh, R.P., Singh, Ashok K., Kulkarni, M.N., Gautam, A.S. and Singh, A.K., 2011. Solar activity, lightning and climate. Sur Geophys., v.32, pp: 659- 703.

Siingh, D., Chate, D. and Ali, K., 2012. Time-elapsed evolution of aerosol size distributions by snow particles after the passage of blizzards over the Maitri (Antarctica). Int. J. Remote Sensing., 33, 962-978.

Siingh, D., Pant, V. and Kamra A.K., 2013. Temperature-dependent of the positive intermediate ion concentrations at Maitri, Antarctica. J. Atmos. Solar Terr. Phys., 104, 67-74.

Singh, S., Soni, K., Bano, T., Tanwar, R.S., Nath, S. and Arya, B.C., 2010. Clear-sky direct aerosol radiative forcing variations over mega-city Delhi. Ann. Geophys., 28, 1157–1166.

Sinnett, G. and Feddersen, F., 2016. Observations and parameterizations of surfzone albedo. Meth. Oceanography., 17, 319-334.

Souhail Boussetta S., Balsamo, G., Dutra, E. and Anton, A., 2015. Clement Albergel Assimilation of surface albedo and vegetation states from satellite observations and their impact on numerical weather prediction. Remote Sens. Environ., 163, 111-126.

Srivastava, M.K., Srivastava, S.K., Saha, A., Tiwari, S., Singh, S., Dumka, U.C., Singh, B.P. and Singh, N.P., 2011. Aerosol optical properties over Delhi and Manora Peak during a rare dust event in early April 2005. Int. J. Remote Sens., 32, 7939-54.

Sun, H., Zhao, N., Zeng, X. and Yan, D., 2015. Study of solar radiation prediction and modeling of relationships between solar radiation and meteorological variables, Energy. Con. Manage., 105, 880-890.

Vincendon, M., Audouard, J., Altieri, F. and Ody, A., 2015. Mars Express measurements of surface albedo changes over 2004–2010. Icarus., 251, 145-163.

Yin, B., Min, Q. and Joseph, E., 2015. Retrievals and uncertainty analysis of aerosol single scattering albedo from MFRSR measurements. J. Quantitative Spectros. Radiative Transfer., 150, 95-106.

Received on: 2.4.18; Revised on: 26.6.18; Accepted on: 29.6.18

J. Ind. Geophys. Union (September 2018)
v.22, no.5, pp: 534-543

The negative relation between the monsoon depressions and the rainfall over Rayalaseema (Andhra Pradesh), India

P. Chandrasekhara Rao* and Archana Shinde[1]
A 44-307, Singapore Township, Pocharam, Hyderabad-500088
[1]India Meteorological Department, Pune
*Corresponding Author: pcsraoimd@gmail.com

ABSTRACT
The spatio-temporal variation of rainfall over India is largely dependent on the formation of cyclonic circulations, low pressure areas and depressions or cyclones in the Bay of Bengal and their movement along the monsoon trough. On the regional scale, the rainfall of Rayalaseema is considerably influenced by the low pressure systems that form in the Bay of Bengal. Rayalaseema receives rainfall in both the southwest and northeast monsoons. During both the seasons, the influence of the low pressure systems in the Bay of Bengal during the monsoon season, usually move in west north-westerly direction and cross the coasts of North Andhra, Orissa or West Bengal. They continue their movement inland and cause copious rainfall along their path. During this period, Telangana and coastal Andhra Pradesh also receive excess rain, but the rainfall received over Rayalaseema subdivision is found to be deficient with even 'no rain' at times. The wind pattern and the associated rainfall during the period of depressions crossing the coast and subsequent period have been analysed pertaining to a period of thirty years and the results are presented with some selected illustrations.

Keywords: Monsoon depression, Cyclonic storms, Rainfall, Rayalaseema (Andhra Pradesh), Bay of Bengal, Convergence.

INTRODUCTION

Rayalaseema is a land-locked region with an area of about 69,043 Km^2 accounting for 30% of the total geographical area of Andhra Pradesh. This region extends approximately from Latitude 12°3′N to 16°15′ N and Longitude 76°55′ E to 79°55′ E. Geographically, the Rayalaseema region forms the south and south eastern part of Deccan Plateau. It is situated almost in the centre of the southern part of the Indian peninsula. It comprises four districts namely, Anantapur, Chittoor, Kudapah and Kurnool. The climate of the region is normally dry sub-humid type and is a part of the semiarid region of the interior Deccan plateau. In Rayalaseema region, Anantapur district is the second driest part of the country next to the Jaisalmer district of Rajasthan. Rayalaseema region is characterized by hot summer from March to May. This region receives more rainfall from south-west monsoon than the northeast monsoon. The average annual rainfall is hardly 672 mm. South-west monsoon spreads from early June till the end of September, while the northeast monsoon, from October to December. Anantapur district receives second lowest rainfall in the country, next to the Thar Desert of Rajasthan. Being far away from the east coast, it does not enjoy the full benefit of north-east monsoon and is also being cut off by the high Western Ghats, which prevents south-west monsoon. October and November form the retreating monsoon season. The average rainfall of the area is 545mm.

Historically known as 'stalking ground of famines', it is estimated that drought occurs once in three years in Rayalaseema region. Among four districts in Rayalaseema, Anantapur is the driest of all districts in the region and also in the state. Rayalaseema region comes under semi-arid area which records rainfall from 375 to 700mm. The Depressions and low-pressure areas contribute significantly to the spatiotemporal variation of monsoon. The quantum of rainfall varies depending on the track of the depressions. Rayalaseema is a region, which would be away from such track. The rainfall over the subdivisions along the track, exceed the normal in many fold. However, the regions along the west coast, which are far away from the tracks, also experience excess rainfall. On the regional scale, the rainfall of Rayalaseema is considerably influenced by such systems that form in the Bay of Bengal. Rayalaseema receives rainfall in both the southwest and northeast monsoons, as mentioned earlier. During both the seasons, the influence of the low pressure systems in Bay of Bengal is clearly felt over the region. Koteswaram and George (1958) studied the causative factors of depression formation in Bay of Bengal. Similarly, Rao and Jayaraman (1958) also made a statistical study of the depressons/storms in the Bay of Bengal. The Rainfall patterns in association with Monsoon Depressions have been studied by Pishoroty and Asnani (1957), while Rao (2004) brought out the clearly deficiency of rainfall over Rayalasema in association with Monsoon Depressions.

The well-marked low pressure areas, depressions and cyclonic storms that form in the Bay of Bengal during the monsoon season, generally move in west north-westerly direction and cross the coasts of North Andhra, Orissa or West Bengal. After the land fall, they further move inland and give widespread to fairly widespread rainfall over most parts of the regions with heavy to very heavy rain, at times. During this period, northern parts of Telangana and coastal Andhra Pradesh also receive excess rain, but the rainfall received over Rayalaseema subdivision is found to be deficient or scanty. There were even some occasions when there were no reports of 'rain'.

DATA AND METHODOLOGY

Thirty years of rainfall data of Rayalaseema subdivision has been analysed to study the extent of depletion of rainfall in association with each depression. In this analysis, the rainfall of the weeks during which there is a movement of depression, right from its formation and its course of movement inland, has been taken into account. The tracks of the depressions are taken from the Cyclone Atlas of IMD. The percentage anomalies evaluated and published in the daily and weekly weather reports of IMD are also considered.

RESULTS AND DISCUSSIONS

Indian economy mostly depends on agriculture. With 65 to 70 per cent of cultivable land being rainfed, agriculture in turn, to a large extent is dependent on the monsoon rainfall. The pulsatory character of monsoon is a matter of concern to the farmer. Prior information regarding assured rainfall a few days in advance, is a vital input for the farming operations. Equally important would be the information regarding the depletion of rainfall during a particular period.

In general, it can be seen that the rainfall over the region is on the negative side during the passage of systems. Even during the cases of excess rainfall, the reason was found to be some other system and not the depression in question. This feature may be used as tool for medium range weather forecasting. Adequate steps may therefore be taken up at formative stage of depressions in the Bay itself for reorganising their agricultural activities, keeping in view the expected deficiency in rainfall.

Deep Depression over Bangaladesh and neighbourhood from 9-17 Aug 2016

A low pressure area formed over north of west Bay of Bengal and adjoining coastal areas of west Bengal in the early morning of 9th August 2016. It lay as a well-marked low pressure area over the same region, with an associated cyclonic circulation extending upto 7.6 kms a.s.l. on 9th. It concentrated as a depression over coastal areas of West Bengal and its neighbourhood. It moved north-eastwards and intensified into a deep depression over south of Bangladesh and its neighbourhood. It can be seen from the vorticity picture shown in Figure 1(a), that when there is positive vorticity over the Bay region, the Rayalaseema region shows negative vorticity. The percentage departures of rainfall over various subdivisions of India are depicted Figure 1(b) taken from Weekly Weather Report 11-17, August 2016. Also from the figure it is evident, that the Rayalseema region is largely deficient in spite of there being a deep depression in the bay.

Depression over Gangetic West Bengal and adjoining area of Jharkhand.

A cyclonic circulation lay over south Bangladesh and adjoining areas of Gangetic West Bengal and North Bay of Bengal, extending upto 7.6 kms a. s. l. on 22nd July 2017 and over Gangetic part of the West Bengal and neighbourhood tilting southwestwards with height on 23rd July2017. Under its influence, a low pressure area formed over Gangetic West Bengal and adjoining areas of Jharkhand on the same evening. It lay as a well marked low pressure area over the same region on 24th – 25th July 2017. It concentrated into a Depression over northwest Jharkhand and its neighbourhood centered near Lat. 24°N/Long. 84°E, close to Daltonganj at 0830 hrs. IST of 26th July 2017. It moved northwestwards and lay over southwest Bihar and neighbourhood centered near Lat.24.5° N / Long.83.5° E, about 80 kms northwest of Daltonganj (Jharkhand) and 170 kms east of Sidhi (east Madhya Pradesh) at 1730 hrs. IST of 26th. The Depression over northwest Jharkhand and neighbourhood moved north-westwards and continued its movement toward east Uttar Pradesh and adjoining northeast Madhya Pradesh, where it weakened into a low pressure area by 27th July 2017. The rainfall during the said week is depicted in Figure 2 which shows that over Rayalaseema, it was largely deficient.

Deep Depression over NW Bay and adjacent parts of north Orissa West Bengal coast from 17-19 June 1993.

It was first observed as a low pressure area over north Bay and neighbourhood. It was first located in north-west Bay and adjoining parts of North Orissa- West Bengal coast. It moved in north northeasterly direction and finally dissipated over Bangladesh. Figure 3a shows the low level convergence which is negative over Rayalaseema region. The rainfall over various subdivisions of India during the week ending 23rd June 1993 is illustrated in Figure 3b. It can be seen that the percentage departure over

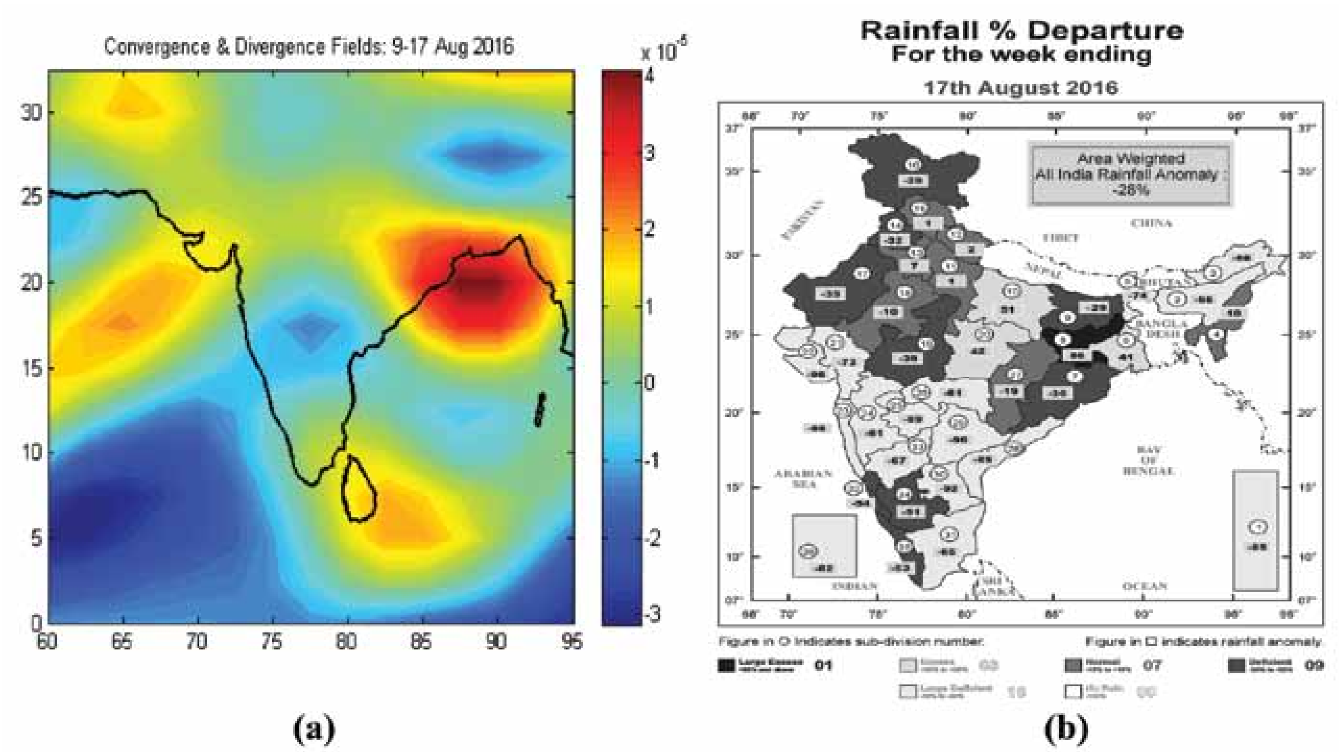

Figure 1. (a) The convergence and divergence fields seen during the Depression over Bay and the Rayalaseema region respectively. (b) The Rainfall percentage departure of Rayalaseema seen in the weekly during the week.

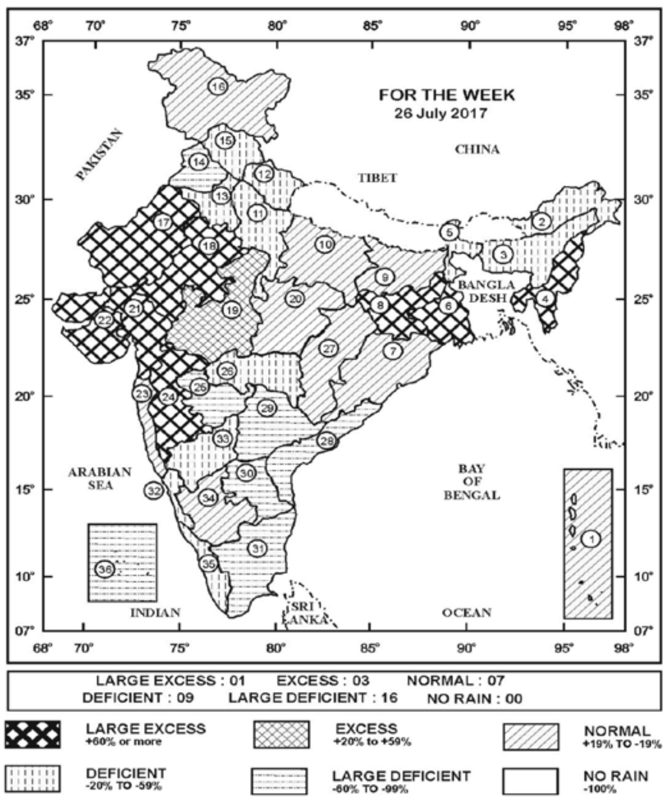

Figure 2. The Rainfall percentage departure over Rayalseema during the depression over the Bay, July 2017.

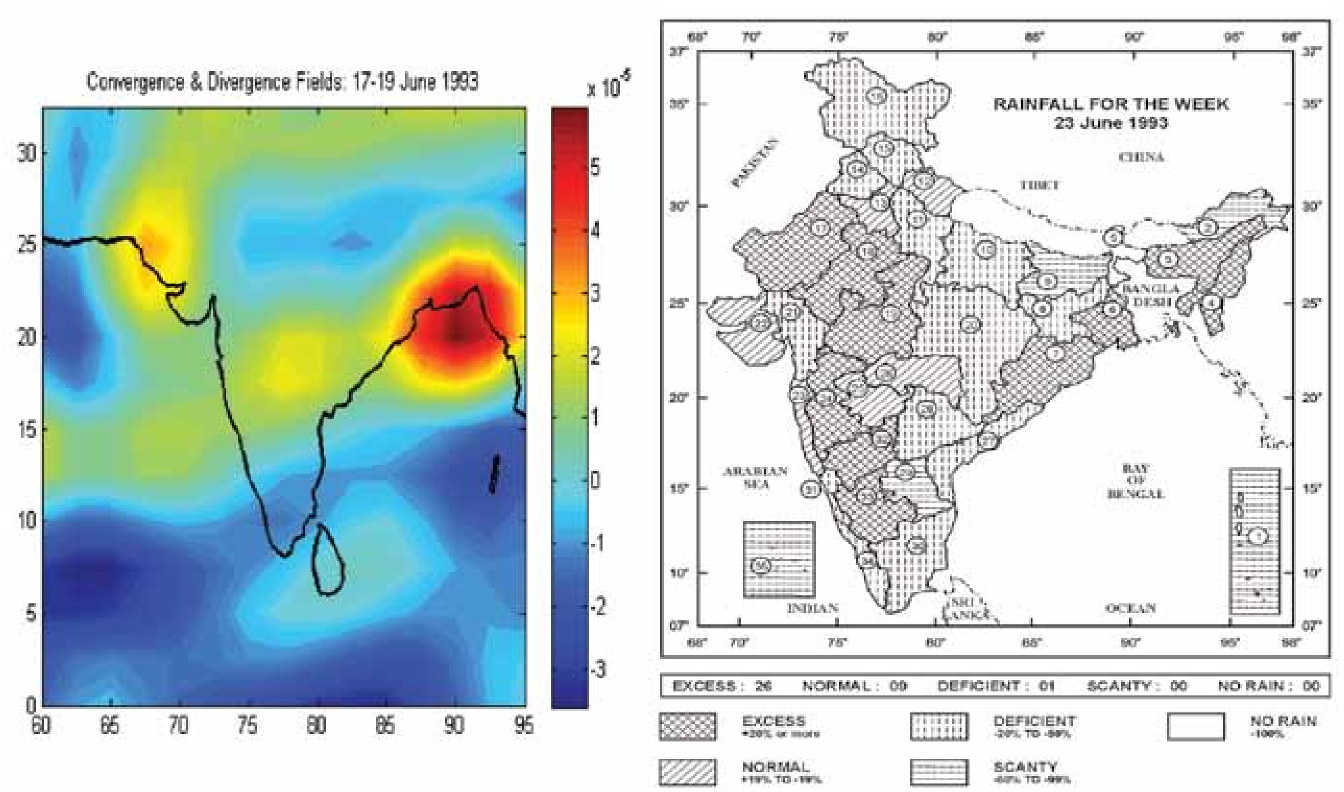

(a) (b)

Figure 3. (a) The convergence and divergence fields over the Bay of Bengal and Rayalaseema region during the depression over Bay of Bengal. (b) The rainfall percentage departure over Rayalaseema during the week.

the neighbouring region of Karnataka is positive. Though they are deficient over the other neighbouring regions of Telangana, coastal Andhra Pradesh and Tamil Nadu, the negativity was highest over Rayalaseema region. The departure was scanty that is -60 to -99 % category.

Well Marked Low Pressure area over West Bay of Bengal: week ending 6th July 2016

Under the influence of a cyclonic circulation, a low pressure area formed over west central and adjoining northwest Bay of Bengal and adjoining areas of north Andhra Pradesh-south Odisha coasts that extended up to mid tropospheric levels on 30th June. It lay over west Bay of Bengal off Odisha coast on 1st July and over North West Bay of Bengal and adjoining areas of Odisha on 2nd July. During the week, the rainfall over the region was either isolated or nil. It was not even scattered even on any one of the days of the week ending 6th July 2016. Figure 4a illustrates the rainfall departure during the week taken from Weather Report 31May-6July 2016 and Figure 4b, the convergence and divergence pattern, clearly indicating negative divergence over Rayalaseema region, while Figure 4c illustrating the mean wind analysis of lower troposphere over the Indian region. It can also be seen that over the region of Rayalaseema, a ridge type of pattern prevailed during the week which inhibited any convection and thereby leading to reduction in rainfall.

Low pressure area over west central Bay of Bengal –August 1989

A low pressure area formed over the west-central Bay of Bengal on 16th August 1989. It intensified into a depression over the west-central Bay off Andhra coast on 16th evening. It intensified into deep depression on the 17th August over west-central Bay and adjoining north-west Bay. It crossed Andhra coast near Kalingapatnam in the afternoon, rapidly weakened into a well-marked low over north coastal Andhra Pradesh in the evening of 17th August and then moved inland towards Vidarbha after weakening further. The track of the depression is shown in Figure 5(a), taken from Storm Atlas. Scanty rainfall during the week over Rayalaseema is illustrated in Figure 5(b). The rainfall percentage departure over Rayalseema during the period was -70%, taken from Weekly Weather Report 17-23, August 1989.

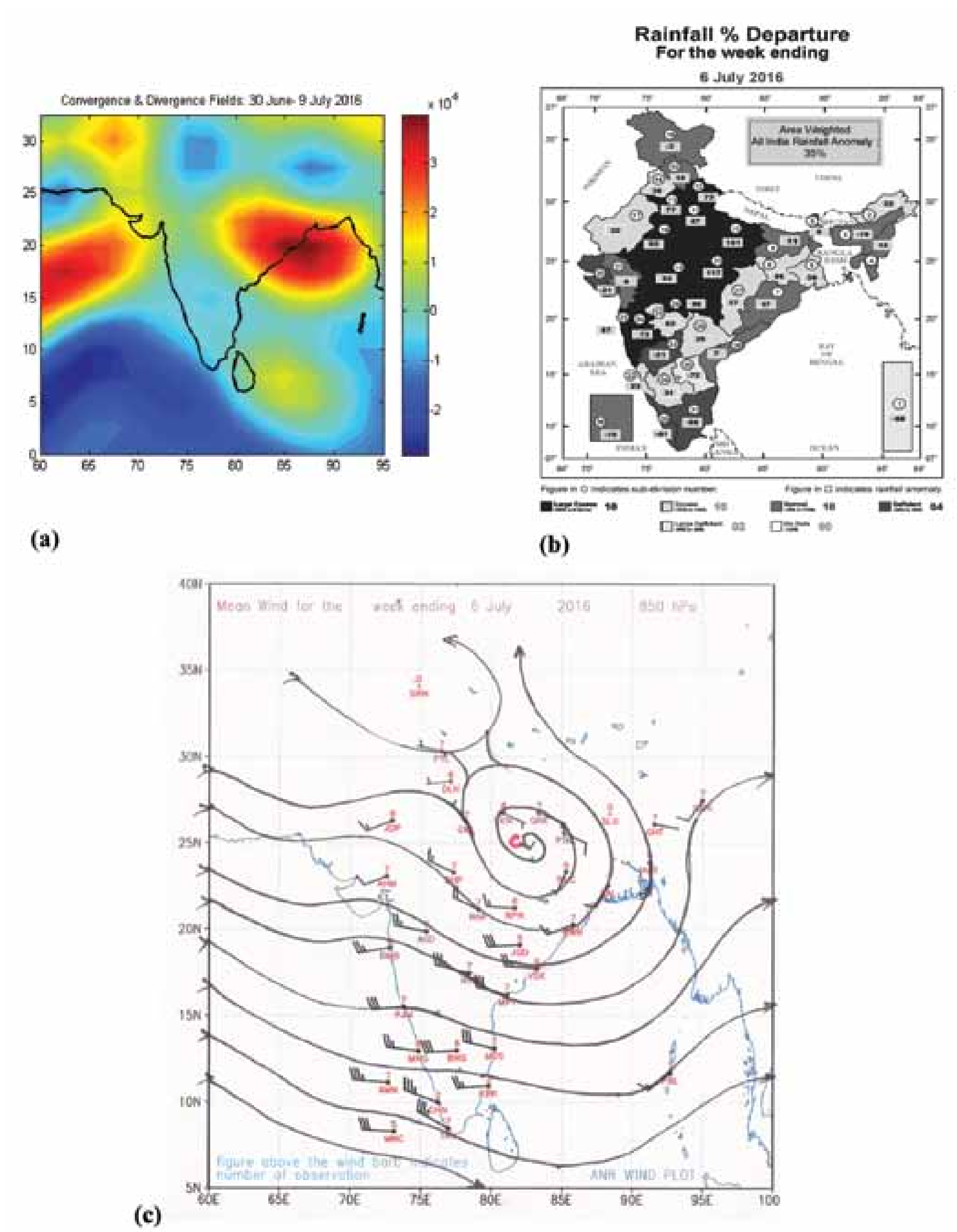

Figure 4. a) The rainfall departure over Rayalaseema during the occurrence low pressure over the Bay. b) Convergence pattern over India and neighbourhood, and c) lower tropospheric wind flow pattern, with mean winds at 850 hPa during the week.

A Low pressure area over North West Bay and adjoining Orissa coast on 21st September 1988

A cyclonic circulation extending upto 1.5 km a.s.l was observed off north coastal Andhra Pradesh and adjoining south Orissa coast in the evening of 20th September. Under its influence a low pressure area formed over North West Bay and adjoining Orissa coast on 21st September. Figure 6 shows the rainfall departures during the week. The rainfall all the neighbouring subdivisions is either excess or normal whereas it is deficient over Rayalaseema. The Rainfall Departure over Rayalseema was estimated as -28% during that period. The departures are computed from the actual rainfall amounts Indian Daily Weather Reports.

Almost all the systems generally result in a similar result. It can be seen from the above graph that if we compare the number of times when there was a system in Bay and the corresponding times when the rainfall was deficient or scanty, we see that it is more than half the number of times when a system occurred and the rainfall

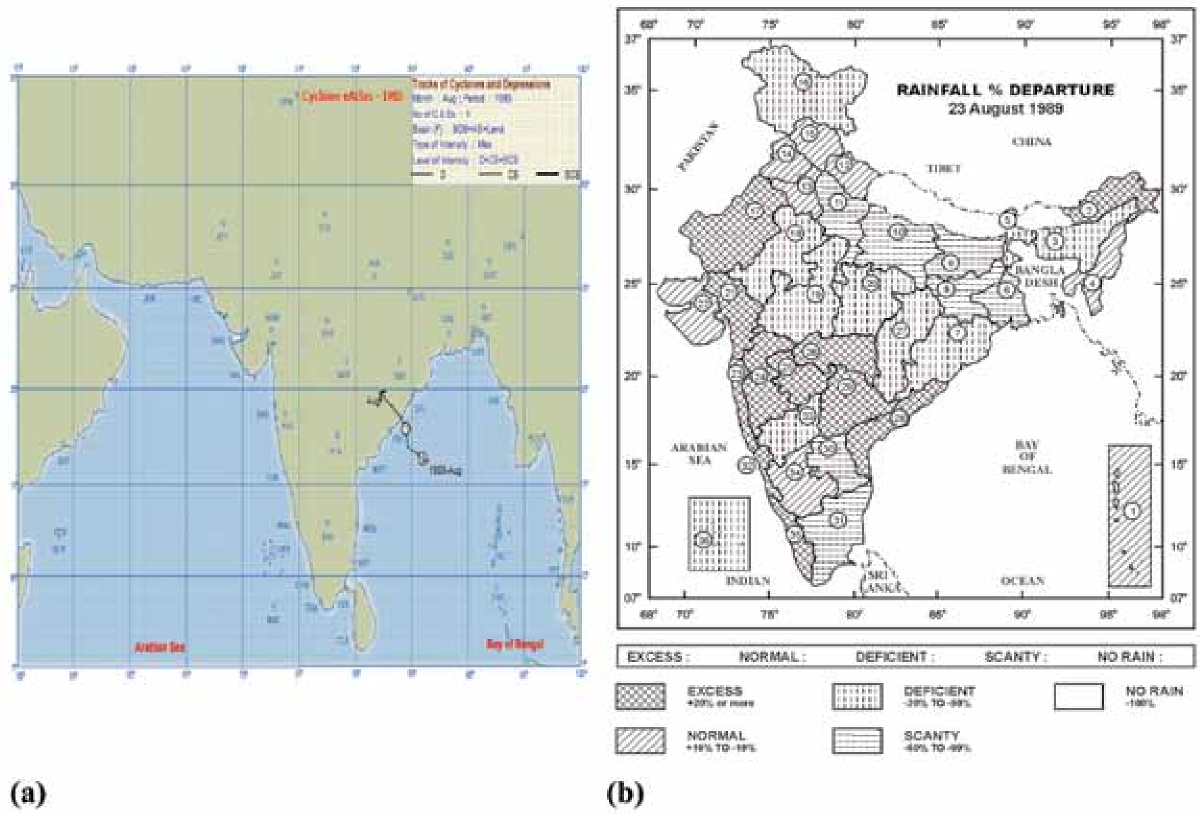

Figure 5. (a) The track of the Depression (b) The rainfall departure over Rayalaseema during the occurrence of low pressure area over the Bay and during its movement inland.

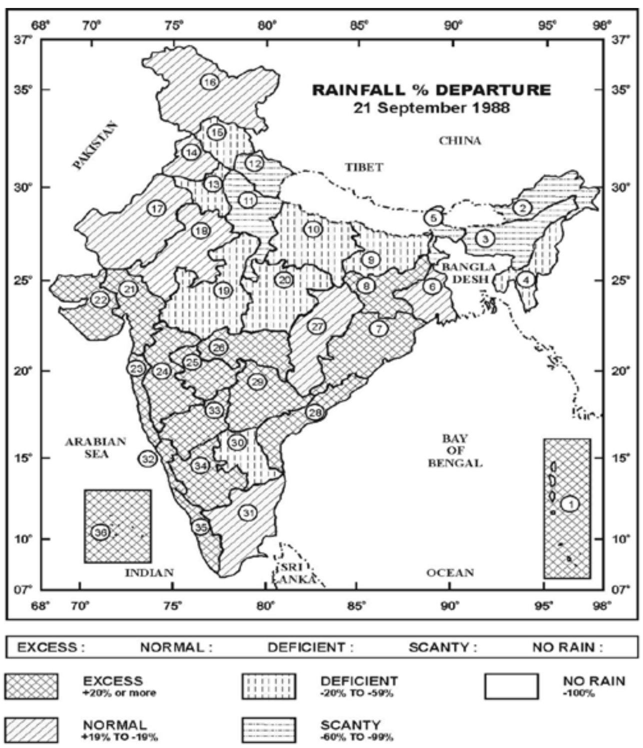

Figure 6. The rainfall departure over Rayalaseema during the occurrence of low pressure area over the Bay.

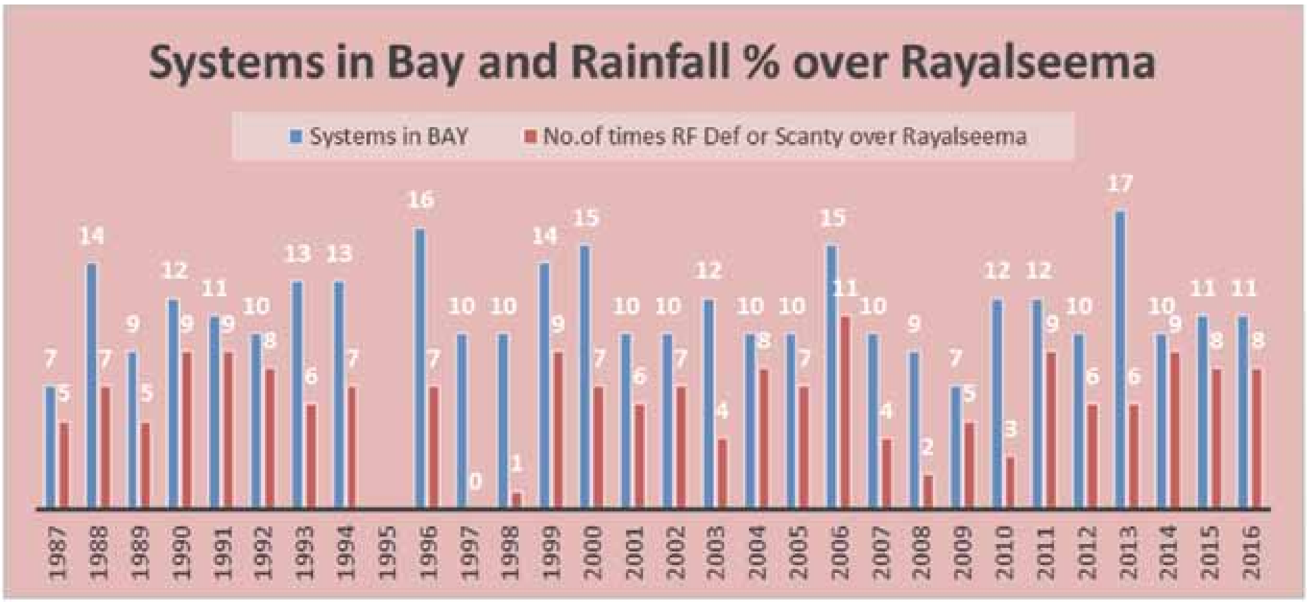

Figure 7. Systems in Bay and the corresponding rainfall percentage over Rayalseema during the systems.

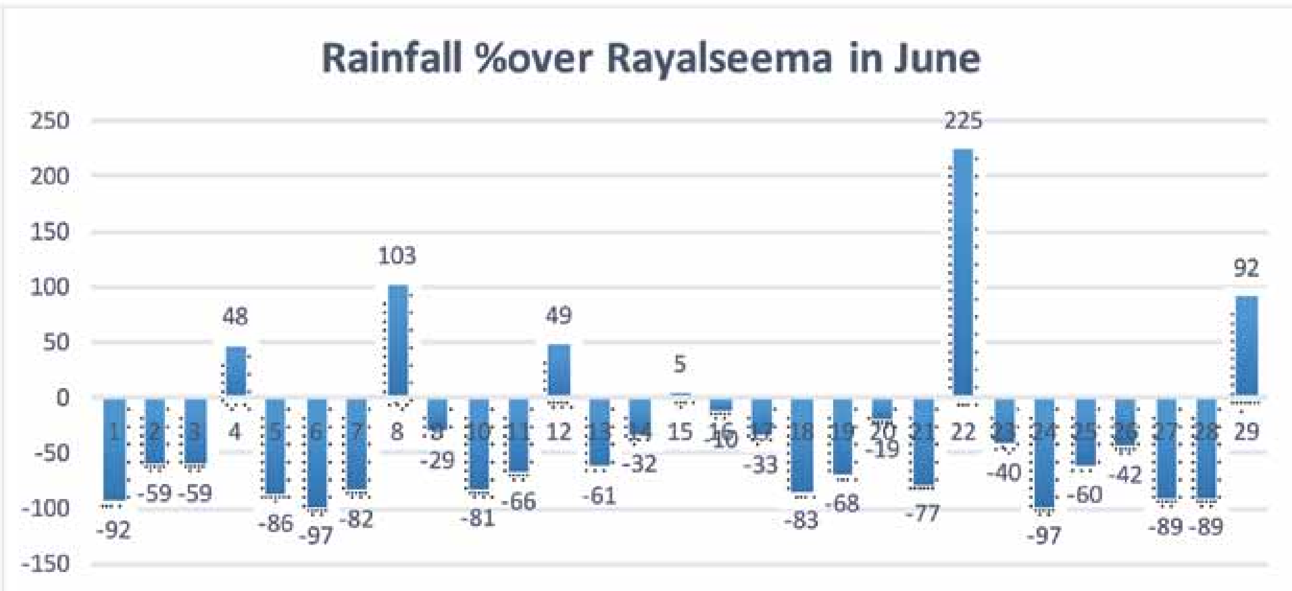

Figure 8. Rainfall percentage over Rayalaseema during the passage of systems over Bay in the month of June.

occurred over Rayalaseema region was deficient or scanty. For the entire data, the probabilities of rainfall to be negative during such a period are 83, 80, 74 and 83 during June, July, August and September respectively.

This is also evident from the latest monsoon situation of 2017. The cyclogenetic activity was more in Arabian Sea. The season witnessed two land systems. Two systems that formed over Bay of Bengal either dissipated or became less marked near the coasts of Bengal and Orissa. The total number of low pressure days had been only 39 as against the normal of 58. The number of low pressure days were 11, 12, 10 and 6 during the four months of the monsoon whereas the normal were 11, 14, 17 and 16 respectively. Thus, the movement of low pressure systems across the south-central India appears to result in negative rainfall over the Rayalaseema region. Figure 7 illustrates the number of systems formed in the Bay during the period of study and the corresponding number of deficient or scanty periods of rainfall.

Figures 8 to 11 show the percentage departures of rainfall over the Rayalaseema region during the months of June, July, August and September respectively. These

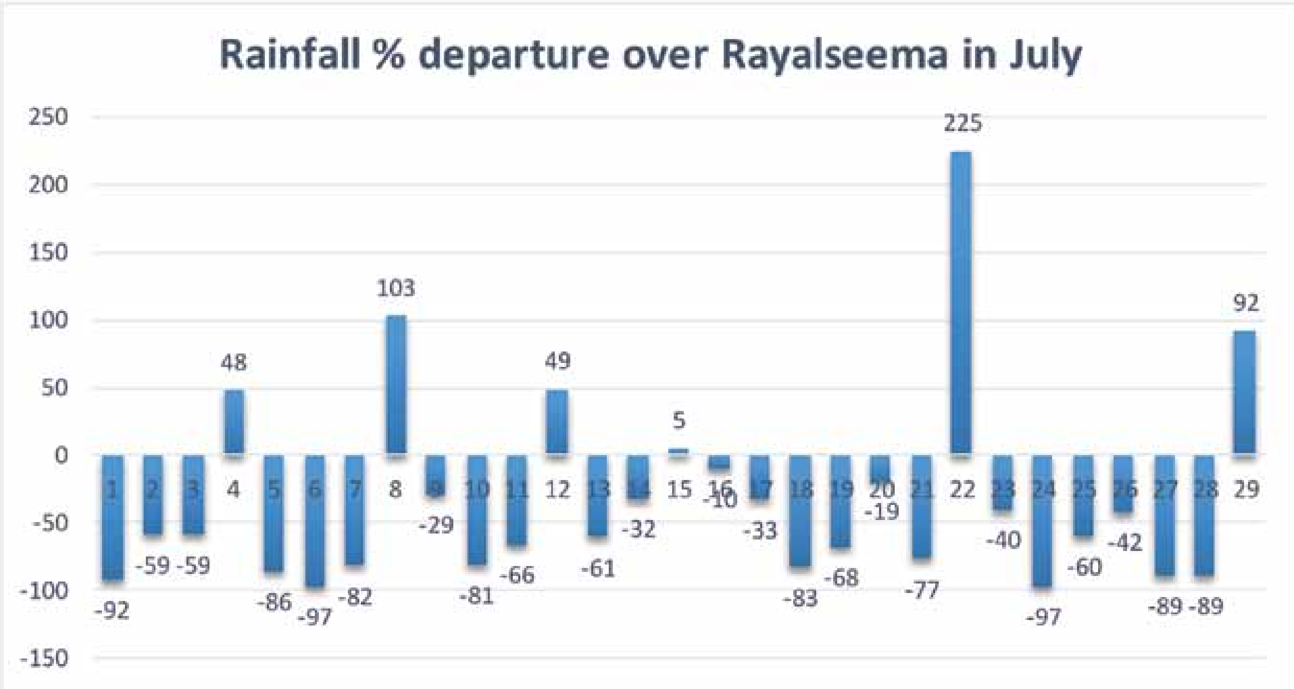

Figure 9. Rainfall percentage over Rayalaseema during the passage of systems over Bay in July.

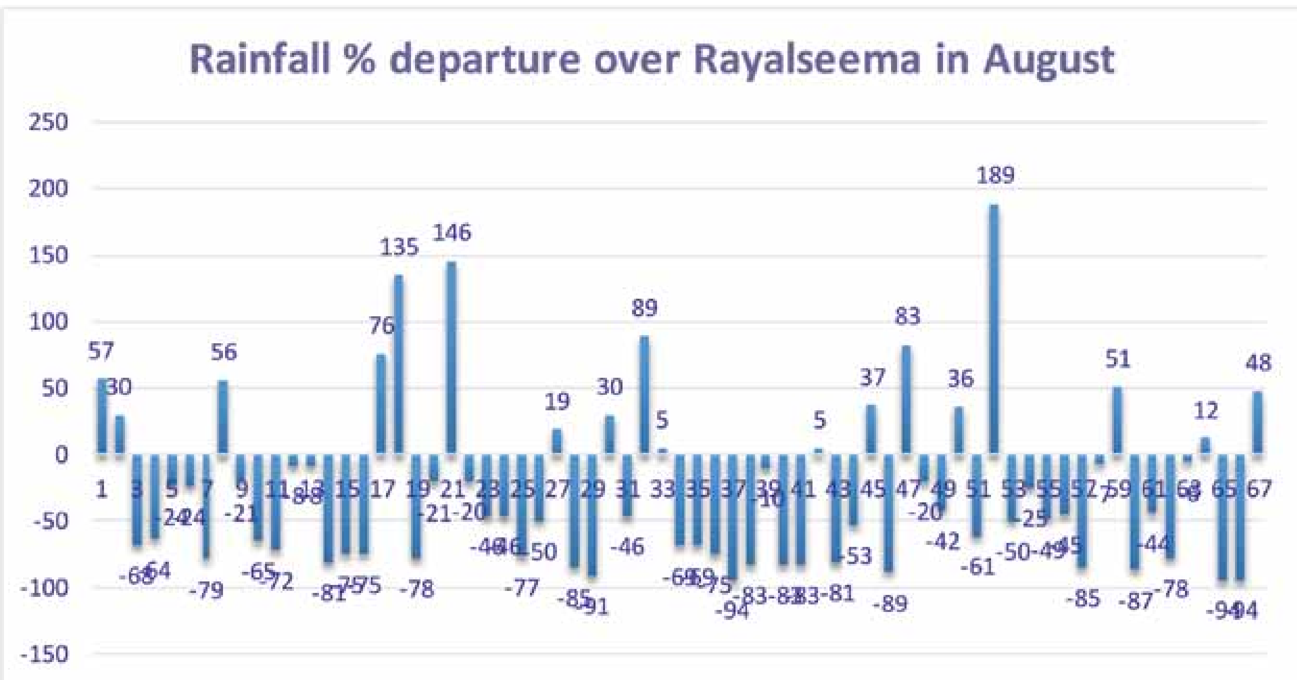

Figure 10. Rainfall percentage over Rayalaseema during the passage of systems over Bay in the month of August.

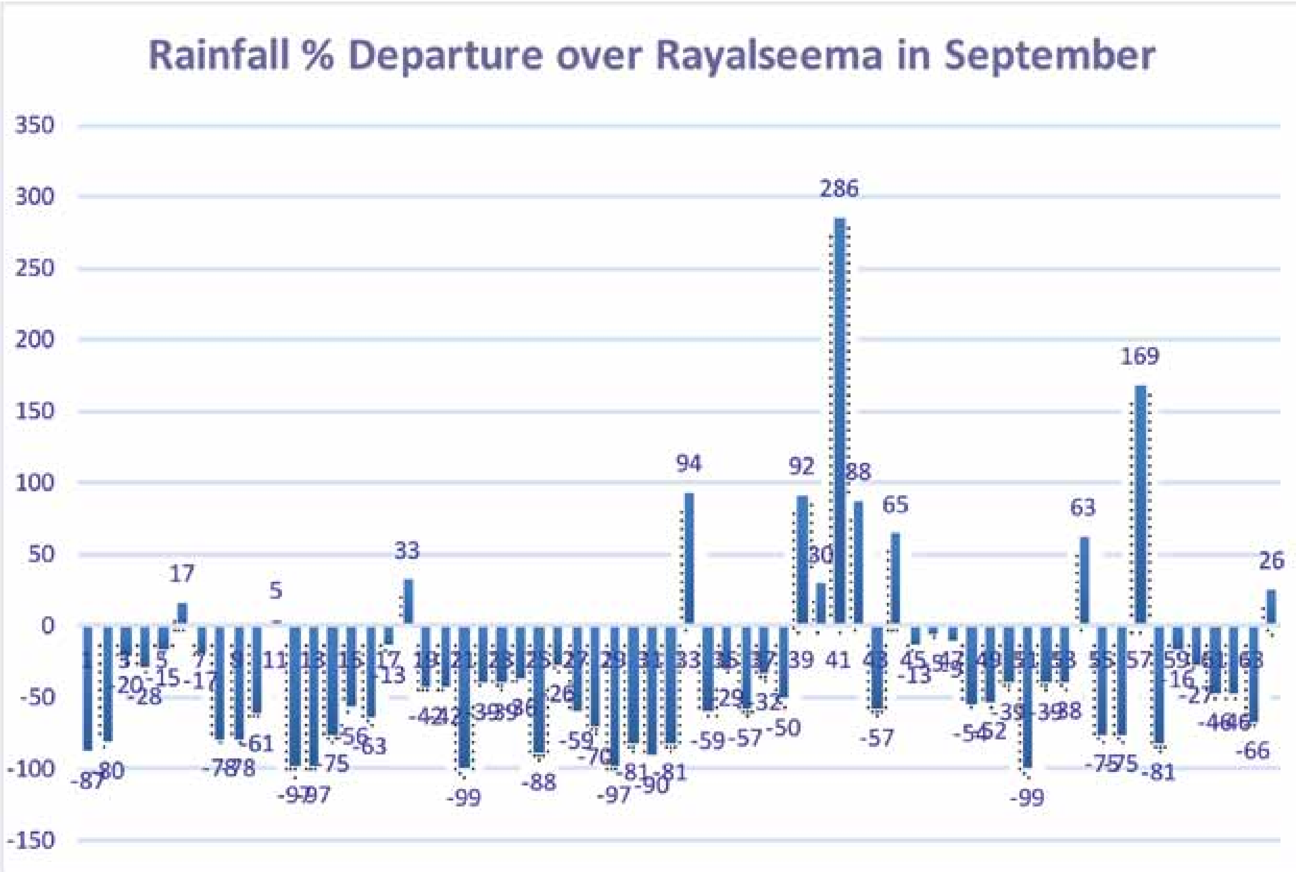

Figure 11. Rainfall percentage over Rayalaseema during the passage of systems over Bay in the month of August.

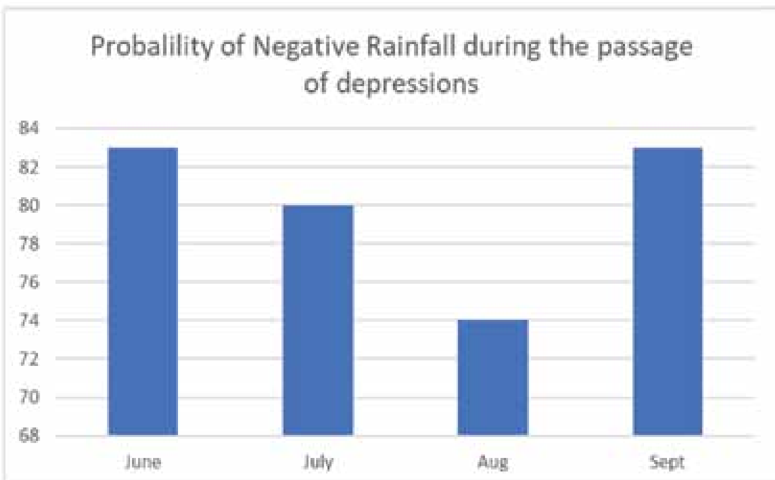

Figure 12. Probabilities of Negative Rainfall over Rayalaseema corresponding to the course of movement of depressions during the four months of monsoon.

departures in rainfall are associated with only the weeks during which the depressions forming the Bay and their subsequent movement inland. Figure 12 summarizes the argument indicating the percentage probability of rainfall to be negative over Rayalaseema region during each month of the monsoon, in association with the periods of the formation of depressions in Bay of Bengal and their subsequent movement.

CONCLUSION

During the southwest monsoon there is a general feeling that the monsoon depressions that form in the Bay of Bengal while moving along the monsoon trough cause good rainfall along its path. The present study shows that it is otherway in the case of Rayalaseema. As the monsoon depressions move inland after the landfall, the entire rainfall is concentrated along the path of the depression. Conversely, due to the development of anticyclonic vorticity over Rayalaseema region, the region is depleted of rainfall during the period which would be much below the normal. The probabilities of rainfall to be negative during such a period are 83, 80, 74 and 83% during June, July, August and September respectively. This may therefore be taken as a tool for short and medium range forecasting, wherein a depression forms in the Bay and likely to cross near Orissa, Rayalaseema may be prepared for a deficient rainfall period.

ACKNOWLEDGEMENTS

The authors express their sincere thanks to India Meteorological Department for the use of rainfall data and the published reports of India Meteorological Department. The authors are also thankful to the referee for the valuable comments and suggestions.

Compliance with Ethical Standards

The authors declare that they have no conflict of interest and adhere to copyright norms.

REFERENCES

Koteswaram, P. and George, C.A., 1958. On the formation of monsoon depressions in the Bay of Bengal, Indian J. Meteorol. Geophys., 9(1), 9-22.

Pishoroty, P.R. and Asnani, G.C., 1957. Rainfall around monsoon depression over India, 'Indian J. Meteorol. and Geophys., 8(1), 15-20.

Rao, K.N. and Jayaraman, S., 1958, "A statistical study of frequency of depressions/cyclones in the Bay of Bengal", 9(3), India Meteorological Department, New Delhi July 1958, 233-250

Rao, P.C., 2004. on the inverse relation between the monsoon depressions and rainfall of rayalaseema', Proceedings of International Symposium on Natural Hazards (Intromet), Hyderabad, by Indian Met. Soc., World Met. Organisation, India Met. Dept., Govt. of Andhra Pradesh., 229-233.

Indian Daily Weather Reports, Weather Forecasting Development Division, Office of Climate Research and Services, India Meteorological Department, Pune.

Weekly Weather Reports, Weather Forecasting Development Division, Office of Climate Research and Services, India Meteorological Department, Pune.

Tracks of Storms and Depressions in Bay of Bengal and Arabian Sea, Storm Atlas 2004, India Meteorological Department.

Received on: 14.1.18; Revised on: 22.4.18; Accepted on: 21.7.18

J. Ind. Geophys. Union (September 2018)
v.22, no.5, pp: 544-557

Role of various geomorphic parameters in landslide susceptibility of the Balason river basin of Darjeeling Himalaya, India

Subrata Mondal[1]* and Sujit Mandal[2]
[1]Department of Geography, University of Gour Banga, West Bengal, India-732103
[2]Department of Geography, Diamond Harbour Women's University, Sarisha, West Bengal, India- 743368
*Corresponding Author: subratapanchagram@gmail.com

ABSTRACT
Occurrences of landslides are affected by geomorphic, tectonic and hydrologic parameters. Balason basin of Darjeeling Himalaya, exhibits these parameters which are analyzed in the context of landslides occurrences. In the present work, we carried out an overlay analysis of various data layers such as elevation, slope, geology, geomorphology, soil, rainfall, drainage density and drainage frequency with the landslide distribution data layer to assess the probability of class of the landslide causative factors. Frequency ratio (FR) value estimate, for both landslide affected pixels and total pixels of a class, help in establishing the relationship between the probability of landslide and each class of the landslide causative factor. The result showed that, those areas which are characterized by elevation of 2130 – 2603 m, slope of 47.00 – 71.00°, rainfall of 2559 – 2617 mm, drainage density 10.60 – 15.10 km/sq. km, 70.35 – 104.30 no. of stream/sq.km drainage frequency are registered with high frequency ratio and high landslide susceptibility. In addition, the probability of landslide occurrences is also found high in Darjeeling gneiss, lower hill and fine loamy to coarse loamy soil textural area.

Key words: Frequency ratio (FR), Susceptibility, RS and GIS, Balason river basin.

INTRODUCTION

Landslides can be defined as the movement of mass of rock, debris or earth materials down the slope under the influence of gravitational force. Many researchers in India (Nautiiyal, 1966, Sengupta, 2000, Mandal and Maiti, 2014) carried out demand based studies in mountainous and hilly areas and tried to find out the causative factors and consequences of landslide occurrences and recommended some mitigation practices to reduce its hazardous impact. In Darjeeling, the spatial extents of landslides are increasing day by day, causing severe damage to lives and properties. The Balason river basin is not an exception to these phenomena, which is characterized by distinct geographical environment. The evolution of landforms is largely dependent on its geological structure, lithology, relief configuration, climatic characteristics and bio-physical processes. Researchers like Tamang (2013) and Lepcha (2012) carried out studies on geophysical set up of Balason River basin. This basin has been experiencing active denudational processes since its origin because of high relief diversity, tectonic influences, human interferences, stream activities, monsoonal rainfall and so on. Free face and rectilinear facets of slope of the landforms situated in higher altitude, especially cliffs, spurs and tea garden areas are more instable in nature of this basin. However, in this study an attempt has been made to understand the role of various geomorphic attributes i.e. elevation, slope, geology, geomorphology, soil, rainfall, drainage density and drainage frequency, to visualize the nature and extent of variations in landforms characteristics and landslide susceptibility.

STUDY AREA

The Balason river basin, situated in the western part of the Darjeeling district, that suffered several large and small landslides and affected many properties and lives, was chosen as the study area (Figure 1). The major right bank tributary of the Mahananda river and the Balason river, originates from Lepchajagat (2361 m) which is located on the Ghum-Simana ridge. Balason river basin covers parts of Darjeeling district in West Bengal having an area of 378.45 sq. km. The main Balason river flows north to south-east, having length of about 51.92 km and joins Mahananda River at around 26°41´28´´ N and 88°24´15´´ E . The highest elevations are 2613 m (SE corner) and lowest 105 m, in Southern part of the basin. The area above 30° slope consists of comparatively harder gneissic rocks and the area in between 0°-5° have the permeable subsurface materials. The average rainfall of the basin is 2300 mm (range 2000-5000 mm), which is dependent on southwest monsoon and occurs mostly in the months of June to September. The mean annual temperature is about 20.94° C. The northern uplands and southern lowlands have a mean annual temperature of 12° C and 24.70° C respectively (Lama, 2003). The area is predominately represented by very shallow to deep soils. The major portion of the basin (about 74%) consists of Darjeeling gneisses, Daling series rocks and the Damuda series.

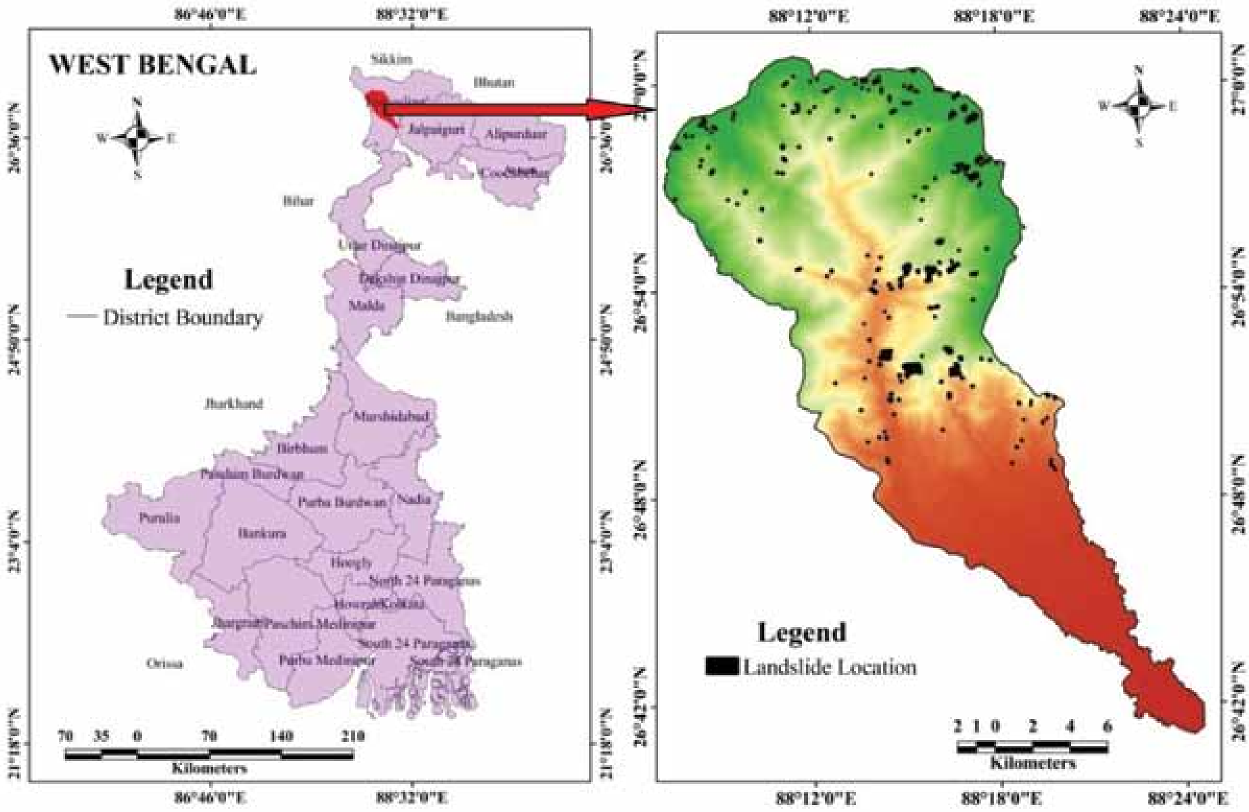

Figure 1. Location map of the study area.

METHODOLOGY

In the present work, eight parameters i.e. elevation, slope, geology, geomorphology, soil, rainfall, drainage density and drainage frequency have been used to assess the role in landslide susceptibility. Basically, landslide susceptibility refers to the possibility or chance or likelihood of potential landslides in a given area of interest based on the local terrain conditions (Grozavu et al., 2013). Elevation and slope data layers were directly derived from SRTM DEM (30m spatial resolution) in Arc GIS 10.1 environment which was downloaded using https://earthexplorer.usgs.gov link. The soil and geological maps were collected from NBSS (National Bureau of Soil Science and Land Use Planning, Kolkata) and GSI (Geological Survey of India, Kolkata) respectively and digitized in Arc GIS 10.1 platform. Geomorphological map was digitized from Unpublished Ph.D. Thesis of Lama (2003) using Arc GIS environment. Rainfall data was downloaded from http://www.worldclim.org link in Continuous raster data format and imported in Arc GIS environment. Drainage network was digitized from Survey of India (SOI), Kolkata. Map nos. 78a/4, 78a/8, 78b/1, 78b/5 and 78b/6 and was checked with and google earth image (2015). Inverse distance weighted (IDW) method was incorporated to prepare drainage density and drainage frequency map in Arc GIS 10.1 software. The database of landslide distribution map was generated from Google earth historical imageries (2000-2016), Landsat 7 ETM+ imageries (2000-2005), Landsat 4-5 TM imageries (2006-2007, 2009-2011), LISS III imageries (2008, 2012-2013), Landsat 8 OLI (2014-2015), High resolution Sentinel-2 imagery (2016), Arc Map high resolution world imagery and intensive field survey data (2015-2016). Total 295 landslide polygons were mapped in an area of 378.45 sq.km (Table 1). The average area of the landslides was 3762.90 m^2.

To establish the relation between each factor and landslide occurrences, the frequency ratio (FR) value was used (Karim et al., 2011).

$$Fr_i = \frac{\{N\ pix\ (Si)/N\ pix\ (Ni)\}*100}{\{\sum N\ pix\ (Si)/\sum N\ pix\ (Ni)\}*100} \quad \text{............. (1)}$$

Where, N pix (Si) is the number of pixels containing landslide in each class (i), N pix (Ni) is the total number of pixels having class (i) in the whole basin, or simply the percentage of landslide pixels to total pixels in a class, ∑N pix (Si) total number of pixels in each class and ∑N pix (Ni) total number of pixels in the whole basin or simply percentage of pixels to total pixels in class. To calculate the number of landslide pixels of each class of the respective

Table 1. Area and location of the landslides in Balason river basin from 2000-2016.

S.No.	Area of the slides (Sq. m)	X coordinate of centroid of the slides area	Y coordinate of centroid of the slides area	S.No.	Area of the slides (Sq. m)	X coordinate of centroid of the slides area	Y coordinate of centroid of the slides area
1	707.199	88.2957	26.866	149	1062.05	88.2308	26.8763
2	1241.36	88.3238	26.8357	150	9596.98	88.2323	26.9005
3	31.7915	88.328	26.8172	151	50.3166	88.1552	26.9443
4	39.2974	88.3282	26.8173	152	1064.16	88.2108	26.9096
5	74.7919	88.3277	26.8153	153	1842.76	88.1723	26.9248
6	202.192	88.3303	26.8127	154	382.255	88.1405	26.9607
7	443.925	88.329	26.8144	155	395.708	88.1413	26.9636
8	182.456	88.1269	26.9448	156	244.159	88.1268	26.9694
9	76.8791	88.2955	26.9618	157	656.173	88.1278	26.9708
10	135.181	88.2954	26.9617	158	2051.94	88.129	26.9697
11	18.0313	88.2936	26.9614	159	826.188	88.1328	26.9755
12	4.79447	88.2935	26.9614	160	1431.73	88.1648	26.9482
13	115.793	88.3003	26.9606	161	2284.52	88.1736	26.9398
14	17.4485	88.2958	26.9627	162	244.237	88.1939	26.911
15	6.26611	88.2958	26.9624	163	473.227	88.2084	26.9073
16	61.9584	88.2918	26.9602	164	1118.3	88.1849	26.9571
17	21.4497	88.2922	26.9603	165	1343.13	88.1822	26.9573
18	20.2991	88.2894	26.9611	166	58.4183	88.1584	26.9833
19	28.2176	88.2895	26.9629	167	75.5655	88.159	26.9858
20	71.8128	88.2903	26.9623	168	114.422	88.1588	26.9855
21	23.3692	88.2905	26.9627	169	1045.16	88.1908	26.9865
22	15.4175	88.2908	26.963	170	72.5905	88.1933	26.9869
23	35.9775	88.291	26.9631	171	162.601	88.1935	26.9898
24	21.1504	88.2911	26.9633	172	1738.58	88.1929	26.99
25	92.1921	88.2908	26.9639	173	167.346	88.1937	26.988
26	32.9415	88.2913	26.9636	174	467.586	88.1856	26.9898
27	53.7706	88.2914	26.9641	175	530.686	88.1938	26.9698
28	17.3334	88.2918	26.9632	176	151.251	88.1858	26.9994
29	38.7774	88.2922	26.9635	177	108.052	88.187	27.0002
30	51.2226	88.2929	26.9635	178	158.193	88.1876	27.0007
31	68.9653	88.2852	26.9596	179	694.12	88.209	26.9963
32	379.161	88.2814	26.9609	180	509.409	88.2095	26.9967
33	1699.4	88.2809	26.9601	181	79.7281	88.2076	26.9966
34	2346.11	88.28	26.9597	182	51.9661	88.2119	26.9981
35	358.216	88.2803	26.9581	183	154.707	88.2041	27.0023
36	282.583	88.2857	26.9548	184	180.331	88.2003	27.0012
37	39.415	88.2862	26.9543	185	237.411	88.1997	26.9865
38	39.1453	88.2856	26.9538	186	192.888	88.2024	26.9888
39	22.5493	88.286	26.9536	187	1740.5	88.2106	26.9734
40	37.5993	88.2872	26.9537	188	337.62	88.243	26.9935
41	35.2606	88.288	26.954	189	383.982	88.2563	27.0058
42	48.6892	88.288	26.9544	190	31.9148	88.2553	27.006
43	166.631	88.2877	26.9547	191	233.374	88.2374	27.0011
44	42.7794	88.2871	26.9549	192	248.928	88.2373	27.0009
45	27.9714	88.2867	26.9549	193	65.6938	88.2373	27.0031
46	22.5377	88.2868	26.955	194	1664.16	88.2354	27.0014
47	41.6531	88.287	26.9551	195	64.8215	88.2367	27.0014
48	77.0869	88.2876	26.9552	196	2662.13	88.2354	27.0007

S.No.	Area of the slides (Sq. m)	X coordinate of centroid of the slides area	Y coordinate of centroid of the slides area	S.No.	Area of the slides (Sq. m)	X coordinate of centroid of the slides area	Y coordinate of centroid of the slides area
49	7.44129	88.2882	26.9551	197	256.755	88.2352	27.0002
50	48.5958	88.2885	26.9552	198	910.659	88.2346	27.0004
51	76.4866	88.2883	26.9555	199	94.6291	88.2305	27.0015
52	23.7807	88.2881	26.9558	200	166.369	88.2298	27.001
53	179.457	88.2893	26.956	201	28.7871	88.2286	27.0013
54	41.638	88.2896	26.956	202	13.5587	88.2304	27.0019
55	42.7744	88.2895	26.9563	203	360.114	88.2283	27.0012
56	25.8678	88.2889	26.9542	204	73.1794	88.2286	27.001
57	80.355	88.2899	26.9543	205	176.405	88.2246	26.9997
58	11.6655	88.2898	26.9544	206	57.8003	88.2282	26.9979
59	13.3572	88.29	26.9543	207	29.0432	88.2317	26.9969
60	52.2182	88.2881	26.9541	208	645.099	88.2233	26.9841
61	17.4687	88.2869	26.9531	209	1045.4	88.2148	26.9871
62	75.9915	88.2793	26.9568	210	106.941	88.254	26.9982
63	201.801	88.2791	26.9567	211	217.025	88.258	26.9959
64	434.811	88.2768	26.957	212	299.998	88.2566	26.996
65	5056.89	88.2778	26.9845	213	32.9966	88.2548	26.9982
66	653.957	88.2758	26.9844	214	9.42264	88.2545	26.9977
67	133.234	88.2764	26.9853	215	45.1092	88.2539	26.9973
68	78.322	88.2765	26.9855	216	6.65395	88.2533	26.997
69	71.0966	88.2772	26.986	217	207.835	88.2505	26.9906
70	92284.2	88.2872	26.9825	218	67.6416	88.2512	26.9901
71	7635.69	88.2885	26.9846	219	61.1047	88.253	26.9904
72	23530.9	88.283	26.9878	220	300.908	88.2541	26.9903
73	1342.71	88.2775	26.9928	221	30.4599	88.243	26.9917
74	2953.5	88.2798	26.9944	222	133.583	88.2508	26.9986
75	20926.3	88.2692	26.9967	223	465.7	88.2459	26.9867
76	649.424	88.2385	26.9974	224	36.006	88.2444	26.9866
77	68.4146	88.2384	26.9956	225	11.4642	88.2444	26.9865
78	982.645	88.2692	26.8557	226	37.306	88.2438	26.9857
79	315.397	88.287	26.8951	227	319.488	88.2328	26.9563
80	7041.19	88.2786	26.9122	228	602.203	88.253	26.9719
81	10350.4	88.2876	26.9076	229	209.096	88.2575	26.9754
82	241.655	88.1912	27.0038	230	174.979	88.2584	26.9764
83	1791.87	88.1862	26.9635	231	675.168	88.2589	26.9768
84	1133.26	88.1853	26.9642	232	253.721	88.2636	26.9773
85	7687.55	88.1851	26.9697	233	172.194	88.2756	26.9829
86	35391.3	88.2693	26.9233	234	41.7062	88.2757	26.9832
87	8668.89	88.1469	26.9579	235	377.121	88.2381	26.9792
88	96.2151	88.2784	26.9603	236	13.6503	88.2592	26.934
89	153.184	88.2796	26.959	237	103.161	88.26	26.9435
90	327760	88.254	26.862	238	83.3302	88.256	26.9453
91	86276.3	88.2515	26.9106	239	39.2229	88.2623	26.9495
92	178297	88.2394	26.869	240	11.7083	88.2612	26.9495
93	51441.1	88.2733	26.8709	241	292.799	88.267	26.9538
94	34320.9	88.2753	26.9101	242	75.0716	88.2831	26.9577
95	26807.8	88.2629	26.9093	243	92.8112	88.284	26.9581
96	50497.7	88.265	26.9098	244	141.598	88.2848	26.9585
97	1356.49	88.1428	26.9831	245	44.7715	88.2842	26.9587
98	302.838	88.2356	26.8291	246	65.5269	88.2836	26.9595

S.No.	Area of the slides (Sq. m)	X coordinate of centroid of the slides area	Y coordinate of centroid of the slides area	S.No.	Area of the slides (Sq. m)	X coordinate of centroid of the slides area	Y coordinate of centroid of the slides area
99	4286.21	88.2783	26.8624	247	30.6295	88.2834	26.9586
100	67.006	88.2906	26.9501	248	19.372	88.2831	26.9592
101	207.329	88.2915	26.9515	249	153.508	88.2832	26.9595
102	3608.52	88.2776	26.8639	250	47.3037	88.2833	26.9596
103	594.788	88.2946	26.9197	251	23.1429	88.2912	26.963
104	8094.87	88.28	26.8669	252	59.9813	88.2839	26.9556
105	293.191	88.2766	26.8611	253	156.932	88.2373	26.916
106	167.62	88.1591	26.9864	254	2103.85	88.243	26.9009
107	205.681	88.2295	26.827	255	1549.07	88.2619	26.9045
108	31.4893	88.1604	26.9424	256	63.8999	88.2639	26.9048
109	529.442	88.226	26.8423	257	251.299	88.2633	26.9045
110	6607.22	88.1428	26.9818	258	64.6839	88.2636	26.9064
111	187.824	88.142	26.9805	259	2342.79	88.2632	26.9066
112	209.821	88.1405	26.9805	260	1326.81	88.2689	26.908
113	81.1721	88.1412	26.9814	261	212.756	88.269	26.9133
114	101.34	88.145	26.9699	262	314.619	88.2756	26.9138
115	48.6915	88.1362	26.9754	263	43.8935	88.2797	26.919
116	25.7825	88.1465	26.9772	264	2120.05	88.2505	26.9079
117	165.093	88.1442	26.9789	265	242.618	88.2634	26.8916
118	93.9419	88.2303	26.917	266	252.802	88.2644	26.8913
119	717.515	88.1491	26.9788	267	262.503	88.2667	26.8917
120	458.494	88.1486	26.979	268	1719.26	88.2677	26.892
121	70.2184	88.2336	26.9036	269	43.2021	88.2662	26.887
122	548.314	88.1479	26.9797	270	27.6787	88.259	26.8683
123	1859.56	88.2423	26.85	271	6.49692	88.2282	26.8839
124	29211	88.2751	26.8605	272	407.037	88.2477	26.8563
125	854.153	88.2477	26.9021	273	279.718	88.2122	26.8555
126	11015	88.2418	26.8472	274	28.7389	88.2281	26.8577
127	328.532	88.1923	26.9103	275	5350.87	88.2772	26.8624
128	252.397	88.2343	26.9044	276	30543.9	88.2777	26.8597
129	3010.4	88.2363	26.8644	277	243.052	88.2809	26.8573
130	1247.26	88.2468	26.8589	278	260.571	88.2803	26.8575
131	789.487	88.2464	26.8472	279	212.472	88.2862	26.8534
132	14854.8	88.2509	26.8593	280	14374.7	88.2736	26.8491
133	1947.98	88.2402	26.8172	281	289.395	88.2698	26.8325
134	416.474	88.2414	26.8869	282	402.556	88.2435	26.8402
135	63.2228	88.2392	26.8897	283	196.266	88.3069	26.8162
136	842.363	88.2418	26.9028	284	1235.7	88.3111	26.8451
137	179.9	88.2487	26.906	285	603.006	88.291	26.8667
138	245.819	88.2485	26.903	286	571.366	88.3095	26.8239
139	1051.9	88.2476	26.9052	287	220.043	88.3099	26.8238
140	424.025	88.2481	26.9056	288	500.193	88.3123	26.8269
141	3158.76	88.236	26.9102	289	497.139	88.3259	26.8376
142	1685.25	88.2513	26.908	290	193.821	88.3303	26.8471
143	4283.61	88.2573	26.909	291	25.5029	88.3269	26.8482
144	826.283	88.2398	26.8187	292	16.4798	88.3262	26.8485
145	2661.94	88.2394	26.8289	293	142.254	88.3176	26.8458
146	440.653	88.2386	26.8318	294	54.7755	88.3173	26.8442
147	8140.19	88.2341	26.8994	295	52.0469	88.3134	26.8371
148	803.776	88.2306	26.8658				

Table 2. Elevation character of the Balason river basin and landslide susceptibility

Factors	Subclasses	Total pixels		Landslide occurrence pixels		FR value
		Absolute	Percentage	Absolute	Percentage	
Elevation (meter)	106-298	368681	21.92	4	0.08	0.00
	298-539	139536	8.30	270	4.93	0.59
	539-792	135130	8.03	876	15.96	1.99
	792-1030	172562	10.26	1240	22.60	2.20
	1030-1240	181438	10.79	1457	26.55	2.46
	1240-1440	189984	11.30	573	10.44	0.92
	1440-1650	169253	10.06	273	4.97	0.49
	1650-1880	144806	8.61	75	1.37	0.16
	1880-2130	118740	7.06	180	3.29	0.47
	2130-2603	61869	3.68	539	9.82	2.67

factor, zonal statistics as a table under spatial analyst tool in Arc GIS 10.1 environment was used. In can be mentioned that, higher the frequency ratio value stronger the relationship between landslide occurrence and the given conditioning factor. As indicated by many researchers, natural break method was applied to determine different subclasses of continuous geomorphic parameters (Poli and Sterlacchini, 2007; Althuwaynee et al., 2014; Mahalingam et al., 2016). Finally, the composite index map of landslide susceptibility was obtained using following equation in Arc Map 10.1 GIS environment.

$$CLS = Fr_1 + Fr_2 + Fr_3 + \ldots\ldots\ldots\ldots + Fr_n \qquad \ldots\ldots\ldots\ldots.(2)$$

Where, CLS is the composite landslide susceptibility index and $Fr_1 + \ldots\ldots FR_n$ is the frequency ratio of each factor.

RESULTS

Elevation character and landslide susceptibility

The elevation of the Balason river basin was classified into 10 categories where elevation ranges from 106 meter to 2603 meter (Figure 2a). Extreme north-western part and north-eastern part of the basin was dominated by higher elevation whereas, southernmost section was characterized by low elevation. However, no direct relationship can be made between elevation and landslide occurrences. Several researchers showed that landslides have the more tendencies to occur at the higher El areas, so the high El areas have the greater landslide susceptibility (Devkota et al., 2013; Umar et al., 2014). Moderate elevation zones were found in the central portion of the basin. Maximum area of 21.92% was covered by 106-298 meter elevation zone while a small area of 3.68% was dominated by 2130-2603 meter elevation zone. The highest and lowest frequency ratio value was found in the elevation class of 2130-2603 meter (2.67) and 106-298 meter (0.00) respectively, which indicated greater and lower chance of slope failures respectively (Table 2).

Slope angle character and landslide susceptibility

The slope map of the Balason river basin was made from the SRTM DEM and it was classified into 10 different slope zones (Figure 2b). Basically, the river basin is attributed with maximum slope angle where slope angle ranges from 0^0 to more than 71.10^0. The basin is dissected by well developed drainage network which made the slope steepened by continuous branching of the drainage and its headword erosion. The slope plays an important role for the growth and development of drainage network, surface run-off and soil erosion, as well as drainage concentration over the space. Not only that the stream power index (SPI) and topographic wetness index (TWI) are influenced by slope steepness, but the study also revealed that there is a positive relationship between slope and landslide frequency ratio. The slope having greater than 26.60^0 is attributed with the frequency ratio value ranges from 1.13 to 13.57, which showed high probability of landslide phenomena (Table 3).

Geology and landslide susceptibility

The geology of Balason river basin was divided into five major categories viz., Darjeeling Gneisses, Daling Series, Damuda Series /Lower Gondwanas, Nahan Group and Alluvium (older and recent) (Figure 3a) (Lama, 2003). The Darjeeling gneisses covered a large part of the basin (68.33%) where it varied from a foliated granitoid rock composed to quartz, felsper and biotite to more or less pure mica schist. The Daling series consists of phyllite, slate and quartzite which are being found in the Middle East and Middle West portion of the basin. Damuda Series /Lower Gondwana series consisted of quartzitic sandstones, shales and slates, semi-anthracitic (graphitic) coal, lamprophyre silts and minor bands of limestone. The Nahan Group or Lower Siwalik deposits are mainly composed of soft greyish sandstone, mudstone, shales and conglomerates.

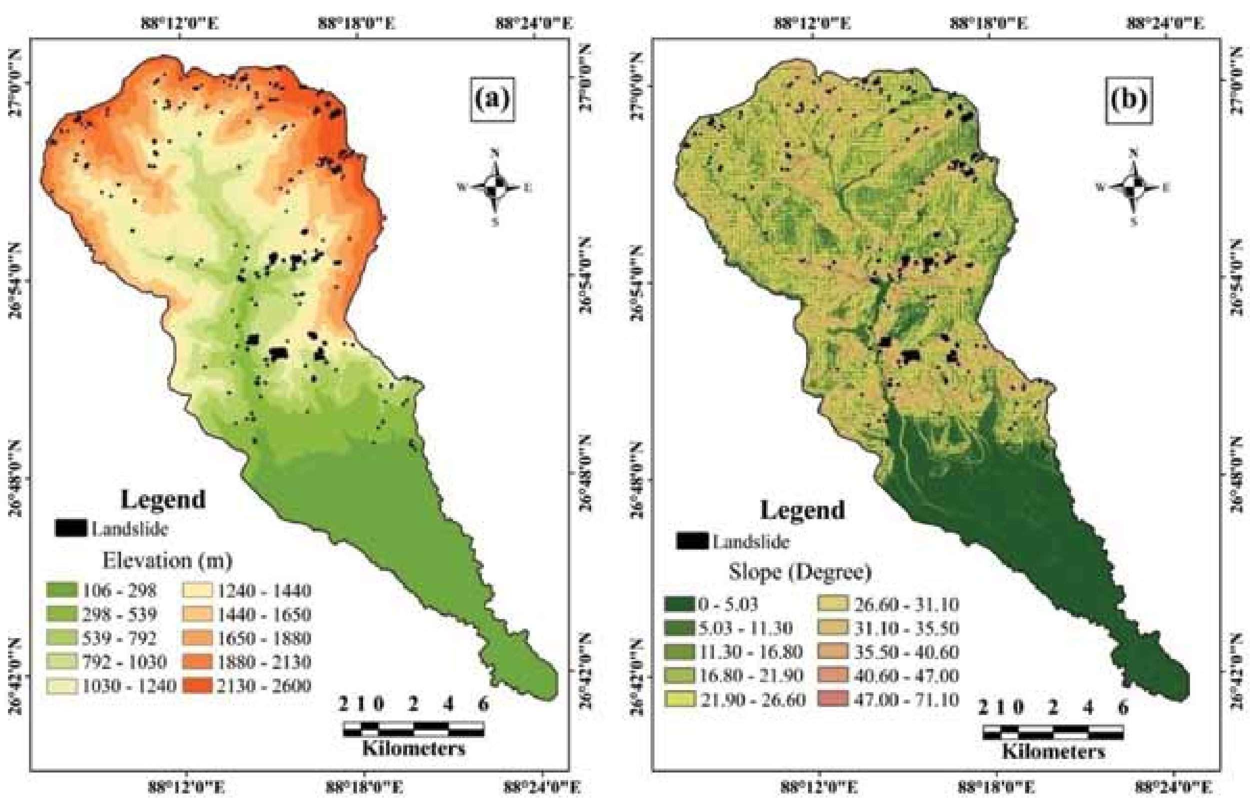

Figure 2. Maps showing data layers of (a) elevation and (b) slope.

Table 3. Slope character of the Balason river basin and landslide susceptibility

Factors	Subclasses	Total pixels		Landslide occurrence pixels		FR value
		Absolute	Percentage	Absolute	Percentage	
Slope (Degree)	0-5.03	400086	23.79	47	0.86	0.04
	5.03-11.30	167825	9.98	202	3.68	0.37
	11.30-16.80	219531	13.05	522	9.52	0.73
	16.80-21.90	231356	13.75	736	13.41	0.98
	21.90-26.60	207903	12.36	601	10.95	0.89
	26.60-31.10	169058	10.05	625	11.38	1.13
	31.10-35.50	126742	7.54	611	11.14	1.48
	35.50-40.60	91415	5.43	663	12.09	2.22
	40.60-47.00	51416	3.06	742	13.52	4.42
	47.00-71.10	16667	0.99	738	13.44	13.57

Alluviums (older and recent) are composed of boulder beds and other sands and gravels. Similarly, Drift Formation and younger flood plain deposits comprise sand and gravel, pebbles, etc. It can be seen that, Darjeeling Gneiss had the greater potentiality of landslide occurrences (1.44) while, Damuda Series /Lower Gondwana and Nahan Group, Lower Siwalik deposits were registered with lowest FR value (0.00), which indicated no chance of slope failures phenomena (Table 4).

Geomorphology and landslide susceptibility

Lama (2003) divided the Balason river basin into 7 distinct geomorphological groups i.e. upper hill (>2000m), middle hill (1000-2000m), lower hill (<1000m), foothill (piedmont), upper alluvial fan, lower alluvial fan and river flood plain (Figure 3b). Middle hill (1000-2000m) covered larger area of the basin (46.22%), while river flood plain had the smallest area of the basin (4.07%). The greater

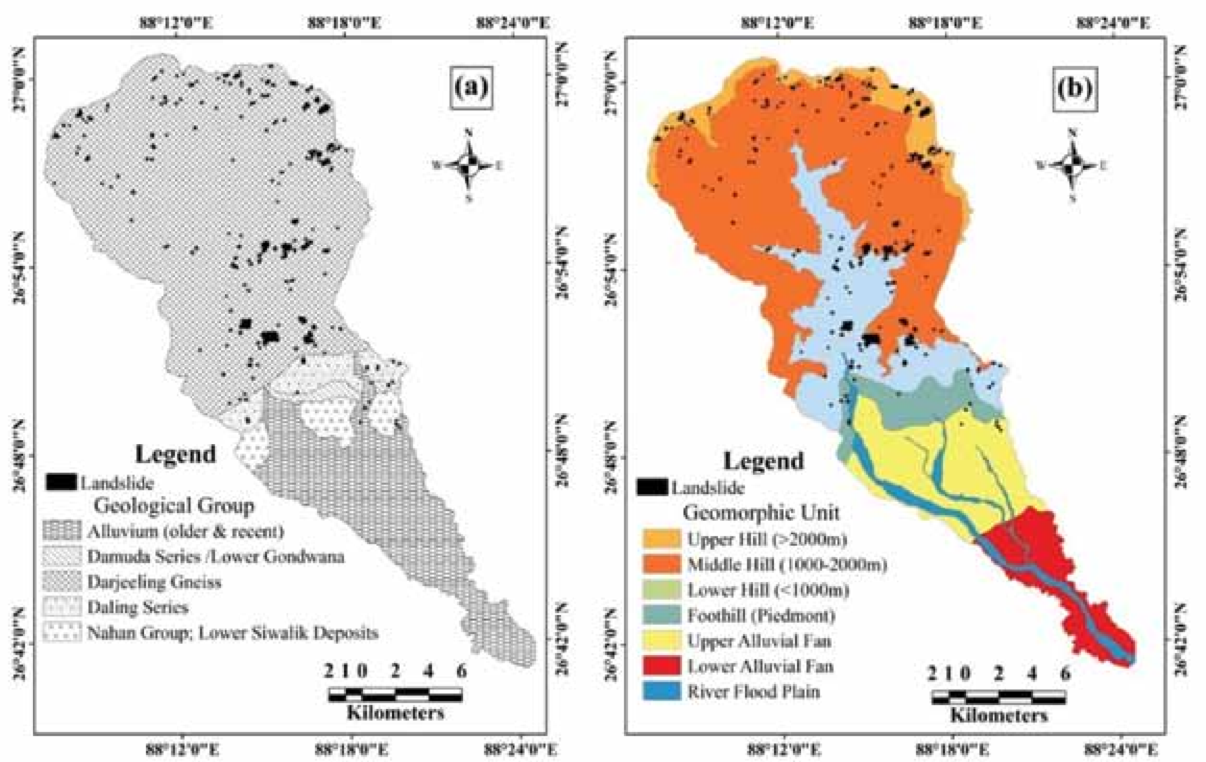

Figure 3. Data layers of (a) geological map and (b) geomorphological map (after Lama, 2003).

Table 4. Geology of the Balason river basin and landslide susceptibility

Factors	Subclasses	Total pixels		Landslide occurrence pixels		FR value
		Absolute	Percentage	Absolute	Percentage	
Geology	Darjeeling Gneiss (Dg)	287309	68.33	1345	98.32	1.44
	Daling Series (Ds)	18518	4.40	21	1.54	0.35
	Damuda Series /Lower Gondwana (DAs)	4784	1.14	0	0.00	0.00
	Nahan Group, Lower Siwalik Deposits (Ng)	16839	4.00	0	0.00	0.00
	Alluvium (older & recent) (Al)	93050	22.13	2	0.15	0.01

potentiality of landslide occurrences was found in lower hill (<2000m) (1.90). The chance of slope failures was lowest in the class of lower alluvial fan and river flood plain, both were registered with 0.00 FR value (Table 5).

Soil character and landslide susceptibility

Five types of soil were identified in the basin i.e. W002, W003, W004, W006 and W009 (Figure 4a). The soil of the Balason river basin is favorable for tea plantation. The original soil of the area is drastically changed either by the process of new soil formation on the truncated top or by removal of soil by erosion (Sarkar, 1990). The parent soil of this region has changed due to its nature and it has formed more than one time (Lama, 2003). In the sandy area, soils are generally siliceous and aluminous. The lower Balason basin is formed by fine grained clay loam. In some cases, the top soils are finer in nature than the subsurface soils. The detailed characteristics of each type of soil of the Balason river basin were presented in Table 7. In this basin, W003 soil type was registered with highest frequency ratio is 1.88. On the other hand, W006 and W009 soil types covering almost 17% area of the basin, have the lowest chance of landslide events (Table 8).

Spatial distribution of Rainfall and landslide susceptibility

Landslides are closely associated with duration, amount and intensity of rainfall. The intensity and amount of

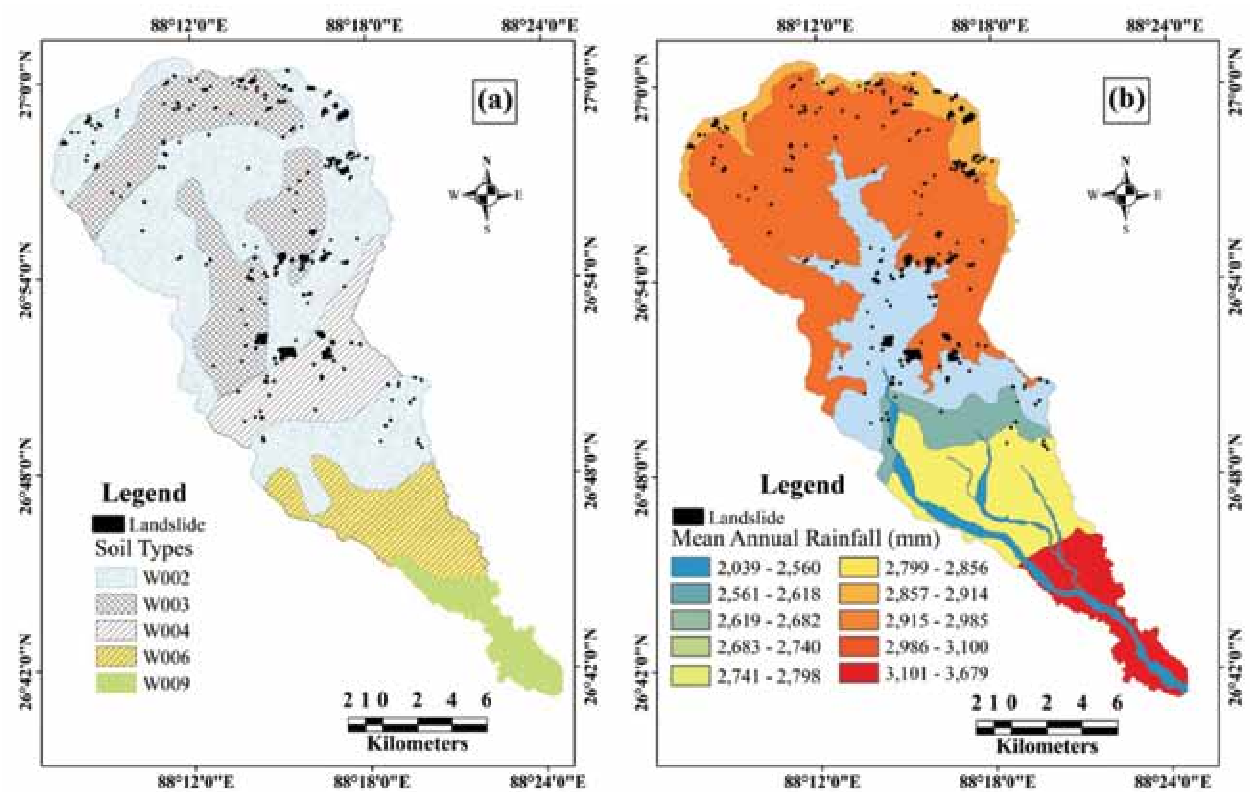

Figure 4. Data layers of (a) soil and (b) rainfall maps**.**

Table 5. Geomorphology of the Balason river basin and landslide susceptibility

Factors	Subclasses	Total pixels		Landslide occurrence pixels		FR value
		Absolute	Percentage	Absolute	Percentage	
Geomorpholoy	Upper Hill (>2000m)	29309	6.97	150	10.96	1.57
	Middle Hill (1000-2000m)	194339	46.22	732	53.51	1.16
	Lower Hill (<2000m)	77058	18.33	477	34.87	1.90
	Foothill (Piedmont)	21111	5.02	7	0.51	0.10
	Upper Alluvial Fan	53984	12.84	2	0.15	0.01
	Lower Alluvial Fan	27588	6.56	0	0.00	0.00
	River Flood Plain	17111	4.07	0	0.00	0.00

rainfall varies from one place to another in the basin due to topographic configuration. The mean annual rainfall ranges from 2041 mm 3673 mm. Based on the rainfall distribution Balason river basin was classified into ten zones (Figure 4b). Around 35% landslide affected area and 50% area of basin are characterized by mean annual rainfall of more than 2790 mm. More than 1 frequency ratio was found in the class ranges from 2559 to 2847mm and 3090-3673 rainfall which was characterized by high landslide occurrences events. Rest of the class having less than 1 frequency ratio value which indicating minimum chance of landslide occurrences. Some high annual rainfall classes i.e. 2847-2905 mm, 2905-2975 mm and 2975-3090 mm, have low FR value because of the unfavorable geo-environmental conditions for landslide occurrences in the concerned area (Table 9).

Drainage density and landslide susceptibility

The drainage network development on both sides of the slope segments make the interfluves area more steep resulting mountain slope instability. The drainage network development, slope steepening, and slope failure are regular processes which promotes equilibrium in the geomorphic system. The concentration of drainage network and their engagement in the process of erosion and transportation make the slope more vulnerable to landslip phenomena. The drainage density varies from one place to another based

Table 7. Soil characteristics of Balason river basin

Symbol	Soil characteristics	Taxonomic name
W002	Moderately shallow, excessively drained, coarse loamy soils occurring on steep side slopes with gravelly loamy surface, severe erosion and strong rockiness, associated with moderately shallow, well drained, gravelly loamy soils with loamy surface and moderate erosion.	Coarse loamy, typic Udorthents; Loamy skeletal, typic Dystrochrepts
W003	Deep, well drained, fine loamy soils occurring on steep side slopes with gravelly loamy surface, moderate erosion and moderate rockiness, associated with moderately shallow, excessively drained, coarse loamy soils with loamy surface, severe erosion and moderate rockiness.	Fine loamy, Umbric Dystrochrepts; Coarse loamy, Typic Udorthents
W004	Moderately shallow, well drained, gravelly loamy soils occurring on steep side slopes with gravelly loamy surface, moderate erosion and moderate rockiness, associated with moderately shallow, somewhat excessively drained, gravelly loamy soil with loamy surface, moderate erosion and moderate rockiness	Loamy skeletal, Typic Haplumbrepts; Loamy skeletal, typic Udorthents
W006	Very deep, imperfectly drained, coarse loamy soils occurring on very gently sloping upper piedmont plains with loamy surface and moderate erosion, associated with very deep, imperfectly drained fine loamy soils.	Coarse loamy, Umbric Dystrochrepts; Fine loamy, Fluventic Dystrochrepts
W009	Very deep, imperfectly drained, coarse loamy soils occurring on nearly level lower piedmont plain with loamy surface, associated with very deep imperfectly drained, fine loamy soils.	Coarse loamy, Aquic Udifluvents; Fine loamy, Fluventic Eutrochrepts

Table 8. Soil of the Balason river basin and landslide susceptibility.

Factors	Subclasses	Total pixels		Landslide occurrence pixels		FR value
		Absolute	Percentage	Absolute	Percentage	
Soil	W002	198569	47.22	524	38.30	0.81
	W003	102249	24.32	626	45.76	1.88
	W004	49222	11.71	218	15.94	1.36
	W006	46327	11.02	0	0.00	0.00
	W009	24133	5.74	0	0.00	0.00

Table 9. Rainfall of the Balason river basin and landslide susceptibility

Factors	Subclasses	Total pixels		Landslide occurrence pixels		FR value
		Absolute	Percentage	Absolute	Percentage	
Rainfall (mm)	2041-2559	40635	9.66	130	9.48	0.98
	2559-2617	42137	10.02	209	15.25	1.52
	2617-2681	44545	10.59	186	13.58	1.28
	2681-2732	38867	9.24	161	11.80	1.28
	2732-2790	45248	10.76	186	13.58	1.26
	2790-2847	41930	9.97	147	10.72	1.08
	2847-2905	41695	9.92	87	6.36	0.64
	2905-2975	42379	10.08	40	2.91	0.29
	2975-3090	42956	10.22	62	4.53	0.44
	3090-3673	40108	9.54	161	11.80	1.24

on the developed drainage network in the basin. Higher the drainage density more is the drainage concentration and slope saturation over the space. The drainage density map was divided into 10 classes (Figure 5a). It was observed that moderate level of drainage density have high frequency ratio and greater probability of slope instability. High drainage density of more than 5.39 covere about 21% area of the basin. 10.60-15.10 class have maximum chance of landslide occurrences (2.94), whereas 0-1.31drainage density class have least chance of slope failures (0.00) (Table 10).

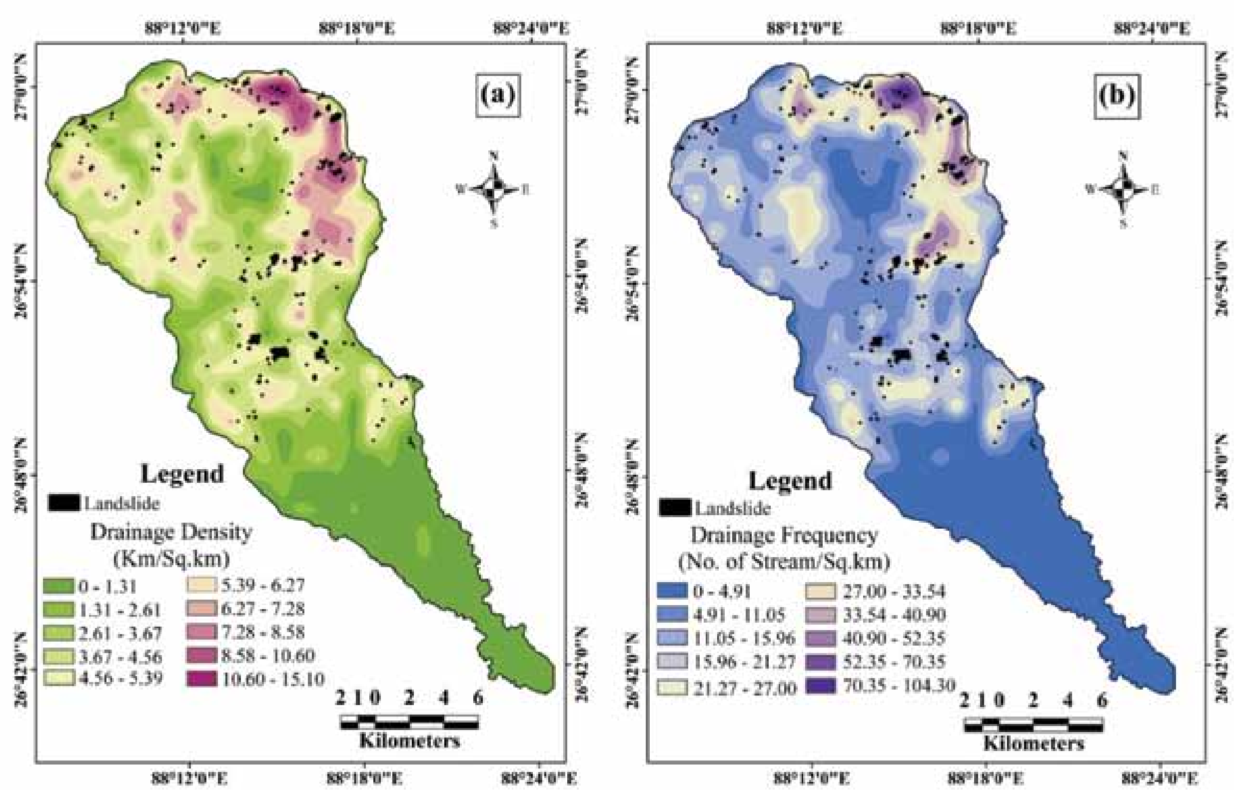

Figure 5. Data layers of (a) drainage density map and (b) drainage frequency map.

Table 10. Drainage density of the Balason river basin and landslide susceptibility

Factors	Subclasses	Total pixels		Landslide occurrence pixels		FR value
		Absolute	Percentage	Absolute	Percentage	
Drainage density (Km/Sq. Km)	0-1.31	338135	20.10	4	0.07	0.00
	1.31-2.61	197209	11.72	8	0.14	0.01
	2.61-3.67	239068	14.21	783	14.27	1.00
	3.67-4.56	284654	16.92	1830	33.35	1.97
	4.56-5.39	246882	14.68	1108	20.19	1.38
	5.39-6.27	177847	10.57	746	13.59	1.29
	6.27-7.28	103596	6.16	494	9.00	1.46
	7.28-8.58	60735	3.61	366	6.67	1.85
	8.58-10.60	25924	1.54	73	1.33	0.87
	10.60-15.10	7951	0.47	76	1.39	2.94

Drainage frequency and landslide susceptibility

Similar to the drainage density map, drainage frequency of the basin was also divided into 10 classes (Figure 5b). About 67% area of the basin registered drainage frequency value of 0 to 15.96. 70.35-104.30 class has the greater potentiality in landslide occurrences (4.59) and 0-4.91 class have the minimum probability of slope failure events (0.00) (Table 11). In addition, the classes having drainage frequency value of 33.54-40.90 (4.37), 52.35-70.35 (2.76), 11.05-15.96 (2.17) and 27.00-33.54 (1.87) were also characterized by high landslide susceptibility.

DISCUSSION

The trend line of FR values reveals that elevation, slope, drainage density and drainage frequency were positively correlated with slope failure which means that slope instability increasing with increasing the value (Figure 6a, b, d and e). On the other hand, there was negative relation

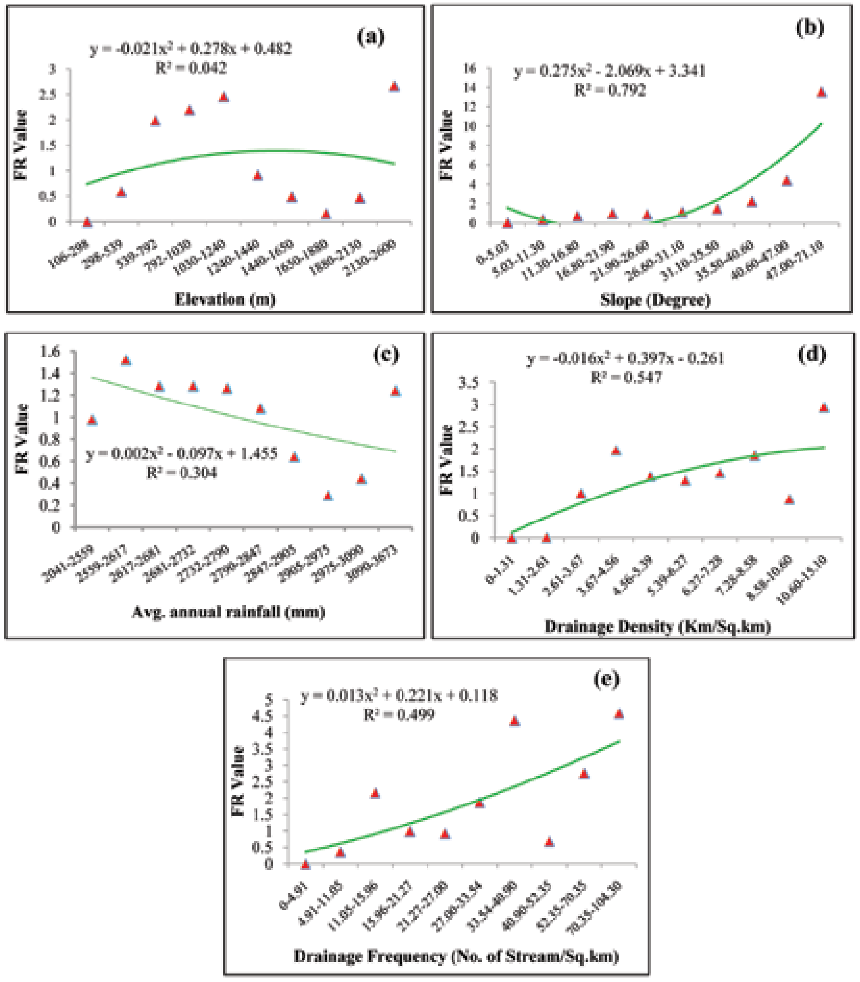

Figure 6. Relation between data layers and FR value (a) elevation (b) slope (c) rainfall (d) drainage density and (e) drainage frequency.

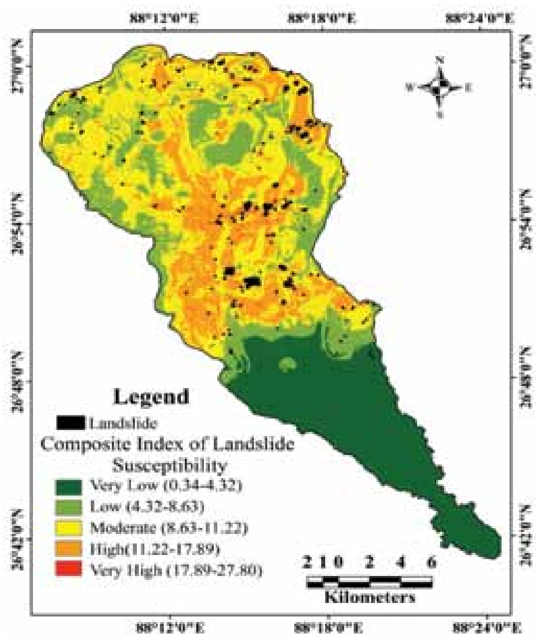

Figure 7. Composite index map of landslide susceptibility using FR value.

Table 11. Drainage frequency of the Balason river basin and landslide susceptibility

Factors	Subclasses	Total pixels		Landslide occurrence pixels		FR value
		Absolute	Percentage	Absolute	Percentage	
Drainage frequency (No. of stream/Sq.km)	0-4.91	446653	26.55	4	0.07	0.00
	4.91-11.05	315499	18.76	370	6.74	0.36
	11.05-15.96	374903	22.29	2657	48.42	2.17
	15.96-21.27	260262	15.47	842	15.35	0.99
	21.27-27.00	131533	7.82	394	7.19	0.92
	27.00-33.54	73153	4.35	446	8.13	1.87
	33.54-40.90	42087	2.50	600	10.94	4.37
	40.90-52.35	27831	1.65	62	1.14	0.69
	52.35-70.35	6621	0.39	60	1.09	2.76
	70.35-104.30	3458	0.21	52	0.94	4.59

Table 12. Spatial correlation between the landslide susceptibility index values and the various geomorphic parameters

Model/ geomorphic parameters	Elevation	Slope	Geology	Geomorphology	Soil	Rainfall	Drainage density	Drainage frequency
Landslide susceptibility index values	0.67	0.62	0.79	0.83	0.68	0.36	0.72	0.61

between rainfall and landslide occurrences (Figure 6c). In case of geology, soil and geomorphology, trend line of FR value was not shown in a diagram due to its categorical nature. In addition, geomorphology was most intimately associated with the determination of landslide susceptibility with correlation value of 0.83. Next highest relationship with landslide susceptibility was observed in case of geology (0.79) followed by drainage density (0.72), elevation (0.67), slope (0.62), drainage frequency (0.61) respectively. Lastly, rainfall exerted lowest influence on landslide susceptibility as indicated by correlation value of 0.36 (Table 12). Finally, composite FR index of landslide susceptibility was made by considering the eight factors, and divided it into five landslides susceptibility zones using natural breaks classification method i.e. very low (0.34-4.32), low (4.32-8.63), moderate (8.63-11.22), high (11.22-17.89) and very high (17.89-27.80) (Figure 7).

CONCLUSIONS

All the geomorphic parameters play a significant role in assessing landslide susceptibility in the Balason basin. Not only the factors but also the individual category of all the landslide occurrence factors showed a distinct level of landslide probability. Generally elevation, slope, drainage density and drainage frequency were positively correlated with landslide susceptibility, whereas rainfall was negatively associated with landslide occurrences. It is assumed that the prepared landslide susceptibility analysis will help the policy makers, developers and engineers for choosing suitable locations to implement slope management plans, land use plans and other development action plans, although this method can be less useful on the site-specific scale.

ACKNOWLEDGEMENTS

The authors would like to express their sincere thanks to Survey of India (SOI), Geological Survey of India (GSI) and National Bureau of Soil Survey and Land Use Planning (NBSS and LUP) for providing necessary data, facilities and support during the study period.

Compliance with Ethical Standards

The authors declare that they have no conflict of interest and adhere to copyright norms.

REFERENCES

Althuwaynee, O.F, Pradhan, B., Park, H. and Lee, J.H., 2014. A novel ensemble bivariate statistical evidential belief function with knowledge-based analytical hierarchy process and multivariate statistical logistic regression for landslide susceptibility mapping, Catena, 114, 21–36.

Devkota, K.C., Regmi, A.D. and Pourghasemi, H.R., et al., 2013. Landslide susceptibility mapping using certainty factor, index of entropy and logistic regression models in GIS and their comparison at Mugling–Narayanghat road section in Nepal Himalaya. Natural Hazards, 65(1), 135-165. DOI: 10.1007/s11069-012-0347-6.

Grozavu, A., Plescan, S., Patriche, C.V., Margarint, M.C. and Rosca, B., 2013. Landslide Susceptibility Assessment: GIS Application to a Complex Mountainous Environment, The Carpathians: Integrating nature and society towards sustainability, Environ. Sci. Eng., 31-44.

Karim, S., Jalileddin, S. and Ali, M.T., 2011. Zoning landslide by use of frequency ratio method (case study: Deylaman region) MiddleEast, J. Sci. Res., 9(5), 578–583.

Lama, I.L., 2003. Study of the environmental geomorphology in the Balason basin, Unpublished Ph. D thesis, North Bengal University, 24-28.

Lepcha, I., 2012. Regional study of Geo-environmental aspects: A study of Balason basin, Darjeeling district, West Bengal. J. Geo-Environ. Observer., 1(2), 24-37.

Mahalingam, R., Olsen, M.J. and O'Banion, M.S., 2016. Evaluation of landslide susceptibility mapping techniques using lidar–derived conditioning factors (Oregon case study). Geomat. Nat. Hazard Risk 7, 1884–1907.

Mandal, S. and Maiti, R., 2014. Semi-quantitative approaches for landslide assessment and prediction, Springer Nat. Hazards series, 2014. DOI: 10.1007/978-981-287-146-6, pp 292.

Nautiiyal, S.P., 1966. On the stability of certain hill slopes in and around Darjeeling WB. Bull. Geol. Surv. India, 15, 31–48.

Poli, S. and Sterlacchini, S., 2007. Landslide representation strategies in susceptibility studies using weights-of-evidence modeling technique. Natural Resources Res., 16(2), 121-134. DOI: 10.1007/s11053-007-9043-8.

Sarkar, S., 1990. Genesis and classification of the soils of the Mahananda basin, Darjeeling Himalaya, The Geographical Memoir, 2(182), 117-129.

Sengupta, C.K., 2000. Report on Landslide Hazard Microzonation of Mirik Municipal area for Urban Planning. Unpublished GSI Report FS 1999-2000.

Tamang, L., 2013. Effects of boulder lifting on the fluvial characteristics of lower Balason basin in Darjeeling district west Bengal, PhD thesis, University of North Bengal, Department of Geography and Applied Geography, p 19.

Umar, Z., Pradhan, B. and Ahmad, A. et al., 2014. Earthquake induced landslide susceptibility mapping using an integrated ensemble frequency ratio and logistic regression models in West Sumatera Province, Indonesia, Catena, 118, 124-135. DOI:10.1016/j.catena.2014.02.005.

Received on: 22.4.18; Revised on: 6.6.18; Accepted on: 9.7.18

J. Ind. Geophys. Union (September 2018)
v.22, no.5, pp: 558-567

A study on textural parameters of beach sands along some parts of the Nellore coast, east coast of India: Implications to Depositional Environment

K. Nagalakshmi[1]*, Madri Pramod Kumar[1], T. Lakshmi Prasad[1], N. Jayaraju[2], M. Lakshmanna[2] and G. Sreenivasulu[3]

[1]Department of Earth Sciences, Yogi Vemana University, Kadapa, (A.P), India
[2]Department of Geology, Yogi Vemana University, Kadapa, (A.P), India
[3]Department of Coastal Process, National Center for Earth sciences Studies, (Kerala), India.
*Corresponding author: ammulu.chani@gmail.com

ABSTRACT

An attempt has been made to evaluate the textural parameters and grain size distribution of coastal sands from Govindampalli to Durgarajupatnam, Nellore coast, east coast of India. The changes in textural parameters were studied by comparison of two seasons, i.e north east monsoon season (NE) in December 2015 and south west monsoon season (SW) in June 2016. A detailed account of textural parameters and grain size distribution of beach sands were carried out at each station in four microenvironments, by measuring various parameters like graphic mean size, graphic standard deviation, skewness, and kurtosis. To measure textural parameters, bivariate plots have been made to know the degree of freedom among various parameters. The analysis of textural parameters for two seasons indicates the prepotency of medium to fine grain and moderately well-sorted sediments with nearly symmetrical distribution. The textural parameters measurement and bivariate plots infer that prevailing intermittent energy conditions coalesced with rampant south west monsoon winds responsible for the platy to leptokurtic nature of sediments. In order to have a proxy on the mode of transportation and depositional environments CM (Percentile and Median) diagrams were plotted on the double logarithmic sheet, which suggests that sediments were transported by rolling, bottom suspension and rolling and graded suspension. Most of the sediments were deposited in tractive currents and beach environment regions. Factor analysis shows the dominance of mean size and kurtosis in NE monsoon season and skewness and kurtosis in SW monsoon season, where these parameters plays a dominant role in dispersal and distribution of sediments. Linear discrimination function (LDF) analysis shows high energy environments at the time of deposition of sediments.

Keywords: Textural studies; Beach sediments; Factor analysis; Linear discrimination function (LDF) analysis; Nellore coast.

INTRODUCTION

Granulometric studies are the fundamental sedimentological tools, which unravels the properties of sediment particles, transportation and their deposition in the sedimentary environments and provides vital information regarding its provenance and depositional conditions (Krumbein and Pettijohn., 1938; Folk and Ward, 1957). The size of the grain in the depositional environment is influenced by many factors like a wave and current activity, onshore and offshore movements, fluctuations in sea level, episodic storms, debouch of streams, rivulets, and rivers into the oceans or seas. In India, about $1.2x10^9$ tons of sediment are carried by the rivers each year (Blott and Pye, 2001). A unique set of foreshore topography and shoreline morphology, is produced by the interaction of sediment supply, energy dispersal pattern, and geology of the area (Senapathi et al., 2011). Grain size parameters were studied between the Gosthani and Champavathi rivers confluence, east coast of India, Andhra Pradesh by Bangaru Naidu et al., (2016) who inferred energy levels and bimodal nature of sediments.

In recent years, many scientists carried out extensive research and emphasized the importance of grain size analysis to understand the grain size parameters and also to differentiate the depositional environments viz., fluvial, lacustrine, marine, estuarine etc., especially in the coastal region (Inman 1952; Passega 1957, 1964; Visher 1969; Veeraiah and Varadachari, 1975; Lingdholmn, 1987; Oaie et al., 2005). An attempt has been made to empathize the textural characteristics and grain size distribution of the sands in the present study area with reference to seasonal variations. This would involve understanding of the energy conditions of the depositional environments through textural parameters, factor analysis and linear discrimination function analysis (LDF).

STUDY AREA

The present study area of Govinadampalli to Drgarajupatnam lies between latitude $14^0 05'10''$- $14^0 01'30''$ N and longitude $80^0 08'20''$ - $80^0 09'36''$ E, that belong to Survey of India topo sheet Nos. 66 B/4, 66 C/1

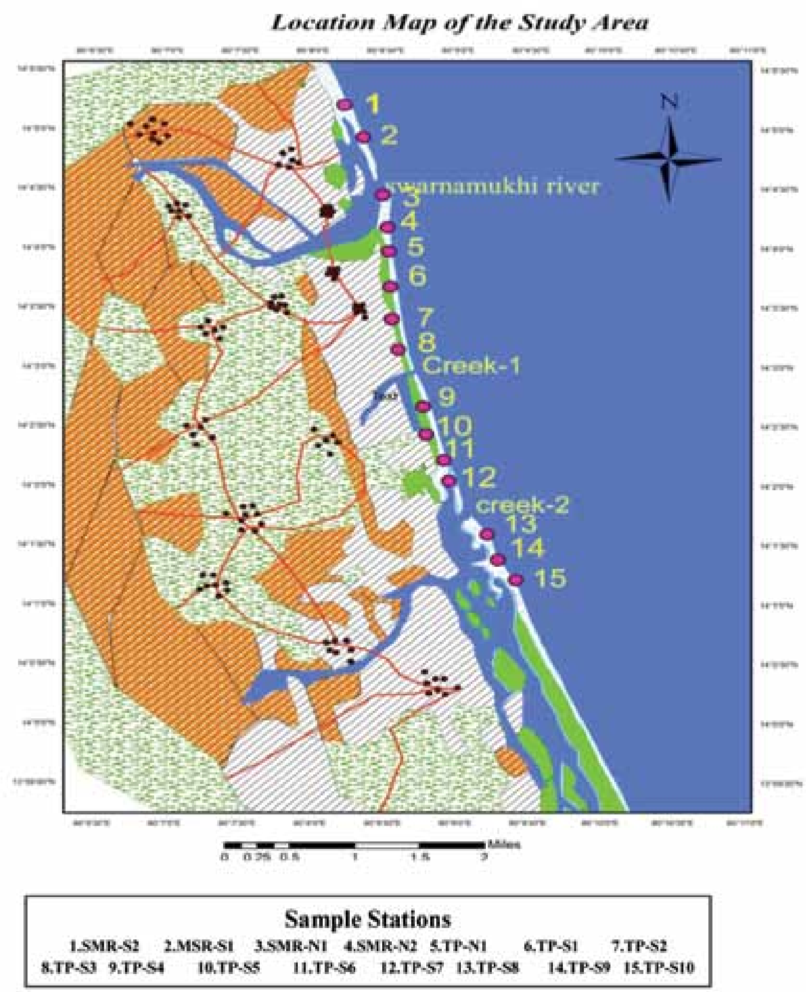

Figure 1. Location map of the study area.

and C/5 on 1:50,000 scale. The major source of sediment is from Swarnamukhi river situated at northern tip of the investigation area (Figure 1). It passes through sacred Tirupathi hills, with no tributaries and later on, debauches into the Bay of Bengal. At the time of first survey i.e., in December 2015, two creeks were observed, one at Tupilipalem village and the other at Durgarajpatnam (Figure 1). From Govendampalli to Durgarajupatnam, the stretch is covered by Quaternary alluvium sediment, underlain by granitic rocks, intersected by phyllites, basic rocks, and metamorphic suite of schist rocks of Precambrian Age.

METHODOLOGY

One hundred and twenty sediment samples (60 in each season) were collected from 15 transects along the study area, in north east (Dec 2015) and south west monsoon season (June 2016) along the 11km stretch from Govindampalli to Durgarajupatnam coast. The sediment samples were collected by using Van Veen grab sampler and recorded location points using handheld GPS. The sediment samples were carefully stored in polythene bags, and 100gms of sample was taken out by using coning and quartering method, and then air dried. The samples were treated with diluted hydrochloric acid (HCl) and ammonia (NH_4) to remove carbonates and organic matter. Later, it is washed with dilute water and air owen dried. Then the samples were subjected to sieving by ASTM sieves with the ½ Ø intervals for 10 to 20 minutes by Ro-Tap sieve shaker for separating the grain with different sizes viz., 16μ, 25μ, 35μ, 45μ, 60μ, 80μ, 120μ, 170μ, 230μ and -230μ (pan). Sieved material was weighed separately and the fractions were properly tabulated for further analysis (Ingram 1970). Grain size parameters like mean size (Mz), standard deviation (SD), skewness (Sk), and kurtosis (K_G), were determined by using the GRADISTAT software (Tables 1a, b). The results obtained from the GRADISTAT software, which is used to draw CM (C=Percentile, M=Median) diagrams, frequency distribution curves, scatter plots. SPSS and graphic prism softwares were used to determine the factor analysis and LDF (Linear discriminate function) analysis respectively.

RESULTS

Grain size parameters

The grain size analysis was carried out and the results were compared, for the two seasons to evaluate the information regarding provenance and depositional conditions.

Graphic mean grain size (Mz)

The average size (ϕ) of the sediments is an indicator of energy conditions. The variations in ϕ represent the differential energy condition, which indicates the kinetic energy of the depositing agents. The grain size values at each measuring point for two seasons are given in Tables 1a and 1b. Grain size analysis was carried out at four microenvironments viz., dune, backshore, berm and foreshore at each station. The ϕ values show medium to fine grain in dune (1.066 φ -2.576 ϕ), backshore (1.506ϕ -2.607ϕ), berm (1.68ϕ -2.415 ϕ) and foreshore (1.14ϕ -2.09ϕ) in NE monsoon season (Table 1a) and in SW monsoon season, dune (0.697ϕ -2.827ϕ) show coarse to fine grain size (Table 1b) and the rest of the microenvironments i.e backshore (1.404ϕ-2.454ϕ), berm (1.642ϕ -2.381ϕ) and foreshore (1.38ϕ -1.96ϕ) show medium to fine grain size. The overall average graphic mean size of the sediment in the study area is 1.865ϕ and 1.801ϕ in NE and SW monsoon seasons respectively. It shows the predominance of medium size particles indicating intermittent energetic conditions (Folk and Ward, 1957).

Standard deviation (σ_1)

Graphic standard deviation (σ_1) quantifies the sorting of sediments in various microenvironments and it represents the wavering pattern of energy conditions of the depositional environment (Sahu, 1964). NE monsoon season shows well to moderately sorting in dune (0.433ϕ – 0.931ϕ), backshore (0.405ϕ -0.787ϕ) and berm (0.399ϕ-0.84ϕ) environments. The foreshore environment (0.62ϕ – 0.92ϕ) shows moderately to moderately well-sorted sediments (Table 1a). In SW monsoon season (Table 1b) dune, backshore, berm show well to moderately sorted sediments, with values ranging in between 0.34ϕ – 0.732ϕ, 0.405ϕ – 0.787ϕ, 0.408ϕ – 0.645ϕ, respectively. The foreshore environment show moderately well sorted to moderately sorted sediments, the value ranges from 0.67ϕ - 0.83ϕ. The average value of all microenvironments in both seasons. 0.649ϕ and 0.62ϕ, indicates moderately well-sorted sediments, which suggests partial winnowing conditions and an addition of sediments to the beach environments. A glance at standard deviation values in both NE and SW monsoon seasons reveals that dune, backshore, berm and foreshore environments, show moderately well sorted in nature, implying that aeolian activity is paramount in sorting of sediments, owing to the continuous panning action by waves and currents (Friedman 1967 ; Giosan et al., 2005).

Skewness (Sk)

Skewness evaluates the symmetry of sediments distribution i.e., prepotency of coarser and finer material. The positive and negative values refer to fine material in the fine tail and coarser material in coarser tail respectively. In the NE monsoon season, the skewness values varies from very coarse to very fine skewed in dune (-0.287ϕ to 0.497ϕ), but in backshore (-0.226ϕ to -0.11ϕ), berm (-0.315ϕ to 0.037ϕ) and foreshore environments (-0.2ϕ to 1.85ϕ), shows coarser to fine skewed sediment distribution (Table 1a). Most of the sediment samples show coarser to fine skewed and depict deposition of sediments in high to low energy environments (Nageswara Rao et al., 2005). Altogether, the average value (-0.059ϕ), indicates nearly symmetrical distribution.

In SW monsoon season, the skewness values of dune (-0.11ϕ to 0.241ϕ), backshore (-0.226ϕ to 0.109ϕ) shows coarser to fine skewed distribution and berm (-0.15ϕ to -0.011ϕ) shows nearly symmetrical and foreshore (-0.193ϕ to 0.053ϕ) show, coarser to near symmetrical distribution of sediments. The overall average value (-0.078ϕ) of the skewness in the study area is nearly symmetrical in nature (Table 1b).

Kurtosis (K_G)

Kurtosis (K_G) ascertains the peak distribution which depicts the mixed (coarse and fine) sediment population distribution and it also gives the ratio of sorting of sediments in the tails as well as in the central portion of the curve (bell-shaped curve). The wide spectrum of kurtosis values reflects the characteristic flow of the depositional medium (Seralathan and Padamalal, 1994; Bangaru Naidu et al., 2016). In NE monsoon season most of the microenvironments i.e., backshore (0.736ϕ – 1.101ϕ), the berm (0.732ϕ – 1.109ϕ) and foreshore (0.72v – 1.07ϕ) exhibits platy to mesokurtic in nature and dune (0.686ϕ – 1.123ϕ) sediment samples of all stations falls under platy to leptokurtic category. The dominance of platy and leptokurtic nature reflects immaturity and maturity of the sand in the depositional environment respectively.

In SW monsoon season all sediment samples shows platy to leptokurtic in nature except foreshore. The extreme high and low kurtosis values reflects that the part of sediments achieved its sorting elsewhere in a high-energy environment (Friedman,1961). The average value of both seasons (0.926ϕ and 0.95 ϕ) represents subsequent accession of coarser and fine material, after the winnowing action and retention of their original character during deposition (Avramidis et al., 2012).

Table 1a. Textural parameters of coast sand from Govindampalli to Durgarajupatnam during north east monsoon season.

SS	DUNE				BACKSHORE				BERM				FORESHORE			
	Mz	SD	S_K	K_G	Mz	SD	S_K	K_G	Mz	SD	S_K	K_G	Mz	SD	S_K	K_G
TP-N-1	2.37	0.46	-0.11	0.99	2.02	0.67	-0.17	0.84	1.68	0.84	-0.12	0.84	1.61	0.92	-0.03	0.75
TP-S-1	2.09	0.55	-0.03	0.94	2.21	0.56	-0.14	1.00	2.42	0.45	-0.17	1.00	1.51	0.88	-0.11	0.87
TP-S-2	1.63	0.93	0.07	0.68	1.41	0.64	-0.04	0.92	2.06	0.56	-0.04	0.92	1.71	0.87	-0.16	0.91
TP-S-3	2.27	0.51	-0.1	0.95	1.96	0.57	-0.08	1.06	2.10	0.54	-0.16	1.06	1.64	0.77	-0.01	0.85
TP-S-4	2.57	0.43	-0.19	1.23	2.19	0.48	-0.09	0.93	2.26	0.65	-0.30	0.93	2.09	0.67	-0.2	0.92
TP-S-5	1.97	0.59	-0.05	0.88	2.38	0.47	-0.15	0.98	2.25	0.59	-0.32	0.98	1.14	0.79	0.25	1.07
TP-S-6	2.19	0.53	-0.17	0.96	2.43	0.46	-0.21	1.10	2.32	0.52	-0.22	1.10	1.72	0.66	-0.08	1
TP-S-7	1.06	0.85	0.50	0.91	2.02	0.62	-0.17	0.96	2.26	0.54	-0.26	0.96	1.72	0.92	-0.06	0.85
TP-S-8	1.18	0.79	0.42	0.78	1.66	0.73	-0.07	0.74	2.22	0.40	0.04	0.74	1.33	0.83	0.16	0.81
TP-S-9	1.96	0.69	-0.19	0.94	1.77	0.71	-0.17	0.89	2.09	0.58	-0.20	0.89	1.48	0.85	-0.02	0.84
TP-S-10	1.52	0.69	0.01	0.84	1.64	0.69	-0.09	0.90	1.88	0.60	-0.13	0.90	1.64	0.67	1.85	1.04
SMR-S-1	2.06	0.74	0.09	0.90	2.45	0.41	-0.23	1.07	2.08	0.65	-0.25	1.07	1.57	0.84	0.18	0.72
SMR-S-2	1.56	0.66	0.07	0.88	1.87	0.59	-0.07	0.87	1.80	0.65	-0.08	0.87	1.57	0.81	0.04	0.79
SMR-N-1	1.96	0.59	-0.13	0.90	2.22	0.52	-0.13	0.98	2.04	0.54	-0.09	0.98	1.56	0.66	0.06	0.94
SMR-N-2	2.35	0.56	-0.28	1.11	1.42	0.79	-0.01	0.82	2.10	0.58	-0.23	0.82	1.79	0.62	-0.08	0.9
Minimum	1.06	0.43	-0.28	0.68	1.41	0.41	-0.23	0.74	1.68	0.40	-0.32	0.74	1.14	0.62	-0.2	0.72
Maximum	2.57	0.93	0.50	1.23	2.45	0.79	-0.01	1.10	2.42	0.84	0.04	1.10	2.09	0.92	1.85	1.07
Average Mean	1.91	0.65	0.01	0.93	1.97	0.59	-0.12	0.94	2.10	0.58	-0.17	0.94	1.60	0.78	0.21	0.88

Mz= Mean Size, SD=Standard deviation, S_K= Skewness, K_G= Kurtosis

Table 1b. Textural parameters of coast sand from Govindampalli to Durgarajupatnam during southwest monsoon season.

SS	DUNE				BACKSHORE				BERM				FORESHORE			
	Mz	SD	S_K	K_G	Mz	SD	S_K	K_G	Mz	SD	S_K	K_G	Mz	SD	S_K	K_G
TP-N-1	1.91	0.69	-0.07	0.95	1.68	0.67	-0.17	0.98	1.76	0.61	-0.07	0.99	1.38	0.67	-0.01	0.96
TP-S-1	1.71	0.54	-0.02	0.88	1.89	0.56	-0.14	0.98	1.64	0.57	-0.03	0.94	1.55	0.73	-0.04	0.86
TP-S-2	2.06	0.55	-0.07	0.96	1.98	0.57	0.11	0.96	1.80	0.54	-0.05	0.99	1.56	0.82	0.05	0.9
TP-S-3	1.79	0.70	-0.08	0.91	1.62	0.64	-0.08	0.86	1.80	0.56	-0.04	1.04	1.61	0.76	-0.06	0.9
TP-S-4	0.70	0.55	-0.09	1.01	1.61	0.48	-0.09	0.92	1.87	0.51	-0.02	1.03	1.59	0.74	-0.02	0.99
TP-S-5	2.23	0.58	-0.11	1.04	1.94	0.47	-0.15	1.01	1.67	0.65	-0.01	0.96	1.38	0.72	0.05	0.93
TP-S-6	2.06	0.69	0.08	0.81	1.51	0.46	-0.21	0.96	1.74	0.63	-0.07	0.96	1.87	0.69	-0.16	1
TP-S-8	2.83	0.59	0.24	1.09	1.70	0.73	-0.07	0.74	1.97	0.54	-0.11	1.11	1.64	0.77	-0.17	0.87
TP-S-9	0.95	0.61	0.08	0.98	1.72	0.71	-0.17	0.73	1.84	0.57	-0.13	1.04	1.62	0.76	-0.07	0.93
TP-S-10	1.44	0.59	0.10	0.92	1.94	0.70	-0.09	0.91	1.79	0.56	-0.04	1.12	1.66	0.79	-0.19	0.83
SMR-S-1	1.27	0.65	0.12	0.89	1.81	0.41	-0.23	1.13	1.87	0.64	-0.08	0.91	1.75	0.83	-0.15	0.77
SMR-S-2	1.38	0.59	0.12	0.94	1.94	0.59	-0.07	0.99	1.87	0.64	-0.07	0.91	1.96	0.74	-0.11	0.85
SMR-N-1	1.31	0.50	0.01	1.01	1.87	0.52	-0.13	0.91	2.13	0.51	-0.05	0.97	1.81	0.74	-0.12	0.88
SMR-N-2	2.06	0.73	-0.10	0.80	1.92	0.79	-0.01	0.92	1.96	0.59	-0.10	1.02	1.93	0.72	-0.1	0.93
Minimum	0.70	0.50	-0.11	0.80	1.51	0.41	-0.23	0.73	1.64	0.51	-0.13	0.91	1.38	0.67	-0.19	0.77
Maximum	2.83	0.73	0.24	1.09	1.98	0.79	0.11	1.13	2.13	0.65	-0.01	1.12	1.96	0.83	0.05	1
Average Mean	1.69	0.61	0.01	0.94	1.79	0.59	-0.11	0.93	1.84	0.58	-0.06	1.00	1.66	0.74	-0.07	0.89

Mz= Mean Size, SD=Standard deviation, S_K= Skewness, K_G= Kurtosis

Scatter plots

The geological significance of the size parameter can be well understood by correlating two variables viz., Mean size vs Standard deviation, Mean size vs Skewness, Mean size vs Kurtosis etc. Owing to the fact that the grain size parameter is environmentally sensitive, it is often used to interpret the various facets of depositional environments (Rammohan Rao et al., 1982). Scatter plots are very helpful to understand the various depositional environments.

Mean size vs standard deviation

The scatter plot between Mean grain size vs Standard deviations evidently show that all the microenvironments show negative relation, signifying that increase in sorting of sediment with decrease in grain size (fine size). In the NE (Figure 2a) season, all environments show negative relation with moderately sorted grains and fine sand sediment as dominant constituents (Mohan and Rajamanickam., 1998). Most of the sediment samples in SW monsoon season show moderate sorting except dune and backshore environment that shows positive relation, signifying increase in sorting of sediments(Figure 3a). Coarse sand is dominant constituent in dune and foreshore environments.

Mean size vs skewness

The scatter plot between Mean grain size and skewness reveals, negative relation in all microenvironments in NE monsoon season (Figure 2b). Generally, increase in mean size value (fine material) exhibits negative skewness. Negative skewness of sediments takes place in high-energy conditions (Angusamy and Rajamanickam, 2006). In SW monsoon season, berm and foreshore shows negative skewness which means that sediments were subjected to high energy conditions. Dune and backshore doesn't show any significant relation with mean size and skewness (Figure 3b).

Mean size vs kurtosis

In NE monsoon season the bivariate plots between mean grain size vs kurtosis values, reveal positive correlation with leptokurtic nature in dune, backshore, berm environments with fine sand as dominant material except foreshore environment (Figure 2c). In SW monsoon season all the environments except dune, show positive relation with leptokurtic nature (Figure 3c).

Standard deviation vs skewness

The scatter plots between standard deviation and skewness in NE monsoon season show positive relationship at all microenvironment levels, signifying increase in skewness, decrease in sorting, this may be due to littoral and alongshore currents, with moderate grain size sediments (Venkatramanan et al., 2011) (Figure 2d). In NE monsoon season berm environment, showing negative relation, signifies moderately sorted with coarse skewness. In SW monsoon season, the plot (Figure 3d) dune environs disclose negative relationship and the backshore and berm, show positive relation further signifying decrease in skewness with increase in standard deviation. However in the foreshore environment shows no relation between standard deviation and skewness.

Standard deviation vs kurtosis

The scatter plot between standard deviation vs kurtosis showing platy to mesokurtic nature, indicates negative relationship between standard deviation with kurtosis. Kurtosis values decrease with increase in sorting of sediments with moderately sorted sediments. In the foreshore environment, there is no relationship between standard deviation and kurtosis (Figure 2e). In SW monsoon season, majority of the samples show platy to leptokurtic nature and moderately well-sorted sediments (Figure 3e).

Skewness vs kurtosis

In NE and SW monsoon seasons, the scatter plots between skewness vs kurtosis shows positive values which implies very fine skewed symmetry (Figure 2f). In NE monsoon season the skewness and kurtosis values show negative relation in dune, backshore, berm and foreshore environments. In SW monsoon season such plot shows positive relationship between two variables except backshore and berm environments (Figure 3f).

CM diagrams

Based on range, size and energy level of transportation, CM diagrams aid in understanding, analyzing the mechanism and mode of transportation of sediments and gives an insight into depositional environments, factors responsible for the formation of clastic sediments. The plotting and interpretation of CM plot are adopted from Passagea. (1957, 1964). C represents one percentile of the grain size distribution plotted against to the M value which represents the median size of the sediment sample on double logarithmic paper. The CM diagrams of NE and SW seasons (Figures 4a and 4b; 5a and 5b) depicts that sediment transported for rolling bottom suspension and rolling and graded suspension representing their deposition by tractive currents and beach processes. Bottom suspension and rolling and graded suspension and rolling mode of transportation is predominant in both NE and SW monsoon seasons.

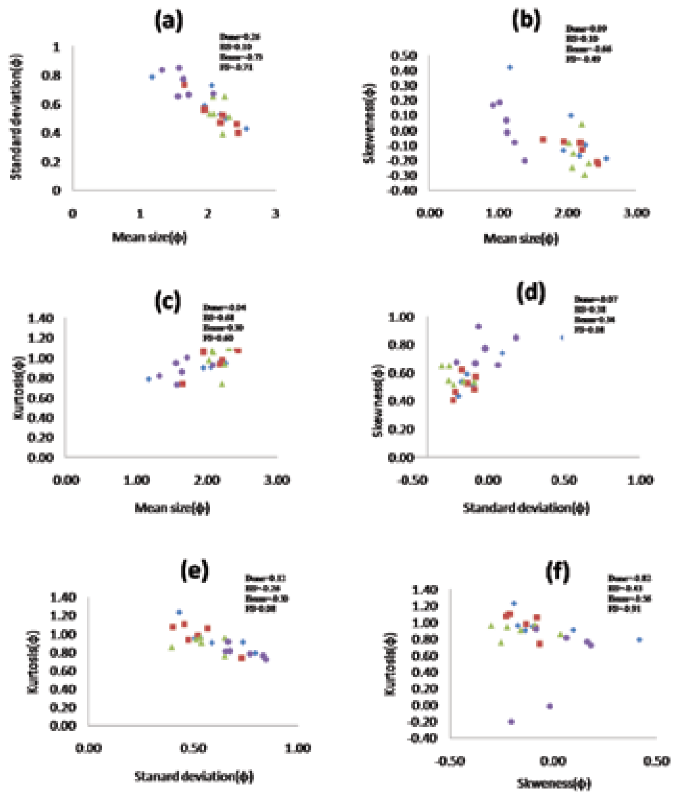

Figure 2. Scatter plots of grain size parameters (a) mean size vs standard deviation, (b) mean size vs skewness, (c) mean size vs kurtosis, (d) skewness vs standard deviation, (e) standard deviation vs kurtosis and (f) skewness vs kurtosis of Govindampalli – Durgarajupatnam coastal sands (NE monsoon season).

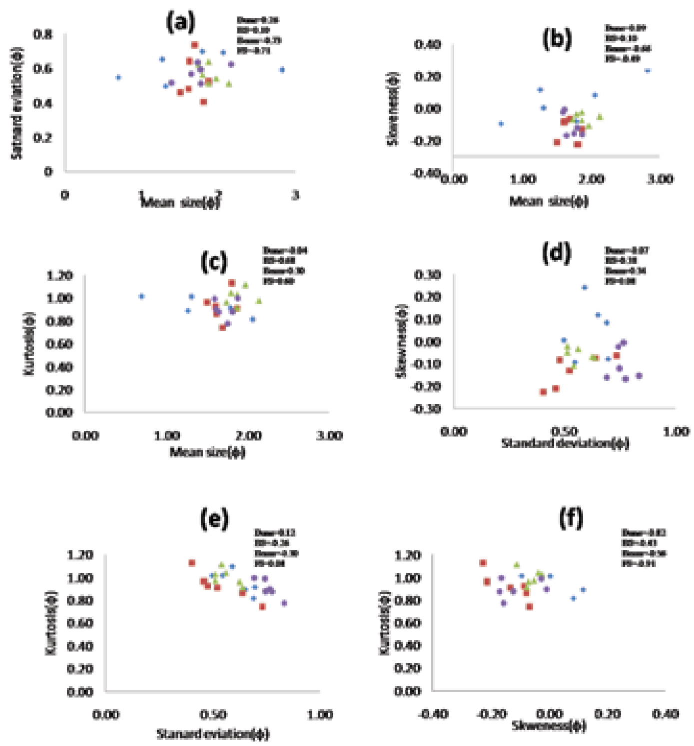

Figure 3. Scatter plots of grain size parameters (a) mean size vs standard deviation, (b) mean size vs skewness, (c) mean size vs kurtosis, (d) skewness vs standard deviation, (e) standard deviation vs kurtosis and (f) skewness vs kurtosis of Govindampalli – Durgarajupatnam coastal sands (SW monsoon season).

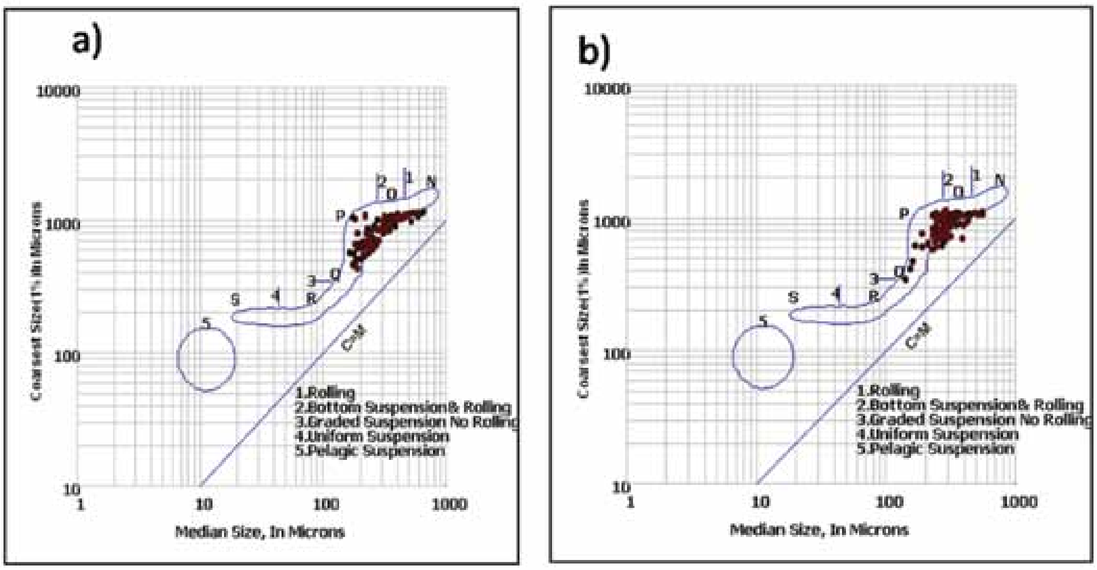

Figure 4. CM diagram showing mode of transportation of sediments (a) NE monsoon season (b) SW monsoon season.

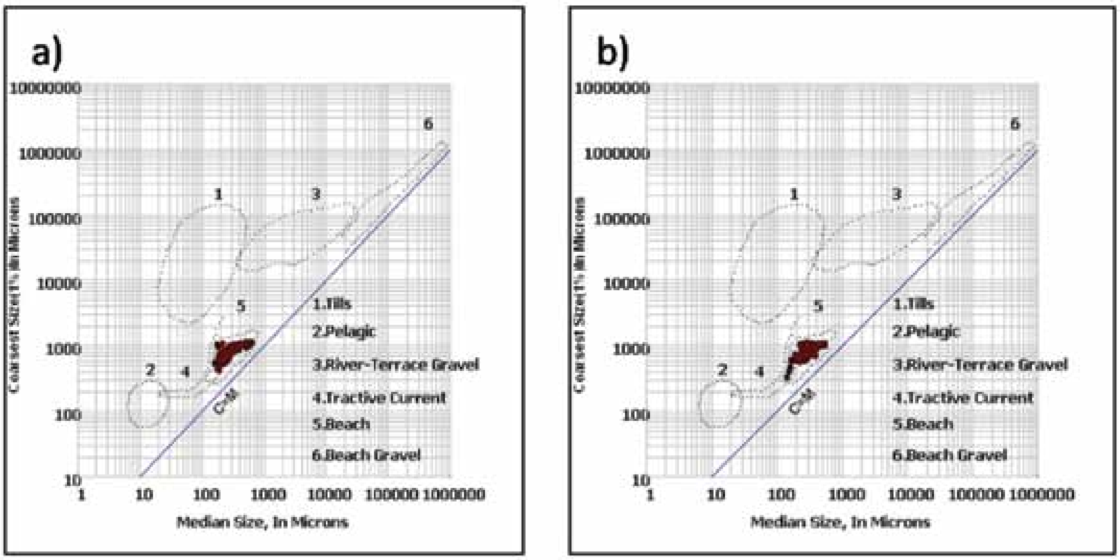

Figure 5. CM diagram showing depositional environments of sediments. (a) NE monsoon season (b) SW monsoon season.

Factor Analysis

Factor analysis was carried out to know the significant parameters contributing the distribution and deposition of sediments in the investigation area.NE and SW monsoon seasons (Table 2a and 2b) show mainly two factor assemblages which are contributing in dispersal and deposition of sediments. Factor analysis shows a total variance of 85.59% and 67.46% for the NE and SW monsoon seasons respectively. In NE monsoon season, first factor assemblage accounted for about 53.69% with substantial loading attributed to kurtosis (K_G) and mean grain size (Mz) assemblage (Table 2a), and second factor component (uncorrelated pairs of element to the first factor assemblage) is skewness (S_K) attributes to 31.89% of variance. Whereas in case of SW monsoon season, majorly two components attribute in a dispersal of the sediments i.e., kurtosis (K_G) and skewness (Sk) with 41.26% and 26.20% of the variance. In NE monsoon season mean size and kurtosis and in SW monsoon season kurtosis and skewness plays dominant role in dispersal and distribution of sediments in the investigation area and the same has been figuratively expressed in Figure 6.

Linear discriminate function analysis (LDF)

Linear discriminate function analysis plays a key role to explain and understand the depositional environments

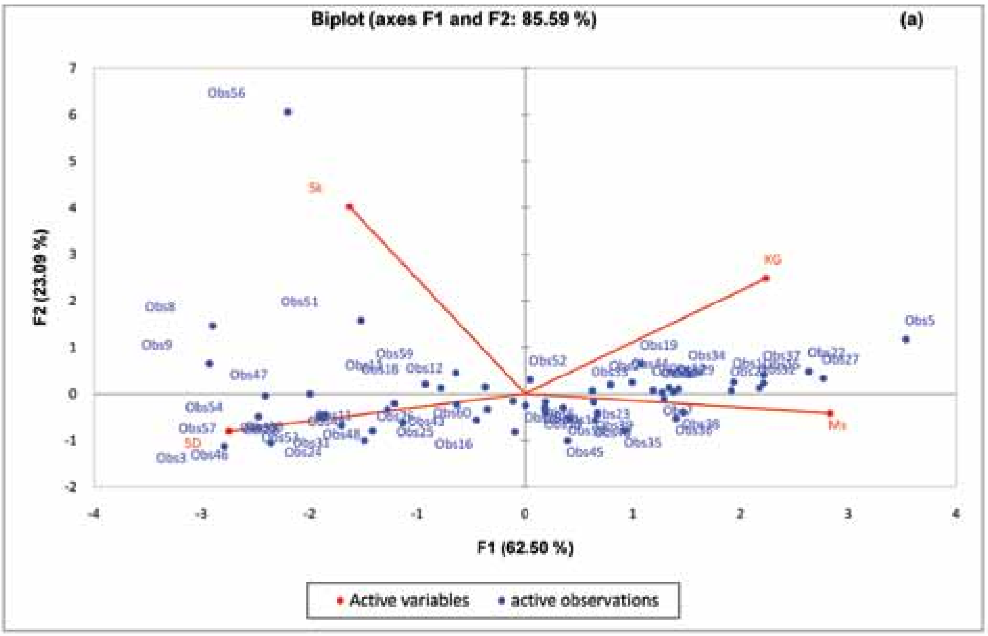

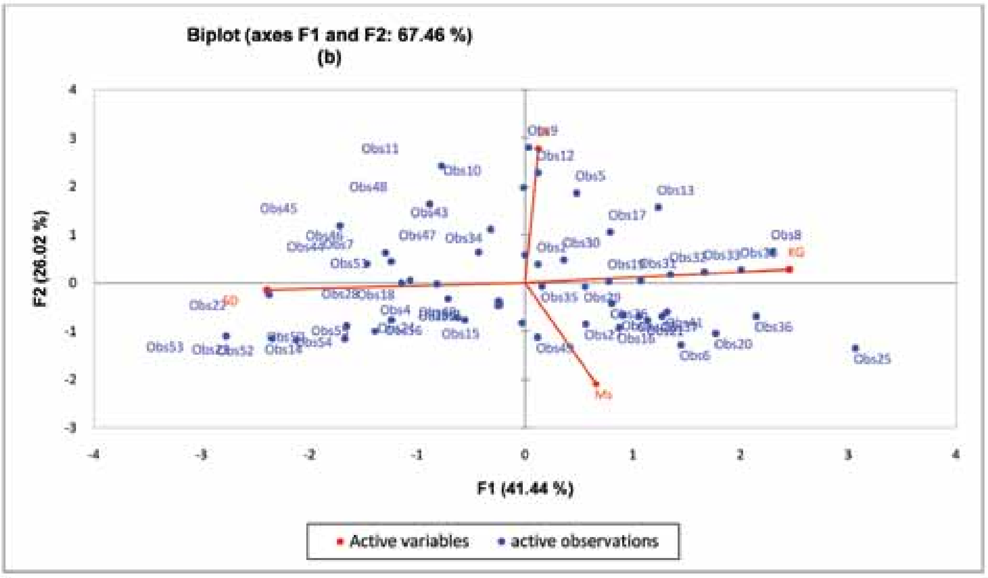

Figure 6. Factor analysis for the (a) NE monsoon and (b) SW monsoon season sediments.

Table 2. Factor analysis for (a) NE monsoon season and (b) SW monsoon season.

Parameters	**Factors (NE monsoon Season)**		**Factors (SW monsoon Season)**	
	1	**2**	**1**	**2**
Mean Size	0.778	-0.514	0.175	-0.634
Standard deviation	-0.872	0.284	-0.883	0.052
Skewness	-0.093	0.961	0.132	0.802
Kurtosis	0.880	0.920	0.907	-0.016
Total	2.148	1.276	1.650	1.048
% of Variance	53.69	31.89	41.26	26.20
Cumulative %	53.69	85.59	41.26	67.46

Table 3. Linear discriminate function analysis of sediments.

NE MONSOON SEASON				SW MONSOON SEASON		
Environments	Y1	Y2	Y3	Y1	Y2	Y3
Dune	-2.4712	75.1440	-3.1589	-1.7479	68.4797	-2.7813
BS	-1.2747	73.8841	-4.8035	-1.7576	66.1101	-1.9559
Berm	-4.0494	105.3245	-5.6338	-2.0832	68.3246	-2.0804
Foreshore	-1.1542	83.1091	-2.3386	-0.9808	77.1682	-3.9383

of beach sediments, (Sahu, 1964). Linear discriminate function analysis has explained to interpret the fluctuations of energy and fluidity factors correlated with different processes and sediment deposition.

To distinguish environment of deposition the following equation has been applied:

Y1 = -3.5688M+ 3.7016r2- 2.0766SK+ 3.1135KG ------(1)

Here Y is $\geq$ -2.7411, environment of deposition is beach, and if Y is $\leq$ -2.7411, environment of deposition is Aeolian.

Y2 = Shallow marine = 15.6534M + 65.7091r2 + 18.1071SK + 18.5043KG ------------ (2)

Here Y is $\geq$ 63.3650, environment of deposition is shallow marine, and if Y is $\leq$63.3650, environment of deposition is beach.

Y3 = 0.2852M- 8.7604r2- 4.8932SK+ 0.0428KG -----(3)

Here Y is $\geq$-7.4190, environment of deposition is shallow marine, and if Y is $\leq$-7.4190, environment of deposition is fluvial.

(M= mean, r = standard deviation, SK= Skewness and KG= kurtosis)

In NE monsoon season 75% samples fall in Y1 environment, (dune, backshore and foreshore) that indicate littoral processes and berm environment shows 25% samples fall in aeolian condition (Table 3).In bothY2 and Y3 environments total samples belong to shallow marine condition. In SW monsoon season most of the samples fall in Y1 environment as a result of littoral process. Both Y2 and Y3 environments most of the samples fall in shallow marine condition (Table 3). The variations of the energy conditions correlated with the tractive currents.

DISCUSSION

The textural parameters reveals most of the samples showing medium to fine grain in all micro environments, which results by the existence of intermittent energy conditions in north east monsoon season. But in south west monsoon season, most of the samples exhibits coarse to fine grains in dune region and medium to fine grain in backshore, berm and foreshore environments. The wide spectrum of grain size of sediment indicates the differential energy conditions at different environments. However, in both seasons the standard deviation values show, well to moderately sorting in dune, backshore and berm environments. It indicates removal of fine material leading to better sorting of sediments. Moderately well to poorly sorting in foreshore environment signifies the dominance of winnowing and panning action by waves and currents. Skewness value ranges in between very coarse to very fine symmetry depicting the prevalence of high to low energy conditions. The average skewness values in both seasons (Table 1a and 1b) indicate the nearly symmetrical distribution. The dominance of platy to leptokurtic nature reflects immaturity as well as maturity of the sediments in the depositional environments. The average values in both seasons reveal the presence of mixed population (both coarse and fine) in the study area. CM plots throw a light on the modes of transportation of sediments and depositional environments. They reveal that sediments were dominantly transported by rolling, rolling and bottom suspension and graded suspension and most of the sediments were deposited by tractive currents and beach processes. Factor analysis was carried out to know the distribution and deposition of the beach sediments. Mean size and kurtosis parameters play dominant role in NE monsoon season where as skewness and kurtosis plays dominant role in dispersal and distribution of sediments in SW monsoon season. Correlation between CM (C=Percentile, M=Median) plots and LDF (Linear discriminate function) analysis establishes the fact that littoral processes with tracative action played vital role in deposition of sediments in shallow marine condition, with an exception at berm microenvironment, where sediments were deposited by aeolian activity in NE monsoon season.

CONCLUSION

Comparison of two season's average values of various parameters viz., mean size, standard deviation, skewness and kurtosis reveal medium to fine grain size, moderately well-sorted sediments, nearly symmetrical distribution and platy to leptokurtic in nature respectively. CM plots of both seasons reveals that sediments were dominantly transported by rolling, rolling and bottom suspension and graded suspension and most of the sediments were deposited by tractive currents and beach processes. Similarly factor analysis results show that mean size and skewness parameters plays dominant role in dispersal and distribution of sediments in NE and SW monsoon respectively. LDF(Linear discriminate function) analysis reveals that in NE monsoon season, sediments were deposited by beach processes and aeolian activity where as in SW monsoon season, only beach processes play major role in deposition of sediments in shallow marine condition.

ACKNOWLEDGEMENTS

Ms. K. Nagalakshmi is thankful to the Department of Science and Technology (DST), Government of India, New Delhi, for the financial support in the form of INSPIRE Fellowship (Grant no. IF131129).

Compliance with Ethical Standards

The authors declare that they have no conflict of interest and adhere to copyright norms.

REFERENCES

Angusamy, N. and Rajamanickam, G.V., 2006. Depositional environment of sediments along the southern coast of Tamilnadu. Oceanologia, 48, 87-102.

Avramidis, P., Samiotis, A., Kalimani, E., Papoulis, D., Lampropoulou, P. and Bekiari, V., 2012. Sediment characteristics and water physicochemical parameters of the Lysimachia Lake, Western Greece. Environ. Earth Sci., 70, 383-392.

Bangaru Naidu, K., Reddy, K.S.N., Ravi Sekhar, Ch., Ganapathi Rao, P. and Murali Krishna, K.N., 2016. Grain size distribution of coastal sands between Gosthani and Champavthi rivers confluence, East coast of India, Andhra Pradesh. J. Indian Geophys. Un., 20, 351-361

Blott, S.J. and Pye, K., 2001. GRADISTAT: a grain size distribution and statistic package and analysis of unconsolidated sediments. Earth surface processes and landforms, 26,11,1237 – 1248.

Folk, R.L. and Ward, W., 1957. Brasos River bar, a study in the significance of grain size parameters, J. Sed. Petrol., 27, 3-26.

Friedman, G.M., 1961. Dynamic processes and statistical parameters compared for size frequency distribution of beach and river sands. J. Sed. Petrol., 32, 327-354.

Friedman, G.M., 1967. Dynamic processes and statistical parameters compared for size analysis (sic) distribution of beach and river sands 37, 327-354.

Giosan, L., Cliff, P.D., Constantinescu, S. and Tabrez, A.R., 2005. Development of the iNuds mega – delta. A Backshore tract of papers presented at the International Conference of deltas. Geological modeling and management Ho Chi Minh City, Vietnam Acad. Sci. Tech., 19.

Inman D.L., 1952. Measures describing size of sediments. J. Sed. Petrol., 19, 125-147.

Ingram, R.L., 1970. Sieve analysis, procedure in sedimentary petrology, Willey Interscience, Newyork.

Krumbein, W.C. and Pettijohn, F.J., 1938. Manual of sedimentary petrology, Appleton Central crafts, New York., 178 – 194.

Lingdholmn, R.C., 1987. A practical approach to sedimentology. Allen. Unwin Publi., 720

Mohan, P.M. and Rajamanickam, G.V., 1998. Depositional environment: Inferred from grain size along the coast of Tamilnadu. J. Geol. Soc. India., 52, 95-102.

Nageswara Rao, P.V., Suryam, R.K. and Ranga Rao, V., 2005. Depositional environment inferred from grain size parameters of the beach sediments between false devi point to Kottapatnam, Andhra Pradesh coast. J. Geol. Soc. India., 65, 317-324.

Oaie, G.H., Secrieru, D., Szobotika, S.T., Fulga, C. and Stanica, A., 2005. Danube river: Sedimentological, mineralogical and geochemical characteristics of the bottom sediments. GeoEcoMarina, 12, 77-85

Passega, R., 1957. Texture as a characteristic of clastic deposition, Am. Assoc. Petrol. geol., 41, 1952-1984.

Passega, R., 1964. Grain size representation by C-M pattern as a geological tool. J. Sed. Petrol., 1-34, 830-847.

Rammohan Rao, T., Shanmukha Rao, Ch. and Sanyasi Rao, K., 1982. Textural analysis and mineralogy of the black sand deposit of Visakhapatnam- Bhuminipatnam coast, Andhra Pradesh, India. J. Geol. Soc. India., 23, 284-289.

Sahu, B.K., 1964. Depositional mechanism from the size analysis of clastic sediments. J. Sed. Petrol. 34, 73-83.

Senapthi venakatraman., Ramkumar, T., Anithamary, I. and Ramesh, G., 2011. Variations in texture of beach sediments in the vicinity of the Tirumalairajanar river mouth of India. Int. J. Sed. Res., 26, 460-470.

Seralathan, P. and Padamalal, D., 1994. Textual studies of surfacial sediments of Muvattupvzha river and central Vembanad estuary, Kerala. J. Geol. Soc. India, 43, 179-190

Veeraiah, M. and Varadachari, V.V.R., 1975. Depositional environments coastal sediments of Calangute, Goa. Sed. Geol., 14, 63-74.

Venkatramanan, S., Ramkumar, T., Anithmary, I. and Ramesh, G., 2011. Variations in texture of beach sediments in the vicinity of the Thirumalai Rajan river mouth of India. Int. J. Sed. Res., 26 (4), 460-470.

Visher, G.S., 1969. Grain Size distribution and depositional process. J. Sed. Petrol., 39,1074-1016.

Received on: 31.5.18; Revised on: 3.8.18; Accepted on: 7.8.18

GUIDE FOR AUTHORS

The Journal of Indian Geophysical Union (J-IGU), published bimonthly by the Indian Geophysical Union (IGU), is an interdisciplinary journal from India that publishes high-quality research in earth sciences with special emphasis on the topics pertaining to the Indian subcontinent and the surrounding Indian Ocean region. The journal covers several scientific disciplines related to the Earth sciences such as solid Earth geophysics, geology and geochemistry, apart from marine, atmosphere, space and planetary sciences. J-IGU welcomes contributions under the following categories:

- Research papers and short notes reporting new findings.
- Review articles providing comprehensive overview of a significant research field.

In addition, J-IGU also welcomes short communications, after communications and report on scientific activity, book reviews, news and views, etc.

The manuscript should be submitted electronically as a single word format (.doc file) including the main text, figures, tables, and any other supplementary information along with the signed "Declaration Letter". The manuscript should be submitted by email (jigu1963@gmail.com) to the Chief Editor.

After acceptance of the manuscript the corresponding author would be required to submit all source files (text and Tables in word format) and figures in high resolution standard (*.jpg, *.tiff, *.bmp) format. These files may be submitted to J-IGU as a single *.zip file along with the "Copyright Transfer Statement".

IMPORTANT INFORMATION

Ethics in publishing
J-IGU is committed to ensuring ethics in publication and takes a serious view of plagiarism including self-plagiarism in manuscripts submitted to the journal. Authors are advised to ensure ethical values by submitting only their original work and due acknowledgement to the work of others used in the manuscript. Authors must also refrain from submitting the same manuscript to more than one journal concurrently, or publish the same piece of research work in more than one journal, which is unethical and unacceptable. Editor of J-IGU is committed to make every reasonable effort to investigate any allegations of plagiarism brought to his attention, as well as instances that come up during the peer review process and has full authority to retract any plagiarized publication from the journal and take appropriate action against such authors if it is proven that such a misconduct was intentional.

Similarly, Editor and Reviewers are also expected to follow ethical norms of publishing by ensuring that they don't use any unpublished information, communicated to them for editorial or review purpose, in their own research without the explicit written consent of the author. They are also expected to keep manuscript/ data/ observations/ any other information related to the peer review confidential to protect the interest of the authors. Reviewers should refrain from reviewing the manuscripts in which they have conflicts of interest resulting from competitive, collaborative, or other relationships or connections with any of the authors, companies, or institutions connected to the manuscript.

Conflict of interest
All authors are requested to disclose any actual or potential conflict of interest including any financial, personal or other relationships with other people or organizations within three years of beginning the submitted work that could inappropriately influence, or be perceived to influence, their work.

Submission declaration
Submission of a manuscript implies that the work has not been published previously and it is not under consideration for publication elsewhere, and that if accepted it will not be published elsewhere in the same or any other form, in English or in any other language, without the written consent of the publisher. It also implies that the authors have taken necessary approval from the competent authority of the institute/organization where the work was carried out.

Copyright
After acceptance of the manuscript the corresponding author would be required to sign and submit the "Copyright Transfer Statement".

MANUSCRIPT PREPARATION

The corresponding author should be identified (include E-mail address, Phone/Mobile number). Full affiliation and postal address must be given for all co-authors.

Abstract:
An abstract of not more than 300 words must be included.

Text:
The manuscript should be structured to include a front page containing the title, Author(s) name, affiliation and address of the institute, where the work was carried out, a short title, and 5-to-6 Key words. Author(s) present address, if different from the above mentioned address, may be given in the footnote. The corresponding author should be identified with an asterisk and his/her email ID should be provided. This page should be followed by the main text consisting of Abstract, Introduction, Methods/ Techniques/ Area description, Results, Discussion, Conclusions, Acknowledgements, and References. Tables and Figures with captions should be inserted at the end of main text. It should not be inserted in the body of the text.

Figures/ Illustrations:
All figures should be provided in camera-ready form, suitable for reproduction (which may include reduction) without retouching. Figures in high-resolution (at least 300 dpi) standard formats (*.jpg, *.tiff, *.bmp) are acceptable. Figures should be numbered according to their sequence in the text. References should be made in the text to each figure. Each figure should have a suitable caption.

Tables:
Authors should take note of the limitations set by the size and layout of the journal. Table should not exceed the printed area of the page. They should be typed on separate sheets and details about the tables should be given in the text. Heading should be brief. Large tables should be avoided and may be provided as supplementary information, if required.

Equations:
Equations should be numbered sequentially with Arabic numerals and cited in the text. Subscripts and Superscripts should be set off clearly. Equation writing software that presents each equation as an object in MS Word will be accepted. Style and convention adopted for the equations should be uniform throughout the paper.

References:
All references to publications cited in the main text should be presented as a list of references in order following the text and all references in the list must be cited in the text. References should be arranged chronologically, in the text. The list of references should be arranged alphabetically at the end of the paper.

References should be given in the following form:
Kaila, K.L., Reddy P.R., Mall D.M., Venkateswarlu, N., Krishna V.G. and Prasad, A.S.S.S.R.S., 1992. Crustal structure of the west Bengal Basin from deep seismic sounding investigations. Geophys. J. Int., 111,45-66.

REVIEW PROCESS:

All manuscripts submitted to the journal are peer-reviewed. It is advisable to send the contact details of 4 potential reviewers along with the manuscript to expedite the review process. Editor has the option to select reviewers from the list or choose different reviewers. The review process usually takes about 3 months. All enquiries regarding the manuscript may be addressed to the Editor.

GALLEY PROOF:

Technical editing of manuscripts is performed by the editorial board. The author is asked to check the galley proof for typographical errors and to answer queries from the editor. Authors are requested to return the corrected proof within two days of its receipt to ensure uninterrupted processing. The editor will not accept new material in proof unless permission from the editorial board has been obtained for the addition of a "note added in proof". Authors are liable for the cost of excessive alterations to galley proof.

PUBLICATION CHARGES:

There are no page charges for publication and printing charges for b/w figures. However, in view of substantial cost involved in printing of color figures, author will be charged for printing of pages containing color figures @ Rs. 2,500/- per page. The charges may be revised at any time based on cost of printing and production. Author will receive an estimate/ invoice of the color figures reproduction cost along with the galley proof. It is the responsibility of the author to remit the color figures reproduction cost within one month of the receipt of the estimate/invoice.

The corresponding author will receive a soft copy (pdf format) of his/her published article. Should the author desire to purchase reprints of his/her publication, he/she must send the duly signed Reprint Order Form (accompanies the galley proof and contains price details) along with the corrected galley proof to the Editor. The reprint charges must be paid within one month of sending the Reprint Order Form.

Any payment related to printing of color figures and/or purchase of reprints should be made in the form of a Demand Draft in the name of Treasurer, Indian Geophysical Union, payable at Hyderabad.

You may download the pdf file from: http://www.j-igu.in/IGU-GuideforAuthors.pdf